

Directed evolution of DNA-wrapped single-walled carbon nanotube complexes for optical sensing

Présentée le 25 novembre 2021

Faculté des sciences de base
Laboratoire de nanobiotechnologie
Programme doctoral en chimie et génie chimique

pour l'obtention du grade de Docteur ès Sciences

par

Benjamin Paul Johanès Gabriel LAMBERT

Acceptée sur proposition du jury

Prof. B. Smit, président du jury
Prof. A. A. Boghossian, directrice de thèse
Dr L. Cognet, rapporteur
Prof. M. Zheng, rapporteur
Prof. F. Stellacci, rapporteur

*We're forever teetering on the brink of the
unknowable, and trying to understand
what can't be understood.*

Isaac Asimov,
The Caves of Steel

À mes parents...

Acknowledgements

I would like first to thank you for reading this thesis. The work presented in this thesis was only made possible because of the help and support I received from many individuals. First, I am very grateful to my research advisor, **Prof. Ardemis A. Boghossian**, who gave me the opportunity to run this research in her group. She guided me throughout the various stages of my PhD, supported my research interests and my research curiosity by encouraging me to try new ideas and to “think outside of the box”. I would also like to thank my thesis committee, **Prof. Ming Zheng, Dr Laurent Cognet, Prof. Francesco Stellacci** and **Prof. Berend Smit**, for their insightful comments and the rich discussions we had both during and after the exam.

I want to thank my colleagues at the LNB, both past and present. I am grateful to **Vitalijs Zubkovs** for teaching me so much about microscopy and spectroscopy and strengthen my passion for optics. I am thankful to **Nils Schürgers** which taught me all I had to know about microbiology and helped me develop rigor and creativity in research. I am deeply grateful to **Shang-Jung Wu** for always being here when I needed help, especially during the most difficult times of the PhD. Thank you again for your precious advices, you truly helped me become a more rigorous researcher than I was when I initially joined the group. To **Alice Gillen**, thank you for all these great memories we had both in and outside the lab (bubblegum). Even with the million things you had to do, you always managed to find some time to discuss with me and to cheer me up. Your energy and your determination will forever remain an inspiration for me. I want to thank **Alessandra Antonucci**, you are probably the kindest person I know (no doubt you are a Hufflepuff), thank you for always being here for me. To **Mohammed Mouhib**, thank you for your never-ending positivity and optimism. Our coffee breaks and bets with Shang really helped brighten many of my days. To **Melania Reggente**, thank you for your help but also thank you for being yourself with your unique personality. I don't know how you manage to find the energy you have to do all the things you do, but I am truly grateful to you for organizing all these activities which helped me relax during the PhD. To **Daniel Molina-Romero**, thanks for all the fun we had during the first year of PhD. To **Sara Behjati**, thank you for being so comprehensive with me, you sure have a bright future ahead of you in the lab. I want to thank the people I had the chance to work with: **Afsaneh Taheri, Yahya Rabbani, Shikhar Goel, Aishwarya Singh, Xingbo Shang** and **Michel-François Legrand**. Thank you all for your hard work and for giving me the opportunity to discover the joys of teaching. I also want to thank the other members of the LNB: **Sayyed Hashem Sajjadi, Niloufar Sharif, Hanxuan Wang, Charlotte Roulier, Niccolo Martinolli** but also **Xuwen Liu**,

Acknowledgements

Mary Wood, Sevil Cikrikci, Mina Ghorbani, Avip Bastakoti and Amirmostafa Amirjani. I also want to thank **Arnaud Gelb, Sadegh Kamaei and Kun-Han Lin.** Thank you all for your help and for the nice moments we shared together.

I am grateful to **Dr Christophe Roussel** for letting me be his teaching assistant. It was a pleasure to work with you and I hope we will have the opportunity to work again together one day. I would also like to thank all the EPFL staff who helped me during the thesis, in particular **Dr Laure Menin** for the mass spectrometry measurements.

I would like to thank all my friends, without whom I could not have made it that far. First, I want to thank **Yoann, Alexandre and Florian.** I have been friend with you for so long that I can consider you as family, thank you for always being there when I come back home. I also want to thank my former Island band members: **Corentin, Alexis, Clémence and Maelig.** What we lived together will always remain a unique experience for me. My stay in Switzerland was also more enjoyable thanks to the Normandy team, **Clémence and Anthony (and Romane).** These University years would never have been the same without my small team of physicists: **Adrien, Aurore, Jean-Baptiste and Yohann.** You have always been around to help me during tough time or to make me laugh, it is difficult to imagine what I would have done without you.

Finally, I want to thank my family for their unconditional support. To my parents, **Anne and Philippe,** thank you for always supporting my choices in life and encouraging me throughout my studies. You have constantly been a source of inspiration for me and I will do my best to continue to make you proud. I would also like to thank my siblings, **Florence, Sophie, Anne-Claire and Pierre-André,** you were invariably there when I needed advices and help. I want to thank my grand-father, **André,** for supporting me during my studies and for inspiring me with your great mind. Lastly, I want to thank **Audrey.** You helped me in every aspect of my life since we first met nearly eight years ago and made me a better person. You and **Gouache** have helped me overcome the many challenges I faced during these times. Thank you for all these perfect years we spent together and for the many future years we will share. I love you and I always will.

Lausanne, November 9, 2021

B. L.

Abstract

Single-walled carbon nanotubes (SWCNTs) have garnered significant interest for their applications in optical biosensing. SWCNTs exhibit a sensitive and photostable fluorescence in the near-infrared (NIR) range, allowing for the continuous monitoring of target analytes *in vivo* with minimal absorption from biological tissue. However, despite their advantages, the behavior of these nanomaterials can be difficult to predict, especially for bioconjugates, such as DNA-wrapped SWCNTs (DNA-SWCNTs), whose interactions are often insufficiently characterized and poorly understood. When non-covalently functionalized with single-stranded DNA, SWCNTs can exhibit improved colloidal stability, biocompatibility and sensing capabilities towards a wide collection of target analytes. These DNA-SWCNT complexes are highly versatile as their optical properties can be modulated by changing the DNA sequence. However, the relationship between the DNA sequence and the optical properties of the resulting DNA-SWCNT complex is unknown, hindering the ability to engineer these complexes in a predictive manner. As a result, the design of DNA-SWCNT sensors currently relies on empirical approaches that often result in sensors with compromised performances.

In this thesis, we take inspiration from strategies developed in the field of protein engineering to engineer the DNA-SWCNTs in a more controlled and directed manner. Using directed evolution, an approach extensively applied for engineering proteins, we engineer improved DNA-SWCNT complexes through iterative cycles of mutation, screening and selection. We first apply this strategy to significantly improve the fluorescence intensity of an existing DNA-SWCNT sensor while retaining the sensor performance. We then extend this approach to engineer new sensors by tuning different sensing properties, such as selectivity and sensitivity, in a chirality-dependent manner for the multimodal detection of mycotoxins in food products. Building on the knowledge acquired from the mutants generated during these previous iteration cycles, we establish DNA design rules allowing us to engineer a new generation of DNA-SWCNT sensors through rational design. We additionally expand our study to explore alternative approaches to further modulate the properties of DNA-SWCNTs beyond the capabilities of natural DNA oligonucleotides through the incorporation of artificial chemical modifications. Finally, we conclude with scalable and high-throughput approaches for mutating, amplifying, purifying, and conjugating DNA sequences to SWCNTs to increase the sizes of the libraries that can be screened for directed evolution. The approaches presented in this thesis therefore provide a means of tackling bottleneck challenges in the design of DNA-SWCNT complexes through the

Abstract

exploitation of bioengineering strategies.

Keywords: Single-walled carbon nanotubes (SWCNTs), DNA-SWCNTs, nanosensors, near-infrared (NIR) fluorescence, directed evolution, synthetic biology, mycotoxins, semi-rational

Résumé

Les nanotubes de carbone mono-paroi (SWCNTs) ont suscité un intérêt tout particulier dans le domaine de la biodétection optique. Ces SWCNTs possèdent une fluorescence photostable et sensible dans le proche infrarouge (NIR), permettant une analyse en continu de molécules *in vivo* tout en limitant l'absorption des tissus biologiques. Malgré ces avantages, le comportement de ces nanomatériaux peut être difficile à prédire, en particulier dans le cas de nanomatériaux bioconjugués, tels que les SWCNTs conjugués à de l'ADN (DNA-SWCNTs), pouvant avoir des interactions mal caractérisées et peu comprises. Lorsqu'ils sont fonctionnalisés avec de l'ADN simple brin de manière non-covalente, les SWCNTs peuvent acquérir une meilleure stabilité colloïdale et biocompatibilité ainsi que des capacités de détection envers une pléthore de molécules. Ces complexes bénéficient d'une importante versatilité dû au fait que leurs propriétés peuvent être modulées en changeant la séquence de l'ADN. Toutefois, la relation entre séquence de l'ADN et propriétés des complexes reste inconnue, entravant la possibilité de perfectionner les complexes de manière prédictive. En conséquence, la conception des DNA-SWCNTs repose actuellement majoritairement sur des approches empiriques, amenant à la création de senseurs présentant des performances plus faibles.

Dans cette thèse, nous nous inspirons de stratégies développées pour l'ingénierie des protéines afin de concevoir les DNA-SWCNTs de façon plus contrôlée et dirigée. A l'aide de l'évolution dirigée, une approche très répandue pour l'ingénierie des protéines, nous démontrons la possibilité de concevoir des DNA-SWCNTs plus performants à travers des cycles de mutation, criblage et sélection. Nous montrons tout d'abord que cette approche peut être utilisée efficacement pour améliorer la fluorescence de DNA-SWCNTs, tout en permettant de garder les capacités de détection des complexes. Ensuite, nous démontrons l'utilité de cette approche pour le développement de nouveaux senseurs en modifiant diverses propriétés telles que leurs sélectivité et sensibilité, et dépendamment de la chiralité des SWCNTs afin d'effectuer une détection simultanée de mycotoxines dans des produits alimentaires. En se basant sur les connaissances acquises lors des cycles d'évolution dirigée, nous montrons l'établissement de règles permettant de concevoir de nouveaux DNA-SWCNTs en changeant la séquence d'ADN de façon rationnelle. De plus, nous explorons des manières alternatives afin de modifier davantage les propriétés des DNA-SWCNTs au-delà des capacités naturelles de l'ADN à travers l'incorporation de modifications chimiques dans les séquences d'ADN. Enfin, nous finissons cette dissertation sur une approche permettant la mutation, l'amplification, la purification et

Résumé

la conjugaison de séquence d'ADN aux SWCNTs à grande échelle afin d'augmenter le nombre et la diversité des échantillons testés lors de l'évolution dirigée. Les approches présentées dans cette thèse offrent des moyens d'aborder les problèmes actuellement limitant la conception des DNA-SWCNTs à travers l'exploitation de stratégies développées pour la bioingénierie.

Mots clés : Nanotubes de carbone mono-paroi (SWCNTs), DNA-SWCNTs, nanosenseurs, fluorescence proche infrarouge (NIR), évolution dirigée, biologie synthétique, mycotoxines, semi-rationnel

Contents

| | |
|---|---------------|
| Acknowledgements | v |
| Abstract | vii |
| Résumé | ix |
| Abbreviations | xv |
| List of Figures | xxv |
| List of Tables | xxviii |
| Introduction | 1 |
| Background and context | 1 |
| Single-Walled Carbon Nanotubes (SWCNTs) | 2 |
| Deoxyribonucleic acid (DNA) | 6 |
| DNA-SWCNT complexes | 8 |
| Engineering of DNA-SWCNTs: state of the art | 10 |
| Protein design in synthetic biology | 13 |
| Objective of the thesis | 18 |
| 1 Modulating the optical properties of DNA-SWCNT sensors by directed evolution | 23 |
| 1.1 Abstract | 23 |

xi

Contents

| | | |
|----------|---|-----------|
| 1.2 | Introduction | 23 |
| 1.3 | Materials and methods | 25 |
| 1.4 | Results and discussion | 31 |
| 1.5 | Conclusion | 37 |
| 2 | Directed evolution of DNA-SWCNT sensors for the simultaneous detection of myco- toxins | 39 |
| 2.1 | Abstract | 39 |
| 2.2 | Introduction | 39 |
| 2.3 | Materials and methods | 41 |
| 2.4 | Results and discussion | 48 |
| 2.5 | Conclusion | 60 |
| 3 | Towards a semi-rational design of DNA-SWCNT sensors | 61 |
| 3.1 | Abstract | 61 |
| 3.2 | Introduction | 62 |
| 3.3 | Materials and methods | 64 |
| 3.4 | Results and discussion | 68 |
| 3.5 | Conclusion | 80 |
| 4 | Modulating the properties of DNA-SWCNTs through DNA chemical modification | 83 |
| 4.1 | Abstract | 83 |
| 4.2 | Introduction | 84 |
| 4.3 | Materials and methods | 85 |
| 4.4 | Results and discussion | 88 |
| 4.5 | Conclusion | 96 |
| 5 | Outlook on the directed evolution of DNA-SWCNTs with long oligonucleotides | 99 |
| 5.1 | Abstract | 99 |

| Contents | |
|---|------------|
| 5.2 Introduction | 99 |
| 5.3 Materials and methods | 101 |
| 5.4 Results and discussion | 105 |
| 5.5 Conclusion | 113 |
| General conclusion and perspectives | 115 |
| A Modulating the optical properties of DNA-SWCNT sensors by directed evolution | 121 |
| B Directed evolution of nanosensors for the detection of mycotoxins | 139 |
| C Towards a semi-rational design of DNA-SWCNT sensors | 183 |
| D Modulating the properties of DNA-SWCNTs through DNA chemical modification | 211 |
| E Outlook on the directed evolution of DNA-SWCNTs with long oligonucleotides | 233 |
| Bibliography | 234 |

Abbreviations

| | |
|-----------------|--|
| 1D | One Dimensional |
| A | Adenine |
| AFB1 | AFlatoxin B1 |
| AFBO | AFB1 exo-8,9-epOxide |
| AFM | Atomic Force Microscopy |
| ANG | ANGelicin |
| ATP | Aqueous Two-Phase |
| bp | base pair |
| BFP | Blue Fluorescent Protein |
| C | Cytosine |
| CD | Circular Dichroism |
| CFP | Cyan Fluorescent Protein |
| CMC | Critical Micelle Concentration |
| CoPhMoRe | Corona Phase Molecular Recognition |
| CoMoCAT | Cobalt Molybdenum CATalyzed process |
| COU | COUmarin |
| CVD | Chemical Vapor Deposition |
| Cys | Cysteine |
| DCE | 1,2-DiChloroEthane |
| DFHBI | (Z)-5-(3,5-Difluoro-4-hydroxybenzylidene)-2,3-dimethyl-3,5-dihydro-4H-imidazol-4-one |
| DI | DeIonised |
| DMSO | DiMethyl SulfOxide |
| DNA | DeoxyriboNucleic Acid |
| DON | DeOxyNivalenol |
| DOS | Density Of States |
| dsDNA | double-stranded DeoxyriboNucleic Acid |
| DTT | DiThioThreitol |
| EDTA | EthyleneDiamineTetraAcetic acid |
| eV | electron Volt |
| FAO | Food and Agriculture Organization |
| FB1 | Fumonisin B1 |

Abbreviations

| | |
|----------------|---|
| FWHM | Full-Width at Half-Maximum |
| G | Guanine |
| G4 | G quadruplex |
| GABA | γ -AminoButyric Acid |
| GFP | Green Fluorescent Protein |
| HEPES | (4-(2-hydroxyethyl)-1-piperazineethanesulfonic acid) |
| HiPco | High-Pressure carbon monoxide process |
| HPLC-MS | High-Performance Liquid Chromatography– tandem Mass Spectrometry |
| IEX | Ion-EXchange chromatography |
| InGaAs | Indium Gallium Arsenide |
| MB | Methylene Blue |
| MCS | Maximum Common Substructure |
| NIR | Near-InfraRed |
| NMR | Nuclear Magnetic Resonance |
| OTA | Ochratoxin A |
| PAGE | PolyAcrylamide Gel Electrophoresis |
| PCI | Phenol-Chloroform Isoamyl |
| PCR | Polymerase Chain Reaction |
| PL | PhotoLuminescence |
| PLE | PhotoLuminescence Excitation |
| QD | Quantum Dot |
| qPCR | quantitative Polymerase Chain Reaction |
| QY | Quantum Yield |
| RMSD | Root-Mean-Square Deviation |
| RNA | RiboNucleic Acid |
| SC | Sodium Cholate |
| SELEX | Systematic Evolution of Ligands by EXponential enrichment |
| SDC | Sodium DeoxyCholate |
| SDS | Sodium Dodecyl Sulfate |
| SDBS | Sodium DodecylBenzene Sulfate |
| ssDNA | single-stranded DeoxyriboNucleic Acid |
| STM | Scanning Tunneling Microscopy |
| SWCNT | Single-Walled Carbon Nanotube |
| T | Thymine |
| TAE | Tris-Acetate-EDTA |
| TBE | Tris-Borate-EDTA |
| TEM | Transmission Electron Microscopy |
| UV | UltraViolet |
| VIS | Visible |
| XNA | Xeno Nucleic Acid |

Abbreviations

| | |
|------------|----------------------------|
| YFP | Yellow Fluorescent Protein |
| ZEN | Zearalenone |

List of Figures

| | | |
|-----|---|----|
| 1 | Description of the SWCNT chiralities and electronic properties | 4 |
| 2 | Optical characterization of SWCNTs | 5 |
| 3 | Structures of double- and single-stranded DNA | 7 |
| 4 | Schematic of possible DNA wrapping conformations | 9 |
| 5 | Engineering of DNA-SWCNT complexes | 11 |
| 6 | Comparison of the approaches used to design proteins and SWCNT complexes | 13 |
| 7 | Schematic representation of the directed evolution approach of proteins | 17 |
| 1.1 | Application of directed evolution to DNA-SWCNT complexes | 31 |
| 1.2 | Increase of fluorescence intensity after two evolution cycles | 33 |
| 1.3 | Response of the DNA-SWCNT complexes to dopamine and glutamic acid | 36 |
| 2.1 | Directed evolution of the AFB1 sensor | 49 |
| 2.2 | Improving sensor performance using DNA shuffling | 50 |
| 2.3 | Directed evolution of the sensor's intensity and selectivity | 52 |
| 2.4 | Application of the evolved mycotoxin sensors | 54 |
| 2.5 | The sensors have two distinct mechanisms of interaction | 55 |
| 3.1 | Factors affecting the sensor's response towards AFB1 and FB1 | 69 |
| 3.2 | The AFB1 response can be improved by modifying the G-content | 71 |
| 3.3 | The G-content is related to the formation of secondary structures | 73 |

List of Figures

| | | |
|------|--|-----|
| 3.4 | Optimization and generalization of the AFB1 sensors | 74 |
| 3.5 | Optimization and generalization of the FB1 sensors | 76 |
| 4.1 | Effect of the modifications on the dispersibility of the DNA-SWCNTs | 89 |
| 4.2 | Effect of the modifications on the fluorescence of the DNA-SWCNTs | 91 |
| 4.3 | Comparison of the intensities after wrapping replacement with SDC | 92 |
| 4.4 | Effect of the modifications on the sensing capabilities of the DNA-SWCNTs . . | 94 |
| 4.5 | Importance of the preparation procedure on the effect of the modifications . . | 95 |
| 5.1 | Effect of the DNA length on the properties of DNA-SWCNTs | 106 |
| 5.2 | High-throughput generation and wrapping of long DNA oligomers | 109 |
| 5.3 | Fluorescence of DNA-SWCNT prepared from amplified colony DNA | 112 |
| A.1 | Kinetics of wrapping exchange | 121 |
| A.2 | Comparison between (AT) ₁₅ -SWCNT and (GT) ₁₅ -SWCNT complexes | 122 |
| A.3 | Influence of the number of mutations on fluorescence intensity variations . . . | 123 |
| A.4 | Absorbance spectra of the DNA-SWCNT complexes | 124 |
| A.5 | Fluorescence spectra of the DNA-SWCNT complexes | 125 |
| A.6 | Comparison of exchanged SWCNTs without and with DNA | 126 |
| A.7 | Fluorescence response of the first round mutants | 127 |
| A.8 | Relationship between intensity change and base content | 128 |
| A.9 | Errors in the first round screening | 129 |
| A.10 | Mutants of the M47-SWCNT complex | 129 |
| A.11 | Mutants of the M13-1-SWCNT complex | 130 |
| A.12 | AFM characterization of the DNA-SWCNT complexes | 130 |
| A.13 | Comparison of the fluorescence of the IR-26 dye and the SWCNTs | 131 |
| A.14 | Relative surface coverage of the DNA-SWCNTs | 132 |
| A.15 | Effect of free DNA removal on the fluorescence intensity of DNA-SWCNTs . . . | 133 |

| | |
|--|-----|
| A.16 Dopamine calibration curves for the (GT) ₁₅ - and M13-SWCNT complexes . . . | 134 |
| A.17 Response of the DNA-SWCNT complexes to GABA, acetylcholine, and glycine . | 135 |
| A.18 Fluorescence spectra for the M13- and M13-6-SWCNT complexes | 136 |
| A.19 Intensity of DNA-SWCNT in NIR confocal microscopy | 138 |
| B.1 Differences between HiPco-SC batches | 139 |
| B.2 Aging of the DNA-SWCNT complexes | 141 |
| B.3 Absorbance of the oxidized AFB1 | 142 |
| B.4 HPLC-MS chromatogram of the oxidized AFB1 sample | 142 |
| B.5 Response towards the oxidized AFB1 | 143 |
| B.6 Solubility of the AFB1 solutions | 143 |
| B.7 Response towards AFB1 for the shuffled mutants | 145 |
| B.8 Purification of AFB1 samples through PTFE filters | 146 |
| B.9 Reversibility of the Q-3 and F-3 sensors | 146 |
| B.10 Reversibility of the Q-3 and F-3 sensors with an additional denaturation step . | 147 |
| B.11 Efficiency of toxin removal step by absorbance spectroscopy | 148 |
| B.12 Comparison of AFB1 removal with filtering and precipitation | 149 |
| B.13 Determination of the amount of DNA lost during DNA-SWCNT precipitation . | 149 |
| B.14 Response kinetics for the AFB1 and FB1 | 150 |
| B.15 Evolution of the peak position with the extracted corn | 150 |
| B.16 Initial screening towards AFB1 | 151 |
| B.17 Intensity change as a function of the shifting response | 151 |
| B.18 Response heatmaps of the mutant sensors | 154 |
| B.19 Evolution of the intensity and response for the improved intensity mutants . . | 155 |
| B.20 Fluorescence of the sensors before and after SDC replacement | 156 |
| B.21 Effect of the AFB1 response improvement on the (10,2) FB1 response and peak position | 157 |

List of Figures

| | |
|---|-----|
| B.22 Evolution of the response for the improved FB1 mutants | 158 |
| B.23 Selectivity of the FB1 response | 159 |
| B.24 Selectivity of the AFB1 response | 160 |
| B.25 Fitting of the FB1 calibration curves | 160 |
| B.26 Limit of detection for the AFB1 and FB1 sensing | 161 |
| B.27 Response of the sensors in presence of almond extract | 161 |
| B.28 Response of the sensors in presence of beer | 162 |
| B.29 Response of the Q-3 and F-3 sensors towards toxin mixtures | 163 |
| B.30 Detection of AFB1 and FB1 in spiked corn samples | 164 |
| B.31 Comparison of the mixtures made of HiPco and HiPco-CoMoCAT sensors | 166 |
| B.32 Effect of the toxins on the near-infrared DNA-SWCNT absorbance | 166 |
| B.33 Response of immobilized sensors towards AFB1 | 167 |
| B.34 Effect of free DNA on the fluorescence peak position | 167 |
| B.35 Effect of free DNA on the shifting response | 168 |
| B.36 HPLC-MS chromatograms of the AFB1 samples | 169 |
| B.37 Comparison of AFB1 and AFB2 responses | 170 |
| B.38 Shifting response of surfactant-SWCNTs to AFB1 | 171 |
| B.39 Intensity response of surfactant-SWCNTs to AFB1 | 172 |
| B.40 Replacement of AFB1 on the surface of DNA-SWCNT sensors | 173 |
| B.41 Shifting response of surfactant-SWCNTs to FB1 | 174 |
| B.42 Intensity response of surfactant-SWCNTs to FB1 | 175 |
| B.43 Estimation of the DNA concentration after toxin interaction | 175 |
| B.44 SWCNT binding affinity for the Q-3 and F-3 sensors | 176 |
| B.45 Reversibility of the AFB1 sensing in a flow chamber | 177 |
| B.46 Impact of the preparation method on the toxin response | 178 |
| B.47 Removal of free DNA with a high-throughput procedure | 179 |

| | | |
|------|--|-----|
| B.48 | Heatmaps for selective and non-selective DNA-SWCNT sensors | 180 |
| B.49 | Influence of preparation volume and ionic strength on AFB1 response | 181 |
| C.1 | Response of the F-3- and Q-3-SWCNT analogues with varying G-content | 184 |
| C.2 | SWCNT concentration for the random G-content variants | 187 |
| C.3 | Response heatmap of the G-content variants to AFB1 | 188 |
| C.4 | Selectivity of the AFB1 response for the G-content variants | 189 |
| C.5 | Variation in (9,4) peak position for the G-content variants | 190 |
| C.6 | Binding affinity of the G-content variants to SWCNTs | 190 |
| C.7 | Comparison of the SWCNT interaction with AFB1 and nucleobases | 191 |
| C.8 | AFM height profiles for the G0- and G90-3-SWCNT complexes | 193 |
| C.9 | Salt dependence of the peak position of the G-content variants | 194 |
| C.10 | Salt dependence of the response of the G-content variants towards AFB1 | 195 |
| C.11 | DNA quantification for the G-content variants | 196 |
| C.12 | Comparison of the G80-3-SWCNT variants and the Q-3-SWCNT sensor | 196 |
| C.13 | Response of SC-SWCNTs towards AFB1, ANG and COU | 197 |
| C.14 | Shifting response of SC-SWCNTs towards ZEN | 198 |
| C.15 | Shifting response for the first round of FB1 mutants | 199 |
| C.16 | Shifting response for the mutants of the R1 _{13.3} -SWCNT complex | 199 |
| C.17 | Effect of the number of mutations | 200 |
| C.18 | Influence of the grouped mutations | 202 |
| C.19 | Response of the mutants of the 3N3-SWCNT complex | 202 |
| C.20 | Improvement of the FB1 sensor reversibility | 203 |
| C.21 | Gel electrophoresis of the FB1 sensors | 204 |
| C.22 | Relationship between binding affinity and FB1 sensing | 204 |
| C.23 | Relationship between surface coverage and FB1 sensing | 205 |

List of Figures

| | |
|---|-----|
| C.24 Relationship between free DNA concentration and FB1 sensing | 205 |
| C.25 Shifting response of SC-SWCNTs towards TB toxin | 206 |
| C.26 Response of the G80-3-SWCNT variants to TB toxin | 206 |
| C.27 Shifting response of SC-SWCNTs towards OTA | 207 |
| C.28 Sequence-dependent selectivity of the analyte response | 208 |
| C.29 Melting curves of DNA and DNA-SWCNT complexes | 209 |
| | |
| D.1 Optimization of the DNA concentration used for exchange | 212 |
| D.2 Chemical structures of the thiol and internal amino modifications | 212 |
| D.3 Gel electrophoresis of unmodified and modified (GT) ₁₅ | 213 |
| D.4 Absorbance of the (AT) ₁₅ - and N ₃₀ -SWCNT complexes | 214 |
| D.5 Comparison of the absorbance spectra after wrapping replacement with SDC . | 217 |
| D.6 PLE maps of the unmodified and modified (AT) ₁₅ -SWCNT complexes | 219 |
| D.7 PLE maps of the unmodified and modified (GT) ₁₅ -SWCNT complexes | 220 |
| D.8 PLE maps of the unmodified and modified N ₃₀ -SWCNT complexes | 221 |
| D.9 Relationship between peak intensity change and peak intensity prevalence . . | 222 |
| D.10 Effect of the modifications on the D/G Raman peak ratio | 222 |
| D.11 Effect of the modifications on the peak position of the DNA-SWCNTs | 223 |
| D.12 Effect of the modifications on the concentration of DNA on the SWCNT surface | 223 |
| D.13 Effect of the modification on the (7,5) intensity for sonicated and exchanged samples | 224 |
| D.14 PLE maps of the sonicated (GT) ₁₅ -SWCNT complexes | 226 |
| D.15 Effect of the modifications on the dispersibility of sonicated samples | 227 |
| D.16 Wrapping replacement of the sonicated and exchanged samples | 228 |
| D.17 Effect on the D/G Raman peak ratio for the sonicated and exchanged samples . | 229 |
| D.18 Effect on the peak position for the sonicated and exchanged samples | 229 |

| | |
|--|-----|
| D.19 Effect on the concentration of DNA wrapping for the sonicated and exchanged samples | 230 |
| D.20 Sensing capabilities of the sonicated and exchanged samples | 230 |
| D.21 Intensities after dopamine addition for the sonicated and exchanged samples . | 231 |
| E.1 Gel electrophoresis of the products from the first PCR | 233 |
| E.2 Gel electrophoresis of the products of the colony PCR reactions | 234 |
| E.3 Effect of the DNA concentration on the dispersibility of DNA-SWCNTs | 235 |
| E.4 PLE maps of the DNA-SWCNTs prepared with DNA of varying lengths | 236 |
| E.5 DNA recovery with silica beads as a function of length | 237 |
| E.6 Aggregation of SC-SWCNTs with methanol and DMSO | 237 |
| E.7 Fluorescence of DNA-SWCNT complexes prepared by methanol- and DMSO-assisted exchange | 238 |
| E.8 Reproducibility of the properties of the DNA-SWCNT prepared from colonies . | 238 |
| E.9 Optimization of the DNA:SWCNT mass ratio based on fluorescence intensity . | 239 |

List of Tables

| | | |
|-----|---|-----|
| 1.1 | Fluorescence intensity change compared to the (GT) ₁₅ -SWCNT complex | 34 |
| A.1 | Description of the DNA sequences discovered in the study | 123 |
| A.2 | Quantum yields of DNA-SWCNTs | 131 |
| A.3 | Response of the DNA-SWCNTs towards dopamine and glutamic acid | 134 |
| A.4 | Increase in emission penetration depth for the M13-1-SWCNT complex | 137 |
| B.1 | Extinction coefficients for the mycotoxins used in the study | 140 |
| B.2 | List of the main sequences discussed in this study | 144 |
| B.3 | Efficiency of toxin removal step by HPLC-MS | 144 |
| B.4 | Summary of the shifting responses of the (9,4) chirality | 152 |
| B.5 | Summary of the shifting responses of the (7,5) chirality | 153 |
| B.6 | Determination of toxin concentration in corn | 165 |
| C.1 | Extinction coefficients for the mycotoxins used in the study | 183 |
| C.2 | Sequences of the F-3 and Q-3 G-content variants | 185 |
| C.3 | Sequences of the random G-content variants | 186 |
| C.4 | Results of the QGRS Mapper software | 192 |
| C.5 | Sequences of the FB1 mutants with random mutations | 201 |
| D.1 | List of the modified sequences studied in this work | 211 |
| D.2 | Summary of the intensity changes compared to the unmodified samples | 215 |

List of Tables

| | | |
|-----|--|-----|
| D.3 | Summary of the intensities after SDC replacement | 216 |
| D.4 | Summary of the DTT responses | 218 |
| D.5 | Summary of the dopamine responses | 218 |
| D.6 | Summary of the intensity changes for the sonicated samples | 225 |
| D.7 | Summary of the intensities after SDC replacement for the sonicated samples . | 228 |
| D.8 | Summary of the DTT responses for the sonicated samples | 231 |
| D.9 | Summary of the dopamine responses for the sonicated samples | 232 |
| E.1 | Sequencing of the DNA extracted from the H2 and H3 colonies | 234 |

Introduction

Portions of the introduction are reproduced with permission from [1]: Lambert B.P.; Gillen, A.J.; Boghossian, A.A. Synthetic Biology: A Solution for Tackling Nanomaterial Challenges, Journal of Physical Chemistry Letters (2020).

Background and context

Richard Feynman's visionary 1959 lecture, "There's Plenty of Room at the Bottom", inspired a new generation of technologies that revolve around the precise control of material properties at the nanoscale. From scanning tunneling microscopy (STM) [2] to atomic force microscopy (AFM) [3], these technologies have become cornerstones for studying, and even manipulating, the individual atoms that compose our universe [4]. The ability to access such a small scale has yielded nanomaterials, materials with at least one dimension below 100 nm, with unique physiochemical properties that can be optimized for a range of diverse applications. These nanomaterials in their various forms have become a pivotal part of our everyday life, surpassing previously inaccessible technological boundaries. They now act as essential components in microelectronics [5, 6], biomedicine [7–10], food science [11–13], renewable energies [14–16], telecommunications [17, 18], and even cosmetics [19, 20].

Among these nanomaterials, single-walled carbon nanotubes (SWCNTs) have gathered strong interest thanks to their unique mechanical, electronic and optical properties [21–23]. In particular, semiconducting SWCNTs have emerged as important candidates for the creation of optical biosensors thanks to their peculiar fluorescence properties. The fluorescence of these SWCNTs is characterized by a high sensitivity [24, 25] and long-term photostability [26], but also by its biotransparency owing to their near-infrared (NIR) emission lying between the first and second biological windows [27]. These properties have enabled the creation of SWCNT-based biosensors for a wide range of *in vitro* and *in vivo* applications [26, 28–35].

However, the advantageous capabilities offered by nanomaterials come at a price: the increased tunability in size, shape, and composition substantiates the need to navigate an even greater combinatorial space of possibilities. To help navigate this vast space, researchers typically rely on predictive rational design approaches, when possible. These approaches are often based on preliminary studies and theories to generate design guidelines for a specific

application, drastically reducing the search space to only a few possibilities. Examples of such rational design have previously been demonstrated for quantum dots (QDs) [36], molecular machines [37–39], block copolymer self-assemblies [40, 41] or DNA origami structures [42, 43]. Despite the relative ease with which rational design allows researchers to navigate vast combinatorial spaces, this approach requires information on the structure-function relationship of the desired nanomaterial. Unfortunately, this relationship is often not well-understood as observed, for example, with catalysts [44, 45] and metal organic frameworks (MOFs) [46, 47]. This limitation is even further exacerbated for bioconjugated nanomaterials, for which the complex interactions between the nanomaterial and biomaterial is even less understood and less predictive [48–50]. This is, in particular, the case for single-stranded DNA wrapped SWCNT complexes.

While the fluorescence of SWCNTs can be rationally designed based on the diameter and chiral angle of the SWCNTs [22, 51], the SWCNT's properties can vary in a less predictive manner following noncovalent biopolymer functionalization. To provide the SWCNTs with colloidal stability in aqueous media as well as with sensing capabilities, SWCNTs can be noncovalently functionalized with various types of biomolecules, including proteins [52] and biopolymers such as nucleic acids [53]. DNA has thoroughly been used for the creation of SWCNT-based complexes, resulting in highly stable [54–56] and biocompatible [35] suspensions. In addition, DNA-SWCNTs have been shown to exhibit sequence-specific properties, making them ideal for the creation of sensors towards a diverse panel of targets [32, 57–59]. However, the relationship between DNA sequence and the structure and properties of the DNA-SWCNT complexes is still not well understood, limiting their design to empirical considerations [58, 60, 61].

In this thesis, we draw inspiration from bioengineering techniques to overcome overlapping challenges in the design of DNA-SWCNT complexes. In particular, we present how directed evolution, an approach used extensively for the engineering of proteins, can be used in order to enhance the properties of DNA-SWCNT sensors. We show that directed evolution can be utilized to efficiently modulate various properties of the nanocomplexes, such as their optical properties, sensing capabilities and SWCNT chirality specificities. We demonstrate that the properties of the complexes can be further improved with a semi-rational design, using the knowledge acquired throughout the evolution of the complexes, or by incorporating chemical modifications in the DNA sequence. Finally, we show that it is possible to apply this approach to all DNA-SWCNT complexes, regardless of length of the DNA wrapping. The approaches that we demonstrate in this work can be used to significantly improve the way DNA-SWCNT sensors are designed, enabling the creation of more efficient sensors for a broad range of applications.

Single-Walled Carbon Nanotubes (SWCNTs)

Single-walled carbon nanotubes (SWCNTs) are cylindrical nanostructures composed of a single carbon atom layer and exhibiting diameters in the order of a few nanometer and lengths

typically around a micron. SWCNTs can be conceptualized as individual sheets of graphene rolled into a tube along the so-called chiral vector C_h (**Figure 1**) [62]. The chiral vector is expressed by the chiral indices (n, m) and the unit vectors of the graphene lattice \vec{a}_1 and \vec{a}_2 :

$$C_h = n\vec{a}_1 + m\vec{a}_2 \quad (1)$$

These integers are further used to determine the diameter d and chiral angle θ of the individual nanotubes according to the following equations:

$$d = \frac{\sqrt{3}}{\pi} a_{cc} \sqrt{n^2 + nm + m^2} \quad (2)$$

$$\theta = \tan^{-1} \left(\frac{\sqrt{3}m}{2n + m} \right) \quad (3)$$

where a_{cc} ($\approx 1.4 \text{ \AA}$) is the length of a carbon-carbon (C-C) bond. Depending on the (n, m) values, SWCNTs are designated as arm-chair ($n = m$, $\alpha = 30^\circ$), zigzag ($n=0$ or $m=0$, $\alpha = 0^\circ$) or chiral ($0^\circ < \alpha < 30^\circ$) (**Figure 1**). The couple of (n, m) integers, further referred as chirality, defines the optical and electronic properties of the SWCNT, considered as either metallic ($n=m$), semi-metallic ($|n - m| = 3k$, k an integer) or semiconducting ($|n - m| = 3k \pm 1$) (**Figure 1**).

Because of their one-dimensional (1D) nature, SWCNTs exhibit Van Hove singularities in their density of electronic states (DOS) [63]. These singularities are represented in **Figure 1** by the presence of sharp peaks labelled v_i and c_i in the valence and conduction bands, respectively, between which the E_{ii} electronic transitions are allowed. As we are interested in fluorescence, we will only consider the case of photo-excited transitions in this introduction. In metallic and semi-metallic SWCNTs, the conduction and valence bands overlap resulting in the presence of only non-radiative relaxations upon photo-excitation and, therefore, the absence of fluorescence (**Figure 1**). In contrast, semiconducting SWCNTs exhibit a band gap between the conduction and valence bands (**Figure 1**) which allows the formation of excitons, an electron-hole pair bound by Coulomb interaction, upon photo-excitation. The excitons can further relax radiatively, giving rise to SWCNT fluorescence [23]. In accordance with Kasha's rule, which states that photon emission occurs from the lowest excited state [64], SWCNT radiative relaxation is observed only for the E_{11} transition. In the case of an excitation *via* the E_{22} transition, excitons will therefore relax first non-radiatively from the c_2 to the c_1 sub-bands and subsequently relax radiatively through the E_{11} transition (**Figure 1**).

When considering the optical properties of SWCNTs, it is important to consider their chirality. In fact, the band gap of a SWCNT depends on the nanotube diameter and chiral angle [22, 51], hence affecting the various transition energies in both metallic and semiconducting SWCNTs. In addition, SWCNTs also exhibit excitonic effects which strongly affect their optical properties [65]. These effects stem from the limited screening effect of free electrons and low impact of

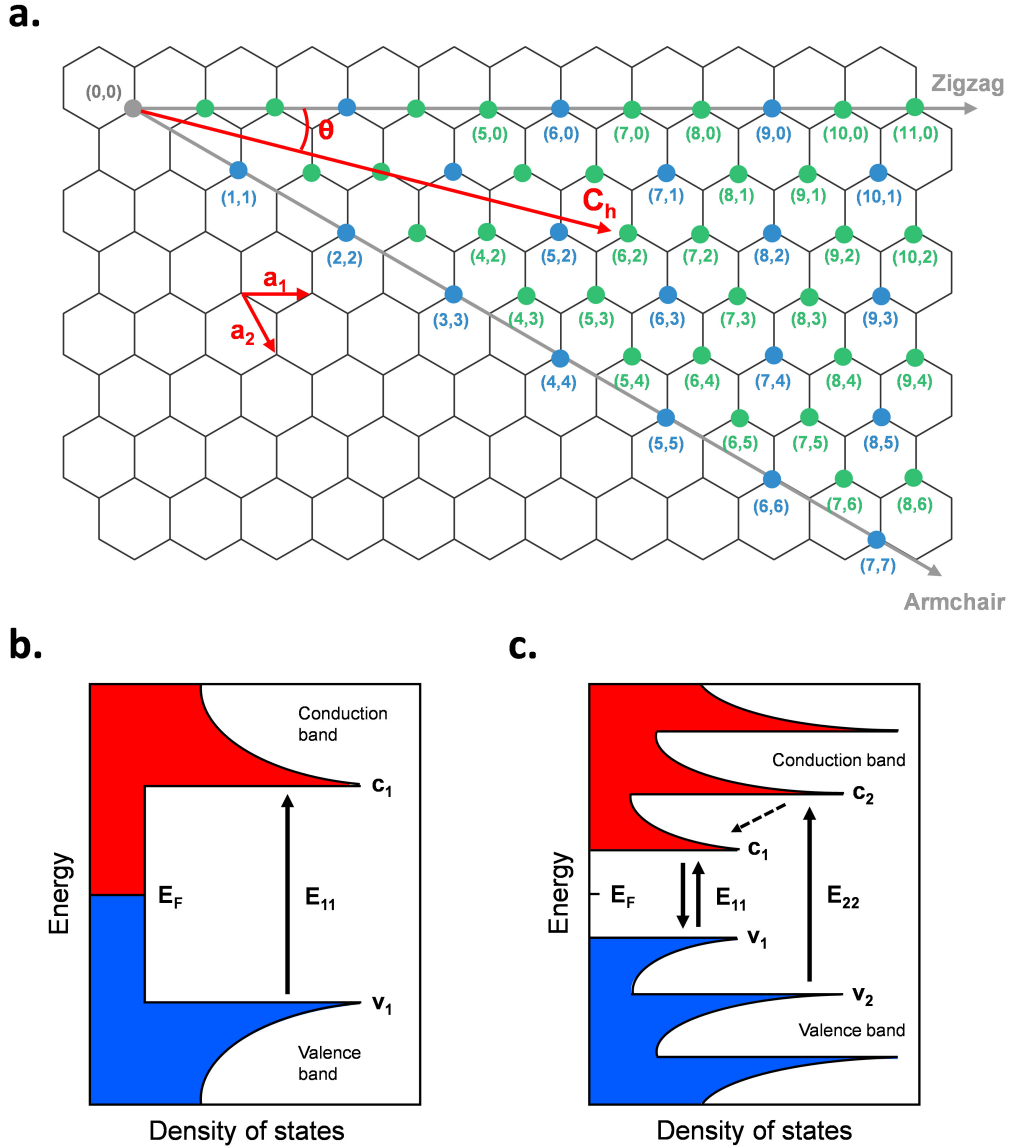


Figure 1 – Description of the SWCNT chiralities and electronic properties. (a) Schematic of the rolling of the SWCNT along the graphene sheet. The chiral vector C_h , chiral angle θ and unit vectors \vec{a}_1 and \vec{a}_2 are represented in red. The blue and green dots represent the metallic and semiconducting chiralities respectively. The zigzag and armchair SWCNTs are represented by gray vectors. Energy as a function of the density of electronic states (DOS) for (b) metallic and (c) semiconducting SWCNTs. The valence band is represented in blue and the conduction band in red. The Van Hove singularities are represented by the sharp peaks in the DOS. The Fermi level is represented by the E_F value. The black arrows represent the possible energy transitions between the singularities represented by the indices c_i and v_i for the conduction and valence bands respectively. The dotted arrow from c_2 to c_1 represents an exclusively non-radiative transition.

the surrounding dielectric constant on the exciton binding energy. By accounting for these excitonic effects, it is possible to define the optical transition energy as:

$$E_{optical} = E_{sp} + E_{e-e} - E_{e-h} \quad (4)$$

with E_{sp} the single-particle transition energy defined by the Van Hove singularities, E_{e-e} the electron-electron repulsion energy and E_{e-h} the exciton binding energy (or electron-hole attraction energy). Although the electronic band gap is fixed for a specific SWCNT chirality, the optical transition energies depend on external factors such as the dielectric constant of the medium which affects both E_{e-e} and E_{e-h} , resulting in a change in optical transition energy known as solvatochromic shift [66].

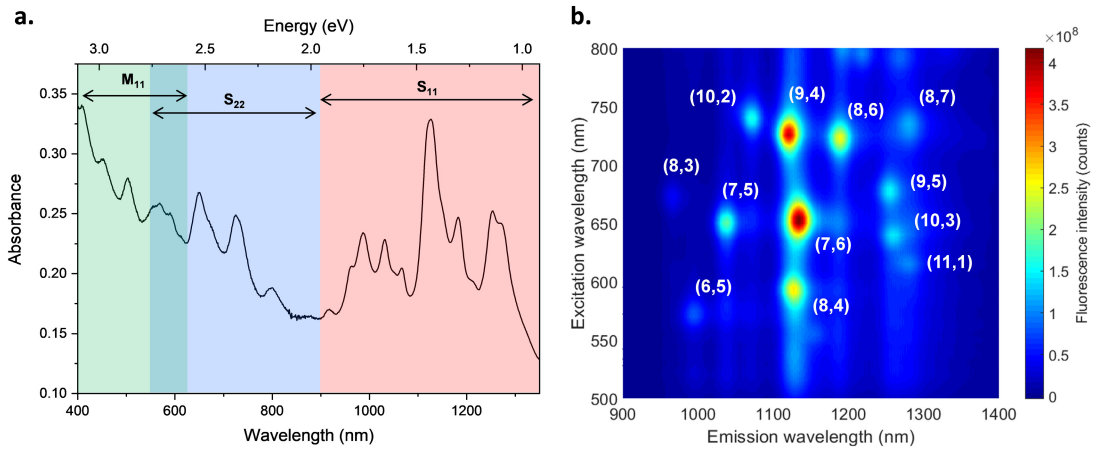


Figure 2 – Optical characterization of SWCNTs. (a) Absorbance spectrum of HiPco SWCNTs suspended in 2 % sodium cholate (SC) represented against energy and wavelength. The range of the M_{11} , S_{22} and S_{11} transitions are indicated in green, blue and red respectively. (b) Photoluminescence excitation (PLE) map of HiPco SWCNTs suspended in 2 % SC. The excitation wavelengths are represented as a function of the emission wavelengths. The Z axis represents the intensity of the fluorescence. The chiralities are indicated next to their respective peak in the PLE map in white.

It is possible to visualize these optical transitions energies by absorption spectroscopy (**Figure 2**). The absorbance peaks located in the visible range, between 550 and 900 nm, represent the E_{22} optical transitions of semiconducting SWCNTs (S_{22}) and the peaks in the near-infrared (NIR) range, between 900 and 1400 nm, their E_{11} optical transitions (S_{11}). The additional peaks located between 400 and 620 nm represent the E_{11} optical transitions of metallic SWCNTs (M_{11})¹ [68]. Although absorbance spectroscopy can be used to characterize the sample's composition, it does not accurately resolve the individual peaks corresponding to the different SWCNT chiralities. This limited resolvability is partly due to the peak broadening, which is linked to the quality of the SWCNT dispersion, and the associated convolution of the absorbance peaks [69]. To tackle this limitation, fluorescence spectroscopy is typically used to more accurately resolve the individual SWCNT transitions, in particular through the

¹The particular 1D geometry of SWCNTs allows the creation of excitons in metallic SWCNTs [67]. While these excitons do not result in a fluorescence, they do affect the absorbance of metallic SWCNTs.

Introduction

construction of photoluminescence excitation (PLE) maps [70]. The PLE map represented in Figure **Figure 2** was obtained by measuring the fluorescence resulting from the S_{11} transitions, between 900 and 1400 nm, for a range of excitations, between 500 and 800 nm. Such a PLE map allows one to accurately identify the individual SWCNT chiralities present in a mixed sample by their individual (S_{22}, S_{11}) excitation-emission couple.

SWCNTs are particularly attractive for fluorescence applications. First, they exhibit fluorescence in the NIR range, which is located within the first and second biological windows [27], enabling imaging *in vivo* with minimal absorption from water and biological tissues while also limiting the auto-fluorescence of biological pigments [71]. In addition, SWCNTs display significant Stokes shifts, which is the difference between the absorption and fluorescence peaks. These shifts are on average about 400 nm, allowing one to monitor the fluorescence with minimal cross-talk from the excitation. Finally, SWCNTs benefit from an indefinite photostability, which allows one to monitor the fluorescence for extended periods of time [26].

SWCNTs are typically fabricated by laser ablation, arc discharge or chemical vapor deposition (CVD) [72]. These preparation techniques result in mixtures of SWCNT chiralities whose distributions depend on the process used. In this thesis, we worked with two types of SWCNT powders produced by two different types of CVD processes, HiPco and CoMoCAT. The CoMoCAT batch contains mostly small diameter nanotubes (average of 0.78 nm) and is enriched in the (6,5) chirality. On the other hand, the HiPco batch contains larger diameter nanotubes (> 0.8 nm) and a higher diversity of chiralities (**Figure 2**).

Following synthesis, SWCNTs typically aggregate due to the strong Van der Waals attractions between the nanotubes. Since such aggregation can result in the quenching of the fluorescence [73, 74], SWCNTs must be further processed to keep them separated. To this end, SWCNTs are usually functionalized with so-called wrapping molecules, enabling the solubilization of individual nanotubes as well as additional properties necessary for the creation of biosensors such as biocompatibility or analyte selectivity. Covalent functionalization is typically not desirable for fluorescence applications as it can result in the quenching of the emission [75–77]. Alternatively, SWCNTs can be non-covalently functionalized with a variety of molecules including surfactants [23, 78], polymers [79, 80], proteins [52, 81] and nucleic acids such as DNA [53, 82]. In this thesis, we focus on the study of DNA-wrapped SWCNTs.

Deoxyribonucleic acid (DNA)

Deoxyribonucleic acid (DNA) is a molecule composed of two polynucleotide chains that carry the essential genetic information in all living organisms. The DNA structure consists of a double helix formed by the two chains stabilized by hydrogen bonding (**Figure 3**), as depicted by Watson and Crick in 1953 [83]. This hybridized DNA is therefore commonly referred to as double-stranded DNA (dsDNA). The individual polynucleotide chains that comprise the double-stranded DNA can each be decomposed into two main components, the nucleobase and the backbone.

The DNA is composed of four types of nucleobases: adenine (A), cytosine (C), guanine (G) and thymine (T). These nucleobases can be grouped into two categories, pyrimidines (C, T) and purines (A, G). The nucleobases commonly interact between each other *via* hydrogen bonds between specific pyrimidine-purine couples, C-G and T-A, known as Watson-Crick base pairing (**Figure 3**). The double helix is formed by two strands containing complementary sequences of nucleobases.

The backbone of a DNA strand consists of alternating phosphate and sugar (2-deoxyribose) groups. The phosphate groups form a phosphodiester bond between the third (3') carbon atom of a sugar and the fifth (5') carbon atom of another adjacent sugar (**Figure 3**) [84]. This bond designates the directionality of the DNA strand, which is usually indicated by the 5'- and 3'-ends. The phosphate groups also confer an overall negative charge to the backbone.

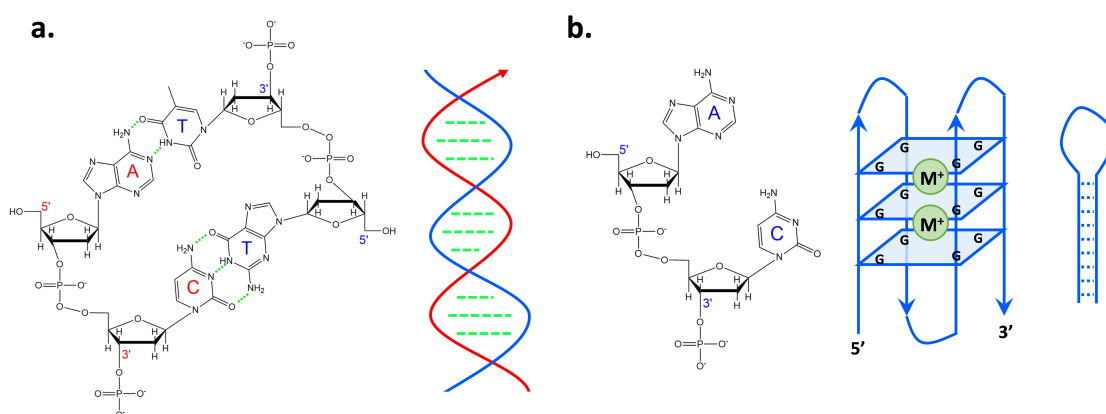


Figure 3 – Structures of double- and single-stranded DNA. (a) Chemical structure of double-stranded DNA and double helix conformation. The green lines represent hydrogen bonds. (b) Chemical structure of single-stranded DNA and secondary structures: G quadruplex (left) and hairpin (right). The green circles in the G-quadruplex (G4) structure represent metallic cations.

The natural form of DNA is known as B-DNA. B-DNA occurs under physiological conditions of pH and salt concentration and is characterized by a right-hand helix. The A-form of DNA is typically obtained under dehydrating conditions and is characterized by a shorter and more compact form of the B-DNA. The Z-form of DNA is usually obtained at high salt concentrations with DNA strands containing complementary sequences of alternating purine and pyrimidine nucleobases. This form of DNA is characterized by a left-handed double helical conformation [84].

Single-stranded DNA (ssDNA) corresponds to an individual polynucleotide chain (**Figure 3**). While ssDNA can be formed naturally, during replication, recombination and transcription processes, for example, ssDNA is typically synthesized as short fragments known as oligonucleotides. Because of their single-stranded nature, the DNA and ribonucleic acid (RNA) oligonucleotides can form analogous types of structures. These structures include hairpins [85, 86], bulges [87], quadruplexes and triplexes [88] (**Figure 3**). The structures of the oligonucleotides are very diverse as they depend on the sequence and experimental

conditions. Such a diversity is exploited, for instance, in the systematic evolution of ligands by exponential enrichment (SELEX) approach which aims to create ligands based on the specific conformation of oligonucleotides [89]. In addition, the folding of ssDNA oligomers has been used in applications such as nanopatterning [42] and molecular computing [90].

Oligonucleotides also present advantages when combined with other substrates, such as nanomaterials. ssDNA oligomers have for example been combined with silver clusters [91] and gold nanoparticles [92] in order to modulate their properties. The next section will discuss the properties of conjugates made of DNA oligonucleotides and SWCNTs.

DNA-SWCNT complexes

DNA-SWCNTs are complexes resulting from the interaction between DNA oligonucleotides and SWCNTs. Although functionalization of SWCNTs with both ssDNA [82] and dsDNA [93] has initially been demonstrated, the use of ssDNA was shown to result in more efficiently dispersed suspensions. This preferential dispersivity was further corroborated by more detailed investigations of the interaction between DNA and SWCNT. The DNA was shown to interact with the SWCNT through π - π stacking between the nucleobases and the nanotube sidewall [82, 94]. While the ssDNA could fully interact with the SWCNT surface, the dsDNA would bind only be able to bind through the ends of the DNA [95] or it would first have to de-hybridize to ssDNA to allow a sufficient interaction [96]. As a result, the use of ssDNA was therefore preferred for the formation of DNA-SWCNT complexes in most applications, including in this thesis. Therefore, unless otherwise indicated, the DNA-SWCNT complexes and DNA wrappings mentioned in this dissertation are hence always prepared with ssDNA sequences.

Early findings showed that the DNA could uniformly wrap the SWCNT in a helical fashion (**Figure 4**) [82, 94, 97–101]. This helical wrapping was confirmed directly by various techniques including AFM [102, 103], transmission electron microscopy (TEM) [96, 104], and STM [97], as well as indirectly through the investigation of the optical properties of DNA-SWCNT complexes [105]. The properties of this helical wrapping, such as pitch size and wrapping angle (**Figure 4**), were found to depend on the length and sequence of the DNA, as well as on the SWCNT chirality [94, 97–100]. In addition, previous studies reported that this helical wrapping could be affected by intra- and inter-molecular interactions within the DNA wrapping molecules resulting in the formation of barrel-like helically wrapped structures around the SWCNT [100, 101, 106]. The helical wrapping was therefore found to be just one of several possible conformations. For example, short ssDNA sequences were shown to preferentially adopt loop and ring structures (**Figure 4**) [61, 107, 108]. The type of wrapping conformation was also shown to further depend on the DNA sequence and/or SWCNT chirality [108, 109]. Furthermore, the DNA wrapping conformation was demonstrated to depend on the environmental conditions such as ionic strength [110–113]. Such diversity among the DNA-SWCNT complexes was not only observed for the DNA wrapping conformation, but also for the other properties of the

DNA-SWCNT complexes such as binding affinity to SWCNT, fluorescence and analyte sensing properties.

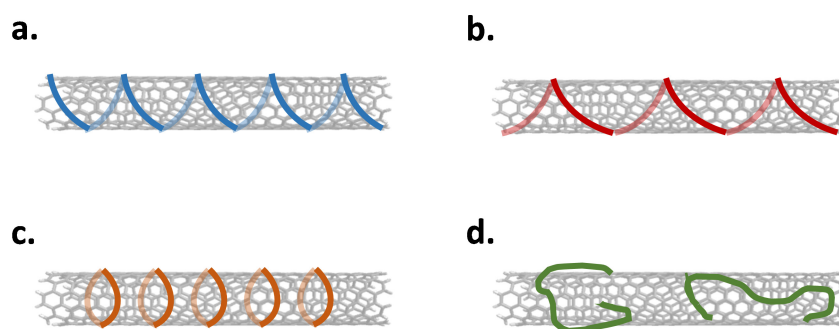


Figure 4 – Schematic of possible DNA wrapping conformations. (a) Compact helix, (b) elongated helix, (c) ring and (d) loop.

Multiple studies reported the dependence of the binding affinity of the DNA wrapping to SWCNT on the sequence and length of the DNA as well as on the SWCNT chirality considered [55, 100, 108, 114–120]. The strength of interaction with SWCNT was shown to depend both on the type of nucleobase [121] as well as on the conformation of the DNA wrapping [100, 108, 115]. This dependence on conformation was suggested to stem from the presence of bound ions and intra- and inter-molecular interactions in the wrapping DNA [100, 108, 115]. These sequence-dependent binding affinities and wrapping conformation have been, for example, used for the separation of SWCNT chiralities through the purification of specific DNA-SWCNT complexes with ion-exchange chromatography (IEX) or aqueous two-phase (ATP) separation [101, 102, 122, 123].

The optical properties of the DNA-SWCNT complexes were also shown to depend on the DNA wrapping and SWCNT chirality [57, 61, 112, 114, 124–126]. Modulations in fluorescence intensity are mostly attributed to variations in the DNA wrapping conformation, resulting in differences in the accessibility of the SWCNT to the solvent [112, 124]. If the SWCNT surface is exposed, the excitons have a higher probability of interaction with oxygen molecules [124] and endoperoxide species [112] which can result in a quenching of the fluorescence. In addition to fluorescence intensity, modulations in emission energies have also been observed for different DNA wrapping sequences [61, 80, 127, 128]. These variations could originate from the interaction between the nucleobases and the SWCNT surface [104, 127]. Alternatively, variations in emission energies may also result from a change in wrapping conformation, which would induce a change in SWCNT surface coverage and lead to a solvatochromic shift of the emission [66, 80, 128].

The DNA wrapping does not serve only as a dispersing agent for the SWCNT, but it can also serve as a recognition element for biosensing. In some instances, a DNA probe attached

to the wrapping can be designed to specifically recognize a target, as is the case with DNA hybridization probes [129, 130] and DNA aptamers [29, 131, 132]. However, these approaches are difficult to apply as the DNA probe has typically a tendency to interact with the SWCNT surface, hindering its interaction with the target. Alternatively, the DNA wrapping can be directly used to modulate the interaction between a target and the DNA-SWCNT complex. In line with the other properties of the DNA-SWCNTs, the sensitivity and selectivity of the optical response of the complexes were shown to depend on the sequence [57, 58] and length [61] of the DNA wrapping, as well as on the SWCNT chirality considered [133, 134]. This variability in the sensing properties was used to develop sensors towards a variety of small molecules by changing only the DNA sequence or length [32, 57–59, 134, 135], exhibiting optical responses based on fluorescence intensity modulation [57, 58, 134, 135] or emission shifting [32, 59, 134].

The dependence of the properties of the DNA-SWCNT complexes on the attributes of the DNA wrapping is a great advantage as it enables the creation of very diverse and versatile SWCNT complexes for a variety of applications. In addition, the DNA-SWCNT complexes benefit from an excellent colloidal stability [54–56] and a biocompatibility in living organisms [35]. Yet, when compared to other SWCNT complexes, the current performances of the DNA-SWCNT complexes are limited, hence restricting their further applicability. First, the DNA-SWCNTs suffer from low fluorescence quantum yields (QYs)², much lower than other SWCNT complexes such as surfactant-suspended SWCNTs [78, 114], therefore limiting the use of the complexes for deep tissue imaging and monitoring. In addition, the sensitivities and selectivities observed for the DNA-SWCNT sensors remain low in comparison with more specific systems such as protein-suspended SWCNT sensors [52, 81]. Finally, despite their SWCNT chirality-specificity, DNA-SWCNT complexes cannot yet achieve the SWCNT sorting efficiencies achieved with certain synthetic polymers [136]. There is therefore a need to engineer the properties of DNA-SWCNT complexes in order to fully exploit their potential. The next section will comment on the current strategies adopted for the engineering of DNA-SWCNTs, their advantages and limitations and the approaches we propose to overcome these challenges.

Engineering of DNA-SWCNTs: state of the art

Several approaches have been developed to improve the various properties of DNA-SWCNT complexes. First, the properties of DNA-SWCNTs can be modulated by changing the SWCNT length or modifying the SWCNT surface chemistry (**Figure 5**). The length of SWCNTs can be modified by optimizing the dispersion conditions. SWCNT complexes are most commonly prepared by direct sonication of the SWCNT powder with the wrapping molecule whose conditions (power, duration, type of probe) were shown to affect the SWCNT length [137–139] and the number of defects on the SWCNT surface [138, 140, 141]. These changes could ultimately result in a modulation of the optical properties of SWCNT complex such as quantum

²The fluorescence quantum yield is defined as the ratio of the number of photons emitted by the number of photons absorbed.

yield (QY), or they could change how the SWCNT complexes interact with living organisms [142]. These effects can also alter the properties of the DNA-SWCNT complexes. Indeed, the characteristics of the DNA wrapping were shown to depend significantly on the preparation method used [143, 144], resulting in a modulation of the properties of the DNA-SWCNT complexes. Yet, the choice of the dispersion conditions is often restrained by the desired sample throughput. In addition, while an improvement in certain properties, such as QY, is observed with specific dispersion conditions, particular attention should be paid to the effect of these dispersion conditions on the other properties of the DNA-SWCNT complex, such as their sensing properties. On the other hand, the surface of SWCNTs can be chemically modified in order to improve their optical properties [145–148]. Although effective, this approach was not yet thoroughly studied on DNA-SWCNT complexes and may potentially impact their other properties [149].

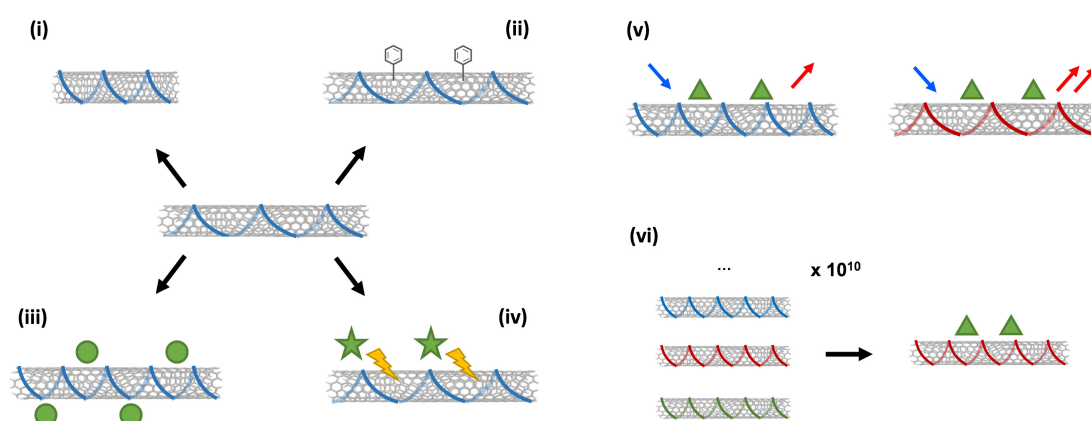


Figure 5 – Engineering of DNA-SWCNT complexes. (i): Optimization of the dispersion conditions to adjust SWCNT length. (ii): Chemical modification of the SWCNT surface. (iii): Introduction of additives (e.g. salts, represented by green circles) to change the wrapping conformation. (iv) Introduction of additives (e.g. reducing agents, represented by green stars) to induce a charge transfer with the SWCNT (represented by the yellow bolts). (v): Random screening of DNA-SWCNT with various sequences or length towards different analytes (represented by green triangles), the fluorescence response being represented by blue and red arrows for the excitation and emission respectively (more arrows representing a greater response). (vi): Selection of DNA-SWCNTs in an extended library of complexes (here 10^{10} complexes) based on the selective affinity towards a target of interest (represented by the green triangles).

In parallel, properties of the DNA-SWCNT complexes can also be modulated through the addition of exogenous agents to the final suspensions (**Figure 5**). Improvements in the QY of SWCNT complexes have, for example, been observed following the introduction of reducing agents [150–152], plasmonic nanoparticles [153], fluorophores [154], salts [112] and rare-earth elements [155]. While these additions allow the substantial enhancement of the optical properties of the complexes regardless of their preparation conditions and throughput, the presence of such additives might nonetheless limit the reactivity of SWCNT sensors [112, 135, 156] and could limit their biocompatibility [157, 158].

As the properties of the DNA-SWCNT complexes depend strongly on the characteristics of

the DNA wrapping, such as sequence and length, the engineering of such complexes has relied mostly on the modulation of the DNA sequence (**Figure 5**). As the relationship between DNA sequence and properties of the DNA-SWCNT complexes is still mostly unknown, the discovery of DNA-SWCNT sensors has mostly relied on random library screening. The corona phase molecular recognition (CoPhMoRe) approach relies on the screening of a library of DNA-SWCNT in order to find complexes exhibiting a response towards analytes of interest (**Figure 5**) [58, 60, 133]. Such a library screening approach was also used for the sorting of SWCNT chiralities, although with a more systematic selection of both the DNA sequence and length [101, 102, 122, 123].

Yet the efficiencies of such approaches are limited by the size of the screening library. A sequence composed of n nucleotides has 4^n possible analogues due to the combination of all four nucleobases. Because each sequence can result in a different DNA-SWCNT complex, there are therefore an extremely large number of possible DNA-SWCNT sensors. Currently, the size of DNA-SWCNT libraries range from a few up to approximately 350 complexes [58, 60, 122]. The majority of the DNA-SWCNT complexes are therefore left unexplored in these applications, restricting the screen to complexes with suboptimal performances. To overcome this limitation, Jeong *et al.* [159] developed a protocol for selecting particular DNA-SWCNTs in an extensive library of complexes ($\approx 10^{10}$ distinct DNA-SWCNTs) based on the affinity towards a target, the serotonin neurotransmitter (**Figure 5**). Although this approach enables one to screen a significantly larger collection of different DNA-SWCNT complexes, it is limited to engineering affinity. In particular, since the selection method is based on target affinity, this approach can only be used to modulate the interaction between DNA-SWCNT complexes and a molecule, and it could not be used to directly engineer other properties of the complexes, such as fluorescence. Recently, an increasing number of studies reported the use of emerging computational techniques such as machine learning in order to predict the best DNA sequence to design DNA-SWCNTs for a specific application [134, 160]. Although promising, these approaches require the prior discovery of an important number of DNA-SWCNT complexes exhibiting the desired properties.

Despite the promising engineering approaches developed thusfar, the rational and guided design of high performance DNA-SWCNT sensors remains in its infancy. The ability to explore the diverse DNA-SWCNTs in a guided manner is therefore crucial for optimizing their properties. In this dissertation, we propose to tackle these bottleneck challenges in the design of DNA-SWCNT complexes using approaches inspired by techniques developed for protein engineering. In particular, we demonstrate the use of the directed evolution to engineer DNA-SWCNTs lacking a defined structure-function relationship. These approaches are further described in the next section.

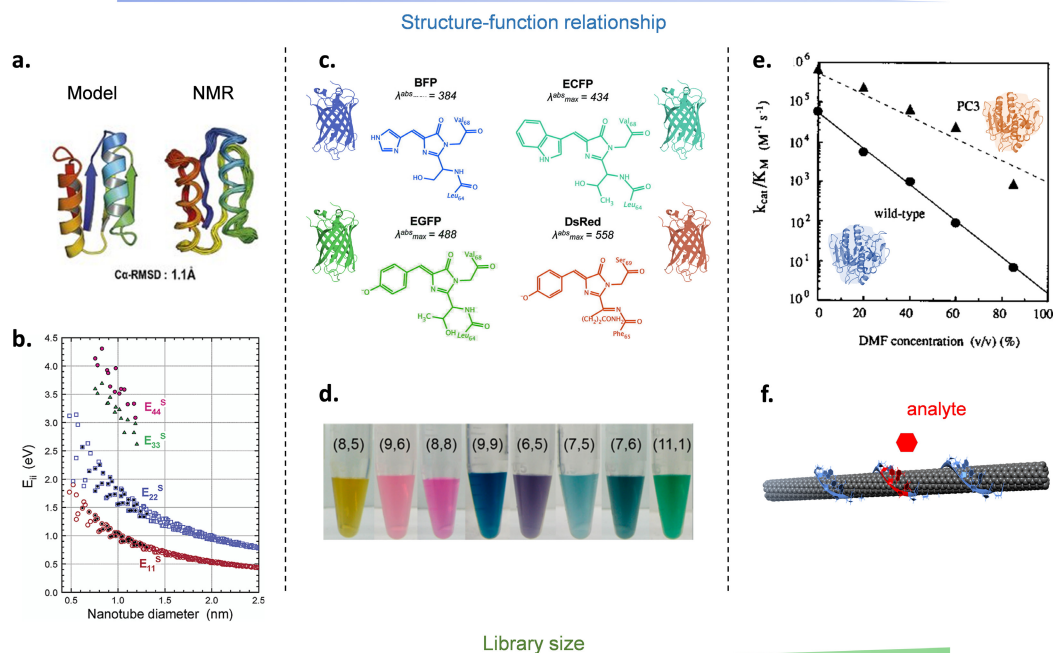


Figure 6 – Comparison of the approaches used to design proteins and SWCNT complexes. The approaches are ordered left to right based on decreasing information on the material's structure-function relationship. If the relationship between structure and function is fully known, the material can be rationally designed (a and b). For example, (a) *de novo* protein design results in accurate correspondence between the modeled structure and the nuclear magnetic resonance (NMR) structure (C_{α} -RMSD represents the root-mean-square deviation between the C_{α} atoms of the two structures). Adapted with permission from ref [161]. Copyright 2015 National Academy of Sciences. Analogously, (b) the SWCNT band gap is modulated by the nanotube diameter based on quantum confinement. Reprinted from ref [51]. Copyright 2013 American Chemical Society. If the structure-function relationship is only partially known (c and d), the material can be engineered in a semi-rational manner, such as (c) the evolution of the GFP into color variants by mutation in the vicinity of the tripeptide chromophore. Adapted from ref [162] (protein structure modified from ref [163]). Copyright 2012 (1996) American Chemical Society (AAAS). Semi-rational design can analogously be applied to (d) the sorting of SWCNT single chiralities with oligomers shorter than 20 bases. Reprinted from ref [123]. Copyright 2016 American Chemical Society. When little information is available on the relationship between structure and function (e and f), the material can be engineered using empirical approaches, such as (e) the directed evolution of subtilisin E activity in organic solvents. Adapted with permission from ref [164] (protein structure modified from ref [165]). Copyright 1993 (1998) National Academy of Sciences (Elsevier). Such an approach can also be used with (f) DNA-SWCNT complexes for the detection of analytes.

Protein design in synthetic biology

The field of protein engineering is faced with challenges analogous to those faced for the design of DNA-SWCNTs. Protein engineering is driven by the need to design proteins with altered functionality. Proteins can, in some instances, be rationally engineered to fulfill a specific function [161, 166]. However, most proteins have an ill-defined structure-function relationship, undermining any rational engineering approach. Although the relationship

Introduction

between a protein's structure and function may not be thoroughly understood, the nearly infinite number of hypothetical protein structures makes proteins among the most statistically versatile materials.

A protein is composed of a specific combination of up to 20 different types of amino acids folded in a unique manner. The identity, sequence, and folding of these amino acids contribute to the protein's properties and ultimately its functionality. For example, typical proteins have sizes around approximately of 235 amino acids [167]. These proteins therefore have 20^{234} , or over 10^{304} , possible amino acid permutations (provided that the first residue is methionine), much greater than the 10^{80} atoms that comprise our universe [168]. This number does not even account for additional variants due to protein secondary and tertiary structures. As most protein screening techniques can screen only a few thousand [169–171] variants per day, or up to $\approx 10^8$ variants with fluorescence-activated cell sorting [172] (FACS), an essentially indefinite amount of time would be required to screen the entire combinatorial space of protein analogues. Protein engineering techniques therefore must rely on a more guided approach for searching through this vast combinatorial space. The size of the search space depends not only on the protein's size but also on the amount of information that is known on the structure-function relationship (**Figure 6**).

De novo design

Proteins that possess well-characterized structure-function relationships can be rationally designed without needing to implement empirical search approaches. This information allows researchers to limit the search space to a handful of sequences or, in certain cases, even a single protein. This can be achieved through the *de novo* design of biological structures, used to engineer such well-characterized systems. This approach was, for example, successfully demonstrated for the rational design of small peptides composed of α -helices and β -barrels (**Figure 6**) [161, 166]. The structures showing the lowest folding energy in the models were selected and either expressed in living organisms (for the genetically encodable peptides) or chemically synthesized [166]. The resulting peptides were shown to present, in almost all cases, quasi-identical structures when compared to their respective models. Using the *de novo* approach, the authors narrowed the 20^{26} possible combinations of a 26-residue peptide down to only one sequence based on well-characterized α -helices and β -barrels [166]. This reduction in search space was also achieved for other peptides of varying sizes. Such a *de novo* design was also used in order to create functional peptides [173]. β -barrels structures were rationally designed for the binding and activation of the DFHBI fluorogenic compound in order to create an analog to the green fluorescent protein. The number of possibilities were first reduced by structural considerations through selection of the proteins forming stable β -barrels structures and allowing the DFHBI to bind while remaining in its fluorescent planar conformation. A total of 56 designs were selected, expressed and experimentally tested, an insignificant fraction of the 20^{110} possible variants of the 110 amino acids protein. From this library, 20 structures were found to be monomeric β -sheet proteins, and only two out of these

20 structures were found to activate the DFHBI fluorescence.

Analogously, SWCNTs can be rationally designed if sufficient information on the structure-function relationship is known (**Figure 6**). As the band gaps of SWCNTs are known to depend monotonically on the nanotube's diameter [22, 51], the excitation and emission wavelengths of the SWCNT's fluorescence can be rationally designed by selecting the appropriate diameter. Rational design is therefore an efficient way to create variants and is commonly viewed as the ultimate goal in the design of a system. Such approach requires, however, substantial knowledge on the structure-function relationship of the system. In some cases, the structure-function relationship is only known for some parts of the system. Although, *de novo* design cannot be applied in this situation, semi-rational design strategies could be used in order to improve the properties of the system while limiting the size of the screening library.

Semi-rational design

Approaches relying on a less rational design have been developed for proteins that do not possess a fully known structure-function relationship. In semi-rational design, information on the protein structure or structure-function relationship is used in order to find ways to engineer the protein, hence reducing the library of protein variants. This can, for example, be facilitated by a better characterization of the protein structure as it was demonstrated for the engineering of variants of the green fluorescent protein (GFP) (**Figure 6**). Following the discovery of the crystal structure of GFP in 1996 [163], Ormo *et al.* were able to identify the cyclic tripeptide chromophore responsible for the protein's fluorescence. Consequently, researchers interested in altering the emission spectrum of the protein could limit the sequence search space to mutations on, or around, the GFP chromophore region [174–176]. By randomly mutating the amino acids within the vicinity of the chromophore, researchers have achieved additional color variants of GFP, including blue (BFP) [175], cyan (CFP) [175], and yellow (YFP) [176] fluorescent proteins. Such screening approaches have also been used to identify variants of GFP [177] that are up to 100-fold brighter. Although less effective than *de novo* design, the semi-rational design of GFP allowed to engineer its fluorescent properties while only screening a fraction (e.g. 2,400 variants [177]) of the 20^{237} possibilities. Moreover, for more intricate mechanisms such as the interaction between an enzyme and a substrate, additional molecular modeling can be performed in order to identify the location of important residues [178]. Further improvements could be obtained by investigating how the type of the amino acids affect the property of interest. This can be achieved by using saturation mutagenesis, which relies on the systematic mutation of amino acids by all their possible counterparts [179]. The use of saturation mutagenesis also enables the discovery of protein variants which would not be possible in random mutagenesis due to the rarity of some mutations [180]. This approach, typically used in combination with site-directed mutagenesis, could be used to find and target residues known to control a desired functionality but also to find and avoid residues known to negatively affect protein folding [181].

Introduction

Semi-rational design approaches also include predictive methods. This is the case for proteins chimeras, proteins designed by combining computationally the structures of two proteins of interest [182, 183]. Such approach was for, for instance, used for the design of a chimera from two distantly-related β -glucosidase [183]. In addition, modern computational and data analysis techniques, such as machine learning, have been used in conjunction with experiments in order to further predict protein design. For example, Saito *et al.* used machine learning to reduce the library size for identifying GFP variants exhibiting yellow fluorescence [184]. In the absence of machine learning, an initial library of 155 mutants yielded only four proteins exhibiting yellow fluorescence (3 %). On the basis of the results from this screening, the authors constructed a machine-learning algorithm to predict the fluorescence properties of the protein mutants based on their sequences. Using this algorithm, an additional 63 mutants were generated, of which 70 % were shown to exhibit yellow fluorescence. This approach also enabled the discovery of other variants exhibiting improved fluorescent properties over YFP. While being less predictive than rational design approaches, semi-rational still enable the efficient engineering of proteins while significantly limiting the size of the screening library. These semi-rational approaches are even more facilitated by the creation of databases identifying important amino acid positions in the protein [185] and enabling the search of protein analogues [186]. Yet, a minimal knowledge on the protein structure-function relationship is needed to apply a semi-rational design, which is lacking for most biological systems.

Semi-rational design approaches have similarly been developed for SWCNT complexes with less defined structure-function relationships. Early studies based on IEX for DNA-assisted SWCNT sorting reported that the length of the DNA sequence had a negligible effect on IEX separation for sequences longer than 20 bases [102]. Subsequent studies showed that the separation exhibited a strong DNA sequence- and length- dependence for oligomers of lengths around 12 nucleotides (8- to 16-mer) [101, 123]. These preliminary findings were used to narrow significantly the search space, ultimately leading to the separation of more than 20 distinct SWCNT chiralities and enantiomers from a screening of over 300 DNA sequences (Figure 6).

Directed evolution

In the absence of any information on the structure-function relationship, more empirical approaches must be used to navigate a biomaterial's search space. These cases especially benefit from techniques such as directed evolution, which is a guided search characterized by sequential rounds of screening or selection [187]. This methodology is based on the principle that the properties of a protein are a continuous function of its amino acid sequence: if a protein exhibits a specific function, a protein with a similar sequence will also likely exhibit that function. Therefore, proteins with significantly different sequences, which constitute the vast majority of the search space, are overall less likely to demonstrate the desired functionality.

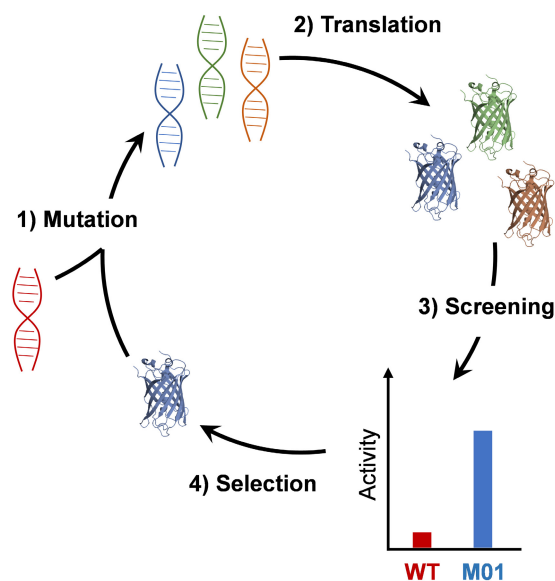


Figure 7 – Schematic representation of the directed evolution approach of proteins. The technique relies on an iterative procedure composed of (1) mutating the sequence coding for the protein of interest; (2) creating a library of mutants by translating the mutated DNA sequences into proteins; (3) screening the library for the enhanced property of interest, such as improved protein activity; and (4) selecting a mutant(s) (M01) exhibiting an improved property compared to the starting (or wild-type, WT) protein.

The general approach, illustrated in **Figure 7**, aims at iterative, incremental improvements of protein function over several cycles of mutation and selection. Briefly, (1) a starting protein with some desired functionality is chosen, and its sequence is mutated; (2) the mutated sequences are translated to generate a library of protein mutants; (3) the resulting protein mutants are screened; and (4) the protein(s) showing improved functionality are selected and further mutated to begin a new round of screening and selection. This cyclic procedure is repeated until the desired functionality threshold has been reached or until no further improvements are observed through additional rounds of mutation. Directed evolution has been used on multiple occasions to enhance proteins and, in particular, the activities of enzymes in organic solvents. Some of the earliest examples of this approach are the engineering of subtilisin E and paranitrobenzyl esterase enzymes [164, 187]. In the first case, a variant of the subtilisin E containing 10 amino acid substitutions was found to show a 256-fold increase in substrate hydrolysis (**Figure 6**) [164]. Similarly, the evolution of the 489-residue paranitrobenzyl esterase enzyme resulted in a 16-fold improvement over the wild-type enzyme in aqueous-organic solvents [187]. In this latter example, the starting protein was subjected to multiple rounds of random mutagenesis, and protein variants were sequentially screened and selected for improved activity. Using this approach, Moore *et al.* were able to navigate a fraction of the 20^{488} possible sequences by screening a total of 12,700 proteins (over four generations) and identifying mutations yielding improved activity under nonnative conditions.

Introduction

Each step of the directed evolution cycle is designed around the available information on the specific protein's structure and function. The starting protein may demonstrate a certain functionality, as in the example above, providing a starting point for a library of mutants likely to demonstrate similar or improved functionality. In cases where the desired functionality is completely unfounded in nature, researchers must rely on more elaborate means of identifying a suitable starting sequence and may rely on semi-rational approaches in order to find an interesting starting point for the directed evolution. In addition to the starting sequence, the mutation rate and library size are adjusted with the specific protein in mind. In the absence of any structural or functional information, a protein library may be generated using random mutations throughout the protein sequence. The mutation rate should be high enough to maximize the diversity of mutants and minimize the number of non-mutated proteins in the library, while low enough that the majority of mutants still retain some functionality [188].

The practical throughput of the screening assay must also be taken into consideration when deciding on a library size. Two ways to assay the protein libraries are possible: screening assays and selection assays [189, 190]. In screening assays, researchers must evaluate all the mutants' functionalities prior to selecting the desired mutants. On the other hand, selection assays are ideally designed to allow only mutants with improved functionalities to emerge from the assay, without the need to necessarily characterize the functionalities of the undesired mutants. While selection assays can benefit from increased throughput for larger libraries, they often rely on selection criteria that are not necessarily related to improved protein functionality, yielding a greater number of false positives [191]. The final round of evolution may result in no further improvement in protein functionality, yielding a protein with properties that fall below a desired threshold. In this instance, increasing the number of mutants screened can improve the probability of identifying a more suitable mutant. In the event that a local maximum has been achieved, additional strategies such as increasing mutation rate, introducing neutral mutations and implementing combinatorial permutations of beneficial mutations (as identified in previous rounds) can be used to relocate the search to an area with a possibly higher optimum [192, 193].

In parallel, as we previously discussed, the properties of the DNA-SWCNT complexes depend on the DNA. This dependence is particularly important for applications such as the creation of sensors selective to specific analytes (**Figure 6**). Yet, these complexes lack a defined structure-function relationship therefore preventing to design them using a rational approach. Alternatively, as for the design of proteins, it could be possible to use evolutionary techniques, such as directed evolution, in order to engineer the properties of the DNA-SWCNTs in a more guided manner.

Objective of the thesis

This thesis aims to address the challenges currently faced in the design of DNA-SWCNTs by applying strategies developed in the field of protein engineering. In particular, we demon-

strate the strength of approaches such as directed evolution over current state-of-the-art methods for the engineering of DNA-SWCNT sensors. We show that directed evolution can be used to selectively and simultaneously enhance various aspects of the complexes, from their optical properties to their sensing capabilities and SWCNT chirality specificities. Moreover, we demonstrate the use of additional approaches, such as the use of a semi-rational design and the incorporation of chemical modifications, in order to further improve the performances of the sensors beyond the capabilities of directed evolution. This dissertation is composed of five chapters that were, or are expected to be, published in peer-reviewed journals.

Chapter 1: *Modulating the optical properties of DNA-SWCNT sensors by directed evolution*

The first chapter of this thesis introduces a novel approach developed for the directed evolution of DNA-SWCNTs. This approach was further demonstrated for the engineering of the fluorescence properties of the complexes. We demonstrate the improvement of the fluorescence QY of the complexes by up to 56 % following two evolution cycles while retaining other properties of the sensors such as their target sensitivities and selectivities. This demonstration therefore allows the creation of brighter sensors with stronger emission signals for in *in vivo* and deep-tissue measurements. More importantly, this chapter provides the first demonstration of directed evolution in engineering the properties of the DNA-SWCNT complexes.

Chapter 2: *Directed evolution of DNA-SWCNT sensors for the simultaneous detection of mycotoxins*

The second chapter focuses on the discovery and subsequent engineering of DNA-SWCNT sensors through directed evolution for the detection of mycotoxins in food products. We successfully demonstrate the creation of sensors for the detection of both the aflatoxin B1 (AFB1) and fumonisin B1 (FB1) mycotoxins based on the specific response of the (9,4) and (7,5) SWCNT chirality fluorescence peaks, respectively. We show that directed evolution can be used to improve the response of our sensors towards mycotoxins, achieving up to 314 % improvement for the AFB1 response after four rounds of evolution. We also show that directed evolution can be used to modulate the selectivity of the response, both to mycotoxins and SWCNT chiralities, as well as to improve the fluorescence intensity of the sensors. Because of the chirality-dependent SWCNT specificity of the response, we show that both mycotoxins can be detected simultaneously in the presence of complex food medium by monitoring the (9,4) and (7,5) chiralities, without the need to separate the chiralities beforehand. **Chapter 2** therefore describes how directed evolution can be used to engineer multiple aspects of the DNA-SWCNT complexes. This chapter also includes the first demonstration of the DNA shuffling approach used to evolve the complexes faster than with conventional mutagenesis cycles. Finally, the findings of this chapter showed that the sensors discovered through directed evolution can be used to elucidate the different interaction mechanisms occurring between the sensor and the target analytes, in this case the AFB1 and FB1 mycotoxins.

Chapter 3: *Towards a semi-rational design of DNA-SWCNT sensors*

The third chapter describes how the DNA-SWCNT complexes can be designed using a more rational approach complement the directed evolution strategy. A systematic investigation of the final mycotoxin sensors acquired in **Chapter 2** was used to identify the underlying sequence contributions towards the AFB1 and FB1 sensor responses. We found that the AFB1 response could be significantly improved by modulating the base content of the sequence, in particular the G-content. We further showed that this increase in response was attributed to both an increase in surface coverage and to the formation of G-quadruplex (G4) secondary structures on the SWCNT surface. In parallel, we found that the FB1 response could be modulated by mutating a specific part of the DNA sequence and managed to improve both the response towards FB1 and the reversibility of the sensors. Finally, we demonstrated that the families of sensors found for the detection of both AFB1 and FB1 could be also used for the detection of other targets interacting with either the SWCNT surface, for the AFB1 sensor family, or with the DNA wrapping, for the FB1 sensor family. Throughout this chapter, we demonstrate the various advantages of a semi-rational approach for the design of DNA-SWCNT sensors. These more rational approaches complement the directed evolution by limiting the library to mutants with more promising prospects for improved performances. Such a semi-rational approach also allows one to understand the complex in greater detail to create sensors for a specific class of molecules or simply to study the interaction between a target and the sensors.

Chapter 4: *Modulating the properties of DNA-SWCNTs through DNA chemical modification*

The fourth chapter explores the use of chemical modifications on the DNA wrapping in order to modulate the properties of the DNA-SWCNT complexes. We show that the introduction of functional groups in the DNA sequence can result in variations in the dispersibility, the fluorescence intensity and the sensing properties of the DNA-SWCNT suspensions. These effects were observed to depend on the sequence of the DNA wrapping as well as on the preparation technique used for the preparation of the DNA-SWCNT suspensions. We observed significant increases in the fluorescence intensities of the modified (AT)₁₅- and (GT)₁₅-SWCNT complexes when compared to their unmodified counterparts. We attribute these variations in intensity to changes in both the SWCNT chirality distribution as well as in the dispersion quality, for which the presence of the modifications is believed to induce a change in the interaction between the wrapping and the SWCNT. Moreover, although we noted a decrease in the response of the modified sensors towards various targets, the sensors retained similar analyte selectivities as the unmodified complexes. The increased fluorescence intensities observed for the modified complexes could make them particularly attractive for sensing applications *in vivo* which necessitate bright probes. The results presented in this chapter therefore demonstrate a new approach for modulating the fluorescence properties of DNA-SWCNT complexes without the need to alter the DNA sequence or the addition of exogenous compounds. This method could therefore be used in combination with other approaches, such as directed evolution, in order to improve the performances of DNA-SWCNTs beyond the limits of natural oligonucleotides.

Chapter 5: *Outlook on the directed evolution of DNA-SWCNTs with long oligonucleotides*

The fifth and final chapter of this thesis presents an outlook on the ability to perform directed evolution on DNA-SWCNTs using long, bioengineered oligonucleotides. The properties of the DNA-SWCNTs have been shown to depend not only on the sequence but also on the length of the DNA wrapping. We show that the use of longer DNA sequences can enable improvements in fluorescence intensity and target selectivity, while not significantly affecting the dispersibility or binding affinity towards the SWCNT. As a result, performing directed evolution on DNA-SWCNTs with long oligonucleotides could allow the development of even more optimized sensors. Because of the low efficiency of the DNA solid-state synthesis for sequences longer than 40 nucleotides, the directed evolution of DNA-SWCNT complexes is restrained to the use of short DNA sequences. To tackle this limitation, we propose a biologically-driven approach to generate DNA variants exhibiting an efficiency that is largely independent of the length of the oligonucleotides. We further demonstrated the use of this method for the creation of a library of DNA-SWCNT complexes in a high-throughput fashion.

1 Modulating the optical properties of DNA-SWCNT sensors by directed evolution

Portions of this chapter are reproduced with permission from [125]: Lambert B.P; Gillen, A.J.; Schuerge N.; Wu S-J.; Boghossian, A.A. Directed evolution of the optoelectronic properties of synthetic nanomaterials, *Chemical Communications* (2019). In addition, we would like to thank Melania Reggente who provided the AFM measurements.

1.1 Abstract

Directed evolution is a powerful approach that has previously been demonstrated to tailor protein properties toward new or enhanced functions. In this first chapter, we use directed evolution to engineer the fluorescent properties of DNA-wrapped single-walled carbon nanotube (DNA-SWCNT) sensors through DNA mutation. Using this approach, we show that it is possible to improve the quantum yields of DNA-SWCNTs, with enhancements up to 56 % in fluorescence intensity following two evolution cycles. We further demonstrate that this improvement in fluorescence intensity does not have a significant effect on the response of the sensors, both in terms of selectivity and sensitivity. This approach therefore enables an improved imaging of DNA-SWCNT sensors, in particular for experiments in which the use of additives to enhance fluorescence could be detrimental.

1.2 Introduction

Synthetic nanomaterials are typically known to rely on a rational approach for tuning their physical and chemical properties. This approach involves modifying the morphology, composition, shape, size, or surface chemistry of the material in a predictive manner to achieve a desired outcome [194–196]. For instance, the optoelectronic properties of quantum dots (QDs) can be readily tuned by changing particle size [36]. Nevertheless, this rational approach is limited to materials for which the relationship between material's structure and function is known. Materials lacking a defined structure–function relationship are commonly encountered in the field of protein engineering. To engineer these biomaterials, directed evolution,

which relies on the iterative screening and selection of mutants from a collection of mutated proteins, is used to enhance or change a desired protein function [187, 197]. Herein, we apply a directed evolution approach to engineer the fluorescent properties of nanomaterials, in particular single-stranded DNA-wrapped single-walled carbon nanotubes (DNA-SWCNTs) complexes, which currently lack a defined structure–function relationship.

SWCNTs are cylindrical one-dimensional nanostructures that can be conceptualised as rolled-up sheets of graphene [62]. The rolling angle of the graphene sheet determines the (n,m) chirality of the SWCNT, resulting in either metallic or semiconducting properties. Semiconducting single-walled carbon nanotubes (SWCNTs) have attracted particular interest in the field of optical biosensing owing to their near-infrared (NIR) fluorescence. This NIR emission, between 950 and 1350 nm for most SWCNTs, lies within the first and second biological windows (NIR-I and NIR-II) where the absorption of water, blood and tissues is minimal [27] and where the autofluorescence of biological pigments is limited [71]. In addition, SWCNTs possess an indefinite photo-stability [26] and a tunable biocompatibility [35], allowing to perform deep-tissue imaging and sensing without noticeable photobleaching. Despite these advantages, the applicability of SWCNT sensors remain limited by their low quantum yields (QYs), 8 % [198] for individual SWCNTs and up to 1.4 % [199] in solution, almost one order of magnitude lower than for their NIR fluorophores counterparts, 11 % for dyes [200] and 45 % for quantum dots (QDs) [201]. It is therefore critical to increase the QY of SWCNT sensors in order to fully exploit their performances for *in vivo* applications.

Various approaches have been proposed in order to increase the QY of SWCNT suspensions. First, fluorescence intensity enhancement was demonstrated through incorporation of chemical moieties on the SWCNT surface [145–148]. The fluorescence intensity of SWCNT suspensions was also improved through the optimization of the dispersion conditions or purification of the suspension in order to increase or select the SWCNT length and reduce the number of defects [137–139]. However, the effect of these methods on the properties of existing SWCNT sensors has yet to be studied as recent reports indicate that both the presence of aryl groups on the SWCNT surface and the SWCNT length could affect the sensing properties of the SWCNT complexes [149]. For SWCNT sensors, improvements in QY have been obtained through the addition of external agents such as reducing agents [150–152], plasmonic nanoparticles [153], fluorophores [154], salts [112] and rare-earth elements [155]. Yet, the presence of such additives might limit the reactivity of SWCNT sensors [112, 135, 156] and could limit their biocompatibility [157, 158]. It would therefore be preferable to improve the fluorescent properties of the sensors without the need of exogenous compounds.

The fluorescence intensity of SWCNT complexes was further shown to depend on their wrapping. Surfactant-wrapped SWCNTs, for example, typically exhibit high fluorescence intensity [23, 202–204] while SWCNTs wrapped by biopolymers, such as DNA or chitosan, exhibit much lower fluorescence intensities [78, 114]. This modulation in intensity was shown to depend mainly on the coverage of the SWCNT surface [112, 124]. If the SWCNT surface is exposed, the excitons may interact directly with oxygen molecules [124] or endoperoxide species [112]

resulting in a quenching of the fluorescence. Although they enable a brightening of SWCNT complexes, surfactants are usually not preferred for SWCNT functionalization as they result in complexes with limited target selectivity [78] and can lower the biocompatibility of the sensors [205]. DNA, on the other hand, is an attractive wrapping for *in vivo* applications as it enables the creation of selective SWCNT sensors towards a large range of targets [33, 58, 59, 134] and can improve the biocompatibility of SWCNT suspensions [35]. Various studies have shown that different DNA sequences could result in DNA-SWCNT complexes with varying fluorescence intensities [57, 61, 114] and surface coverages [124, 126, 206]. It should therefore be possible to tune the QY of DNA-SWCNTs solely by altering the DNA sequence.

Yet, a general understanding of how the DNA sequence affects the properties of the DNA-SWCNT complexes is lacking. So far, random library screening has been the main approach used to improve the properties of the DNA-SWCNT sensors such as fluorescence properties [114] or analyte response [58, 60, 61]. In these cases, the DNA sequences are usually around 30 nucleotides long resulting in a total of 4^{30} different possible sequence combinations. As the number of DNA-SWCNT screened reported so far is roughly around 350 complexes [122], the performance of the majority of DNA-SWCNT sensors is overlooked.

To tackle this issue, we demonstrate in this chapter the use of directed evolution, which offers a guided search through this vast DNA sequence space, for the improvement of the QY of DNA-SWCNT complexes and more specifically the (GT)₁₅-SWCNT sensor. The (GT)₁₅-SWCNT sensor has been thoroughly studied for the detection of the dopamine neurotransmitter [58, 60] and was more recently used for *in vitro* and *in vivo* sensing of dopamine [28, 34]. Through the use of directed evolution, we show it is possible to increase the QY of the (GT)₁₅-SWCNT sensor by up to 56 % for the (8,6) chirality, theoretically allowing an imaging in brain tissue approximately 193 μm deeper, after two rounds of evolution. We also demonstrate that the mutant sensors showing increased QY do not show significant differences in the overall sensing capabilities compared to the (GT)₁₅-SWCNT sensor, both in terms of selectivity and sensitivity.

1.3 Materials and methods

1.3.1 Materials

Purified SWCNTs were ordered from NanoIntegris (HiPco, batch HP29-064). All DNA oligomers were purchased from Microsynth. The IR-26 dye was purchased from Radiant Dyes. All chemicals were purchased from Sigma-Aldrich, unless otherwise indicated.

1.3.2 Design of the mutant sequences

The mutant sequences were created computationally using Matlab (Matlab R2017b, Mathworks) according to the following approach: (1) the selection of a random nucleotide position number, (2) a random substitution by a different nucleotide among the three others (1/3

probability for A, C, G, or T). In the case where more than one mutation is needed, the position of the first substitution is removed from the list of possible positions in order to not mutate two times the same nucleotide. In this case, the number of possible sequence mutants is:

$$N = 3^k \binom{n}{k} \quad (1.1)$$

with N the number of sequence mutants, n the length of the DNA sequence and k the number of mutants. For a length of 30 nucleotides and 3 mutations, there are 109 620 possible sequence mutants. As this number is way beyond our screening capabilities and to save computational resources, we only generated 1000 mutants. As the creation of the mutations is random, it is possible to have redundant sequences with the same mutations, we therefore performed an addition step to remove the redundant sequences at the end of the process. Moreover, we can also choose to remove sequences similar to some reference sequences in order to avoid generating mutants with the same sequence as mutants of the previous round. Finally, we selected randomly 100 sequences for the first round and 10 sequences for the second rounds from the generated libraries.

1.3.3 DNA-SWCNT complexes preparation

Direct sonication is the most popular technique for the dispersion of DNA with SWCNTs [82]. However, this method allows the process of only a few samples as a time (typically no more than 10) and requires a rather large sample volume (> 0.5 mL). For directed evolution, this method is not suitable as the preparation of a large number of samples would be required in order to have an efficient screening. In addition, as the sample size is large in directed evolution, it would be more cost-effective to process lower sample volumes. In this regard, it was necessary to develop a protocol for the high-throughput wrapping of SWCNTs with DNA sequences. This procedure consists of two steps: (1) the exchange of wrapping between surfactant-suspended SWCNTs and DNA, and (2) the purification of the DNA-SWCNT sensors.

For the first step, we adapted a previous procedure used to suspend SWCNTs with DNA [207]. The wrapping exchange between surfactant-suspended SWCNTs and DNA was performed in the presence of methanol, used to increase the critical micelle concentration (CMC) of the surfactant. In our study, sodium cholate (SC) was used as the dispersant for SWCNTs. Although other studies demonstrated similar exchange protocols with SWCNTs suspended in sodium dodecyl sulfate (SDS) [207] or sodium deoxycholate (SDC) [143], we preferred the use of SC as it allowed the preparation of DNA-SWCNT suspensions with lower DNA:SWCNT mass ratios, allowing the use of lower DNA concentrations (see **Chapter 5**). As we obtained satisfying results with the preparation of DNA-SWCNTs with the SC surfactant, we decided to continue with the same protocol throughout the thesis.

For the second step, we adapted the ethanol precipitation procedure usually performed in nucleic acid research to desalt and purify DNA samples. Using this technique, we show that it

is possible to prepare DNA-SWCNT complexes in a high-throughput scale while also allowing a greater flexibility in the preparation volume and the use of lower DNA concentrations. We describe the steps of the DNA-SWCNT preparation below.

Preparation of SC-SWCNT complexes

30 mg of SWCNTs (HiPco, batch HP29-064, NanoIntegris) were suspended in 30 mL of 2 % (w/w) SC in deionized (DI) water. The suspension was homogenized for 20 min at 5,000 rpm (PT 1300D, Polytron) and sonicated for 1 h using a probe-tip ultrasonicator (1/4 in. tip, Q700 Sonicator, Qsonica) at 10 % amplitude in an ice bath. The SWCNT suspension was centrifuged at 30,000 rpm ($\approx 164,000 \times g$) for 4 h at 25°C (Optima XPN-80, Beckman Coulter), and the supernatant was collected. The concentration was measured by UV-VIS absorbance spectroscopy (UV-3600 Plus, Shimadzu) in quartz cuvettes (10 mm Quartz SUPRASIL, Hellma Analytics) at 632 nm using the extinction coefficient $\epsilon_{632} = 0.036 \text{ L.mg}^{-1}.\text{cm}^{-1}$ [208]. The SWCNT suspension was diluted to a final concentration of 108 mg/L in 2 % SC solution.

SWCNT wrapping exchange

The DNA oligomers were dissolved in DI water, the DNA concentration was measured by absorbance at 260 nm (Nanodrop 2000, Thermo Scientific) and diluted to a final concentration of 50 μM with DI water. To yield a final volume of 500 μL , 100 μL of DNA solution was mixed with 100 μL of SC suspended SWCNT and 300 μL of methanol (VWR Chemicals). The suspension was incubated at room temperature for 2 h. The incubation time was chosen based on preliminary experiments (**Figure A.1**) showing that the peak of the SWCNT complexes shifts and stabilizes after less than 30 min, regardless of the DNA sequence used. A longer incubation time was chosen in order to make sure that the wrapping exchange occurred even for sequences exhibiting low affinity to SWCNT.

DNA-SWCNT complexes purification

In order to remove the methanol and SC from the suspension, the complexes were purified using a protocol similar to the ethanol precipitation procedure commonly used in the purification of nucleic acids [209]. 76.9 μL 1.5 M sodium chloride (NaCl) solution was added to yield a final concentration of 200 mM NaCl. Following this addition, 1,142 μL (2.5x total volume) of ice-cold ethanol (VWR Chemicals) was added. The suspension was incubated at -20°C for 1 h and centrifuged at 21,130 $\times g$ for 30 min (5424 R, Eppendorf). The supernatant was discarded and the pellet washed vigorously and vortexed with 1,666 μL (2.9x total volume) of 70 % (v/v) ethanol. The suspension was centrifuged at 21,130 $\times g$ for 1 h (5424 R, Eppendorf). The supernatant was discarded, and the pellet was air dried for 12 min and re-suspended in 500 μL of 100 mM NaCl in DI water. The final suspension was centrifuged at 21,130 $\times g$ for 30 min (5424 R, Eppendorf) and the supernatant collected to remove potential aggregates.

The suspension was diluted to achieve an absorbance of 0.1 at 632 nm (≈ 0.066 after blank correction) for a 100 μL aliquot placed in a 96-well plate (EIA/RIA plate, Corning) using a plate reader (Varioskan LUX, Thermo Scientific).

1.3.4 Near-infrared microscopy setup

A custom-built near-infrared microscope [81] was used to monitor SWCNT fluorescence. The setup consists of a supercontinuum laser (SuperK Extreme EXR-15, NKT Photonics) coupled to a tunable band-pass filter unit (SuperK Varia, NKT Photonics) that operates between 400 and 830 nm. A short-pass filter (890 nm BrightLine, Semrock) was used to remove near-infrared contributions from the laser (near-infrared pumping). The laser light is focused on the sample plane (illumination spot of $350 \times 350 \mu\text{m}^2$) by a 20X objective (M Plan Apo NIR, NA 0.4, Mitutoyo Corporation) coupled with a dichroic beam-splitter (LP 830nm, Semrock). The SWCNT emission is focused onto the entrance slit of a spectrometer (IsoPlane SCT-320, Princeton Instruments) and collected by an InGaAs NIR detector (NIRvana 640 ST, Princeton Instruments) using a 70 lines.mm^{-1} grating. Measurements were recorded with LightField (Princeton Instruments) in combination with a custom-built LabView (National Instruments) software for automation of the measurements.

1.3.5 Fluorescence spectroscopy measurements

The fluorescence measurements were performed in 384-well plates (MaxiSorp, Nunc) using an exposure time of 5 s for all experiments except the surfactant replacement assay experiments, which were performed using an exposure time of 2 s. For all measurements, the laser excitation had a bandwidth of 10 nm and a relative power of 100 %. The screening measurements were performed under 575, 660 and 745 nm excitation. The photoluminescence excitation (PLE) maps were acquired between 500 nm and 800 nm with a 5 nm step. The dopamine and glutamic acid experiments were recorded under an excitation of 745 nm. The excitation of 745 nm was chosen for the integrated fluorescence measurements in this study because it simultaneously excites the (10,2), (9,4), and (8,6) chiralities. All measurements were performed at room temperature and the plates were sealed (Empore, 3M) to avoid evaporation. Spectral and statistical analysis was done using a custom Matlab code (Matlab R2017b, Mathworks). The fluorescence results were standardized by the SWCNT concentration of each sample. The peak intensities and positions of the individual chiralities were determined by performing a single Lorentzian fitting of the peaks in the fluorescence spectrum. Unless otherwise indicated, the p -values reported correspond to one-way ANOVA tests.

1.3.6 Surfactant replacement assay

The DNA wrapping was replaced using the SDC surfactant following a previously reported procedure [120]. The SDC was dissolved to a concentration of 1 % (w/w) in DI water. 45

μL of DNA-SWCNT suspension was mixed with 5 μL of 1 % (w/w) SDC in a 384-well plate (MaxiSorp, Nunc) and incubated at room temperature for 15 min. The near-infrared fluorescence of the suspension was recorded before and after SDC addition. The absorbance was recorded in quartz cuvettes (10mm Quartz SUPRASIL, Hellma Analytics) using a UV-VIS-NIR spectrophotometer (UV-3600 Plus, Shimadzu).

1.3.7 Relative QY measurements

In this work, we determined the relative QY by comparing the integrated intensities and absorbances of the DNA-SWCNT and the IR-26 reference dye. The IR-26 dye was chosen as its NIR emission overlaps with the SWCNT emission (**Figure A.13**). In addition, its relatively low QY of 0.11 ± 0.023 % [201], in the same order of magnitude as SWCNTs, allows the use of solutions of comparable absorbance hence limiting differences in light re-absorption. The IR-26 dye was dissolved in 1,2-dichloroethane (DCE) to a final absorbance of approximately 0.04 at 808 nm (in 50 μL). The concentration of DNA-SWCNT was the same as used for the other experiments. The measurements were done in 96-well plate with glass bottom (Corning) to avoid the effect of the DCE on the plate. The dye and nanotube solutions were diluted to four concentrations: 100 % (stock concentration), 80 %, 60 % and 40 %. The absorbance of the samples was measured with plate reader (Varioskan LUX plate reader, Thermo Scientific) at 808 nm. The 808 nm excitation wavelength was chosen as it allowed to excite both the SWCNTs and the IR-26, as it was previously shown [31]. Using the same excitation wavelength is critical as it allows to consider the same losses in excitation light for both the reference and sample. The integrated intensities were plotted as a function of absorbance and the slopes were used to determine the QY values using the formula:

$$\Phi_X = \frac{A_{ref}}{A_X} \frac{F_X}{F_{ref}} \left(\frac{n_X}{n_{ref}} \right)^2 \Phi_{ref} \quad (1.2)$$

with Φ_X and Φ_{ref} the QYs of the DNA-SWCNT and the reference dye, F_X and F_{ref} their integrated intensities under 808 nm excitation, A_X and A_{ref} their absorbances at 808 nm, and n_X and n_{ref} the refractive indexes of water and DCE respectively.

1.3.8 Free DNA removal

The free DNA, DNA not bound to the SWCNT surface, was removed using Amicon Ultra-0.5 100 kDa devices. The membrane of the device was first rinsed with 500 μL DI water. Then, DNA-SWCNT suspension and DI water were added to the device for a total volume of 500 μL and the device was centrifuged at 14,000 x g for 1 min. The flow through was discarded. DI water was added to the device to reach a final volume of 500 μL and the DNA-SWCNTs stuck on the membrane were resuspended by pipetting up and down. The samples were centrifuged, washed and resuspended again for 5 additional times in order to remove all traces of free DNA. The last centrifugation was done for 5 min instead of 1 min. Finally, the samples

were resuspended in 0.1 M NaCl and centrifuged to remove SWCNT aggregates. The final suspensions were diluted to the same concentration as the initial suspensions before filtering ($A_{632}(100 \mu\text{L}) \approx 0.066$ after blank correction).

1.3.9 Analyte detection assay

10 mM solutions of glutamic acid (L-glutamic acid monosodium salt monohydrate), γ -amino-butyric acid (GABA), acetylcholine (acetylcholine chloride), glycine, and dopamine (dopamine hydrochloride) were prepared in aqueous NaCl solution (0.1 M). The fluorescence of 49.5 μL of ssDNA-SWCNT was measured initially in a 384-well plate (MaxiSorp, Nunc). After this measurement, 0.5 μL of analyte (final concentration of 100 μM) was introduced to the SWCNT suspension and mixed by pipetting up and down several times. The suspension was incubated for 20 min at room temperature prior to recording the second fluorescence spectrum. For the calibration curves, stock solutions of 1 mM, 0.1 mM, and 0.01 mM dopamine were prepared from the 10 mM stock solution and analysis was carried out using the same procedure described above.

1.3.10 Light imaging depth calculation

The following calculations are based on the findings of Lee *et al.* for determining light imaging depth in biological tissue [210] and are derived from the Beer-Lambert law, considering an equal concentration of fluorophores and the same excitation and emission wavelengths ((8,6) chirality). We apply these calculations for the comparison of two DNA-SWCNT sensors:

$$\log\left(\frac{F_{0n}}{F_n}\right) = \gamma_{em} d_n \quad (1.3)$$

with γ_{em} representing the extinction coefficient of the tissue at the emission wavelength; F_{0n} ($n=1,2$) representing the initial fluorescence intensities before tissue penetration for the sensors 1 and 2 respectively; F_n ($n=1,2$) representing the fluorescence intensities after tissue penetration; and d_n ($n=1,2$) representing the corresponding imaging depths in biological tissue. The initial fluorescence intensities are defined by:

$$F_{02} = \alpha F_{01} \quad (1.4)$$

where α is a scaling factor relating the fluorescence intensity with that of the mutant. Since we want to compare the difference in light imaging depth between the two sensors under the same conditions, we set $F_1 = F_2$ to indicate that the final recorded signal should be equal for both complexes (to achieve a similar signal-to-noise ratio). Hence, we have:

$$d_2 = d_1 + \log(\alpha) \frac{1}{\gamma_{em}} \quad (1.5)$$

We consider an extinction coefficient γ_{em} of approximately 10 cm^{-1} for biological tissues like the brain cortex [211]. For the wavelengths considered in this study for SWCNT emission (1000 to 1300 nm), we can estimate the increase in imaging depth between the mutant and the reference complexes by calculating the difference $d_2 - d_1$.

1.4 Results and discussion

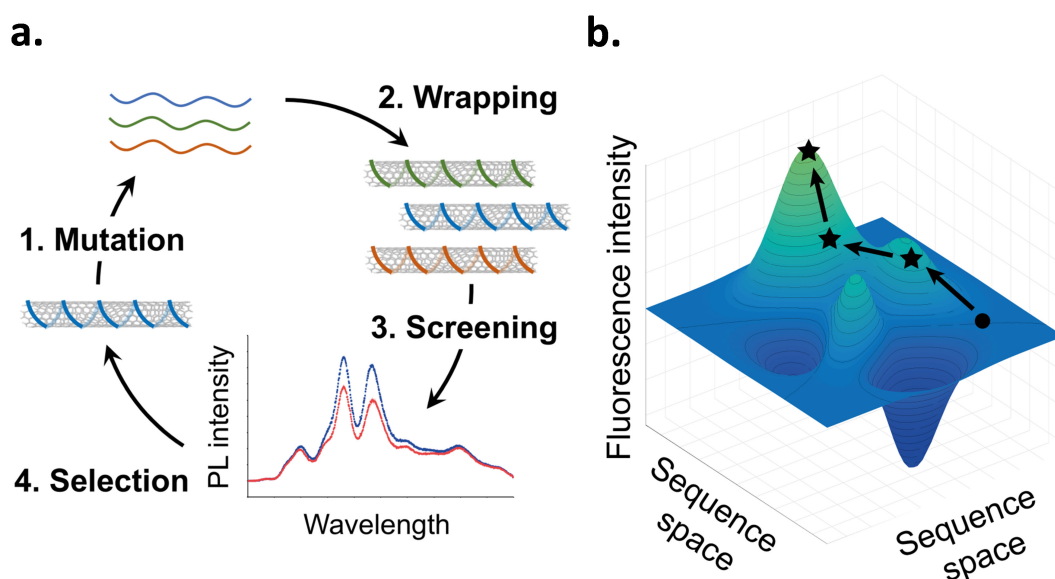


Figure 1.1 – Application of directed evolution to DNA-SWCNT complexes. (a) Scheme of an evolution cycle for DNA-SWCNTs. Various DNA sequences are wrapped on SWCNTs, and the library of DNA-SWCNTs is screened for increased integrated fluorescence intensity. (b) Graphical representation of a hypothetical fitness landscape for DNA-SWCNTs. This plot illustrates how a particular property of the complexes may be evolved through DNA mutation. The fitness, in this case fluorescence intensity, of the sensors is represented as a function of the different DNA sequences. A representative evolution pathway is shown in black, where the circle represents a starting complex, and the stars represent the successive, improved hypothetical mutants obtained after each round of screening.

The evolution of the DNA-SWCNT sensor was done through the cyclic procedure illustrated in **Figure 1.1**: (1) random mutation of a selected sensing oligomer; (2) wrapping of the mutated oligomers on SWCNTs; (3) screening of the DNA-SWCNT complexes for enhanced fluorescence; and (4) selection of the mutants showing the highest fluorescence intensity for the next round of mutation. This approach assumes a smooth fitness landscape (**Figure 1.1**) whereby the evolution of a particular DNA-SWCNT property, in this case the fluorescence intensity, is envisioned as a continuous path among peaks and valleys which represent the respective enhancement or attenuation of this property. In addition, as the $(\text{GT})_{15}$ -SWCNT sensor is characterized by a low fluorescence intensity, even compared to other DNA-SWCNT sensors such as the $(\text{AT})_{15}$ -SWCNT sensor (**Figure A.2**), we believe the $(\text{GT})_{15}$ -SWCNT sensor is not located on an absolute maximum in the fitness landscape and it is therefore possible to evolve

it for fluorescence intensity.

Three random nucleotide substitutions were introduced computationally at randomized locations within the sequence (see **Methods**). The number of mutations per cycle was chosen based on preliminary results where the fluorescence intensities of DNA-SWCNT complexes containing one, two, or three random mutations were compared (**Figure A.3**). Whereas small variations in fluorescence intensity were observed between the sequences containing either one or two mutations, we found that sequences containing three mutations showed the greatest variability. We therefore decided to perform the experiments with three mutations on every round in order to maximize the diversity in sequences and our chances to find better performing mutants, while limiting the size of the screening library. The sequences of the DNA mutants are provided in **Table A.1**. We monitored the position of the absorbance and fluorescence peaks before and after wrapping exchange between sodium cholate (SC)-SWCNT and DNA to verify if the nanotubes were suspended by the DNA (**Figure A.4**, **Figure A.5**). We observed a shift towards longer wavelengths (red-shift), consistent with the observations of Kato *et al.* [117], conforming that the DNA replaced the surfactant on the SWCNT surface. We also independently confirmed DNA wrapping by comparing the behavior of the SC-SWCNT suspension in methanol in the presence and in the absence of DNA (**Figure A.6**). Without DNA, we observe aggregation of SC-SWCNTs upon addition of 60 % (v/v) methanol due to the increase in critical micelle concentration (CMC) of SC caused by the organic solvent. In contrast, no aggregation is observed upon addition of 60 % (v/v) methanol to SC-SWCNTs in the presence of DNA. This further demonstrates that the DNA replaced the SC on the SWCNT surface.

For the first evolution cycle, 99 mutants of the (GT)₁₅ sequence were first screened for increased fluorescence intensity integrated over the whole spectrum for the 575, 660 and 745 nm excitations (**Figure A.7**). Although we observed differences in intensity compared to the (GT)₁₅-SWCNT complex, no simple correlation could be found between the sequences of the variants and the changes in intensity (**Figure A.8**), hence confirming the need for directed evolution to improve such property. We mostly compared the integrated fluorescence intensities under 745 nm excitation, that we later denote as *integrated fluorescence intensities*, as we observed most fluorescence intensity increases under these conditions. We first identified three mutant complexes that demonstrated increased integrated fluorescence intensity compared to the (GT)₁₅-SWCNT complex: the M13- and M47- and M71-SWCNT mutants (**Figure 1.2**, **Table 1.1**). The M31- and M38-SWCNT mutants also exhibited increase in intensity compared to the (GT)₁₅-SWCNT complex but were not selected because of their larger error (**Figure A.9**). A second round of mutagenesis was performed by introducing three random nucleotide substitutions to the M13 and M47 mutants that exhibited the greatest increase in integrated fluorescence intensity. For this round, a library of 10 sequences was generated and screened to identify mutants exhibiting fluorescence enhancement. For the M47 sequence, no mutant exhibited higher fluorescence intensity compared to their parent complex (**Figure A.10**). On the other hand, the mutagenesis performed on the M13 sequence yielded two additional mutants, M13-1- and M13-6-SWCNT, that showed increased integrated fluorescence intensity

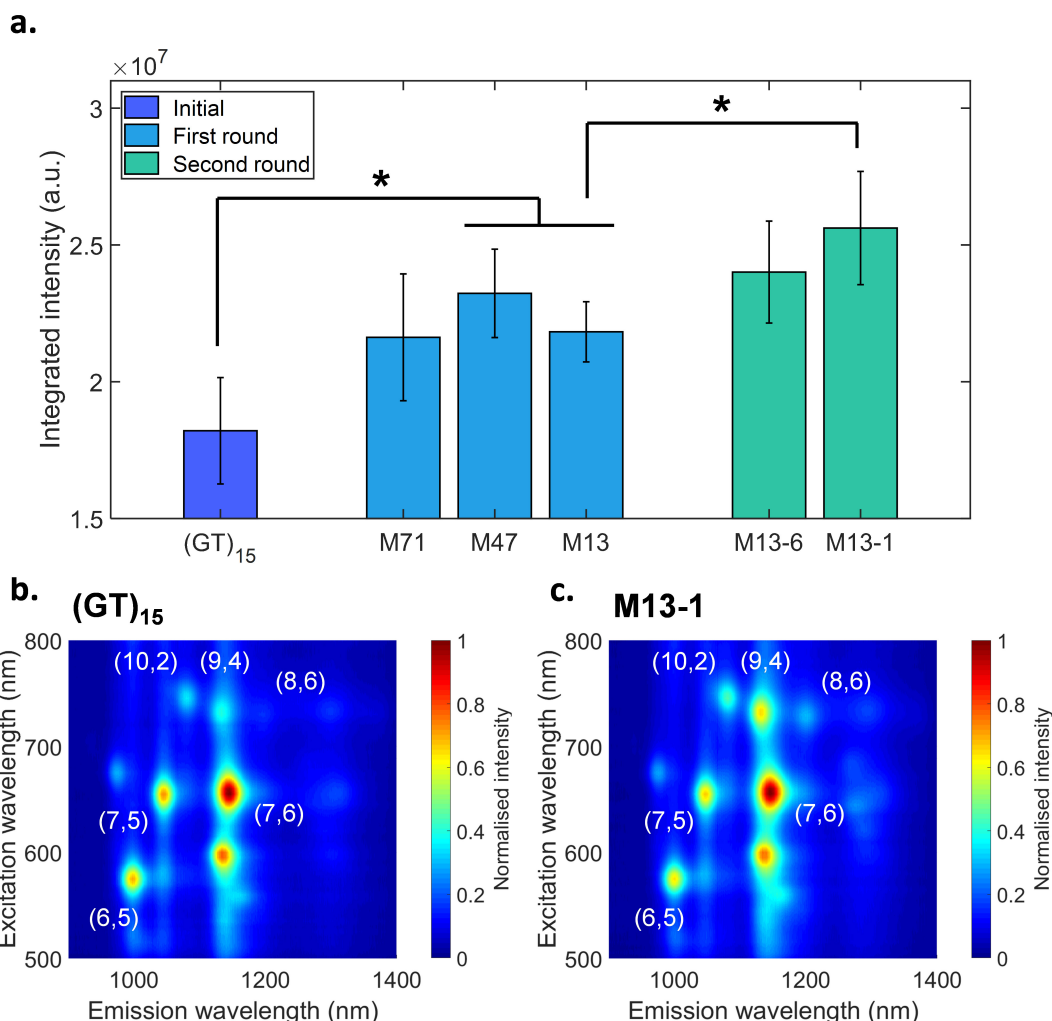


Figure 1.2 – Increase of fluorescence intensity after two evolution cycles. (a) Integrated fluorescence intensity under 745 nm excitation of the DNA-SWCNT mutants. The integrated intensity is calculated from the additive emissions for wavelengths between 900 and 1400 nm. Error bars represent 1σ ($n=3$). The * symbol indicates $p < 0.05$ according to two-sample student t-tests. (b) Photoluminescence excitation (PLE) maps of (b) the (GT)₁₅-SWCNT and (c) M13-1-SWCNT complexes. The SWCNT chiral indices (n,m) studied in this work are indicated in white. The fluorescence intensities are normalised between 0 and 1.

compared to the M13-SWCNT complex (**Figure 1.2, Table 1.1**). Although both complexes showed significant intensity increase compared to the (GT)₁₅-SWCNT complex, only the M13-1-SWCNT mutant showed significant increase compared to the M13-SWCNT mutant. We noted a strong chirality dependence on fluorescence enhancement. As shown in the photoluminescence excitation (PLE) maps (**Figure 1.2**), the increase in fluorescence intensity was larger for the (9,4), (10,2), and (8,6) chiralities. A quantitative comparison of the fluorescence changes for the different chiralities and the integrated intensity relative to the starting (GT)₁₅-SWCNT complex is shown in **Table 1.1**. Overall, the M13-1-SWCNT showed

Chapter 1. Modulating the optical properties of DNA-SWCNT sensors by directed evolution

the greatest fluorescence enhancement with an improvement in the integrated intensity of 41 % compared to (GT)₁₅-SWCNT. Moreover, the (9,4), (10,2), and (8,6) chiralities showed fluorescence intensity increases of up to 43 %, 54 %, and 56 %, respectively. Although the increase in the integrated intensity of the M71-SWCNT was not statistically significant compared to (GT)₁₅-SWCNT (**Figure 1.2**), significant increases (+38 %) were observed for the (10,2) chirality (**Table 1.1**). In addition to the two evolution cycles described in the main text, a third round of mutation was performed on the M13-1-SWCNT with a library size of 10, although no significant improvements in fluorescence were observed (**Figure A.11**).

Table 1.1 – Fluorescence intensity change compared to the (GT)₁₅-SWCNT complex. Fluorescence intensity change (in %) for the DNA-SWCNT mutants compared to the (GT)₁₅-SWCNT complex for the (6,5), (7,5), (7,6), (9,4), (10,2) and (8,6) chiralities and for the integrated fluorescence intensities under 575, 660 and 745 nm excitations. The error represents 1 σ (n = 3 replicates). The * symbol indicates $p < 0.05$ for two-sample student t-tests between the complex and (GT)₁₅-SWCNT.

| Mutant | 575 nm | 660 nm | 745 nm | (6,5) | (7,5) | (7,6) | (9,4) | (10,2) | (8,6) |
|--------|---------|---------|----------|--------|---------|---------|----------|----------|----------|
| M13 | 7 ± 10 | 7 ± 11 | 20 ± 14* | 1 ± 8 | 3 ± 9 | −3 ± 11 | 22 ± 17 | 35 ± 16* | 13 ± 18 |
| M47 | 10 ± 14 | 10 ± 12 | 28 ± 16* | 6 ± 10 | 7 ± 10 | −8 ± 11 | 21 ± 18 | 46 ± 17* | 40 ± 24* |
| M71 | 8 ± 14 | 9 ± 15 | 19 ± 18 | 3 ± 10 | 13 ± 13 | −2 ± 15 | 13 ± 20 | 38 ± 20* | 20 ± 24* |
| M13-1 | 16 ± 14 | 16 ± 14 | 41 ± 19* | 5 ± 11 | 1 ± 11 | 2 ± 13 | 43 ± 21* | 54 ± 19* | 56 ± 26* |
| M13-6 | 13 ± 14 | 10 ± 14 | 32 ± 17* | 2 ± 9 | −7 ± 10 | −5 ± 13 | 28 ± 20* | 44 ± 18* | 49 ± 25* |

Although we observed an increase, it does not necessarily correlate with an increase in QY. Indeed, the increase in intensity could result from a change in SWCNT chirality distribution as some DNA sequences may favor the dispersion of some specific SWCNT chiralities, resulting in an apparent increase in intensity for the same overall SWCNT concentration. To verify this, we replaced the DNA with the sodium deoxycholate (SDC) surfactant following a previously reported procedure [120]. We confirmed that the surfactant wrapping replaced the DNA by comparing the positions of the absorbance and fluorescence peaks before and after the displacement (**Figure A.4**, **Figure A.5**). The positions of the absorbance and fluorescence peaks were shifted towards shorter wavelengths (blue-shift), indicating a replacement of the DNA wrapping in correspondance with previous reports [120]. No variations were observed for the position of neither the absorbance nor fluorescence peaks after wrapping replacement, suggesting that the DNA wrapping was completely replaced for all complexes. All complexes had overlapping absorbance and fluorescence spectra (**Figure A.4**, **Figure A.5**) following SDC replacement of the DNA, suggesting that there was no change in the chirality distribution between the mutants and (GT)₁₅-SWCNT dispersions. Considering that all SDC-coated SWCNTs exhibit the same fluorescent properties (same QY), the lack of difference in peak intensity between the SDC-replaced complexes suggests that all complexes have the same SWCNT chirality distribution. Furthermore, we hypothesized that the differences in fluorescence intensity could be due to a sequence-specific selection of the SWCNT length, the mutant

complexes preferring longer and therefore brighter SWCNTs. To verify this, we performed atomic force microscopy (AFM) on the (GT)₁₅- and the M13-SWCNT sensors (**Figure A.12**). These first results seemed to indicate that the DNA did not significantly affect the SWCNT length, the SWCNTs having in the two cases an average length of approximately 460 nm. These experiments therefore confirmed that the changes in fluorescence intensity were not due to changes in the SWCNT distribution nor to changes in the SWCNT length and should then stem from variations in the QY of the complexes. To further confirm this, we measured the relative QYs of both (GT)₁₅- and M13-1-SWCNT complexes by comparison with the IR-26 NIR dye (see **Methods**) and observed an increase in QY for the mutant (**Table A.2**). Although this increase is not as high as the differences in intensity noted in this study, probably due to the fact that all SWCNT chiralities are considered in the QY calculation and that the excitation was done at 808 nm, it confirmed that the variations in intensity are due to a difference in QY.

Since variations in QY can originate from differences in surface coverage of the DNA-SWCNT complexes, we hypothesized that the mutant sequence is wrapped more tightly than the (GT)₁₅ sequence. By comparing the positions of the peaks of 7 SWCNT chiralities, we calculated relative surface coverage of the SWCNT complexes similarly to what was done by Bisker *et al.* [80] and found that the relative surface coverage has the same trend as the increase in intensity (**Figure A.14**). Such a dependence on SWCNT surface coverage could partially explain the chirality- and sequence-dependence of the fluorescence changes observed in this work as previous studies have shown that the binding energy and wrapping angle of the DNA on the surface of the SWCNT can depend on the DNA sequence and the SWCNT chirality [98]. We also investigated the effect of removing the free DNA on the fluorescence intensity of the complexes (**Figure A.15**). We observed that the mutant complexes do not only retain their improvement in intensity after free DNA removal, but exhibit an even higher intensity increase. Upon free DNA removal, we observed an overall decrease in intensity for all complexes that we attribute to the destabilization of the DNA wrapping. However, in the case of the mutant complexes, this decrease is limited compared to the (GT)₁₅-SWCNT complex therefore resulting in the increase in intensity. This therefore suggests that the mutant wrappings are more stable and therefore less prone to changes upon suspension filtering.

Next, we tested if the improvement in QY had an effect on the other properties of the complexes. The starting (GT)₁₅-SWCNT complex is responsive towards certain neurotransmitters, including dopamine, which on addition results in a fluorescence increase [58]. Dopamine detection assays were performed on the (GT)₁₅-SWCNTs and the mutant complexes in order to test whether the sensing capability was compromised post-mutation. A summary of these sensing responses is provided in **Table A.3**. Overall, we did not observe any significant difference in response between the (GT)₁₅-SWCNT and the M13-, M13-1- and M13-6-SWCNT complexes when considering the integrated intensities. Dopamine was also found to increase fluorescence in a chirality-specific manner (**Figure 1.3**), with more pronounced responses for the (8,6) chirality observed for both the (GT)₁₅- and M13-SWCNTs (p -value < 0.05). No significant differences in dopamine response were observed between the (GT)₁₅ and mutant complexes for the (9,4) chirality or for the integrated intensity. For the (10,2) chirality, the

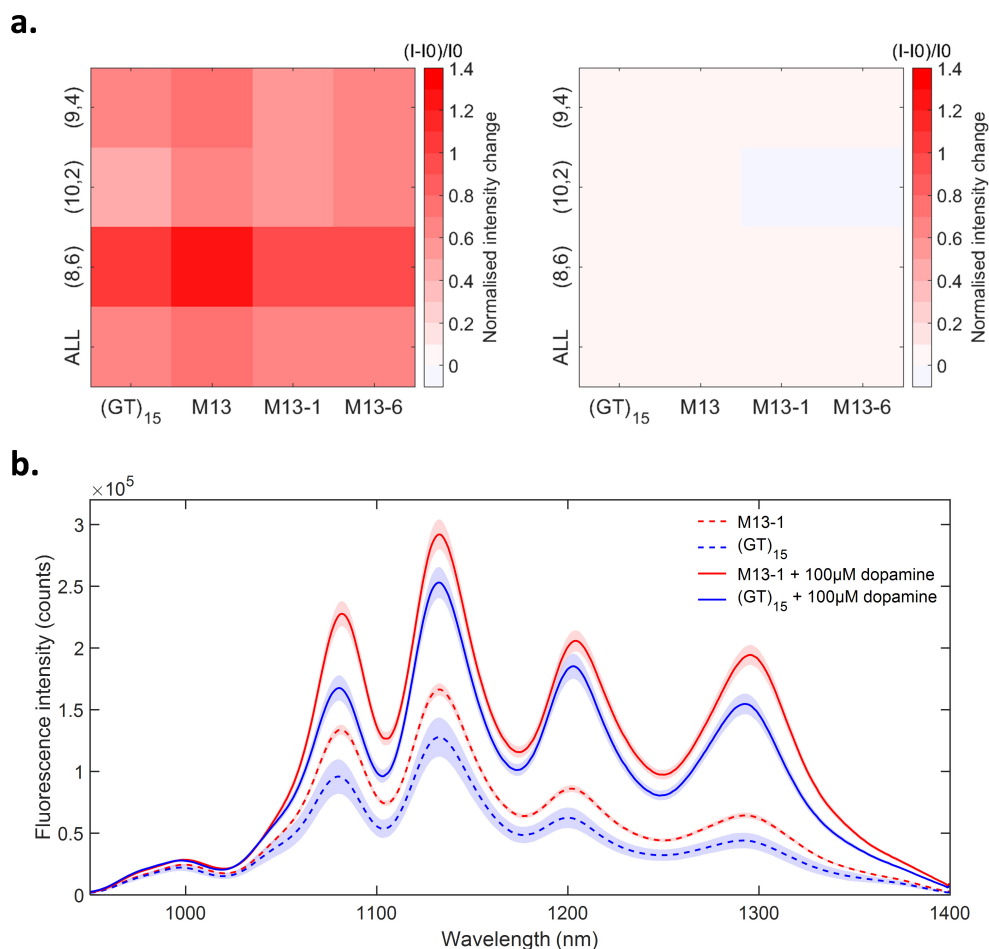


Figure 1.3 – Response of the DNA-SWCNT complexes to dopamine and glutamic acid. (a) Response of the DNA-SWCNT sensors towards dopamine and glutamic acid (final analyte concentrations of 100 μ M) as a function of the intensity of the (9,4), (10,2), and (8,6) chiralities as well as the integrated intensity under 745 nm excitation (labelled “ALL”). The response I is normalised to the intensity before dopamine addition I_0 . (b) Fluorescence spectra of the (GT)₁₅-SWCNT (blue curves) and M13-1- SWCNT (red curves) complexes before (dotted lines) and after (solid lines) dopamine addition. The shaded areas represent 95 % confidence intervals.

M13-, M13-1-, and M13-6-SWCNTs showed overall stronger responses towards dopamine compared to the starting (GT)₁₅-SWCNT complex (p -value < 0.05). In addition, a comparison of the calibration curves for the (GT)₁₅- and M13-SWCNT complexes (**Figure A.16**) confirmed that both the mutant and initial sensors are able to detect dopamine down to 100 nM. This therefore indicates that the mutations did not have a significant effect on the overall response of the sensors towards dopamine. Then, we compared the selectivity of the (GT)₁₅-SWCNT and mutant sensors by investigating the response towards other neurotransmitters, including glutamic acid, γ -aminobutyric acid (GABA), acetylcholine, and glycine (**Figure 1.3**, **Figure A.17**). The same lack of response was observed for the (GT)₁₅- or mutant complexes towards these neurotransmitters, demonstrating that selectivity towards dopamine is retained post-

mutation. These results show that the mutant complexes demonstrate increased fluorescence intensities while simultaneously retaining the dopamine responsivity of the original sensor. In addition, the fluorescence enhancement of the mutant complexes relative to the (GT)₁₅-SWCNT complex is sustained even following the addition of dopamine (**Figure 1.3**, **Figure A.18**). This improvement in the fluorescence intensity of these sensors, both before and after dopamine addition, can enable *in vivo* imaging at imaging depths up to 193 μm deeper (see **Methods**, **Table A.4**), without compromising dopamine detection. We further showed that this increase in intensity is retained at the single SWCNT level by performing NIR confocal microscopy on both (GT)₁₅- and M13-1-SWCNT complexes (**Figure A.19**). This increase in fluorescence intensity was not observed for the whole population of SWCNTs but only for a small fraction. This phenomenon is attributed to the chirality-specificity of the increase in fluorescence as previously discussed (**Figure 1.2**). We observed a maximum increase in intensity for the (9,4), (10,2) and (8,6) chiralities. However, these chiralities are present in relatively low abundance in the HiPco SWCNT samples. As the fluorescence recorded in confocal microscopy represents the fluorescence of all SWCNT chiralities, it is therefore not surprising to observe an increase in intensity only for a fraction of the SWCNTs present in the sample plane.

1.5 Conclusion

In this chapter, we evolved brighter DNA-SWCNT sensors through directed evolution of the DNA wrapping. While the reasons for the fluorescence intensity enhancement remain mostly unclear, we demonstrated a guided approach that can be used to tune DNA-SWCNT properties in the absence of a defined structure–function relationship. Whereas previous work has focused on monitoring the response of a relatively small collection of random DNA sequences against a variety of analytes, we have instead focused on screening the performances of a larger library of mutants for a single characteristic, in this case fluorescence intensity. Although the observed SWCNT fluorescence increase is lower than other reported methods [112, 135, 145, 150, 153, 212] the enhancement described herein was achieved without the addition of any exogenous compounds or modification of the SWCNT surface. This achievement is of particular importance for *in vivo* sensing applications since additives, such as reducing agents or nanoparticles, can lead to increased cytotoxicity and diminished sensitivity and selectivity of the sensor [112, 135, 156–158]. While further enhancement may be achieved by refinements, such as screening even larger DNA libraries over additional evolution cycles, the results of this study aim to demonstrate the applicability of a new technique in navigating the fluorescence intensity landscape of DNA-SWCNTs. More generally, this work establishes a new, guided technique that can be applied not only to improve properties of existing optical SWCNT sensors, such as sensitivity and selectivity, but also to engineer new sensors with capabilities that are yet to be discovered.

2 Directed evolution of DNA-SWCNT sensors for the simultaneous detection of mycotoxins

Portions of this chapter are reproduced from the manuscript in preparation: Lambert B.P.; Taheri A.; Wu S-J.; Gillen, A.J.; Kashaminejad M.; Boghossian, A.A. Directed evolution of nanosensors for the detection of mycotoxins (2021).

2.1 Abstract

In this second chapter, we build our previous findings in order to engineer the properties of DNA-wrapped single-walled carbon nanotubes (DNA-SWCNTs) beyond fluorescence intensity. For that, we design and evolve sensors towards mycotoxins, a class of molecules critical to detect in the food industry. We successfully demonstrate the creation of sensors for the detection of both the aflatoxin B1 (AFB1) and fumonisin B1 (FB1) mycotoxins based on the specific response of the (9,4) and (7,5) SWCNT chirality fluorescence peaks, respectively. The resulting chirality-specific responsivity, was used to demonstrate the multimodal detection of both mycotoxins at different wavelengths of light in presence of complex food medium. Moreover, we show that directed evolution can be used not only to improve the chiral-dependent selectivity of our sensors to the mycotoxins, but also the sensor sensitivity and fluorescence intensity through multiple rounds of evolution. The approach demonstrated in this study is versatile and could be generalized to other SWCNT sensors as well as other nanosensors comprising a biological element.

2.2 Introduction

Nanosensors, sensors with at least one dimension below 100 nm, have garnered significant interest in a variety of fields including health care [213], environmental monitoring [214] and the food industry [215]. However, despite their many advantages, the interaction and performances of such sensors in the presence of a desired target analyte can be difficult to predict, and therefore difficult to engineer, because of uncertainties surrounding the sensor's structure-function relationship. In such cases, the sensors are typically engineered using

empirical approaches [50, 57, 58], that are based on extensive screening of random configurations yielding sensors with suboptimal performances. Analogous challenges in engineering complexes with ill-defined structure-function relationships have already been addressed in the field of protein engineering, where synthetic biologists have relied on directed evolution to engineer proteins in a guided manner [1]. With this approach, a continuous relationship between protein's structure and function is assumed, limiting the screening to variants of an initial protein with residual, albeit sub-optimal, performance. This strategy therefore biases the screening to variants that likely to show at least some desired activity to enable the relatively efficient identification of optimized protein mutants that would, otherwise, be almost impossible to find through random screening [193].

Recently, the applicability of directed evolution has been demonstrated beyond the field of protein engineering for DNA-wrapped single-walled carbon nanotube (DNA-SWCNT) nanosensors [125]. Semiconducting SWCNTs are particularly attractive materials for the creation of optical sensors owing to their sensitive and photostable near-infrared (NIR) fluorescence, as well as their ability to be functionalized with a wide variety of molecules [78]. When non-covalently conjugated with single-stranded DNA, SWCNTs can exhibit various sensing capabilities where the sensitivity and selectivity depend on the DNA sequence [57, 58, 61]. So far, how the DNA sequence and SWCNT chirality determines the sensing properties of DNA-SWCNT complexes remains unknown, limiting the performance and applicability of such sensors. In previous work, we demonstrated the application of directed evolution to improve the fluorescence quantum yield (QY) of DNA-SWCNT complexes by up to 56 % in the absence of information on the complex's structure. Herein, we use directed evolution to engineer the properties of DNA-SWCNTs beyond fluorescence intensity. Specifically, we demonstrate the first DNA-SWCNT sensors for the detection of mycotoxins and show how directed evolution can be used to engineer their performance.

Mycotoxins are secondary metabolites produced by fungi in food products that are responsible for a range of diseases in humans [216, 217]. The Food and Agriculture Organization (FAO) estimates that at least 25 % of the global food crop is contaminated with mycotoxins [218]; Aflatoxin B1 (AFB1), fumonisin B1 (FB1), ochratoxin A (OTA), zearalenone (ZEN), and deoxynivalenol (DON) are the most commonly occurring toxins in cereals such as corn [219]. AFB1 is of particular concern owing to its high prevalence and toxicity. The rapid, sensitive, and specific detection of mycotoxins is therefore crucial to increase food security and avoid economic losses associated with contamination. Conventional methods for assaying mycotoxins in food sources include chromatographic and immunoassay-based approaches. However, these methods tend to be time consuming, expensive, non-reversible or require extensive sample preparation [216, 217].

In this study, we propose a label-free approach for the rapid multimodal detection of mycotoxins. As this approach is based on the NIR fluorescence of SWCNTs, it enables a non-destructive, *in situ* detection of mycotoxin, while simultaneously reducing the optical background from the food matrix at visible wavelengths [220]. Although the initial DNA-SWCNT sensors found

by random screening exhibited weak responses towards mycotoxins, we were able to engineer sensors towards two mycotoxins, AFB1 and FB1, by monitoring two different SWCNT chiralities. We further demonstrated that we could use directed evolution to enhance the performance of these sensors, increasing the AFB1 response by more than 3-fold. Moreover, we demonstrate the accelerated engineering of mutants with enhanced performances using a DNA shuffling recombination technique. Finally, our studies enabled us to elucidate two distinct modes of interaction for the AFB1 and the FB1 sensors, allowing a better understanding of the sensors' underlying properties such as sensor reversibility. This work therefore demonstrates the strength of directed evolution for engineering the overall properties of DNA-SWCNT sensors as well as nanosensors in general that comprise a biological component.

2.3 Materials and methods

2.3.1 Materials

All mycotoxins were purchased from Enzo Life Sciences. All DNA oligomers were purchased from Microynth AG. Super-purified HiPco SWCNTs were purchased from NanoIntegris (Batch No. HP32-130). All chemicals were purchased from Sigma-Aldrich, unless otherwise indicated. The corn powder, almond powder and beer used in the experiments were purchased from a local grocery store.

2.3.2 Instruments

Absorbance measurements were collected using a UV-3600 Plus spectrophotometer (Shimadzu) and quartz suprasil cuvettes (Z600393, Hellma Analytics). Absorbance measurements were also performed in 96- and 384-well plates using a plate reader (Varioskan LUX, Thermo Fisher). The near-infrared fluorescence measurements were acquired on a custom-made microscope as previously described [81]. Briefly, the system is built on a Nikon Ti-E inverted microscope body and illuminated by a supercontinuum laser (SuperK Extreme EXR-15 and SuperK VARIA, NKT Photonics) in the 400-830 nm range. The emitted light is diffracted between 900-1400 nm by a spectrometer (IsoPlane SCT-320, Princeton Instruments) using a 70 lines.mm⁻¹ grating and recorded by an InGaAs detector (NIRvana 640 ST, Princeton Instruments). The measurements were recorded automatically using a custom LabVIEW (National Instruments) program. The fluorescence data was analyzed by a custom code in Matlab (R2017b, MathWorks), in which individual fluorescence peaks were fitted with a single Lorentzian curve.

2.3.3 Preparation of the SWCNT suspensions

The sodium cholate (SC)-SWCNT suspension was prepared by mixing 45 mg HiPco SWCNT powder with 45 mL 2 % (w/w) SC prepared in deionized (DI) water. This mixture was homo-

geneized at 5,000 rpm (Polytron PT 1300 D, Kinematica) at room temperature for 20 min, prior to 60 min ultrasonication (amplitude 10, 1/4 in. tip, Q700 Sonicator, Qsonica) in an ice bath (the ice was changed after 30 min). The resulting suspension was centrifuged for 10 min at 15,000 x g at 25°C (Allegra 25R, Beckman Coulter) and the supernatant was further centrifuged for 4 h at 30,000 rpm at 25°C (SW32 Ti, Optima XPN-80, Beckman Coulter). The supernatant (top 90 %) was further concentrated using centrifugation filtration devices (Amicon Ultra-15 3kDa, Merck). Briefly, 10 mL was added to an Amicon device and centrifuged at 4,000 x g for 30 min (Allegra 25R, Beckman Coulter) at 25°C. An additional 10 mL was added to the device and the previous step was repeated. The concentrated nanotube suspension was resuspended using 2 % (w/w) SC to a total volume of 6.5 mL and centrifuged at 3,300 x g for 30 min at 25°C (5810R, Eppendorf) to remove aggregates. The supernatant was collected and diluted using 2 % (w/w) SC to a final concentration of 108 mg/L (measured using the extinction coefficient $\epsilon=0.036 \text{ L.cm}^{-1}.\text{mg}^{-1}$ at 632 nm [125]). The concentration step was important as most batches could reach only a concentration of approximately 70 mg/L, not enough for our experiments. Moreover, as the batches prepared on different days would not result on the same SWCNT yield, it is important to fix the final concentration in order to improve reproducibility. Nevertheless, a slight variation of SWCNT chirality distribution was observed between various batches of SC-SWCNT suspensions (**Figure B.1**). We attribute these variations to variations in sonication conditions due to the lack of automation in the process. Such differences in SC-SWCNT could explain the slight variations in DNA-SWCNT sensor behavior observed between different experiments.

The DNA-SWCNT sensors were prepared using a wrapping exchange protocol between the sodium cholate (SC)-SWCNTs and the DNA oligomer as previously described [125]. The DNA solutions were dissolved in DI water to a concentration of 50 μM (measured using Nanodrop 2000, Thermo Scientific). Ratios of 0.2:0.2:0.6 of DNA:SC-SWCNT:methanol were mixed gently (DNA and SC-SWCNT mixed first) and incubated for 2 h at room temperature. The DNA-SWCNTs were then purified to remove the free SC and methanol. First, 1.5 M NaCl was added to the mixture to a final concentration of 0.2 M, followed by the addition of 2.5 volumes of cold ethanol (kept at -20°C) and the solution was gently mixed. The resulting suspension was incubated at -20°C for 1 h and then centrifuged at 21,130 x g (5424R, Eppendorf) for 30 min at 4°C. The supernatant was removed, and the SWCNT-containing pellet was washed with 70 % (v/v) ethanol (the pellet should break into small clumps), vortexed briefly, and centrifuged at 21,130 x g for 1 h at 20°C. The supernatant was discarded, and the pellet was air-dried for 12 min at room temperature. The pellet was then resuspended in the desired volume of 0.1 M NaCl, briefly vortexed, and finally centrifuged at 21,130 x g for 30 min at 20°C. The supernatant of this suspension was collected and its concentration was determined by measuring the absorbance of 90 μL of suspension in 96-well plate (Varioskan LUX plate reader, Thermo Scientific). The suspensions were all diluted with 0.1 M NaCl to a final concentration of 7.4 mg/L (corresponding to a background-subtracted absorbance of 0.066). All samples were freshly prepared and used on the same day for experiments in order to avoid variations between samples due to possible aging of the samples. Indeed, we noted a slight aging of our

samples which seemed to stabilize after one day at room temperature (**Figure B.2**). This aging was characterized mostly by a significant decrease in fluorescence intensity, but did not seem to strongly affect the response of the sensors. We attribute this aging to the reorganization of the DNA wrapping from a meta-stable stable (post-resuspension) to an equilibrium (after one day), consistent to the conclusions of Yang *et al.* [143].

DNA-CNT prepared by sonication were prepared by mixing 1 mg HiPco SWCNT with 1 mL of DNA solution at 100 μ M concentration (\approx 1 mg/mL) followed by 90 min ultrasonication (amplitude 1, cuphorn, Q700 Sonicator, Qsonica) in an ice bath. The resulting suspension was centrifuge for 4 h at 21,130 x g at 4°C (5424R, Eppendorf) and the supernatant was stored at 4°C before use.

2.3.4 Preparation of the mycotoxin solutions

Unless otherwise indicated, mycotoxin powders were dissolved in dimethyl sulfoxide (DMSO) in a nitrogen-controlled glovebox (E-line, GS Glovebox). The concentrations of all mycotoxins, except for FB1, were verified using their respective extinction coefficients in the 200-400 nm range listed in the **Table B.1**. All dissolved mycotoxin samples were aliquoted and stored at -20°C in the dark. It is important to note that different batches of mycotoxins were used over the course of the study (mainly for AFB1 and FB1). Although the concentrations were fixed by absorbance for AFB1, slight variations may arise between batches. Such variations may then result in slight variations in DNA-SWCNT response observed between different batches of experiments.

The toxin batches prepared before December 2019 were not prepared in an inert atmosphere and could therefore present traces of toxin oxidation. The most striking evidence of such toxin degradation occurred for one AFB1 batch which changed color from transparent to light pink (**Figure B.3**). Although we have not found any relationship between the change of color and the composition of the toxin batch, we performed toxin characterization by high-performance liquid chromatography–tandem mass spectrometry (HPLC-MS) and noted the presence of AFB1 exo-8,9-epoxide (AFBO) for the colored batch and the absence of such compound for batches dissolved under inert atmosphere (**Figure B.4**). In addition, we noted that the purity of the toxin batch can affect the response of the DNA-SWCNT sensors. We tested the Δ (AG) and A-2 sensors in presence of the oxidized batch and a batch dissolved under inert atmosphere (**Figure B.5**). We observed that the response was higher in presence of the oxidized batch for the same concentration of toxin. In order to avoid possible misleading comparisons between two toxin batches of different purity, we indicate clearly in the figure legend if the result was obtained with a batch dissolved under non-controlled atmosphere. Furthermore, some results were obtained with toxins dissolved in methanol instead of DMSO. Indeed, while some toxins are more soluble in methanol than DMSO, DMSO was finally chosen in order to have a unique solvent for all toxins and limit further variations. We therefore also indicate in the figure legend if the toxin was dissolved in methanol instead of DMSO.

Despite the great solubility of FB1 in water, reports in the literature mention a solubility limit of only approximately 60 μM in aqueous medium for AFB1. We tested this solubility limit by measuring the concentration of AFB1 in solution whether in DMSO or in a 1:100 DMSO:0.1 M NaCl to mimick our experimental conditions (**Figure B.6**). We noted that the concentrations of the AFB1 solution in aqueous medium were not higher than 46 μM , therefore confirming a solubility limit of approximately 46 μM for AFB1 in our experimental conditions. This solubility limit was too low to reach the saturation of our sensors, preventing us to calculate an equilibrium dissociation constant for our sensors.

2.3.5 DNA mutant library

Mutants of the DNA sequences were generated by a custom code in Matlab. For the creation of the single mutation library, a random base position (between 1 and 30) was first chosen and then randomly replaced by any of the three other bases with the same probability. For the creation of more than one mutation, the process explained above was repeated on the rest of the non-mutated bases. The initial screening library used to find sensors responsive to AFB1 was composed of repeating sequence variants, constructed by introducing three random mutations in (AT)₁₅, (AG)₁₅, (CT)₁₅, and (AC)₁₅ sequences. The choice of repeating sequences with alternating bases was made considering the extensive body of research on SWCNTs functionalized with such sequences, in particular for the creation of sensors [57, 58, 60, 61]. The (GC)₁₅ sequence variants were not considered due to the high GC-content of the sequences preventing the synthesis of the oligonucleotides, as mentioned by the provider (Microsynth). As previously observed [125], the introduction of three mutations enables high enough diversity in the starting search library. In this study, we have screened 438 sequences in total: an initial library composed of 100 (AT)₁₅, (AG)₁₅, (CT)₁₅ and (AC)₁₅ variant sequences and 338 mutants derived from the $\Delta(\text{AG})$ sequence. We have summarized the main sequences used in the study in the **Table B.2**.

2.3.6 DNA shuffling

DNA shuffling can be used to generate improved mutants with a high degree of fitness by combining the beneficial mutations of one or multiple sequences. To generate the shuffled sequences, the selected sequences are first cut into n fragments (n equals the length of the sequence divided by the fragment size). The small fragments are then randomly shuffled and the number of fragments necessary to achieve the specified sequence length are selected and combined to create the so-called shuffled sequence. The library of all recombined sequences is given by the permutations of all fragments into sequences composed of n fragments.

As we performed the sequence shuffling computationally, we had the advantage of being able to choose a fixed fragment length. In this study, we tested fragment sizes of 5, 6 and 10 nucleotides (**Figure B.7**). We estimated this range to be optimal for the discovery of mutants as smaller fragments might be too short to contain a recognition site and longer fragments

would be too large to enable sufficient sequence diversity. We also ruled out the sequences that contained more than half of unmutated fragments to maximize the presence of beneficial mutations in the sequence.

2.3.7 Spiking and extraction from corn matrix

The extraction was performed using a modified version of a previously reported protocol [221]. In a 1.5 mL Eppendorf tube, 100 mg of corn powder was mixed with 20 μ L of toxin solution at a final concentration of 2.5 mM. The solution consisted of 5 μ L toxin at 10 mM, 5 μ L DMSO (or toxin if there were two toxins at the same time) and 10 μ L 60 % methanol. The powder was vortexed for 15 s and left to incubate with the toxin for 30 min at room temperature. Subsequently, 180 μ L of 60 % methanol was added and the tube was shaken at 1,500 rpm for 30 min at 20°C (Thermomixer C, Eppendorf). The tube was then centrifuged at 21,130 x g (5424R, Eppendorf) for 1 min. The supernatant was filtered through a 0.22 μ m PTFE filter to remove large corn particles. We verified that the AFB1 could go through the PTFE filters by absorbance measurements (**Figure B.8**). Control samples without corn were made by mixing 20 μ L of the toxin solution described above with 180 μ L of 60 % methanol.

Corn extract was also used alone or in combination with the toxins in order to assay response selectivities. For that, 5 g of corn powder was mixed with 25 mL 100 % methanol and shaken at 3,000 min^{-1} (uniTEXER, LLG) for 1 h. Then, the solution was centrifuged at 3,000 x g for 10 min at 4°C (5810R, Eppendorf) and the supernatant was filtered (Whatman 597). The filtrate was further centrifuged at 21,130 x g for 10 min and stored at room temperature (5424R, Eppendorf). The same protocol was used for the almond flour extract, except it was filtered using a 0.22 μ m PTFE filter because of the smaller volume. The beer sample was used directly out of the bottle.

2.3.8 Preparation of the immobilized DNA-SWCNTs

Films of DNA-SWCNTs were created in order to test the reversibility of the sensors. First 20 μ L of DNA-SWCNTs was added to a 96-well plate with glass bottom and the sensors were dried at 70°C for 1 h. This method allows to obtain films with a SWCNT concentration sufficient to perform spectroscopy. Then, 40 μ L of warm 2 % (w/v) agarose (in 0.1 M NaCl) was added on top of the dried SWCNTs in order to avoid sample removal from the focal plane upon analyte addition. 100 μ L 0.1 M NaCl was added and the fluorescence was monitored for 20 min (time interval of 150 s with laser off between measurements). The NaCl solution was removed and replaced with 100 μ L of 20 μ M AFB1 solution in 0.1 M NaCl and the fluorescence was monitored for 1 h (time interval of 150 s with laser off between measurements).

2.3.9 Mycotoxin removal protocol

The washing process to remove mycotoxins from DNA-SWCNT suspensions is illustrated in **Figure B.9**. The DNA-SWCNT were first mixed with the toxins and the response was measured. Following overnight incubation with the toxin, the DNA-SWCNTs were precipitated by salt-assisted ethanol precipitation following the same protocol described previously for the purification of the DNA-SWCNT suspensions. The samples were incubated with ethanol at -20°C for 1 h and centrifuged at 21,130 g for 30 min at 4°C. The DNA-SWCNT pellet was washed with 70 % ethanol and centrifuged at 21,130 g for 1h at 20°C. The supernatant was discarded and the pellet was air-dried for 12 min. Finally, the DNA-SWCNT pellet was resuspended in 0.1 M NaCl and centrifuged at 21,130 g for 30 min at 20°C to remove aggregates and the response of the sensor towards mycotoxins was measured again. For washing under denaturing conditions (**Figure B.10**), the DNA-SWCNTs were heated to 95°C for 5 min (Thermomixer C, Eppendorf) immediately before the salt-assisted ethanol precipitation step. We verified that our DNA-SWCNT washing procedure was effectively removing the toxin both in the absence (**Table B.3**) and presence of DNA-SWCNTs (**Figure B.11**), using HPLC-MS and UV absorbance, respectively.

We also tested the use of Amicon Ultra-0.5 3kDa centrifugal devices in order to remove the toxins (**Figure B.12**). For that, we mixed 1 μ L AFB1 with 99 μ L 0.1 M NaCl or DNA-SWCNT in 0.1 M NaCl and 400 μ L DI water and ran the mixture in the device (pre-rinsed) at 14,000 x g for 10 min. The absorbance of the first flow-through was assayed, which showed absence of any AFB1 absorbance peak. We washed a second time the device with 400 μ L 50 % ethanol (the toxin being more soluble in ethanol but also avoiding damage to the filter membrane) and the device was centrifuged at 14,000 x g for 20 min. Again, the flow-through was assayed, exhibiting traces of AFB1. Finally, the filter was washed a third time with 50 % ethanol and centrifuged at 14,000 x g for 30 min. The flow-through of this fraction did not show any presence of AFB1. Finally, the filter was run three times with DI water (in order to replace the ethanol) and the filter fraction was assayed, demonstrating the absence of AFB1. While the filtering seems to result in removal of the toxins, it necessitates the use of organic solvent in the device which can damage the membrane and contaminate the sample with undesired compounds from the filter. In addition, the filtering method results in significant losses of DNA-SWCNTs which are limited when using the precipitation technique. Finally, the precipitation method offers a greater flexibility in the volume and concentration of the DNA-SWCNT used (a too large concentration of SWCNT can block the filter membrane).

2.3.10 Surfactant replacement assays

The DNA wrapping was replaced using both sodium deoxycholate (SDC) and sodium dodecylbenzenesulfonate (SDBS) surfactants following previously reported procedures [115, 120]. The SDC was dissolved to a concentration of 1 % (w/w) in DI water. 45 μ L of DNA-SWCNT suspension was mixed with 5 μ L of 1 % SDC (final concentration of 0.1 %) in a 384-well plate

(MaxiSorp, Nunc) and incubated at room temperature. The fluorescence of the suspension was recorded before, 15 min and after SDC addition and after an overnight incubation. The SDBS was dissolved in DI water and diluted to concentrations ranging from 0.0138 to 0.55 % (w/w). 20 μ L (or 50 μ L) of DNA-SWCNT suspension was mixed with 2 μ L (or 5 μ L) of SDBS solution, with final SDBS concentrations ranging from 1.25×10^{-3} to 0.05 %, and were incubated at room temperature before the fluorescence was recorded.

2.3.11 Free DNA removal

The free DNA was removed using Amicon Ultra-0.5 100 kDa devices. The membrane of the device was first rinsed with 500 μ L DI water at $14,000 \times g$ for 5 min. Then, DNA-SWCNT suspension and DI water were added to the device for a total volume of 500 μ L and the device was centrifuged at $4,000 \times g$ for 2 min. The centrifugation speed used in this study was lower than in the previous chapter in order to limit the effects of SWCNT aggregation on the device filter, which can limit sample resuspension. If analysis of the free DNA concentration is required, the flow through can be stored for further processing. DI water was added to the device to reach a final volume of 500 μ L and the DNA-SWCNTs stuck on the membrane were resuspended by pipetting up and down. The samples were centrifuged, washed and resuspended again for 5 additional times in order to remove all traces of free DNA. The last centrifugation was done for 5 min instead of 2 min. Finally, the samples were resuspended in 0.1 M NaCl and centrifuged to remove SWCNT aggregates. The final suspensions were diluted to the same concentration as the initial suspensions before filtering ($A_{632}(90 \mu\text{L}) \approx 0.066$ after blank correction).

2.3.12 DNA quantification

The DNA concentrations of the flow-throughs of centrifugation devices and supernatants of the DNA-SWCNTs were assayed using the fluorescence of the Sybr Gold nucleic acid dye. For the ethanol supernatants, ethanol was removed by filtrating the supernatant (500 μ L) with Amicon Ultra-0.5 10 kDa centrifugation devices (pre-rinsed) two times with DI water followed by resuspension of the DNA in the filter in DI water (50 μ L). For the measurement, 10 μ L of DNA sample was added to 40 μ L 1X Sybr Gold in 10 mM HEPES buffer (pH 8). The HEPES buffer was used to keep the pH within the optimized range for the dye (between pH 7.0 and 8.5). The samples were then incubated in the dark for 10 min and the fluorescence at 537 nm under 495 nm excitation was recorded with an exposure of 100 ms (Varioskan LUX, Thermo Fisher). We constructed calibration curves of Sybr Gold fluorescence and DNA concentration for each sequence (**Figure B.13**) and used the slopes to find the concentration of DNA in our samples.

2.3.13 Measurements

Fluorescence measurements were acquired with an exposure time of 5 s, a laser power of 100 % and a illumination bandwidth of 10 nm. For the monitoring of the (7,5) and (7,6) chiralities, an excitation of 660 nm was used while the monitoring of the (10,2) and (9,4) chiralities was done with an excitation of 745 nm. 49.5 μL aliquots of diluted DNA-SWCNT suspension were added to a 384-well plate (Nunc Maxisorp, Thermo Scientific) and fluorescence spectra were collected prior to the addition of any analyte. Following the initial measurement, 0.5 μL of analyte solution (concentration specified in the experiment) was added to the well and briefly mixed by pipetting up and down. Spectra were acquired at several time intervals, starting 80 min post-addition and repeated every 120 min for a total of at least 200 min. All measurements were taken at room temperature and the laser was switched off in between measurements. The measurements were also done with sealing tape (CLS6524, Corning) on the plates to avoid evaporation. As the kinetics showed that the steady state of the response for both toxins occurred after approximately 200 min (**Figure B.14**), most measurements were compared 200 min post-addition. For the experiments in presence of corn extract, the measurements were compared 320 min post-addition, as this was the time point where the background response due to the corn extract stabilized (**Figure B.15**). The shifting responses labelled as $\Delta\lambda_{\text{solvent}}$, "Peak shift" or "Wavelength shift" were calculated as the difference in peak position between the toxin and the negative control (DMSO or methanol depending on the sample). The shifting responses labelled as $\Delta\lambda_{\text{corn}}$ correspond to the difference in peak position between the toxin and the negative control both containing corn extract. The shifting responses labelled as $\Delta\lambda_{t0}$ was calculated compared to the peak position before addition (t_0).

2.4 Results and discussion

We studied the response of DNA-SWCNT complexes towards a range of mycotoxins commonly found in corn-related products (**Figure 2.1**): AFB1, FB1, OTA, ZEN and DON. Owing to its prevalence in the food industry, we first searched for promising DNA sequences for the detection of AFB1. To this end, we initially screened a library of 100 diverse DNA-SWCNT complexes (see **Methods**) against AFB1 and monitored the fluorescence response of the SWCNTs (**Figure B.16**). From this screening, we identified an analogue of the (AG)₁₅ sequence, $\Delta(\text{AG})$, that exhibited a strong selective response towards AFB1 (**Figure 2.1**). Specifically, we observed a red-shifting of the SWCNT emission towards higher wavelengths, especially for the (9,4) chirality (1.65 ± 0.16 nm). Although we observed strong shifting response, the intensity of the (9,4) peak post-addition (**Figure B.17**) was not significantly different from the control (intensity change equal to zero within error).

We then applied the directed evolution approach on the $\Delta(\text{AG})$ sequence to increase the shifting response of the (9,4) chirality towards AFB1 (**Figure 2.1**). We sequentially introduced random base substitutions, one per round of evolution, and selected the mutants that showed an increased shifting response towards AFB1. The sequences of the main DNA mutants are

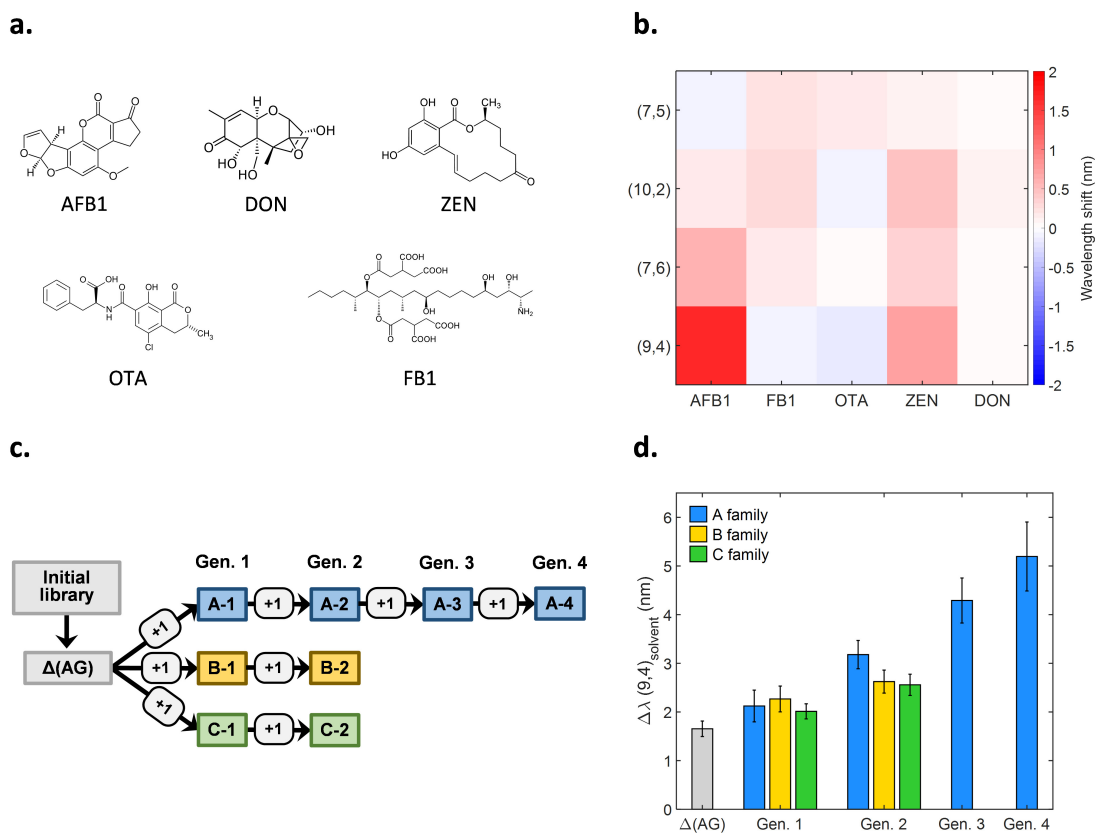


Figure 2.1 – Directed evolution of the AFB1 sensor. (a) Structures of the mycotoxins screened: AFB1, DON, ZEN, OTA, FB1. (b) Fluorescence wavelength shifting response of the $\Delta(\text{AG})$ sensor following the addition of different toxin solutions ($10 \mu\text{M}$). Wavelength shifts were calculated for the (7,5), (10,2), (7,6) and (9,4) SWCNT chiralities as the difference in peak position with and without toxin. (c) Schematic of the evolution of the AFB1 sensor. The sequences were selected based on increases in the shifting response of the (9,4) peak in the presence of AFB1. The $\Delta(\text{AG})$ sensor was selected from an initial library (light grey). Three families of mutants were created (blue, yellow and green for the A, B, and C families, respectively) from individual mutants harboring a distinct random substitution in the $\Delta(\text{AG})$ sequence. The "+1" denotes the introduction of a single, random base substitution. The numbers following the family letters correspond to the generation of the mutant. (d) Response of the AFB1 sensors across multiple rounds of evolution. The colors correspond to the families of sensors shown in (c). All measurements were taken in the presence of AFB1 ($10 \mu\text{M}$) following 200 min incubation. Error bars represent 1σ ($n = 4$).

listed in the **Table B.2**. From the first library of mutants originating from the $\Delta(\text{AG})$ sequence, we selected three sensors, A-1, B-1 and C-1, which showed the greatest increase in shifting response (**Figure 2.1**, **Table B.4**). These mutants were subsequently subjected to another round of mutagenesis, resulting in the selection of one additional mutant per sequence family (A-2, B-2 and C-2). As the A family of sensors demonstrated the greatest improvement of all three mutant families, we performed two additional rounds of mutagenesis resulting in the discovery of the A-3 and A-4 mutants (**Figure 2.1**, **Table B.4**). Using our directed evolution approach, we managed to successfully improve the shifting response of the sensors by 314 %

Chapter 2. Directed evolution of DNA-SWCNT sensors for the simultaneous detection of mycotoxins

compared to the starting sequence after four rounds of evolution (**Figure 2.1**, **Table B.4**). When considering the selective engineering of DNA-SWCNT sensors, the increase demonstrated here by directed evolution is greater than what was previously shown for serotonin sensors through high-throughput selection from an even larger library size [159]. Moreover, this improvement was achieved without compromising the selectivity of the response (**Figure B.18**). This systematic improvement of a single sensing property without drastic perturbations to other properties is otherwise unlikely in screens consisting of random DNA-SWCNT sensors exhibiting large differences across multiple properties [58, 60].

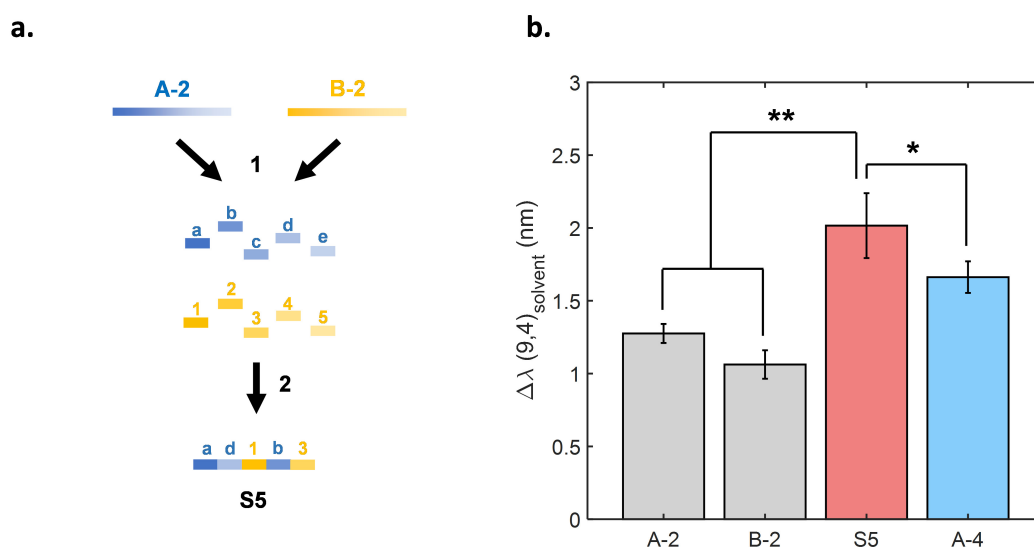


Figure 2.2 – Improving sensor performance using DNA shuffling. (a) Schematic of the methodology used to create shuffled sequences. The parent sequences, A-2 (blue) and B-2 (yellow), were decomposed into small fragments of fixed length, which were subsequently randomly recombined to form a library of shuffled sequences, including the S5 chimera sequence. (b) AFB1 response for the parent sensors (A-2 and B-2), the resulting shuffled sensor (S5) and the sensor selected after 4 rounds of mutagenesis (A-4). Measurements were taken in the presence of 2.5 μM AFB1 following 200 min incubation. * $p < 0.05$ and ** $p < 0.01$ (two-sample t-test, $n = 4$). Error bars represent 1 σ ($n = 4$).

Although this approach has been shown to yield mutants with improved performances during the initial rounds of evolution, further improvements may eventually stagnate after subsequent attempts at evolution, in agreement with previous observations on the directed evolution of proteins. According to protein engineering theory [193], the likelihood of identifying a sequence with improved performance is expected to decrease after several evolution rounds, particularly as one approaches a local optimum. To circumvent this limitation, one approach is to screen a larger library size to increase the search space within the vicinity of the local optimum. This approach increases the probability of including increasingly rare mutants with performances that exceed the already improved performance of the previous mutant. Another approach is to create a new library based on the combinatorial shuffling of mutations and fragments from the mutants from the previous rounds of evolution [222]. This approach may benefit from not only synergistic coupling of beneficial mutations that

may lead to enhancements beyond those achieved with the original mutants, but also the ability to navigate the sequence space towards a new local optimum with higher performance. Applying an analogous approach to our engineering strategy, we implemented a DNA shuffling approach to recombine the fragments of mutants from the previous evolution rounds [222]. In particular, we selected the two best sensors from the second round of mutagenesis, A-2 and B-2, combined them using DNA shuffling and screened the resulting mutants for improved AFB1 response (**Figure 2.2**). We screened libraries created by shuffling with fragment sizes of 5, 6 and 10 nucleotides (**Figure B.7**). From this screening, we identified the S5 sensor (or S5-12 in **Figure B.7**), resulting from a shuffling with a fragment size of 5 nucleotides, that exhibited the highest increase in response compared to its parent sequences (up to 90 % higher, **Figure 2.2**). Interestingly, this shuffled sequence also demonstrated a significantly higher response compared to the A-4 sequence (**Figure 2.2**) that was achieved after 4 rounds of evolution. This observation confirmed the DNA shuffling strategy as an effective means of further engineering DNA-SWCNT sensors.

Despite the improved response of our DNA-SWCNT sensors towards AFB1, we observed a simultaneous decrease in the fluorescence intensity of the sensors with progressing rounds (**Figure 2.3**), an observation that is analogous to the decrease in stability observed in protein engineering after several rounds of evolution [188]. For example, the S5 sensor suffered from an intensity decrease of almost 50 % compared to the intensity of the $\Delta(\text{AG})$ sensor. As the performance of fluorescence sensors is often linked to their brightness, this decrease could be detrimental to the applicability of the sensor. To address this issue, we applied additional rounds of mutagenesis on the S5 sensor to improve the fluorescence intensity. We performed three rounds of mutagenesis on the S5 sequence (**Figure B.19**). The final Q-3 sensor showed an increase in the fluorescence intensity of 21 % versus the S5 sensor, without significant changes to the AFB1 response (**Figure 2.3**). Furthermore, the Q-3 sensor showed a comparable intensity to the A-2 and B-2 sensors, while exhibiting a greater shifting response (+35 % and +58 %, respectively). We replaced the DNA wrapping using sodium deoxycholate (SDC, final concentration 0.1 %) in order to identify the origin of the increase in intensity (**Figure B.20**), as previously demonstrated [125]. We collected fluorescence spectra after both 15 min and overnight incubation. We noted that the complete replacement only occurred after overnight incubation. Interestingly, the increase in intensity was retained post-SDC replacement, indicating that the intensity change is not due to a QY effect but rather due to a change in the SWCNT chirality distribution.

While improving the sensors for AFB1 detection *via* the (9,4) chirality, we noted a concurrent improvement in the sensors' response towards FB1 for the (7,5) and (10,2) chiralities (**Figure 2.3**, **Figure B.21**). As for the AFB1 response, these chiralities did not exhibit a significant change in intensity in the presence of FB1, once more yielding sensors based on wavelength shifting responses (**Figure B.17**, **Table B.5**). We performed three rounds of mutagenesis on the S5 sensor (**Figure B.22**) to improve the FB1 response on the (7,5) and (10,2) chiralities, as was done to improve fluorescence intensity. The final mutant, F-3, exhibited both an increased FB1 response as well as a decreased AFB1 response thus resulting in a sensor with increased

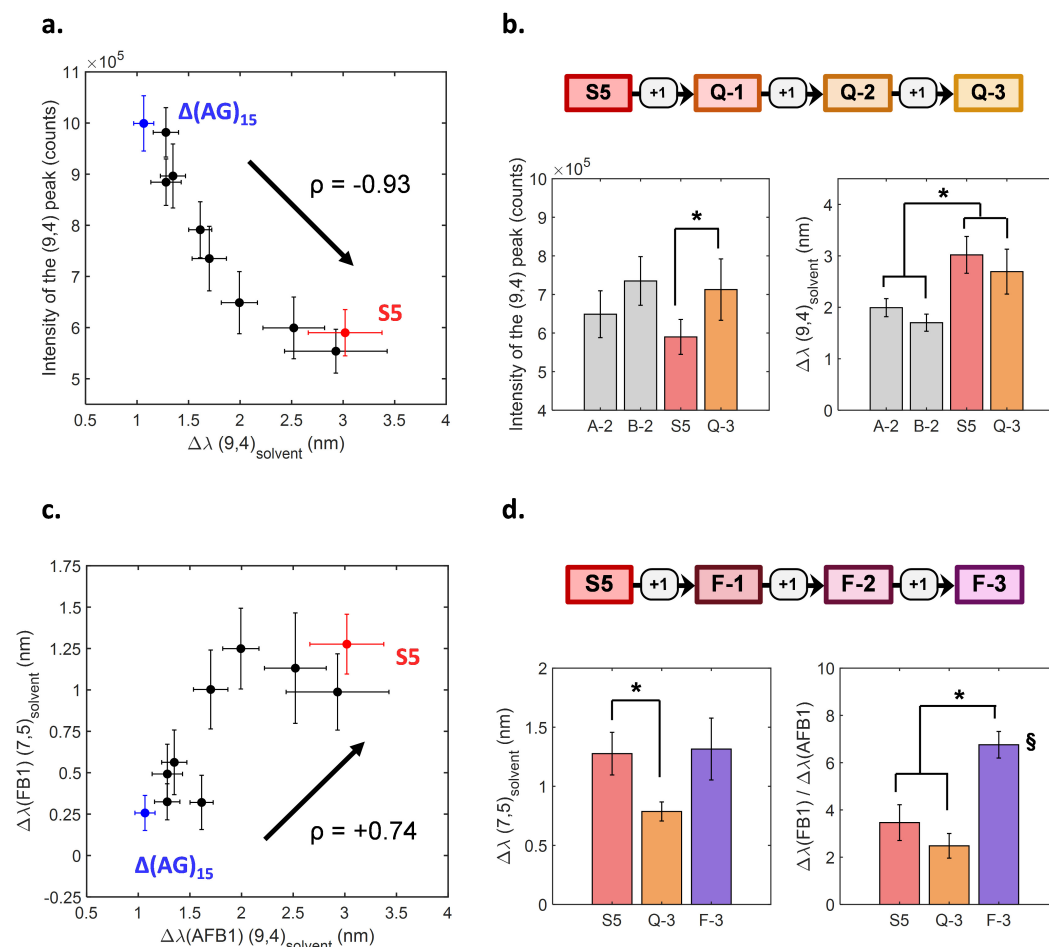


Figure 2.3 – Directed evolution of the sensor's intensity and selectivity. (a, c) Correlation between (a) the fluorescence intensity and the (9,4) response to AFB1 and between (c) the (7,5) response to FB1 and the (9,4) response to AFB1 for the selected mutants (**Figure 2.1**), the $\Delta(AG)$ and the S5 sensors. The increase in AFB1 response is accompanied by (a) a decrease in peak intensity (Spearman: $\rho = -0.95$, $p < 0.05$) and (c) an increase in FB1 response (Spearman: $\rho = 0.81$, $p < 0.05$). (b) Comparison of the fluorescence intensity (left) and AFB1 response (right) between the A-2, B-2, S5 sensors and the Q-3 evolved for intensity (top). (d) Comparison of the FB1 response (left) and selectivity (right) between the S5, Q-3 sensors and the F-3 evolved for FB1 sensing (top). The selectivity is calculated as the ratio of the FB1 response to the AFB1 response for the (7,5) chirality. All measurements were taken in the presence of $5 \mu\text{M}$ of the corresponding toxin following 200 min incubation. The * indicates a significant difference between the means ($p < 0.05$, two-sample t-test, $n = 4$). All error bars represent 1σ ($n = 4$, $n=3$ if marked by §).

selectivity to FB1 compared to AFB1 for the (7,5) and (10,2) chiralities (**Figure 2.3**, **Figure B.22**, **Figure B.23**). The (7,5) chirality, in particular, showed greater FB1 selectivity owing to a lower response of this DNA-SWCNT towards AFB1 (**Figure B.23**) and therefore chose to monitor the FB1 response exclusively on the (7,5) chirality in the following experiments. In addition, we observed an improved selectivity of the Q-3 sensor towards AFB1 for (9,4) chirality compared to the S5 sequence, due to its reduced sensitivity towards FB1 (**Figure B.24**).

Having engineered AFB1 and FB1 sensors, we further applied these sensors for the real-time detection of mycotoxins in food samples. In particular, the Q-3 and F-3 sensors were used to detect both AFB1 and FB1 at (9,4) (ca. 1140 nm) and (7,5) (ca. 1050 nm) chirality wavelengths, respectively, in corn flour media. The corn flour used in our study contains a variety of compounds including different proteins and starch. Even post-centrifugation, the supernatant still retained a strong yellow color indicating the presence of additional compounds, which have the potential of affecting the DNA-SWCNT response. We observed fluorescence shifting following the addition of corn extract for both the (7,5) and (9,4) chiralities (**Figure B.15**). This shifting stabilized after approximately 320 min incubation time. Owing to this, all measurements performed in the corn matrix were incubated for a minimum of 320 min to allow sufficient time for the background to stabilize. In addition, the shifting responses towards the toxins were calculated with respect to the negative control containing corn extract.

Calibration curves were constructed to determine the sensitivity of the Q-3 sensor towards AFB1 (**Figure 2.4**) and the F-3 sensor towards FB1 (**Figure 2.4**) using the (9,4) and (7,5) chirality peaks, respectively. In our experiments, we fitted the calibration curve of the (7,5) chirality for the F-3 sensor towards FB1 with a linear fit as we were mainly interested by concentrations below 4 μM (**Figure 2.4**) but noted that a single exponential fit could fit the response data better at concentrations above 4 μM (**Figure B.25**). The calibration curves were used to determine the limit of detection (LOD) of the Q-3 and F-3 sensors towards AFB1 and FB1, respectively (**Figure B.26**). In our experiments, we obtained a peak position accuracy of approximately 0.2 nm. Following the addition of AFB1 and FB1 to the Q-3 and F-3 sensor, respectively, we observed shifts of ≥ 0.24 (AFB1) and ≥ 0.35 nm (FB1) at a concentration of 1 μM , which is above the error in peak position in our analysis. We can therefore consider a LOD of 1 μM for the Q-3 sensor towards AFB1 and for the F-3 sensor towards FB1 in the presence of corn extract. This LOD, coupled with the relatively easy sample preparation and rather fast analysis using our sensors, makes the evolved DNA-SWCNT sensors attractive for applications monitoring the presence of these toxins in food and agricultural feed products [223, 224]. We also investigated the applicability of our sensors to other food matrices such as almond flour (**Figure B.27**) and beer (**Figure B.28**). We noted that the presence of almond extract had almost no effect on the position of the (9,4) chirality, therefore allowing an efficient sensing of AFB1 in almond products. For the beer, we observed a large red-shifting upon addition for both the (7,5) and (9,4) chiralities, preventing the detection of toxins in this medium with our current sensors.

We evaluated the selectivity of these sensors by analyzing their response to toxin mixtures (**Figure B.29**). The selectivity of the response was defined as the difference between the response towards a single toxin versus towards the mixture of toxins. By monitoring the (9,4) chirality of the Q-3 sensor, we were able to detect AFB1 from a mixture of both AFB1 and FB1 with very little interference from the FB1. Similarly, by monitoring the (7,5) chirality for the F-3 sensor, FB1 could be detected from a mixture of AFB1 and FB1, with no significant difference in response compared to the sample containing only FB1. The invariance in response between individual and combined toxin solutions indicates no competitive interaction nor cooperative interactions between the two toxins and the nanotube sensor. We further

Chapter 2. Directed evolution of DNA-SWCNT sensors for the simultaneous detection of mycotoxins

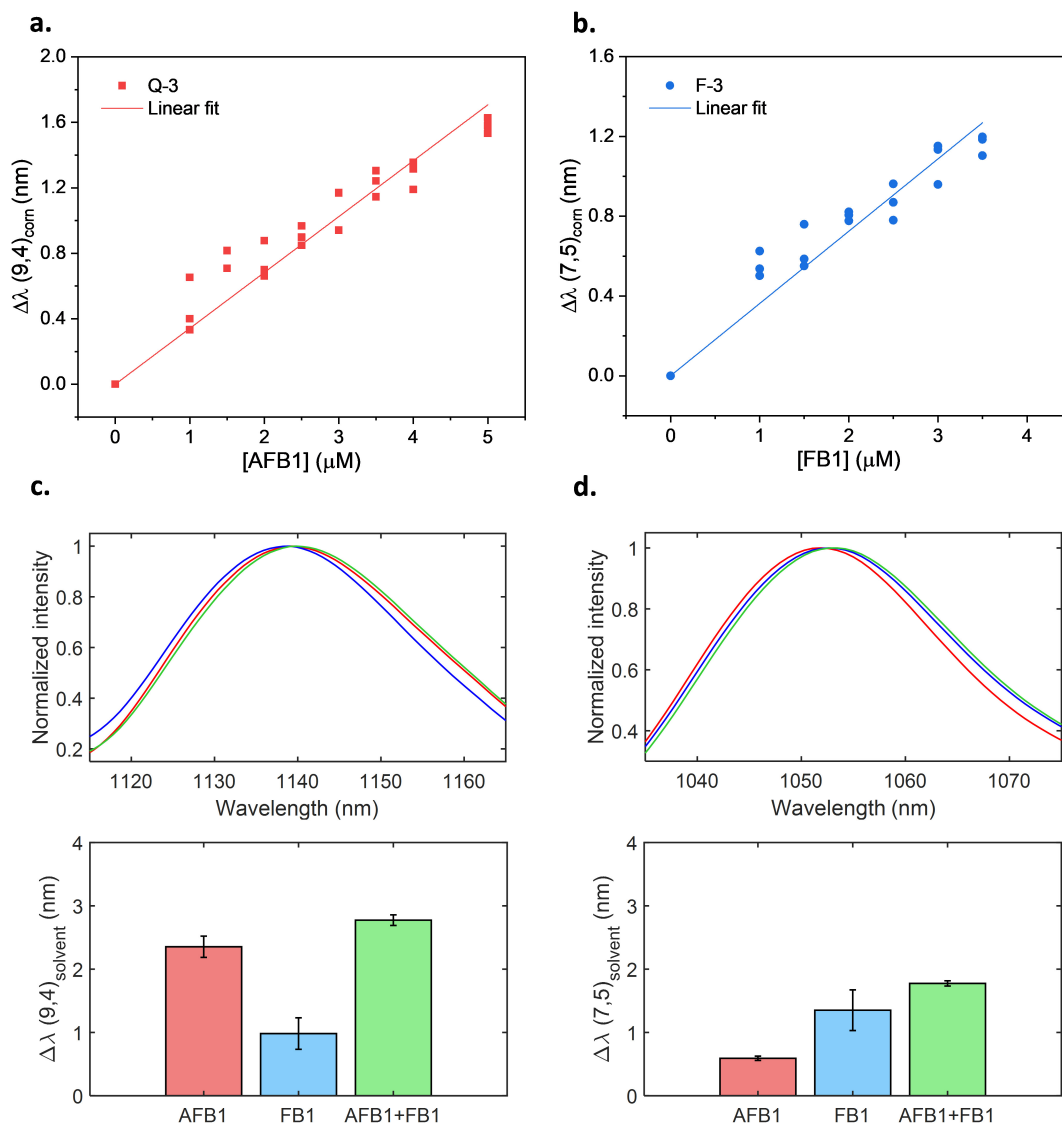


Figure 2.4 – Application of the evolved mycotoxin sensors. Calibration curves for the wavelength shifting response of (a) the (9,4) chirality of the Q-3 sensor and (b) the (7,5) chirality of the F-3 sensor. Measurements were taken for increasing concentrations of toxins suspended in a corn extract solution. The response was normalized to the response of the solvent (60 % methanol) containing only corn extract. Measurements were taken following 320 min incubation. (c) The response of the (9,4) chirality of the mixed sensors after incubation with AFB1 (red, 10 μM), FB1 (blue, 10 μM) and the mixture of both toxins (green, 10 μM for each toxin). (d) The response of the (7,5) chirality of the mixed sensors after incubation with AFB1 (red, 10 μM), FB1 (blue, 10 μM) and the mixture of both toxins (green, 10 μM for each toxin). Top: the normalized emission spectra. Bottom: the shifting response compared to addition of control (DMSO). Measurements were taken following 200 min incubation. Error bars represent 1 σ (n = 3).

tested the accuracy of our sensors by comparing the concentrations measured by SWCNT fluorescence to the concentrations as determined by HPLC-MS (**Figure B.30, Table B.6**) for AFB1 and FB1 extracted from spiked corn flour. For the AFB1 response on the (9,4) chirality,

the Q-3 sensor fluorescence showed greater agreement with the values determined by HPLC-MS compared to the F-3 sensor, the latter overestimating the AFB1 concentration due to the shifting contribution from FB1. On the other hand, for the FB1 response on the (7,5) chirality, the F-3 fluorescence gave better concentration estimations compared to the Q-3 sensor, both for single-toxin and mixed-toxin solutions.

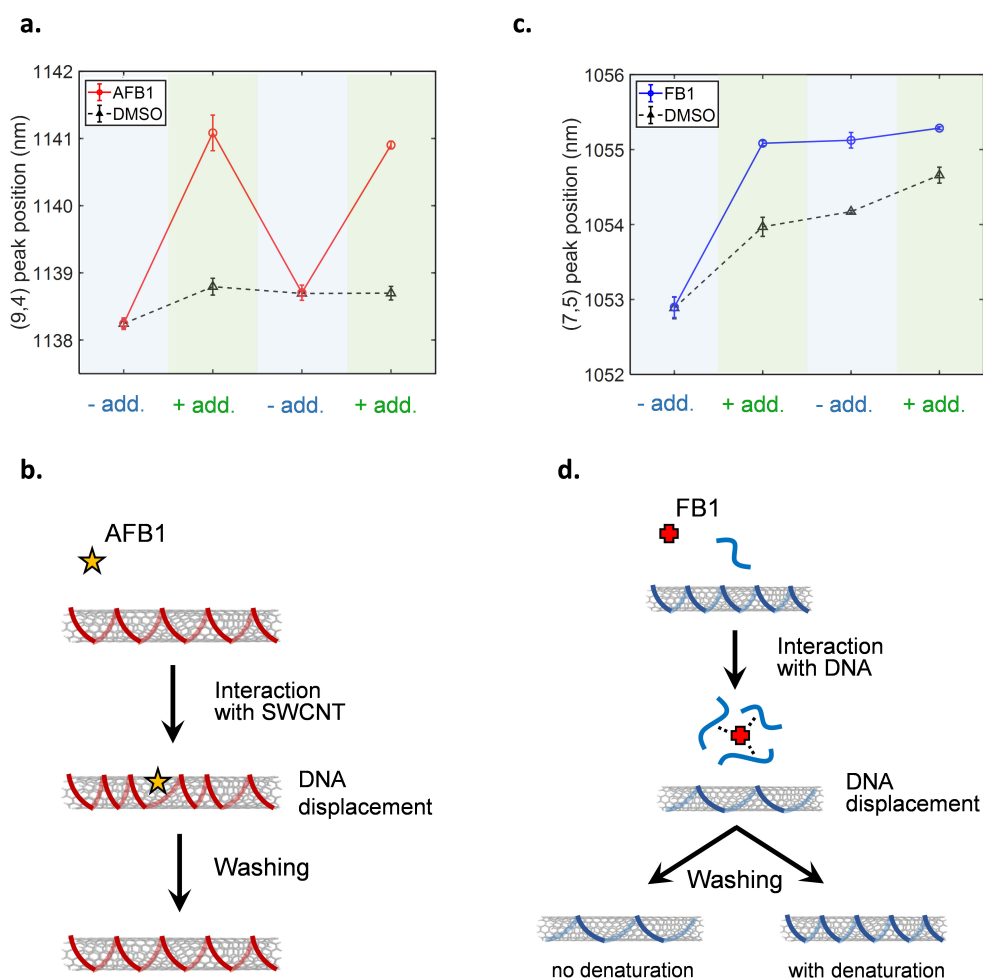


Figure 2.5 – The sensors have two distinct mechanisms of interaction. (a, c) Peak position of the (a) Q-3 and (c) F-3 sensor in the absence ("-add") and presence ("add") of AFB1 (red), FB1 (blue) and DMSO (black) for the (9,4) and (7,5) chiralities. Measurements were taken in the presence of 5 μM of the corresponding toxin following 200 min incubation. Error bars represent 1 σ ($n = 3$). (b, d) Schematics of the proposed interaction between (b) AFB1 and DNA-SWCNT sensors, and (d) FB1 and DNA-SWCNT sensors. The AFB1 interacts directly with the SWCNT surface resulting in a displacement of the DNA wrapping. Upon washing, the AFB1 is removed from the SWCNT surface and the DNA wrapping recovers its initial conformation. The FB1 interacts with the DNA (bound to SWCNT and unbound), leading to a conformational change of the wrapping. Upon washing, the sensor can be reverted back to its initial state only if the toxin-sensor interaction is disrupted by thermal denaturation.

Next, we took advantage of the SWCNT chirality-specific responses of the Q-3 and F-3 sensors in order to perform multimodal sensing of both toxins in a mixture by combining both sensors

in a same solution (**Figure 2.4**). We specifically demonstrate the ability to simultaneously detect AFB1 and FB1 by monitoring the (9,4) and (7,5) chiralities. Although previous works have demonstrated multimodal sensing using distinct fluorescence responses of different chiralities [207, 225] these studies required the separation of SWCNT chiralities, a typically tedious endeavors that is incompatible with scalable applications and limited to only certain nanotube chiralities. In this study, we obviate the need to separate SWCNTs by exploiting the preferential chirality-specificity of each DNA-sequence response. Since batches of mixed-chirality SWCNTs were prepared separately with the Q-3 and F-3 sequences, the mixture of these batches yielded chiralities wrapped with both sequences. In particular, the final mixture contained a fraction of the (9,4) SWCNTs wrapped with the F-3 sequence and the desired Q-3 sequence for detecting AFB1 at the corresponding wavelength, as well as a fraction of the (7,5) SWCNTs wrapped with the Q-3 sequence and the desired F-3 sequence for detecting FB1 at the corresponding wavelength. This mixture of off-target and on-target DNA sequences for each chirality was shown to yield an overall decrease in selectivity for the mixed sensors compared to the selectivity of the individual sensors towards their specific toxins (**Figure B.29**). To further improve the selectivity of the mixed sensors, we therefore wrapped HiPco SWCNTs (rich in the (9,4) chirality) with the Q-3 sequence and CoMoCAT SWCNTs (rich in the (7,5) chirality) with the F-3 sequence to bias the distribution of chiralities towards their respectively engineered wrapping in the final mixture (**Figure B.31**). We were able to confirm an uncompromised (9,4) response towards AFB1 even in the presence of the residual F-3 wrapped (9,4) SWCNTs from the CoMoCAT solution in the mixture. By contrast, the (7,5) sensitivity towards the FB1 response was still affected by the presence contaminating Q-3 wrapped (7,5) SWCNTs, as HiPco SWCNTs contain a substantial portion of (7,5) SWCNTs. Therefore, while directed evolution provides a promising avenue for achieving multimodal sensing in the absence of chirality separation, one must also consider possible compromises to sensitivities in mixtures when deciding on the desired minimum sensitivity threshold to achieve using directed evolution. Alternatively, directed evolution and systematic evolution of ligands by exponential enrichment (SELEX) approaches could be combined to engineer the binding affinity of the DNA sequence towards the desired chirality of interests (i.e. preferential binding of the Q-3 DNA sequence to the (9,4) chirality and of the F-3 DNA sequence to the (7,5) chirality).

While our sensors did not require chirality sorting, they could depend strongly on the chirality distribution, which can vary depending on the type of preparation used for the DNA-SWCNTs [144]. We therefore further compared the AFB1 and FB1 responses for the Δ (AG), A-4, and S5 sensors prepared by both surfactant exchange and direct sonication (**Figure B.46**). The sonicated samples and exchanged samples were both able to sense AFB1, however the response of the sonicated A-4 sensor was reduced compared to the exchanged sensor. On the other hand, no FB1 response was observed for sensors prepared by sonication. This lack of response for FB1 may be due to both the different wrapping structures that can occur on the SWCNT surface depending on the suspension protocol used [143, 144] and differences in the amount of free DNA present in the exchanged and sonicated samples, as we will discuss after. In

summary, these findings further demonstrate the capability of sensors evolved using directed evolution, highlighting the benefits of directed evolution to take advantage of chirality-specific responses to perform multimodal sensing. Moreover, this work can be achieved without the need of separated chiralities, allowing for easier sensor preparation and greater scalability, and could be generalized for AFB1 sensing for all kinds of sample preparations enabling a more flexible preparation.

To explore the underlying mechanism of the toxin-induced responses of the evolved sensors, we examined the effect of possible changes in the local dielectric environment. As discussed in the **Introduction**, changes in the local dielectric environment can trigger wavelength shifting of nanotube emission [66]. While such a response could arise from the toxin's direct effect on changing the dielectric constant of the solvent, previous studies have shown that AFB1 at concentrations used in our study does not effectively alter the dielectric constant of the solvent [226]. Alternatively, solvatochromic shifts can also result from changes in the exposed surface area of the nanotube [66, 227]. Change in SWCNT surface coverage modulates the accessibility of water on the SWCNT surface, which can consequently alter the local dielectric environment of the SWCNT. Surface coverage-induced wavelength shifting has been observed extensively for various SWCNT sensors including surfactant-covered and DNA-wrapped SWCNTs [33, 112, 113, 130, 227]. Herein, we hypothesize that the interaction between the toxins and the DNA-SWCNTs could result in a change in SWCNT surface coverage, leading to the characteristic red-shifting observed in fluorescence and NIR absorbance (**Figure B.32**).

In the case of AFB1, we tested this hypothesis by first examining the reversibility of Q-3 sensor. Though we initially attempted to study the reversibility of the immobilized DNA-SWCNTs on a glass substrate (**Figure B.33**), we ultimately developed a liquid-state washing protocol that showed improved AFB1 sensitivity compared to immobilized samples. The washing protocol (see **Methods**) was used to remove the toxins from the DNA-SWCNT suspension while allowing a resuspension of the sensors. We applied the washing protocol to the Q-3 sensor after overnight incubation with AFB1 and monitored the position of the (9,4) peak (**Figure 2.5**, **Figure B.9**). After washing, we observed that the peak position was the same irrespective of whether the sensor had previously interacted with AFB1 or DMSO (negative control). In addition, we also noted that the washed Q-3 sensor showed a similar response as the unwashed Q-3 sensor upon subsequent additions of AFB1. A similar result was observed for the F-3 sensor (**Figure B.9**). These findings suggest that AFB1 interacts with DNA-SWCNT non-covalently and that the interaction between AFB1 and the DNA-SWCNTs is reversible. Interestingly, we note a minimal red-shifting of the peak position as well as a slight decrease in shifting response for the washed samples. We attribute these observations to the removal of free DNA that occurs during the precipitation process (**Figure B.13**), as confirmed when free DNA was purposely removed (**Figure B.34**, **Figure B.35**).

We further examined whether this reversibility stems from a reversible interaction with the SWCNT, the DNA, or both elements. Previous studies have reported the interaction of AFB1 with DNA. In particular, the 8,9-epoxide exo isomer of AFB1 (AFBO) can form covalent adducts

with guanine nucleobases, leading to the acute toxicity of the toxin [228]. The AFBO is typically formed by the P450 cytochrome in the human metabolism [229], but additional studies have also confirmed the production of AFBO through the photo-oxidation of AFB1 [230]. Since the interaction AFB1 – DNA-SWCNT is reversible, we infer the lack of covalent interaction between the AFB1 and the DNA. In addition, we verified the absence of AFBO in our samples by HPLC-MS (**Figure B.36**) and by additional measurements that confirmed a SWCNT fluorescence response towards aflatoxin B2 (AFB2) (**Figure B.37**), which cannot form covalent adducts with DNA. In parallel, multiple studies have reported the non-covalent interaction of AFB1 to both double- and single-stranded DNA [231–233] *via* AFB1-nucleobase binding. In the DNA-SWCNT hybrids, the DNA nucleobases are inaccessible, hence preventing their interaction with AFB1 molecules.

The unlikely covalent and non-covalent means of interacting with DNA therefore suggests that the AFB1 primarily interacts with our sensor directly *via* the SWCNT sidewall. To test this hypothesis, we investigated the fluorescence response of sodium cholate (SC)-SWCNTs in the presence of AFB1 at various SC concentrations (**Figure B.38**), equivalent to different surface coverages as previously described [227]. As expected, no response was observed for the high coverage sample (46 mM SC); however, a strong red-shift of the (9,4) peak was detected upon addition of AFB1 for the sample with the lowest coverage (0.5 mM SC). Interestingly, for the other low-coverage samples (1 and 1.5 mM SC), the (9,4) peak first red-shifted before returning to the initial value over time. We attribute the observed shifting to the destabilization or reorganization of the SC corona upon AFB1 binding to SWCNT, therefore resulting in a change in water accessibility and a red-shifting of the emission. The red-shifting was also linked to a decrease in fluorescence intensity, indicative of a change in the SC corona on the SWCNT surface (**Figure B.39**). While this change seemed to be permanent for the 0.5 mM SC sample, the interaction AFB1 – SWCNT might not be thermodynamically favorable over the SC – SWCNT interaction for the 1 and 1.5 mM SC samples, explaining the reversibility of the shifting. To verify the interaction between the AFB1 and the SWCNT sidewall, we added low concentrations of sodium dodecylbenzenesulfonate (SDBS) to DNA-SWCNT after interaction with AFB1 to replace the toxin on the SWCNT surface while leaving the DNA wrapping intact (**Figure B.40**). At SDBS concentrations below 5×10^{-3} %, we observed that only the samples previously reacted with AFB1 would exhibit a blue-shift of the (9,4) peak, indicating a removal of AFB1 from the SWCNT surface. Based on these observations, we propose that the AFB1 interacts with the SWCNT surface, resulting in a displacement of the DNA on the SWCNT surface and the observed red-shift response (**Figure 2.5**).

In the case of FB1, we observed that the (7,5) response of the F-3 sensor was not reversible even following the toxin washing (**Figure 2.5**, **Figure B.9**), indicating a relatively strong interaction between FB1 and the DNA-SWCNT. To verify this hypothesis, we designed a modified version of the washing protocol where the samples were heated to 95°C before sample precipitation to denature any strong non-covalent interactions between the toxin and the F-3 sensor (**Figure B.10**). With this additional denaturation step, we noted that the FB1 response to be reversible, as evidenced by the equivalent the (7,5) peak position for both the FB1 and DMSO samples

after washing. This heat-activated reversibility therefore implies that the FB1 interacts in a strong, non-covalent manner with the DNA-SWCNT. This hypothesis is further supported by the hydrophilicity of the FB1, which would diminish its interaction with the hydrophobic SWCNT surface, as supported by the lack of response towards FB1 for low coverage SC-SWCNT samples (**Figure B.41**, **Figure B.42**). The interaction between DNA and FB1 has not been thoroughly studied, but the discovery of aptamers towards FB1 [234] confirms the possibility of a non-covalent interaction such as hydrogen bonding with both the bases and backbone. The role of free DNA in the F-3 sensor response supports the hypothesis that FB1 interacts with the DNA in the hybrid. Upon removal of free DNA, the sensors exhibited a red-shifting of the emission and a much lower FB1 response (**Figure B.35**). This decrease in response is similar to the lack of response observed after washing for both the non-denatured and denatured samples (**Figure B.9**, **Figure B.10**). This similarity was attributed to the loss of free DNA during the washing step (**Figure B.13**), indicating that the free DNA is crucial for the FB1 interaction. Furthermore, we also observed an increase in the concentration of free DNA for the sensors that reacted with FB1 compared to those reacted with AFB1 or DMSO (**Figure B.43**). This observation implies that the interaction with FB1 could result in the facilitated removal or weakening of the DNA interaction with the SWCNT surface. Together, these observations suggest that the FB1 interacts non-covalently with wrapped and free DNA in solution, contributing to a displacement of the DNA on the SWCNT surface and a red-shifting of the emission (**Figure 2.5**). Upon washing, denaturation can be used to dissociate the DNA from the toxin and restore the initial wrapping (**Figure 2.5**).

This hypothesis was further corroborated by the response behavior of the Q-3 sensor towards FB1 post-washing. While the F-3 sensor was unresponsive after toxin washing, the Q-3 sensor exhibited a slight response towards FB1 (**Figure B.9**, **Figure B.10**). This observation is in accordance with the fact that the free DNA removal has a lower effect on the FB1 response of the Q-3 compared to the F-3 sensor (**Figure B.35**). We believe this difference could be linked to the strength of the interaction between the DNA wrapping and the SWCNT surface. In order to determine the binding affinity of the Q-3 and F-3 sequences to SWCNT, we performed surfactant replacement experiments (**Figure B.44**) using SDBS. We observed that the surfactant replacement occurred faster for the F-3 sensor compared to the Q-3 sensor, indicating that the F-3 sequence has a lower binding affinity to the SWCNT surface. In addition, measurements of the free DNA concentrations (**Figure B.43**) showed that the F-3 sensor had more unbound DNA than the Q-3 sensor, further suggesting a weaker binding of the DNA to the SWCNT surface. These results suggest that the wrapping could be more prone to conformational changes on free DNA removal as well as on toxin interaction, as we observe both phenomena for the F-3 sensor compared to the Q-3 sensor.

These findings were used to further engineer our constructs in a working flow chamber. Since the reversible AFB1 sensors showed minimal responsivity when immobilized (**Figure B.33**), we constructed a liquid-phased flow chamber consisting of a dialysis membrane separating the sensors and the analyte. The F-3 in this flow configuration showed a reversible shifting upon washing of the AFB1 (**Figure B.45**) demonstrating a working device for the continuous

monitoring of AFB1 contamination in corn- and almond-based products. Moreover, we previously showed that DNA-SWCNT sensors can be sensitive to the presence of free DNA which could limit their applicability. Yet, the current methodology for free DNA removal is not scalable as it relies on the use of expensive filters and requires tedious sample processing. In parallel, we observed that some free DNA was lost during the precipitation of DNA-SWCNTs (**Figure B.13**). From these observations, we designed a protocol based on the precipitation of DNA-SWCNT complexes and subsequent ethanol washings on the nanotube pellet in order to remove the free DNA (**Figure B.47**). We verified that this protocol could remove more than 94 % of the free DNA after 6 washes, demonstrating a powerful, scalable approach to creating and screening DNA-SWCNT libraries without the influence of free DNA.

2.5 Conclusion

In this study, we demonstrated the applicability of directed evolution for the creation of DNA-SWCNT sensors for mycotoxin detection. We showed that it is possible to significantly improve the response of DNA-SWCNT sensors towards two distinct mycotoxins, without requiring any prior knowledge on the interaction mechanisms of these toxins with DNA-SWCNTs. In addition, we showcased how DNA shuffling can be used to drastically accelerate the evolution of these sensors. We further demonstrated that directed evolution can be used to evolve not only the magnitude of response, but also the brightness and selectivity of our sensors. Moreover, we showed that it is possible to independently evolve these sensors for two specific chiralities, (9,4) and (7,5), advantageous for multimodal sensing applications. The applicability of these sensors for toxin detection was also showed in food samples, specifically a dissolved corn flour matrix, without any need for complicated sample preparation. We discovered two distinct sensing interactions that were dependent on the mycotoxin, highlighting the power of directed evolution in the discovery of new nanotube sensors.

We envision this study will have an important impact on the engineering of DNA-SWCNT sensors. As shown herein, the directed evolution methodology can be used to tune several aspects of DNA-SWCNT sensors, to optimize their performance for a range of applications. While applied here for the sensing of mycotoxins, the same methodology could be applied to variety of targets such as small molecules [58, 130], biomarkers [59, 134] and viruses [235]. Moreover, we believe that the findings of this study will have an impact on the identification of more rational design rules for DNA-SWCNT sensors. Beyond SWCNT sensors, directed evolution presents a very powerful tool for engineering other kinds of nanocomplexes exhibiting unknown structure-function relationships. As such, this study helps catalyze the fusion of synthetic biology approaches with nanomaterials, with the aim of unlocking the true potential of these hybrid materials.

3 Towards a semi-rational design of DNA-SWCNT sensors

Portions of this chapter are reproduced from the manuscript in preparation: Lambert B.P.; Reggente M.; Lin K-H.; Boghossian, A.A. DNA-assisted semi-rational design of carbon nanotube sensors (2021). We would like to thank the Prof. Christian Heinis for letting us use his circular dichroism apparatus and Zsolt Bognár for providing the explanations on how to use it. We would also like to thank the Prof. Nicolas Mermod for letting us use his qPCR apparatus and Yves Dusserre for providing the explanations on how to use it.

3.1 Abstract

Although directed evolution has thusfar been shown to be effective in engineering DNA-wrapped single-walled carbon nanotube (DNA-SWCNT) sensors, the current approach relies on subsequent screening and selection cycles that are both time- and resource-consuming. In addition, the performance of the engineered sensors are often limited by library and screening throughput. In this third chapter, we demonstrate a semi-rational approach for the design of DNA-SWCNT sensors. This approach relies on a systematic characterization of the structure-function relationship of the complexes to identify the parameters most critical for sensor performance. Herein, we demonstrate the power of this approach through the semi-rational design of aflatoxin B1 (AFB1) and fumonisin B1 (FB1) sensors. We show that AFB1 sensors can be designed through appropriate selection of base content of the sequence, while the design of the FB1 sensors could be engineered through strategic positioning of modified bases. We further show the sensing characteristics to be correlated with morphological characteristics of the wrapping such as the presence of secondary structures. Finally, we show that these designs can be generalized to other families of molecules depending on their affinity to either the SWCNT surface or the DNA wrapping.

3.2 Introduction

Nanomaterials are celebrated for the predictive control of their optoelectronic and mechanical at the molecular level. This control enables the rational engineering of breakthrough technologies in fields ranging from energy to medicine and food science [213–215]. For many of these applications, the nanomaterial surface is often functionalized with a variety of chemicals and biological systems in order, for instance, to improve its interaction with targets [236] or to provide the material with additional functionalities [237]. In many cases, the design of these nanomaterials is done in a rational manner, following established design rules based on the known structure-function relationship of the nanomaterial [194–196]. However, the introduction of biological moieties in particular can yield nanoconjugates with unpredictable properties stemming from the elusive interactions at the nanomaterial's surface [44, 46, 48, 49]. The resulting lack of knowledge on the structure-function relationship for such complexes can undermine the applicability of the complex and the inherent advantages of using a nanomaterial.

DNA-wrapped single-walled carbon nanotubes (DNA-SWCNT) complexes are among the several bioconjugated complexes that lack a defined structure-function relationship. In the absence of their bioconjugates, SWCNTs remain as cylindrical, one-dimensional nanostructures characterized by well-defined and largely predictable mechanical, electronic and optical properties [21–23]. Semiconducting SWCNTs are particularly interesting for optical sensing owing to their photostable near-infrared (NIR) fluorescent properties, which enabled the monitoring of various targets in complex environments such as blood and tissues for extended periods of time [26, 238]. When conjugated non-covalently with DNA, the SWCNTs exhibit optical [124, 125], colloidal [100, 114] and sensing [58, 60] properties specific to the DNA sequence. Yet, despite the extensive number of studies on these complexes, the relationship between DNA sequence and the resulting properties of the DNA-SWCNT complex remains unknown. Consequently, DNA-SWCNT complexes are designed based on empirical considerations that result in sensors with compromised performances.

To tackle this issue, directed evolution was used to optimize the properties of the DNA-SWCNT sensors in a guided, more rational manner [125]. Directed evolution is a synthetic biology technique used to engineer proteins through sequential mutation, screening and selection steps. Since the mutants consist of variants of an original protein that shows a desired, albeit limited, capability, the screened library is biased towards a distribution of mutants that have an increased likelihood of demonstrating the desired capability, at least to some extent. When applied to DNA-SWCNTs, we showed that directed evolution could be used to engineer the fluorescence properties of the complexes [125], but also their sensitivity and selectivity towards analytes (see **Chapter 2**). In particular, we engineered two families of sensors for the detection of the aflatoxin B1 (AFB1) and fumonisin B1 (FB1) mycotoxins in food based on the fluorescence shifting of the (9,4) and (7,5) SWCNT chiralities, respectively. Despite the 438 DNA-SWCNT complexes screened and the significant improvements in toxin response achieved by directed evolution, we explored only a small fraction of the 4^{30} possible complexes.

It is therefore reasonable to consider that our final sensors are not the most optimized both in terms of response sensitivity and selectivity.

In protein engineering, so-called semi-rational approaches have been developed in order to improve the protein's properties beyond what was achieved by directed evolution, while also reducing the screening size [239]. These semi-rational approaches exploit information on the protein structure and sequence in order to determine what parts of the protein may govern the properties of interest, therefore reducing the library size while also allowing a higher probability of positive mutants. This approach was, for example, done for the engineering of the green fluorescent protein (GFP) for which a specific part of the protein was identified as responsible for the protein's fluorescence [163] and was further mutated by site-directed mutagenesis in order to result in brighter proteins [177] and protein exhibiting different colors [175, 176] while simultaneously limiting the screening size.

In this study, we demonstrate a semi-rational design of the DNA-SWCNT sensors for the sensing of both AFB1 and FB1. Since the DNA-SWCNT structure and structure-function relationship are unknown, we first systematically investigated the main factors affecting the responses towards each mycotoxin. We found that the AFB1 response could be modulated by altering the overall base content, more specifically the G-content, of the sequence. Additional observations suggested that the observed improvement in AFB1 response could be due to an increase in surface coverage. Moreover, we observed that sequences having G-contents greater than 80 % could form G-quadruplex (G4) secondary structures on the SWCNT surface, leading to an even larger surface coverage and a stronger response. In parallel, we found that the FB1 response could be improved by mutating a specific part of the DNA sequence, allowing to reduce the library size by approximately four times. By performing mutagenesis on this specific site, we found a mutant exhibiting not only improved response, but also enhanced reversibility. Although we could not identify the underlying mechanism responsible for the site-specificity in the sequence, we observed possible relationships between surface coverage, free DNA concentration and FB1 response, which need to be further investigated in future work. Finally, we showed that the both AFB1 and FB1 sensors could react with other targets exhibiting a similar interaction mechanism with the sensors, such as the zearalenone (ZEN) mycotoxin for the AFB1 sensors and both the AAL TB toxin and ochratoxin A (OTA) for the FB1 sensors. This work therefore demonstrates that semi-rational design can also be used for DNA-SWCNT sensors, resulting in more efficient sensors than those found by directed evolution while enabling the screening of smaller, albeit more informed, library of mutants. We also show that the families of sensors created for both AFB1 and FB1 sensing can be used to detect a variety of other molecules that rely on the same interaction mechanisms. We therefore expect these sensors to form an interesting basis for the creation of sensors based on the interaction with either the SWCNT surface or the DNA wrapping. We also believe these findings could be used to better understand the mechanisms of interaction between targets and DNA-SWCNT sensors as well as the structure-function relationship of the DNA-SWCNT complex.

3.3 Materials and methods

3.3.1 Materials

All mycotoxins were purchased from Enzo Life Sciences. All DNA oligomers were purchased from Microynth AG. Super-purified HiPco SWCNTs were purchased from NanoIntegris (Batch No. HS37-007). All chemicals were purchased from Sigma-Aldrich, unless otherwise indicated.

3.3.2 Instruments

Absorbance measurements were collected using a UV-3600 Plus spectrophotometer (Shimadzu) with quartz suprasil cuvettes (Z600393, Hellma Analytics) as well as a plate reader (Varioskan LUX, Thermo Fisher) in 96- and 384-well plates. The fluorescence measurements were acquired on a custom-made microscope designed for near-infrared spectroscopy. As previously described [81], the system is built on a Nikon Ti-E inverted microscope body, illuminated in the 400-830 nm range by a supercontinuum laser (SuperK Extreme EXR-15 and SuperK VARIA, NKT Photonics) and monitors the fluorescence light diffracted between 900-1400 nm using an InGaAs detector (NIRvana 640 ST, Princeton Instruments) coupled to a spectrometer with a 70 lines.mm⁻¹ grating (IsoPlane SCT-320, Princeton Instruments). The measurements were automatized using a custom-made LabVIEW (National Instruments) program. The fluorescence data was analyzed by a custom Matlab (R2017b, MathWorks) code, which fits individual fluorescence peaks with single Lorentzian curves.

3.3.3 Preparation of the SWCNT suspensions

The DNA-SWCNT sensors were prepared by wrapping exchange between the sodium cholate (SC)-SWCNTs and the DNA oligomers as previously described [125]. For the preparation of the SC-SWCNT suspension, 45 mg HiPco SWCNT powder was mixed with 45 mL 2 % (w/w) SC prepared in deionized (DI) water. The resulting mixture was homogenized at 5,000 rpm (Polytron PT 1300 D, Kinematica) at room temperature for 20 min, followed by 60 min ultrasonication (amplitude 10, 1/4 in. tip, Q700 Sonicator, Qsonica) in an ice bath (the ice was changed after 30 min). The suspension was centrifuged for 10 min at 15,000 x g at 25°C (Allegra 25R, Beckman Coulter) and the supernatant was centrifuged another time for 4 h at 30,000 rpm at 25°C (SW32 Ti, Optima XPN-80, Beckman Coulter). In order to reach a high-enough concentration of SWCNTs, the supernatant (top 90 %) was concentrated using centrifugation filtration devices (Amicon Ultra-15 3kDa, Merck). For that, approximately 10 mL of SC-SWCNT suspension was added to the centrifugation device and centrifuged at 4,000 g for 30 min (Allegra 25R, Beckman Coulter) at 25°C. An additional 10 mL was added to the device and the previous step was repeated. The nanotubes were resuspended using 2 % (w/w) SC to a total volume of 6.5 mL and centrifuged at 3,300 g for 30 min at 25°C to remove aggregates. The supernatant was collected and diluted using 2 % (w/w) SC to a final concentration of 108 mg/L (measured using the extinction coefficient $\epsilon=0.036 \text{ L.cm}^{-1}.\text{mg}^{-1}$ at 632 nm [125]).

The DNA solutions were dissolved in DI water to a concentration of 50 μ M (measured using Nanodrop 2000, Thermo Scientific). Volume ratios of 0.2:0.2:0.6 of DNA:SC-SWCNT:methanol were mixed by pipetting (DNA and SC-SWCNT mixed first) and incubated for 2 h at room temperature. The DNA-SWCNTs were subsequently purified to remove the SC and methanol. First, 1.5 M NaCl was added to the mixture to a final concentration of 0.2 M, followed by the addition of 2.5 volumes of cold ethanol (kept at -20°C) and gentle mixing. The resulting suspension was incubated at -20°C for 1 h and centrifuged at 21,130 g (5424R, Eppendorf) for 30 min at 4°C. The supernatant was removed, and the SWCNT pellet was washed with 70 % (v/v) ethanol, vortexed briefly, and centrifuged at 21,130 g for 1 h at 20°C. The supernatant was discarded, the pellet was air-dried for 12 min at room temperature and resuspended in the desired volume of 0.1 M NaCl. Finally, the suspensions were centrifuged at 21,130 g for 30 min at 20°C and the concentration of the supernatants was determined by measuring the absorbance of 90 μ L of suspension in 96-well plate (Varioskan LUX plate reader, Thermo Scientific). The suspensions were all diluted with 0.1 M NaCl to a final concentration of 7.4 mg/L (corresponding to a background-subtracted absorbance of 0.066). All samples were freshly prepared and used on the same day for experiments in order to avoid variations between samples due to possible aging of the samples.

3.3.4 Preparation of the mycotoxin solutions

Unless otherwise indicated, mycotoxin powders were dissolved in dimethyl sulfoxide (DMSO) in a nitrogen-controlled glovebox (E-line, GS Glovebox). The concentrations of all mycotoxins, except for FB1 and AAL TB toxin, were verified using their respective extinction coefficients in the 200-400 nm range listed in the **Table C.1**. All dissolved mycotoxin samples were aliquoted and stored at -20°C in the dark.

3.3.5 DNA mutant library

Mutants of the DNA sequences were generated by a custom code in Matlab. The saturation mutagenesis library was generated by replacing each base position with a N base corresponding to random combination of the four nucleobases. The variants of the F-3 and Q-3 sequences with varying G-contents were generated by manual random substitution of G bases to A (lower G-content) or A to G (higher G-content). The G-rich sequence library was constructed by random permutation of G and H bases in a 30-nucleotide long sequence, the H base corresponding to either C, G or T with the same probability. Three random sequences were randomly selected for each G-content between 10 and 90 %. The G₃₀ sequence could not be synthesized by the provider because of the high prevalence of G4 structures in the sequence. The library of DNA mutants were created by random introduction of a single base mutation between the positions 7 to 14 (from 5' to 3') following a strategy defined previously [125].

3.3.6 Methylene blue measurements

The coverage of the DNA-SWCNT complexes was investigated by titrating the suspensions with the methylene blue (MB) dye following a previously reported protocol [126]. The MB was dissolved in DI water in concentrations ranging from 5 to 60 μM . 47.5 μL of DNA-SWCNT suspension was mixed with 2.5 μL of MB, with final concentrations ranging from 0.25 to 3 μM , and incubated at room temperature for 1 h prior to the measurement.

3.3.7 Circular dichroism measurements

Circular dichroism measurements were performed on a Jasco J-810 spectropolarimeter. The N_2 flow was set to 5 λ/min , the scanning speed was set to 100 nm/min and measurements were done between 220 and 300 nm (0.5 nm intervals) using a 1-mm path length quartz cuvette (Suprasil quartz, Hellma). The DNA samples were diluted to 0.5 μM in 0.1 M NaCl.

3.3.8 AFM measurements

20 μL DNA-SWCNT suspension ($A_{632}(90 \mu\text{L}) \approx 0.066$ after blank correction) were deposited on freshly exfoliated mica. The suspension was dried at room temperature for 2 h and then washed two times with 100 μL DI water. The AFM measurements were acquired on a commercial AFM setup (Cypher, Asylum Research). Standard tapping mode was used to record topography, phase, and amplitude images. Images were analysed with Gwyddion 2.59.

3.3.9 Free DNA removal

The free DNA was removed using Amicon Ultra-0.5 100 kDa devices following a previously reported procedure (see **Chapter 2**). Briefly, DNA-SWCNT suspension and DI water were added to the device (pre-rinsed) to a total volume of 500 μL and the device was centrifuged at 4,000 $\times g$ for 2 min. The DNA-SWCNT were resuspended from the membrane after every washing step. The samples were rinsed again for 5 additional times in order to remove all traces of free DNA, with the last centrifugation done for 5 min instead of 2 min. Finally, the samples were resuspended in 0.1 M NaCl and centrifuged to remove SWCNT aggregates. The final suspensions were diluted to the same concentration as the initial suspensions before filtering ($A_{632}(90 \mu\text{L}) \approx 0.066$ after blank correction).

3.3.10 Gel electrophoresis

In order to investigate the various conformations of the DNA sequences, we performed electrophoretic mobility shift assay (EMSA) by running the DNA sequences on a native polyacrylamide gel (PAGE). A volume of 12 μL , containing 0.25 μM DNA in 0.1 M NaCl and 1X glycerol loading buffer, was loaded and run on a 15 % native PAGE in 1X Tris-Borate-EDTA (TBE) buffer at 150 V for 45 min (Mini-PROTEAN Tetra Cell, Biorad) in a cold bath to avoid a possible

heating of the gel. The gel was soaked in a staining solution (0.4X Sybr Gold final in 1X TBE) for a total of 30 min and imaged on a Fusion Solo S Imager (Vilber) with a 315 nm excitation.

3.3.11 DNA quantification

In this study, we assayed the concentrations of free DNA using the flow throughs of filtering devices and the concentration of DNA wrapping extracted from DNA-SWCNTs. In order to extract the DNA wrapping, we removed the free DNA of DNA-SWCNTs by centrifugal filtration and replaced the DNA wrapping with the sodium dodecylbenzenesulfonate (SDBS) surfactant. For that, we incubated the DNA-SWCNTs with 1 % SDBS (final concentration) at 60°C for 10 min. The DNA was then precipitated by ethanol precipitation with 0.3 M sodium acetate, 1 mg/mL glycogen (Carl Roth) and ethanol. After salt removal with 70 % ethanol, the DNA pellet was air dried and resuspended in DI water. The concentrations of the free DNA and DNA wrapping were assayed using the fluorescence of the Sybr Gold nucleic acid dye. For the measurement, 10 μ L of DNA sample was added to 40 μ L 1X Sybr Gold in 10 mM HEPES buffer (pH 8). The samples were then incubated in the dark for 5 min and the fluorescence at 537 nm under 495 nm excitation was recorded with an exposure of 100 ms (Varioskan LUX, Thermo Fisher). We constructed calibration curves of Sybr Gold fluorescence and DNA concentration for each sequence for concentrations ranging from 10 to 75 nM and used the slopes to calculate the concentration of DNA in our samples.

3.3.12 Surfactant replacement assays

The DNA wrapping was replaced using the sodium dodecylbenzenesulfonate (SDBS) surfactant following previously a reported procedure [115]. The SDBS was dissolved in DI water to a concentration of 0.11 % (w/w) in DI water. 50 μ L of DNA-SWCNT suspension was mixed with 5 μ L of 0.11 % SDC (final concentration of 0.01 %) in a 384-well plate (MaxiSorp, Nunc) and incubated at room temperature. The fluorescence of the suspension was recorded every 10 min for a total of 150 min. The kinetics of replacement were fitted with single exponential curves in order to determine the time constant of replacement.

3.3.13 Measurements

Fluorescence measurements were performed with an exposure time of 5 s, a laser power of 100 % and an illumination bandwidth of 10 nm. The monitoring of the (7,5) and (7,6) chiralities was done with an excitation of 660 nm and the monitoring of the (10,2) and (9,4) chiralities with an excitation of 745 nm. 49.5 μ L aliquots of diluted DNA-SWCNT suspension were added to a 384-well plate (Nunc Maxisorp, Thermo Scientific) and fluorescence spectra were collected prior to the addition of any analyte. Following the initial measurement, 0.5 μ L of analyte solution (concentration specified in the experiment) was added to the well and briefly mixed by pipetting up and down. The incubation times between measurements depended on

the time of experiment and is therefore indicated for each dataset. All measurements were performed at room temperature with the laser switched off in between measurements. In addition, the plates were sealed (CLS6524, Corning) in order to avoid evaporation. The shifting responses labelled as $\Delta\lambda_{solvent}$, $\Delta\lambda$ or "Peak shift" were calculated as the difference in peak position between the toxin and the negative control (DMSO).

3.3.14 Melting curves

The melting curves were carried out using a LightCycler 480 qPCR system (Roche Applied Science). All DNA stocks (50 μ M concentration) were first annealed in 10 mM TRIS buffer pH 8 by heating at 95°C for 2 min and subsequent gradual cooling to room temperature. The DNA-SWCNT samples were prepared by methanol-assisted exchange, as described previously, using the annealed DNA stocks (10 μ M final concentration) and a SC-SWCNT batch at a SWCNT concentration of 165 mg/L (33 mg/L final concentration). The DNA-SWCNTs were resuspended in DI water and filtered in order to remove the free DNA, as previously described. The DNA samples were prepared by diluting the DNA stocks to a final concentration of 0.5 μ M in DI water. The Sybr Green I batch was prepared fresh at a 10X concentration in 10 mM TRIS buffer pH 8. The measurements were performed by mixing 18 μ L of sample (diluted DNA samples or filtered DNA-SWCNTs) with 2 μ L of 10X Sybr Green I dye in a 96-well plate (04729692001, Roche Applied Science). The dye was excited at 465 nm and the emission peak at 510 nm was recorded with sample temperature varying from 20 to 95°C.

3.4 Results and discussion

We first investigated the effect of the base content on the AFB1 and FB1 responses on the (9,4) and (7,5) chiralities based on data acquired for sequences analogue to the starting sequence (**Figure 3.1**). We observed a strong positive correlation between the AFB1 response and the G-content, as well as a smaller positive correlation for the T content. In addition, we noted a strong negative correlation between the AFB1 response and the A content and a smaller negative correlation for the C content. For the FB1 response, we noted a strong positive correlation with the A content. We also noted a strong negative correlation between the FB1 response and the T content, and a smaller negative correlation with the C content. The G-content did not seem to be correlated with the FB1 response. These results suggest that it could be possible to engineer the AFB1 and FB1 response only by modifying the base content of the sequences.

We then investigated the dependence of the AFB1 and FB1 responses on the (9,4) and (7,5) chiralities on the base position (**Figure 3.1**). For that, we systematically randomly mutated every base of the sequence and compared the response of the resulting sequences towards AFB1 and FB1 with the starting sequence. For the AFB1 response, we did not observe any dependence on the position of the mutated bases compared to the starting sequence. For the FB1, on the other hand, we observed an increase in response when the bases were mutated at

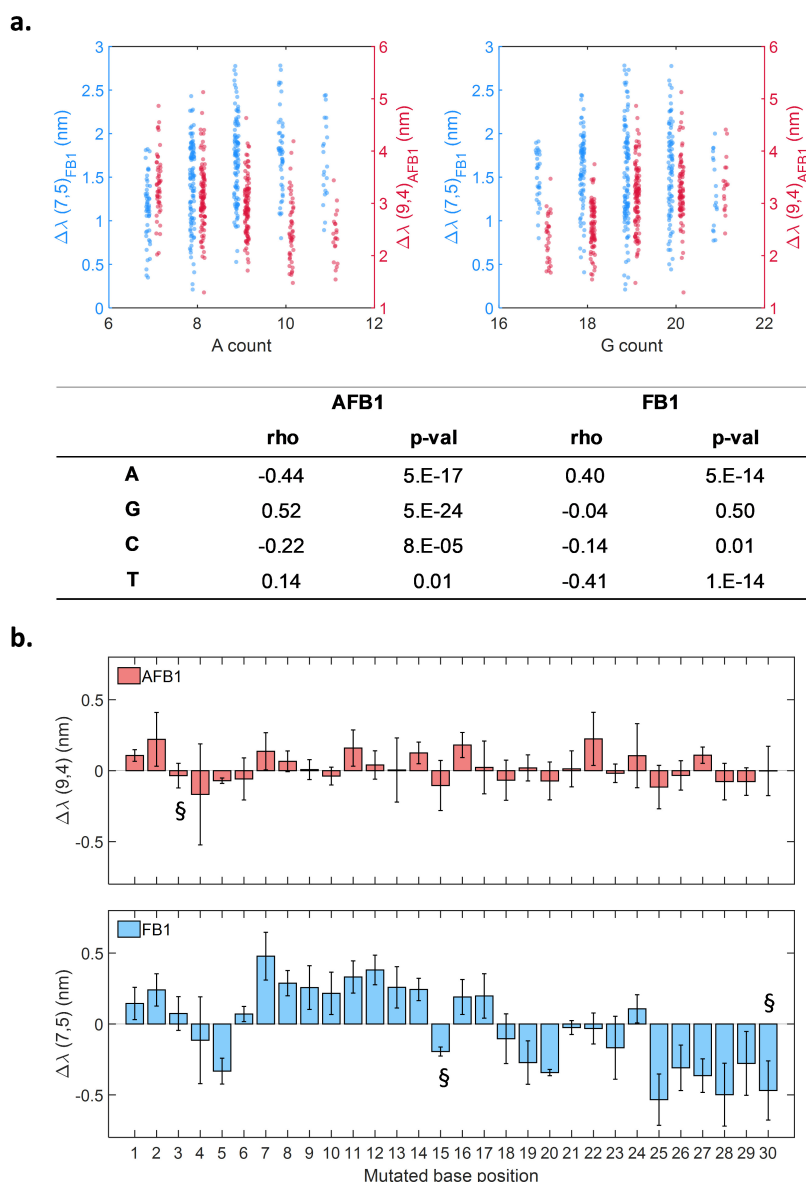


Figure 3.1 – Factors affecting the sensor’s response towards AFB1 and FB1. (a) Top: Dependence of the (7,5) response to FB1 (blue) and the (9,4) response to AFB1 (red) on the A (left) and G (right) base contents in 282 DNA-SWCNTs (109 distinct sequences) analogous to the Q-3 and F-3 sensors. The measurements were acquired in presence of 10 μM toxins following 200 min incubation. Bottom: Results of Spearman correlations between the response and the base content for the A, G, C, T bases. (b) Dependence of the (9,4) response to AFB1 (top) and the (7,5) response to FB1 (bottom), on the position of the base mutated from the F-3 sensor. The shift indicated is calculated as the difference of response between the mutated sequences and the initial F-3 sensor. The measurements were acquired in presence of 5 μM toxins following 200 min incubation. The error bars represent 1 σ ($n = 3$ for all except for the bar marked by § for which $n=2$).

the positions 7 to 14 (from 5’ to 3’). In addition, the FB1 response was decreased when the bases at the positions 25 to 30 were mutated. This observation therefore indicates that, while

Chapter 3. Towards a semi-rational design of DNA-SWCNT sensors

the AFB1 response is independent of the location of the mutation in the sequence, the FB1 response can be engineered by mutating certain positions in the DNA sequence.

The AFB1 response on the (9,4) chirality was subsequently semi-rationally designed based on these observations. In particular, we changed the G-content in the previously identified F-3 and Q-3 sequences between 40 and 80 % G-content (initial G-content around 60 %) and noted an increase in AFB1 response with G-content (**Figure C.1**, sequences listed in **Table C.2**). To confirm further this observation, we designed 28 random sequences with varying amounts of G, from 0 % to 90 % (**Table C.3**). We observed a dependence of the wrapping efficiency on the G-content with a maximum DNA-SWCNT concentration for the sequences having between 20 and 50 % G-content and a strong decrease in SWCNT concentration with increasing G-content between 60 and 90 % G-content (**Figure C.2**). We tested 25 DNA-SWCNTs out of 28 as the 80-1, 90-1 and 90-2 sequences failed to suspend the SWCNTs (final concentration below 7.4 mg/L). We noted an increase in AFB1 response with increasing G-content (**Figure 3.2**). Interestingly, for the sequences below 60 % G-content, we noted relatively low variation in AFB1 response for sequences with the same G-content while this variation was larger for sequences with G-content above or equal to 60 %. We also noted two linear regimes in the increase of AFB1 response: a lower regime between 0 and 60 % G-content (blue line) and a higher regime between 60 and 90 % G-content (red line). Our AFB1 sensors are not only characterized by a strong red-shifting of the (9,4) chirality but also by a strong SWCNT chirality selectivity of the red-shifting, with only minimal shifting on the (7,5), (10,2) and (7,6) chiralities (see **Chapter 2**). We investigated the effect of G-content on the SWCNT chirality specificity of the AFB1 response (**Figure 3.2**, **Figure C.3**, **Figure C.4**). For sequences below 60 % G-content, the shifting was similar for the (10,2), (7,6) and (9,4) chiralities, while a little lower for the (7,5) chirality, with only a small increase in selectivity with increasing G-content. The selectivity of the response towards the (9,4) chirality was stronger for the sequences from 60 to 90 % G-content, the selectivity increasing with G-content. This result therefore indicated that not only can the magnitude of the response be engineered by changing the base content, but also that the SWCNT chirality selectivity of the response can be engineered in a similar fashion. In addition, we hypothesized the mechanism governing the AFB1 interaction at low G-content (below 60 %) to be different from the mechanism of interaction at high G-content (60 % or above).

In order to understand the origin of the increase in the AFB1 response with G-content, we characterized the wrapping morphology. As we previously hypothesized, the AFB1 is believed to primarily interact with the SWCNT surface (see **Chapter 2**), and the interaction could depend on surface accessibility of AFB1 and consequently the surface coverage of the DNA-SWCNT complexes. To investigate the surface coverage of our sensors, we titrated the DNA-SWCNT suspensions with methylene blue (MB) dye and monitored the fluorescence quenching on the (9,4) chirality caused by the dye (**Figure 3.2**) as previously reported [126]. We observed that the DNA-SWCNTs with higher G-content exhibited a lower quenching in the presence of the MB dye. Consistently to what was observed for the AFB1 response, we observed two regimes with an overall higher quenching for the sequence between 0 and 60 % G-content and

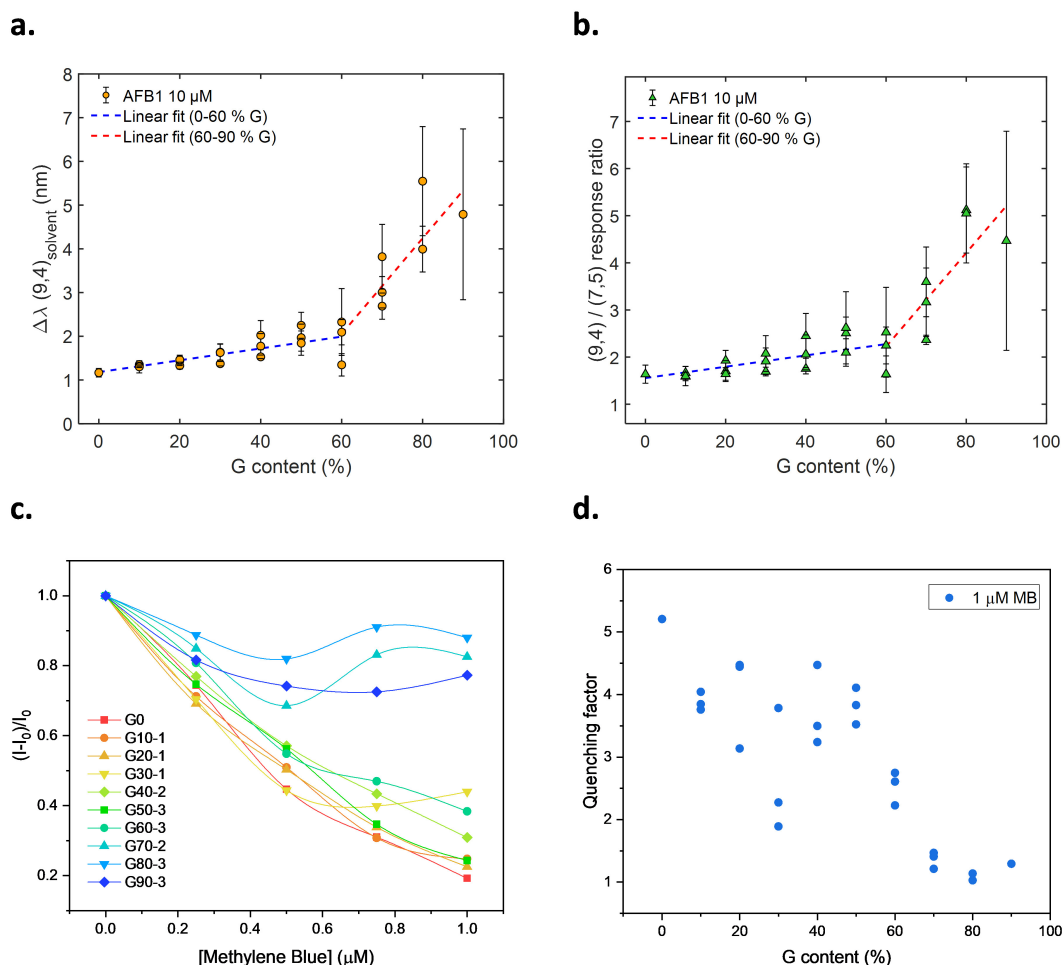


Figure 3.2 – The AFB1 response can be improved by modifying the G-content. (a) Shifting response towards AFB1 for the (9,4) chirality as a function of G-content. The response is measured as the shifting caused by AFB1 compared to the addition of solvent (DMSO). Linear fits were calculated between 0 and 60 % G (blue line) and between 60 and 90 % G (red line). (b) Ratios of the (9,4) and (7,5) shifting responses towards AFB1 as a function of G-content. This ratio illustrates the selectivity of the response for the (9,4) chirality compared to the (7,5) chirality. Linear fits were calculated between 0 and 60 % G (blue line) and between 60 and 90 % G (red line). The measurements were done with a toxin concentration of 10 μM and 200 min after addition. The error bars represent 1 σ (n = 3). (c) Fluorescence intensity change $(I-I_0)/I_0$ as a function of the concentration of MB dye for sequences with varying G-contents. The lines are guides for the eye. (d) Quenching factor I_0/I (I_0 and I the intensities after addition of DI water and MB respectively) for the final MB concentration of 1 μM as a function of G-content. The quenching factor is negatively correlated with G-content ($\rho = -0.76$, $p < 0.05$, Spearman correlation test). The measurements were performed after an incubation of 60 min post addition.

a lower quenching for the samples between 60 and 90 % G-content. This observation therefore suggested that the sequences with higher G-content possess a denser surface coverage. While we also observed red-shifting of the emission for the (9,4) chirality with increasing G-content (**Figure C.5**), which is usually associated with a decrease in surface coverage and a higher water accessibility [66], this red-shifting could also result from the interaction between the

nucleobases and the SWCNT as previously reported [127]. In addition, we also investigated the binding affinity of the DNA sequences to the SWCNTs, hypothesizing the AFB1 response to be linked to a displacement of DNA wrapping. Such a displacement would be facilitated by sequences that show lower affinities to the nanotube. To compare the effective binding affinity of the different sequences, we monitored the kinetics of the replacement of the DNA wrapping by sodium dodecylbenzenesulfonate (SDBS) (**Figure C.6**). In accordance with what was observed with surface coverage, we observed an increase in binding affinity with increased G-content. Such an increase in binding affinity is consistent with previous studies that show guanine to have the highest binding affinity to both carbon nanotubes and graphene among the nucleobases [121].

A solvatochromic shift, as observed for the AFB1 response, is an indirect measure of the interaction with the DNA-SWCNT as it essentially reflects the change in the water accessibility of the SWCNT surface. We previously hypothesized that the shifting response observed was due to a conformational change of the DNA wrapping caused by the interaction between the AFB1 and the SWCNT surface (see **Chapter 2**). The observations above further suggest the extent of the response to depend mainly on the surface coverage, with a denser coverage resulting in a higher response. In the case of a DNA wrapping with high surface coverage, such as a sequence with high G-content for example, the higher coverage would limit the accessibility of AFB1 for binding. As the AFB1 has a larger affinity to SWCNT compared to the DNA bases (**Figure C.7**), the AFB1 could partially unwrap or displace the DNA wrapping in order to bind, hence contributing in the observed red-shift. On the other hand, in the case of DNA-SWCNT with low coverage such as a sequence with low G-content, the AFB1 could bind to free sites without significantly affecting the DNA wrapping, resulting in a minimal red-shifting. Even though we observe an increase in binding affinity with increasing G-content, which should limit the AFB1 interaction, we assume the AFB1 binding affinity to the SWCNT to be larger than that of the DNA wrapping regardless of the G-content.

Despite the overall trend with increasing G-content, we note a stark difference between the sequences with less than and with more than 60 % G-content. In particular, complexes with significantly higher G-content, such as those exceeding 60 %, may form G4 structures, therefore affecting both the surface coverage of the wrapping and the AFB1 response. To verify this hypothesis, we performed circular dichroism (CD) measurements on the DNA sequences (**Figure 3.3**). We noted that the sequences G70-2, G80-2, G80-3 and G90-3 exhibited a very distinct positive band near 260 nm, characteristic of a parallel-stranded G4 structure [240]. These findings are in accordance with the predictions of the QGRS Mapper software [241] which predicted a much greater likelihood of G4 formation for these sequences (**Table C.4**). These results were further confirmed by electrophoretic mobility shift assay (EMSA) of the DNA sequences on 15 % native polyacrylamide (PAGE) gel (**Figure 3.3**). In this experiment, a shift in the position of the main peak is visible for the sequences G70-2, G80-2, G80-3 and G90-3. We believe the band between 20 and 30 nucleotides could correspond to the formation of a uni-molecular (intra-molecular) G4 structure, which is more compact than the oligomer and is therefore expected to run faster on the gel [242]. In addition, the band located around

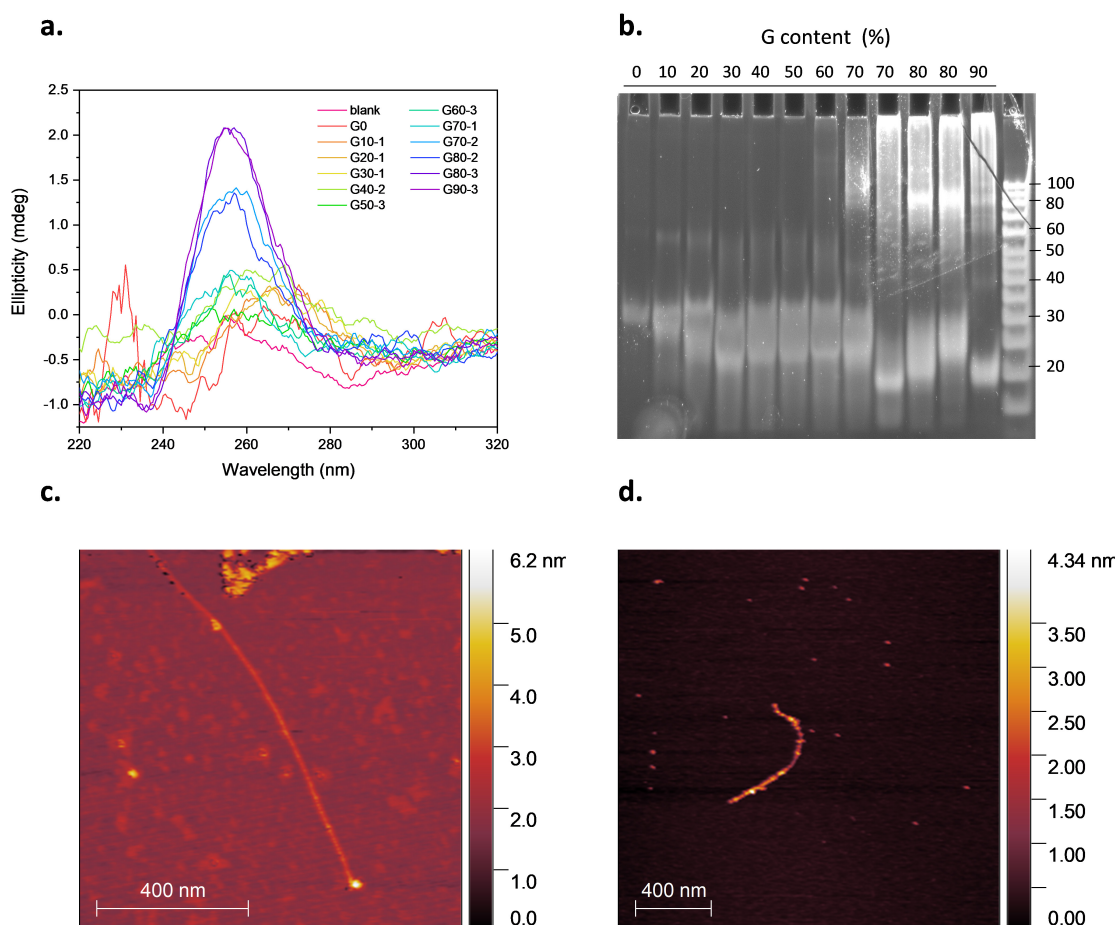


Figure 3.3 – The G-content is related to the formation of secondary structures. (a) CD spectra of DNA sequences with varying G-content. (b) Native PAGE gel electrophoresis of DNA sequences with varying G-content. The order of the sequences is the same as for the (a) panel. (c,d) AFM measurements of the topography of the (c) G0-SWCNT and (d) G90-3-SWCNT deposited on a mica surface. The Z axis represents the height.

80 nucleotides is believed to correspond to sequences forming bi- or tetra-molecular (inter-molecular) G4 structures [243]. We attribute the smear observed for the other sequences below 70 % G-content to the presence of secondary structures due to the random nature of the sequences, which could contain hairpins or form dimers. Furthermore, we think the presence of G4 structures could explain the low wrapping efficiency observed for the sequences whose G-content was above 70 % (**Figure C.2**), since hybridized oligomers exhibit much lower affinity to the SWCNT [244].

While DNA sequences can form secondary structures in solution, they may not be able to retain these structures on the nanotube surface [245]. The presence of secondary structures was confirmed by atomic force microscopy (AFM) of the G0- and G90-3-SWCNT complexes (**Figure 3.3, Figure C.8**). A rough surface was observed for the G90-3 samples while a smooth surface was observed for the G0 sequence. In addition, when comparing the height profiles of

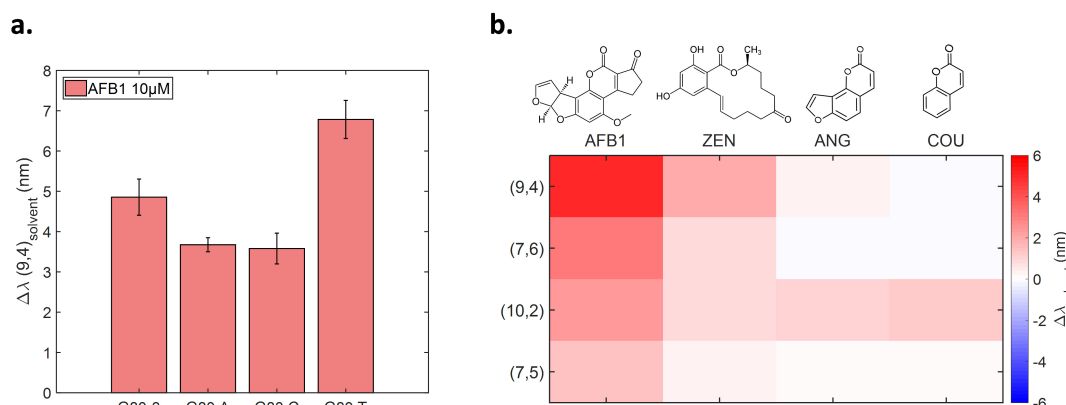


Figure 3.4 – Optimization and generalization of the AFB1 sensors. (a) Shifting response of the (9,4) chirality towards AFB1 for the G80-3-SWCNT complex and its derivatives. (b) Shifting response of the (9,4), (7,6), (10,2) and (7,5) chiralities in presence of AFB1, ZEN, ANG and COU for the G80-3-SWCNT complex. The structures of the various molecules are indicated on top of the heatmap. The measurements were done with a toxin concentration of 10 μM and 200 min after addition. The error bars represent 1 σ ($n = 3$).

the G0 and G90-3 samples, we noted a 2-nm increase in wrapping height for the G90-3 complex (**Figure C.8**) in accordance with the literature [246]. As the G4 form in the presence of metallic cations such as Na^+ , we monitored the peak positions and AFB1 response of the different DNA-SWCNTs in the presence of varying salt concentrations (**Figure C.9**, **Figure C.10**). We first observed that the sequences having between 0 and 30 % G-content showed no salt dependence on both AFB1 response and peak position. For the sequences with G-content between 40 and 70 %, we noted a blue-shifting of the emission and a concomitant decrease in AFB1 response with increasing salt concentration. Finally, for the sequences between 80 and 90 % G-content, we observed a blue-shifting of the emission with increasing salt concentration and a non-linear trend in AFB1 response. For the G80-2 and G80-3 samples, the AFB1 response first increased drastically from 0 to 25 mM NaCl and then decreased with increasing ionic strength, with higher responses still observed for concentrations up to 150 mM compared to solutions in the absence of salts. Finally, for the G90-3 sample, the AFB1 response increased linearly with increasing salt concentration up to 75 mM and then stabilized between 75 mM and 100 mM. We believe that the difference in AFB1 response seen between the samples below and above 80 % G-content indicates a difference in wrapping conformation, which may be due to the presence of G4 structures on the SWCNT surface. This hypothesis was further corroborated by the measured concentrations of DNA unwrapped from SWCNTs for the G0, G20-1, G40-1, G60-2 and G80-3 samples (**Figure C.11**). We noted a much higher DNA concentration for the G80-3 complex (more than 4 times higher), consistent expected results for SWCNTs wrapped with smaller molecules such as G4 structures. Based on these observations, we therefore conclude that some sequences can form G4 structures on the SWCNT surface, allowing an even greater surface coverage that can contribute to a higher AFB1 shifting response.

These findings laid the framework for engineering an optimized AFB1 sensor (**Figure 3.4**). A G-content of 80 % was chosen because of the balance between high AFB1 response as well as the improved wrapping efficiency compared to the 90 % G-content (**Figure 3.4**, **Figure C.2**). We chose the G80-3 sequence configuration as it showed the greatest AFB1 response. As previously discussed, the AFB1 response seemed to depend not only on the G-content but also on the other bases (**Figure 3.1**). We therefore replaced the H random bases with either A, C or T and to test the AFB1 responses of the resulting sensors. We observed that the sequence containing both 80 % G and 20 % T (G80.T sequence) showed the greatest AFB1 response, approximately 2 nm greater than that of the G80-3 sensor, in accordance with the findings of **Figure 3.1**. We noted that this response is almost four times larger than the response reported for the Q-3 previously engineered for the sensing of AFB1 (**Figure C.12**). In addition, the G80.T sensor exhibited a slightly lower shifting in the presence of FB1 for the (9,4) chirality therefore drastically increasing the selectivity of the sensor towards AFB1 for the (9,4) chirality (**Figure C.12**). The successful application of these rational design rules therefore demonstrates a means of creating sensors with performances that can exceed empirical and high-throughput screening techniques.

We next examined if the sensors designed for AFB1 response could be used to detect other molecules with similar structures. For these sensors, we tested the library of sequences with varying G-content with angelicin (ANG) and coumarin (COU), two furanocoumarins that share structural similarities with the AFB1 (**Figure 3.4**). Interestingly, the sensors did not exhibit any response in presence of both molecules for the (9,4) chirality. We tested if ANG and COU could interact with the SWCNT surface by testing them in the presence of sodium cholate (SC)-suspended SWCNTs (**Figure C.13**) and noted the absence of any shifting, even at low SC concentrations (0.5 mM SC) equivalent to low surface coverage, while AFB1 would result in a large red-shift in the same conditions. We previously observed that the zearalenone (ZEN) mycotoxin could result in a similar response signature as for the AFB1 (see **Chapter 2**). We observed that, even though the molecules possess distinct structures and interact differently with SC-suspended SWCNTs (**Figure C.14**), our sensors responded to ZEN on the same chiralities as for the AFB1 response, however to a lower extent (**Figure 3.4**). As both COU and ANG do not result in any response, this observation could suggest that a threshold in interaction energy is needed to displace the DNA wrapping (or the SC in the case of SC-suspended SWCNTs).

After the engineering of the AFB1 response, we further investigated the factors influencing the FB1 response on the (7,5) chirality. Through systematic mutation, we observed that the FB1 response could be engineered by specifically mutating the positions 7 to 14 (**Figure 3.1**). Based on this observation, a library of 24 sequences was created to contain all possible mutants with one base substitution between the bases 7 to 14. We note that whereas a single base substitution on the whole sequence would have required a library size of 90 sequences, the targeted sequence range between bases 7 to 14 reduces the screening size by almost four times (24 sequences). From the first screening, we identified several mutants exhibiting an increase in the FB1 response (**Figure 3.5**, **Figure C.15**). We selected the best performing mutant, R1_{9,2}

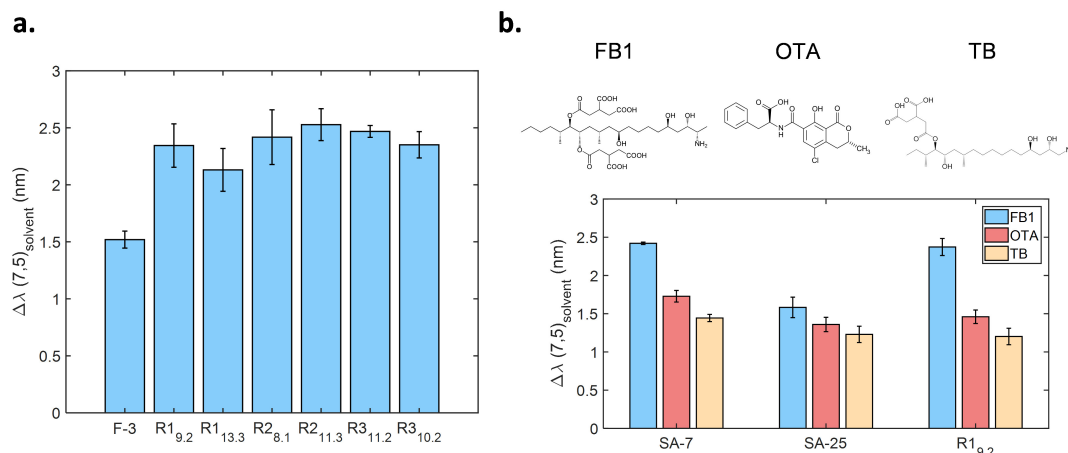


Figure 3.5 – Optimization and generalization of the FB1 sensors. (a) Shifting response of the (7,5) chirality towards FB1 for the F-3-SWCNT complex and the mutants from the first (R1) to the third (R3) round of mutagenesis between the positions 7 to 14. The measurements were acquired 210 min after addition. (b) Shifting response of the (7,5) chirality in presence of FB1, OTA and TB for the SA-7, SA-25 and R1_{9,2}-SWCNT complexes. The SA-7 and SA-25 are the random mutants at the positions 7 and 25. The structures of the various molecules are indicated on top of the graph. The measurements were acquired 200 min after addition. All measurements were done with a toxin concentration of 10 μM . All error bars represent 1 σ ($n = 3$).

presenting a G replacing a A on the 9th position, and we created another library of mutants by once more introducing a single base substitution in the positions 7 to 14. However, this screen did not identify any mutant exhibiting a higher FB1 response, with the best mutants (R2_{8,1} and R2_{11,3}) exhibiting a similar response to that of the R1_{9,2} sensor (**Figure 3.5**). While the stagnated performances of these screened sensors could be indicative of achieving a local or global maximum in the fitness landscape [247], one may overcome this limit through the introduction of neutral mutations, mutations with little to no effect on the desired property, also known as neutral drift. In this regard, the best mutant from the second mutant library, the R2_{8,1} sequence, can be considered a neutral mutant as its FB1 response was not significantly different from the response of the R1_{9,2} sensor. An additional round of mutagenesis was performed on the neutral R2_{8,1} mutant. However, we were unable to identify any mutants from this third library that exhibited a higher FB1 response, with the best mutants (R3_{11,2} and R3_{10,2}) exhibiting a response that was only comparable to the R1_{9,2} and R2_{8,1} sensors (**Figure 3.5**). Although an improvement could be obtained after the incorporation of several neutral mutations, the incorporation of an increasing number of mutations could affect other properties of the complex [193]. In addition, some parts of the R1_{9,2} mutant could be limiting any further improvements in FB1 response, due to incompatibilities with other mutations for example. In such cases, the search can be attempted using another starting point, analogous to the previous starting sequence. We therefore created a new mutant library based on the R1_{13,3} sequence, which exhibited a FB1 response similar to that of the R1_{9,2} (**Figure C.16**). However, we were unable to observe new mutants with an increased FB1 response compared to the starting complex. As we could not improve further the FB1 response by mutating the

positions 7 to 14, we selected the the R1_{9,2} mutant as our optimized FB1 sensor in the next experiments.

We also investigated the ability to improve sensors by introducing multiple mutations in the positions 7 to 14. We created a library of 21 sequences comprising of mutants with 3 to 8 random mutations (**Figure C.17**). We tested 4 random configurations for all mutants having between 3 and 7 mutations. None of the mutants exhibited a FB1 response higher than that of the F-3 sensor but we observed a decrease in response with increasing number of mutations, confirming the deleterious effects of introducing too many mutations. Since the highest responses were observed for samples containing 3 mutations, and especially mutations that were grouped next to each other, we tested different configurations of grouped mutations for locations between the positions 7 to 14 (**Figure C.18**). Based on these results, the configurations consisting of 3 grouped mutations in the middle of the sequence, between positions 9 to 11, resulted in a higher FB1 response. In parallel, we mutated the 3N3 complex, the third configuration obtained with 3 mutations, as it showed the highest response among the mutant library previously discussed (**Figure C.17**). We introduced one random mutation to each of the bases in the 3N3 sequence, except those that were previously mutated, and created a library of 27 new sequences (**Figure C.19**). Among these sequences, we found one complex (3N3-5) that exhibited a strong increase compared to the F-3 sensor. This sensor could therefore be used as the starting point of a new family that could possibly surpass the capabilities of the R1_{9,2} sensor.

As we previously observed the reversibility of the FB1 response of the F-3 sensor to depend on the presence of free DNA (see **Chapter 2**), we further investigated the reversibility of the newly engineered R1_{9,2} sensor. In particular, we compared the position of the (7,5) peak after interaction with FB1 or DMSO before and after sensor washing following the same procedure. As observed in **Chapter 2**, the F-3 sensors retained a red-shifting of the emission post-washing for the samples that reacted with both FB1 and DMSO (**Figure C.20**). These red-shifted sensors exhibited a ca. 74 % decrease in FB1 response for the sensors that previously interacted with DMSO and a ca. 374 % decrease for the sensors that reacted with FB1. The R1_{9,2} sensors, on the other hand, were much less affected by the washing step, demonstrating only a 5 % decrease in FB1 response for the sensors that reacted with DMSO and a 37 % for the sensors that interacted with FB1 (**Figure C.20**). We attribute the larger decrease in response for the sensors that interacted with FB1 to the interaction between FB1 and DNA since no denaturation steps were performed during the washing. These results therefore indicate that the R1_{9,2} could be used as a reversible sensor, hence allowing a greater applicability of our FB1 sensors.

Although the improvement of the FB1 sensor was achieved through semi-rational engineering of a specific part of the DNA sequence, the significance of this part of the sequence in the underlying sensing mechanism remains unclear. We therefore investigated the effects of different mutations in this region on other properties of the complexes. Since the FB1 response was improved through modification of a specific location within the sequence, the DNA may form secondary structures on the SWCNT surface that could be stabilized or disrupted by mutations

in this region. The presence of possible secondary structures was therefore examined by gel electrophoresis (**Figure C.21**), which confirmed the presence of a single band, indicating the lack of secondary structure formation. We then investigated the effect of the binding affinity of the DNA wrapping with the SWCNT surface by monitoring the kinetics of DNA replacement by SDBS (**Figure C.22**), as previously done [115]. As we previously hypothesized that the interaction with FB1 could result in a removal of DNA from the SWCNT surface (see **Chapter 2**), a DNA wrapping with a lower binding affinity to SWCNT could therefore result in facilitated DNA wrapping removal or displacement, thus yielding a higher FB1 response. As we did not observe any relationship between the time constants of SDBS replacement and the FB1 response, these results suggest that the interaction with FB1 is not likely to be modulated by the binding affinity of the DNA-SWCNTs. We also investigated the effect of surface coverage on the FB1 response by titrating the DNA-SWCNT suspensions with MB dye, similarly to what was done with the AFB1 sensors (**Figure C.23**). Based on the hypothesized mechanism, a lower coverage could lead to a facilitated interaction between the DNA wrapping and the FB1. However, no significant correlation was found between MB-induced quenching and FB1 response. Finally, we tested the effect of the concentration of free DNA on the FB1 response (**Figure C.24**). As the FB1 is expected to interact with the DNA wrapping as well as the free DNA, we expected a larger response for sensors exhibiting a lower free DNA concentration because of the higher probability of interaction between the FB1 and the DNA wrapping. However, we did not observe any significant correlation between free DNA concentration and FB1 response. Even though both surface coverage and free DNA concentrations were not significantly correlated to FB1 response, they demonstrated characteristic trends. These observations could suggest that, while not inducing strong effects, the surface coverage and free DNA concentration could both minimally affect the FB1 response.

As for the AFB1 sensors, we tested if the sensors designed for FB1 response could be used for other molecules with similar structures. For these measurements, we first examined the performances of our sensors against the AAL TB toxin, a molecule sharing a maximum common substructure (MCS) similarity of 0.7 with the FB1 (Tanimoto coefficient, calculated with the ChemMine Tool software [248]). Though the sensors exhibited a red-shift in presence of the AAL TB toxin, the extent of the shifting was lower than that obtained in presence of FB1 (**Figure 3.5**). In addition, we previously noted that the ochratoxin A (OTA) resulted in a similar response signature as FB1 (see **Chapter 2**). Interestingly, upon OTA addition, our sensors exhibited a response similar in magnitude to the response towards AAL TB toxin despite the drastically different molecular structure. We previously hypothesized the FB1 to interact with the DNA, either on the SWCNT surface or in free solution, *via* hydrogen bonding with the nucleobases or the DNA backbone (see **Chapter 2**). In the case of AAL TB toxin, the lower shifting response could be correlated to the lower number of hydrogen bond-donating and -accepting groups in the molecule that could result in a weaker interaction with the DNA compared to FB1. On the other hand, as the OTA exhibits a lower number of hydrogen bond donating and accepting groups compared to the AAL TB toxin, we expected a lower shifting response. We believe that the interaction between DNA and OTA could be stabilized

by π -stacking between the OTA and the nucleobases, hence resulting in a similar interaction energy with DNA as for the AAL TB toxin and a similar shifting response. To confirm if the AAL TB toxin and OTA were interacting with the DNA or with the SWCNT surface, we monitored the response of low coverage SC-suspended SWCNTs in the presence of both toxins. For the AAL TB toxin, we noted a red-shifting response for the 1 and 0.5 mM SC concentrations (**Figure C.25**). We further investigated if the AAL TB toxin could interact with the SWCNT surface of DNA-SWCNT sensors by testing it against G80-3 variant sensors that can detect the interaction between a target and the SWCNT sidewall (**Figure C.26**). We noted the absence of any response in the presence of the G80-3 variant sensors, which could suggest a lack of interaction between the toxin and the SWCNT surface for DNA-SWCNT sensors. For the OTA toxin, we noted a lack of response for all concentrations of SC-suspended SWCNTs, confirming that OTA interacts exclusively with DNA (**Figure C.27**). Although a blue-shift response can be observed for the (7,5) chirality of the 1.5 mM SC-SWCNTs, this response is similar to the one observed in presence of FB1 (see **Chapter 2**) and is attributed to the interaction between SC and the target. These results therefore indicate that our FB1 sensors can be used to detect a range of molecules with a particular affinity towards DNA. While the selectivity towards one type of target or another has not yet been optimized, the specificity is sequence-dependent (**Figure C.28**) and could be further improved by directed evolution, as demonstrated in our previous work.

Future work in elucidating the structure-function relationship of these sensors could be oriented towards achieving a more precise characterization of DNA secondary structures on the SWCNT surface, such as G4 structures for the AFB1 sensors, or structures formed by the interaction between the DNA wrapping and FB1. Such characterization could be achieved by performing melting curves of the DNA-SWCNT complexes. We demonstrated the applicability of such technique for the characterization of (AT)₁₅ and (GT)₁₅ wrappings on SWCNTs. The (AT)₁₅ sequence is self-complementary and can form dimers, while the (GT)₁₅ sequence should stay single-stranded and therefore serves as a negative control in this experiment. Using a quantitative PCR (qPCR) apparatus and the Sybr Green I dye, we performed melting curves on the (AT)₁₅ and (GT)₁₅ sequences as well as on the (AT)₁₅-SWCNT and (GT)₁₅-SWCNT complexes (**Figure C.29**). The melting temperatures of the DNA sequences and DNA-SWCNT complexes were determined by using the first derivative of the melting curves (**Figure C.29**). The (AT)₁₅ sequence exhibited a strong Sybr Green I signal and two melting temperatures around 49°C and 58°C, which would suggest the presence of two structures. The (GT)₁₅ sequence exhibited a much lower Sybr Green I signal, as expected, with a melting temperature around 42°C. This lower temperature could correspond to the denaturation of wobble base pairs within the sequence as previously reported [249]. For the DNA-SWCNT complexes, we did not observe any peak in the first derivative for the (GT)₁₅-SWCNT, which is indicative of the absence of any secondary structure on the SWCNT surface. However, we did observe a double peak around 32°C and 50°C, which would indicate the presence of two types of secondary structures on the SWCNT surface. This method could therefore be used to not only assay the presence of secondary structures on the SWCNT surface, but also to determine if different

types of structures exist and what are their melting temperatures.

3.5 Conclusion

In this study, we demonstrated the semi-rational design of DNA-SWCNT sensors for AFB1 and FB1 sensing. We systematically investigated the primary factors affecting the responses towards each mycotoxin, which include the overall base content of the sequence and position of the mutations introduced in the sequence. We engineered these factors based on derived design rule to optimize the responses of our sensors. In particular, we improved the sensor response towards AFB1 by increasing the G-content in the DNA sequence. We also observed that the response can be selective to a SWCNT chirality depending on the G-content, with higher G-contents resulting in increased (9,4)-selective responsivity. We further showed an increase in the G-content to result in an increase in SWCNT surface coverage, hence correlating the AFB1 response with surface coverage. Moreover, G4 secondary structures were observed for G-contents exceeding 80 %, leading to further increases in surface coverage and sensor response. We demonstrated that the newly designed sensors could react to the ZEN toxin, also capable of interacting with the SWCNT surface, but not to the ANG and COU targets hence suggesting that a threshold in interaction energy would be required to induce a shifting response.

In parallel, we also found that the response towards FB1 depends on the location of the mutated base in the sequence. More specifically, we showed that the response can be improved by mutating the sequence between the position 7 and 14 (from 5' to 3'). Based on this finding, we generated a mutant library by confining our mutations to these positions, allowing us to decrease the library size for screening. From this first round of mutagenesis, we selected the R1_{9,2} mutant that exhibited a significant increase in the FB1 response compared to the F-3 sensor. Interestingly, this mutant could not be further improved over additional rounds of mutagenesis on the positions 7 to 14, even through the introduction of neutral mutations. In order to elucidate the role of this part of the sequence for FB1 sensing, we investigated possible relationships between the FB1 response and various other properties of the mutants such as binding affinity of the wrapping to SWCNT, SWCNT surface coverage and free DNA concentration. While we did not find any notable relationship between the parameters, surface coverage and free DNA concentration were found to minimally affect the FB1 response. Finally, the R1_{9,2} mutant was shown to not only exhibit increased FB1 response but also demonstrate better sensor reversibility. As with the AFB1 sensors, we generalized the use of our FB1 sensors for AAL TB and ZEN toxins. By comparing the structures of the compounds tested, we hypothesize that the response is modulated by the strength of the interaction between the toxins and DNA.

While in our previous work, we demonstrated the use of directed evolution to create DNA-SWCNT sensors for AFB1 and FB1 sensing from scratch, here we identify and apply specific design rules for improving these sensors. In addition, we show that these guidelines are valid

not only for the AFB1 and FB1 but also for other targets with a similar interaction mode, either *via* interaction with the SWCNT surface directly or *via* the DNA wrapping. These findings carry with them major implications on the discovery of new DNA-SWCNT sensors based on similar interaction mechanisms. In particular, analytes could be tested against the families of AFB1 or FB1 sensors based on their structural characteristics, and the sensors can be further engineered either based on the factors listed in this study or through directed evolution in order to improve sensitivity or selectivity. A starting sensor for the evolution could therefore be found without the need for an initial random library search, hence greatly limiting the necessary screening size. In addition, as AFB1 and FB1 sensor families are characterized by their specific interaction modes, the sensors could be used as an indirect way to determine the interaction of the target analyte with the DNA-SWCNT.

Finally, future work should be oriented towards improved characterization of the toxin-sensor interaction in order to identify additional design rules on improving sensitivity and selectivity. For example, the characterization of secondary structures on the SWCNT surface could be achieved using melting curves. Moreover, computational approaches such as machine learning could be used to predict design rules based on our previous findings. With the emergence of new characterization techniques for the DNA-SWCNTs, we expect to gain a better understanding of the DNA-SWCNT structure, therefore allowing one to relate the DNA sequence, the DNA wrapping conformation and the DNA-SWCNT behavior. These possibilities could eventually lead to the complete rational design of DNA-SWCNT sensors, enabling researchers to exploit the under-utilized potential of these nanomaterials for diverse sensing applications.

4 Modulating the properties of DNA-SWCNTs through DNA chemical modification

Portions of this chapter are reproduced with permission from [144]: Lambert B.P.; Gillen A.J.; Antonucci A.; Molina-Romero D.; Boghossian, A.A. Modulating the properties of DNA-SWCNT sensors using chemically modified DNA, bioRxiv (2021). My contribution in this study includes: sample preparation, sample testing, data analysis and writing.

4.1 Abstract

Properties of DNA-SWCNT complexes such as brightness and sensing capabilities strongly depend on the characteristics of the wrapping used to suspend the nanotubes. Although it is possible to modulate the properties of the complexes by altering the DNA sequence as we showed in the previous chapters, the performances of the DNA-SWCNTs remain ultimately restricted by the inherent limits of the complexes. In this fourth chapter, we explored ways to modify the properties of DNA-SWCNT sensors beyond DNA sequence modulation by using chemically-modified DNA sequences, with the aim of creating sensors more suitable for use in *in vivo* applications. We demonstrated that the incorporation of chemical modifications in the DNA sequence can result in an enhancement of the DNA-SWCNT fluorescence intensity. We attributed these improvements mainly to both a change in dispersion efficiency as well as to a change in SWCNT chirality distribution. We also observed that the effect of the chemical modifications was different depending on the DNA sequence as well as on the method used for the preparation of the DNA-SWCNT complexes. We further showed that the modified complexes showed similar analytes selectivities as the unmodified DNA-SWCNTs, but exhibited a decrease in the magnitude of the turn-on response. The intensity increases achieved for the modified complexes could therefore allow a monitoring of analytes at deeper imaging depths in *in vivo* environments.

4.2 Introduction

Single-walled carbon nanotubes (SWCNTs) are particularly interesting for the creation of optical biosensors. Their near-infrared fluorescence is located within the first and second biological windows [23], where biological tissues absorb minimally [27], facilitating their use for *in vivo* applications. Moreover, the fluorescence of SWCNTs benefits from an indefinite photostability [26] and a high sensitivity [24]. DNA-wrapped SWCNTs (DNA-SWCNTs) are commonly considered for the creation of biosensors because of their long-term stability [56], biocompatibility [35] and, more importantly, their versatility allowing to create sensors towards a wide range of targets [32, 58, 130, 134].

Despite their many advantages, the DNA-SWCNTs also exhibit low fluorescence quantum yields (QYs), much lower than surfactant-suspended SWCNTs [78, 114], therefore limiting their applicability in deep-tissue applications. Several approaches have been proposed in order to improve the QYs of DNA-SWCNTs, by optimizing the dispersion conditions [137–139], chemically-modifying the SWCNT surface [145–148], or through the addition of exogenous compounds [112, 152–155]. Yet, these methods may affect the response capabilities of the sensors [112, 135, 149, 156] and could affect their biocompatibility *in vivo* [157, 158]. Alternatively, as the properties of the DNA-SWCNT complexes depend on the DNA sequence, approaches have also relied on the modulation of the DNA sequence in order to improve the QYs of the DNA-SWCNTs. This was particularly demonstrated by the directed evolution of DNA-SWCNT sensors, which is based on iterative steps of DNA-SWCNT library generation by DNA mutation, and subsequent screening and selection of the best performing DNA-SWCNT complexes [125]. Using this approach, it was possible to significantly improve the fluorescence properties of DNA-SWCNT sensors, while minimally affecting the other properties of the complexes. This approach was also shown to be effective for the engineering of other attributes such as the sensing capabilities of the DNA-SWCNTs (see **Chapter 2**).

Nonetheless, all existing DNA-SWCNTs are ultimately restrained by the inherent limits and performances natural DNA oligonucleotides. Indeed, even the most optimized DNA-SWCNT sensors may never match the fluorescence quantum yields (QYs) of surfactant-suspended SWCNTs [78, 114] or the selectivities of protein-suspended SWCNT sensors [52, 81]. To reach beyond the limits of the DNA-SWCNT complexes, one can change the characteristics of the DNA by altering its building blocks. This change, for example, can be achieved using xeno nucleic acids (XNAs) that exhibit modified nucleotides [1]. The use of these XNAs was recently demonstrated on DNA-SWCNTs in order to decrease the impact of salts on the properties of the complexes [113, 250].

In this study, we propose to introduce chemical modifications in the DNA sequence in order to alter the fluorescence properties of the DNA-SWCNT complexes. We introduced functional groups in the (AT)₁₅, (GT)₁₅ and N₃₀ DNA sequences and examined the effect these groups on the properties of the DNA-SWCNT complexes such as dispersion efficiency and quality, fluorescence intensity, and sensor response to analyte. We investigated the effects of two

types of functional groups, amino and azide, and the effect of their position in the DNA sequence. We observed a strong dependence of the DNA sequence and preparation method on the effect of the modifications. Through the introduction of chemical modifications, we showed that it is possible to significantly enhance the fluorescence intensity of complexes, such as (AT)₁₅-SWCNTs, which may not be easily improved by mutagenesis. In addition, this increase in intensity was achieved without losing the sensing capabilities of the sensors towards dithiothreitol (DTT) or dopamine, hence theoretically enabling more efficient sensing *in vivo*. These findings therefore demonstrate a new approach for tuning the properties of DNA-SWCNTs without alterations of the DNA sequence or requiring the addition of any exogenous compounds.

4.3 Materials and methods

4.3.1 Materials

All DNA oligomers were purchased from Microsynth AG. Purified CoMoCAT SWCNTs were purchased from CHASM Technologies, Inc. (SG65i, batch LOT No. SG65i-L59). Chemicals were purchased from Sigma-Aldrich, unless otherwise specified.

4.3.2 Instruments

Absorbance spectra were recorded using a UV-3600 Plus spectrophotometer (Shimadzu) with quartz suprasil cuvettes (Z600393, Hellma Analytics). Fluorescence emission spectra were acquired using a custom-built optical set-up with an inverted Nikon Eclipse Ti-E microscope (Nikon AG Instruments), as described previously [81]. Briefly, samples were excited using a supercontinuum laser coupled with a tunable filter unit (SuperK Extreme EXR-15 and SuperK VARIA, NKT Photonics). The fluorescence signal was collected using an IsoPlane SCT-320 spectrometer (Princeton Instruments) coupled to an InGaAs NIR camera (NIRvana 640 ST, Princeton Instruments). Measurements were recorded with LightField (Princeton Instruments) in combination with a custom-built LabView (National Instruments) software for automation purposes.

4.3.3 Preparation of the SWCNT suspensions

Suspensions of purified CoMoCAT (Sigma Aldrich SWeNT SG65i, batch MKBN5945V) SWCNTs were prepared using two different methods: direct sonication and surfactant exchange. All DNA-SWCNT suspensions were stored at 4°C between measurements in order to mitigate aggregation of the SWCNTs. Three DNA sequences were used in this study, (GT)₁₅, (AT)₁₅, and N₃₀, with or without chemical modifications (see **Table D.1** for more information on the modifications used). The N₃₀ sample is a mixture of random 30 nucleotides-long DNA sequences. The concentrations for all samples were calculated using an extinction coefficient

Chapter 4. Modulating the properties of DNA-SWCNTs through DNA chemical modification

$\epsilon = 0.0253 \text{ L.cm}^{-1}.\text{mg}^{-1}$ at 739 nm [81]. All nanotube suspensions were diluted to 33 mg/L unless otherwise specified.

Sodium cholate (SC)-suspended SWCNTs used for the surfactant exchange protocol were prepared by mixing 25 mg of CoMoCAT SWCNTs to 25 mL of 2 % (w/v) SC solution. The mixture was homogenized for 20 min at 5,000 rpm (Polytron PT 1300 D, Kinematica) and subsequently sonicated using probe-tip sonication (amplitude 10, 1/4 in. tip, Q700 Sonicator, Qsonica) for 60 min in an ice bath. The resulting solution was centrifuged at 30,000 rpm for 4 h at 20°C (Optima XPN-80 Ultracentrifuge, Beckman) to remove any remaining nanotube aggregates. The surfactant exchange was a modified version of the protocol developed previously [125]. 400 μL of SC-SWCNTs were mixed with 400 μL of DNA solution (75 μM in DI water). The same SC-SWCNT stock was used for all suspensions to ensure a similar starting distribution of nanotube chiralities and lengths for all samples. DNA concentrations were measured and adjusted based on absorbance measurements (Nanodrop 2000, Thermo Scientific). 1.2 mL of methanol (VWR Chemicals) was added to the DNA and SC-SWCNT mixture to obtain a final solvent percentage of 60 % (v/v) and a final DNA concentration of 15 μM (**Figure D.1**). The solution was vortexed briefly to mix and subsequently incubated for 2 h at room temperature. Following the incubation, the methanol, surfactant, and unbound DNA were removed by filtering the solutions according to the procedure detailed below.

DNA-CNT prepared by sonication were prepared by mixing 1 mg of CoMoCAT SWCNTs to 1 mL solution of DNA (100 μM in DI water, Microsynth) and sonicated (amplitude 1, cuphorn, Q700 Sonicator, Qsonica) for 90 min in an ice-bath. This was followed by a 4 h centrifugation step (5424R, Eppendorf) at $21,130 \times g$ and 4°C to remove SWCNT aggregates. The supernatant of the suspensions (≈ 80 % of the solution) was extracted and subsequently filtered, as detailed below, to remove any impurities and unbound DNA from the solution.

4.3.4 Amicon rinsing for DNA-SWCNT purification

In order to remove impurities (such as remaining catalyst particles), surfactant, methanol and unbound DNA from the DNA-SWCNT suspensions, all solutions were purified using Amicon centrifugal ultra-filtration devices (Amicon Ultra-2 100 kDa, Merck). Prior to use, the filtration devices were rinsed two times with DI water. The of DNA-SWCNT suspensions were subsequently added to the filtration device and rinsed eight times with 1 mL DI water by centrifuging at $3,000 \times g$ 4°C for 2 min for each rinsing step. The rinsed suspensions were collected from the filtration device and centrifuged for a minimum of 1 h at $21,130 \times g$ and 4°C to remove any additional SWCNT aggregates that may have formed during the rinsing process.

4.3.5 Photoluminescence measurements

An exposure time of 5 s and laser excitation with bandwidth of 10 nm and relative power of 100 % was used for all measurements, unless stated otherwise. Fluorescence emission spectra

were collected at wavelengths between 900 nm and 1400 nm using a dispersive grating of 75 lines.mm⁻¹. All experiments were performed in 384-well plates (Nunc Maxisorp, Thermo Scientific) with 50 µL aliquots of DNA-SWCNT solution. The plates were sealed (Empore Sealing Tape Pad, 3M) prior to each fluorescence measurement to prevent evaporation. Photoluminescence excitation (PLE) maps were acquired between 500 nm and 800 nm using a 5 nm step and 5 s exposure time. Additional samples were used to acquire fluorescence emission spectra for the (6,5) chirality and (7,5) chirality, under 575 and 660 nm excitations respectively. All spectra were normalised to the concentration determined at 739 nm (Varioskan LUX, Thermo Fisher) Results were analysed using a custom Matlab code (Matlab R2017b, Mathworks) for the PLE maps, and custom Python codes for spectra at 575 and 660 nm as described previously [227].

4.3.6 Analyte detection assay

Fluorescence spectra were initially acquired for all DNA-SWCNT solutions (49.5 µL) in a 384-well plate using a laser excitation of 575 nm. Following the initial measurement, 0.5 µL of analyte solution was added to the SWCNT suspension. Solutions were mixed by pipetting up and down several times. The suspensions were incubated for 10 min at room temperature in the dark prior to recording the second fluorescence spectrum. The solutions of dopamine hydrochloride were freshly prepared in DI water immediately prior to measurement.

4.3.7 Surfactant replacement assay

Surfactant replacement of the DNA-SWCNT solutions was performed using 1 % (w/w) sodium deoxycholate (SDC). For the fluorescence measurements, 5 µL of SDC was mixed with 45 µL DNA-SWCNTs and incubated at room temperature for 10 min. Fluorescence spectra were acquired before and after SDC addition using an excitation of 575 nm. For the absorbance measurements, SDC replacement samples were prepared by mixing 90 µL of SWCNT solution with 10 µL of SDC 1 % (w/w). Spectra for the samples were collected prior to addition and following a period of 10 min incubation post-addition.

4.3.8 Confocal Raman microscopy

Samples were prepared for Raman microscopy by drop casting 10 µL of DNA-SWCNT solution (10 mg/L) onto cleaned glass slides (Coverslip 24×55×0.15 mm, Fisher Scientific). Raman spectra were recorded at an excitation wavelength of 532 nm at 100 % relative power with 5 s exposure time. The spectrometer was calibrated before measurements using an internal standard. Spectra were collected between 100–2750 cm⁻¹ using a water-immersion 100X objective on a confocal spectroscope (inVia Raman Microscope, Renishaw) with a grating of 1,800 lines.mm⁻¹.

4.3.9 Gel electrophoresis

DNA-SWCNT were diluted to a concentration of 1 mg/L and the DNA wrapping was extracted by phenol-chloroform isoamyl (PCI) extraction. For that, 300 μ L of DNA-SWCNT suspension was mixed with 300 μ L of PCI solution (25:24:1, Sigma-Aldrich) and vortexed for 30 s. The solution was incubated 5 min at room temperature and centrifuged at $16,000 \times g$ for 5 min at room temperature. The aqueous top phase was collected ($\approx 265 \mu$ L) and the DNA was subsequently precipitated by ethanol precipitation in the presence of 0.3 M sodium acetate and 1 mg/mL glycogen (Carl Roth). The DNA pellet was washed with 70 % ethanol to remove salts, pelleted again and finally resuspended in 10 μ L of DI water. Extracted DNA was mixed with equal volumes of 2X formamide loading buffer. The samples were denatured by incubating the mixture at 95°C for 5 min and immediately quenching it on ice before loading the solution onto the gel. The samples were run on a denaturing 15 % urea-polyacrylamide gel in 1X Tris-Borate-EDTA (TBE) buffer at 200 V for 1 h. Three dilutions (1X, 0.5X, and 0.2X) were run for each DNA sequence. Sybr Gold dye (0.2X, Thermo Fisher) was used to stain the DNA. Fluorescence was recorded following 30 min of staining on a blue-light gel image (E-Gel, Thermo Fisher).

4.3.10 DNA quantification

Because of the important losses of DNA observed when using the PCI extraction technique, we used another method based on the replacement of the DNA wrapping by the sodium dodecylbenzenesulfonate (SDBS) surfactant in order to extract the DNA wrapping from DNA-SWCNT samples. For that, 40 μ L of the DNA-SWCNTs suspension (10 mg/L) was mixed with 10 μ L 10 % (w/w) SDBS and 50 μ L DI water. The mixture was incubated at 50°C for 1 h with gentle shaking (300 rpm, Thermomixer C, Eppendorf) to allow complete replacement of the DNA wrapping [115]. The DNA was further precipitated by ethanol precipitation in the presence of 0.3 M sodium acetate and 1 mg/mL glycogen (Carl Roth). The DNA pellet was washed with 70 % ethanol to remove salts and finally resuspended in 30 μ L of DI water. The DNA concentration was estimated by using the fluorescence of the Sybr Gold dye. For that, 2 μ L of extracted DNA was added to 97 μ L DI water and 1 μ L 100X Sybr Gold in 1X Tris-Acetate-EDTA (TAE) buffer. The dye was excited at 495 nm (Varioskan LUX, Thermo Fisher) and the fluorescence spectra obtained between 515 and 565 nm (100 ms exposure) were integrated for comparison.

4.4 Results and discussion

Modified DNA sequences were chemically synthesized to contain amino or azide functional groups (**Figure 4.1**, **Figure D.1**). We also tested sequences containing a thiol functional group (**Figure D.2**), however we observed the formation of disulfide bonds as evidenced by the presence of DNA dimers in gel electrophoresis (**Figure D.3**). As a result, thiol-modified DNA sequences were excluded from this study in order to ensure accurate comparisons between the functionalized sequences. To investigate the impact of the location and number of modifi-

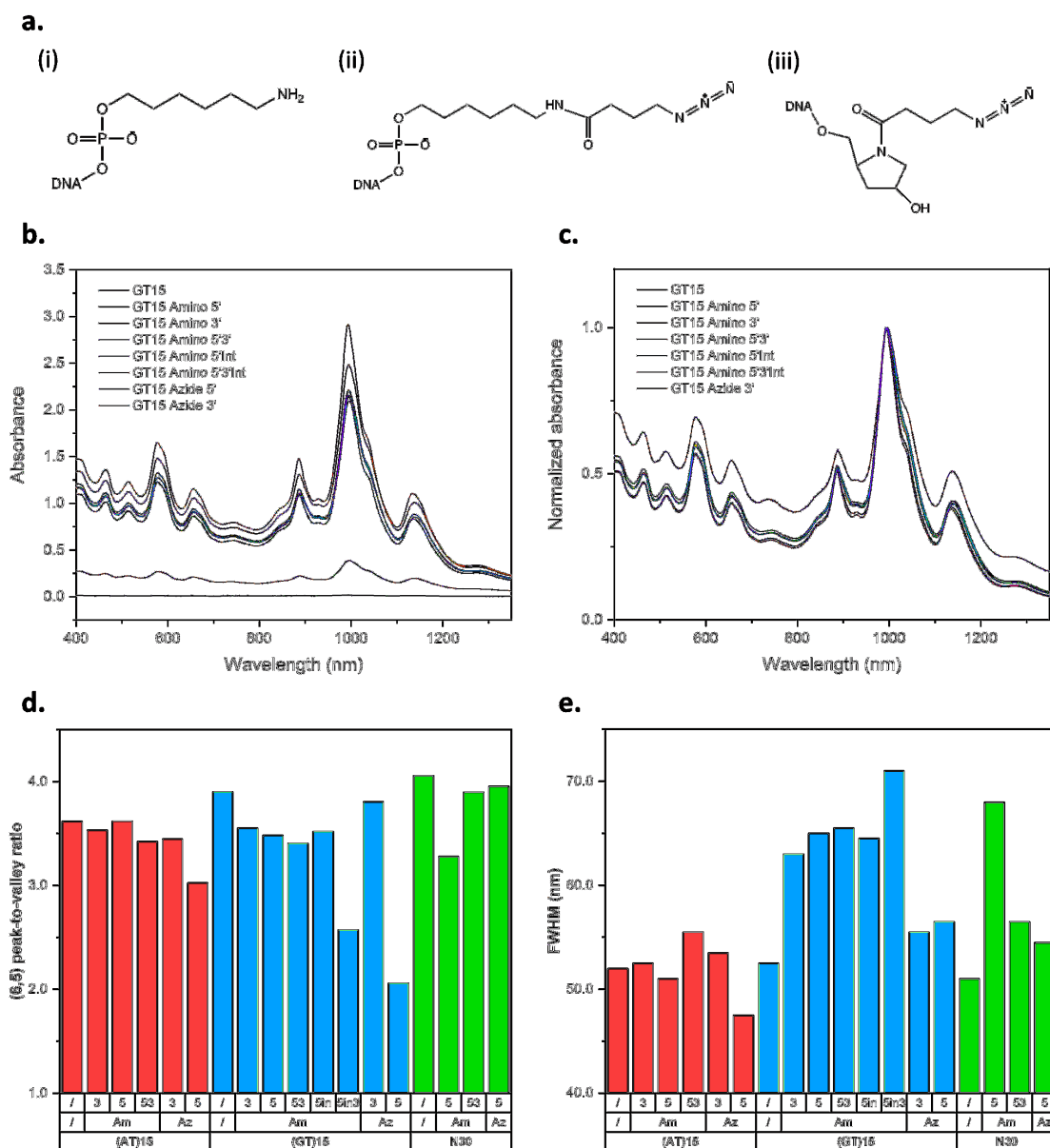


Figure 4.1 – Effect of the modifications on the dispersibility of the DNA-SWCNTs. (a) Chemical structure of the functional groups and linker molecules used for the terminal DNA modifications: (i) amino (5' or 3'), (ii) azide 5' and (iii) azide 3'. (b) Absorbance spectra and (c) absorbance spectra normalized to the (6,5) E_{11} absorption peak for the unmodified and modified (GT)₁₅-SWCNT complexes. (d) Peak-to-valley ratio and (e) full width at half maximum (FWHM) for the (6,5) E_{11} absorption peak for the unmodified and Amino (“Am”) or Azide (“Az”) -modified (AT)₁₅- (red), (GT)₁₅- (blue) and N₃₀-SWCNT (green) complexes. The numbers above the modification type indicate the position of the modification: 5' (“5”), 3' (“3”), 5' and 3' (“53”), 5' and interior (“5in”) and 5', 3' and interior (“5in3”). We define the valley as the minimum in absorbance around 1100 nm.

cations on the properties of the DNA-SWCNTs, modifications were inserted either at the 5' or 3' end of the DNA sequence, or in the middle of the sequence (referred as *Int*, **Figure D.2**). We

Chapter 4. Modulating the properties of DNA-SWCNTs through DNA chemical modification

tested the effect of functional groups in three different 30 nucleotides-long DNA sequences: (GT)₁₅, (AT)₁₅ and N₃₀. Because of its high prevalence in neurotransmitter sensing, both *in vitro* and *in vivo* [28, 34], the (GT)₁₅ sequence was considered as the main sequence of interest and was therefore tested with all chemical modification's combinations. The (AT)₁₅ sequence was used because of its distinct sensing properties compared to the (GT)₁₅ sequence [57, 58, 60], therefore allowing to investigate the effect of chemical modifications on analyte selectivity. Finally, the N₃₀ sample, a combination of 30 nucleotides-long sequences of random base composition, was used as a control in order to examine the importance of the DNA sequence on the effect of chemical modifications. Details on the modifications and sequences examined during this study are included in **Table D.1**.

The DNA-SWCNTs were prepared by wrapping exchange on CoMoCAT SWCNTs. In order to only account for the effect of the DNA wrapping, we removed the free DNA by centrifugal filtration. All DNA sequences were able to suspend the SWCNTs, as evidenced by the distinct bands in the absorbance spectra and low background (**Figure 4.1**, **Figure D.4**) [69]. Variations in the dispersion efficiency were observed depending on both the modification and the sequence, as evidenced by large differences in the absorbance spectra (**Figure 4.1**). To further compare the samples, the peak-to-valley ratio and full-width at half maximum (FWHM) for the (6,5) absorption peak were used to compare the quality of the suspensions (**Figure 4.1**), indicative of the relative amounts of impurities and aggregates in solution [69, 251]. A suspension of better quality is hence characterized by a higher peak-to-valley ratio and a lower FWHM. In the case of the (GT)₁₅ and (AT)₁₅ sequences, the unmodified samples resulted in the most concentrated dispersions and best suspension quality while the Amino 5'Int3', for the (GT)₁₅ sequence, and Azide 5' modifications resulted in remarkably low concentration suspensions and poor suspension quality. For the Amino 5'Int3' sample, we attribute this effect to the presence of too many modifications in the sequence compared to the other amino-modified samples, while the different behaviors observed between the Azide 3' and Azide 5' samples could be explained by the difference in linker molecule (**Figure 4.1**, **Table D.1**). In contrast, the N₃₀ sequence exhibited a different trend, with the Azide 5' sample resulting in a more concentrated dispersion than the unmodified sample. These observations suggest that the introduction of functional groups in the DNA sequence has an effect on the efficiency of the wrapping exchange process and that this effect would depend strongly on the DNA sequence. Such variations could additionally stem from the free DNA removal as some samples exhibited significant aggregation post-filtration.

We then monitored fluorescence under 575 and 660 nm excitations for solutions of equal concentration and compared the intensities of the (6,5) and (7,5) chiralities (**Figure 4.2**, **Table D.2**). We first noted strong variations in intensities between the various sequences. Overall, the (AT)₁₅-SWCNTs exhibited higher intensities compared to both the (GT)₁₅-SWCNTs and N₃₀-SWCNTs, in particular for the (7,5) chirality for which the intensity of the (AT)₁₅-SWCNTs was more than two times that of (GT)₁₅-SWCNTs (**Table D.2**), in accordance with previous observations (**Figure A.2**). In addition, we observed differences in the fluorescence behaviour of the samples depending on both the number and type of modification. For the

(GT)₁₅-SWCNTs, all modifications resulted in a decrease in intensity, except for the Azide 3' modification which exhibited a significantly higher intensity for both the (6,5) and (7,5) chiralities by $19.5 \pm 12.9\%$ and $27.9 \pm 14.9\%$ respectively (**Table D.2**). For the (AT)₁₅-SWCNTs, we noted an increase in intensity for the Amino 3' and Amino 5' modifications for both SWCNT chiralities. More specifically, the Amino 5' exhibited a significant increase intensity of $8.6 \pm 4.5\%$ and $13.9 \pm 5.5\%$ for the (6,5) and (7,5) chiralities (**Table D.2**). This finding is particularly interesting as only a few of the previously tested analogues of the (AT)₁₅ sequences exhibited fluorescence intensities higher than that of the (AT)₁₅-SWCNTs ([57], **Figure A.3**). On the other hand, the Azide 3' and the Amino 5'3' modifications resulted in either no change or a decrease

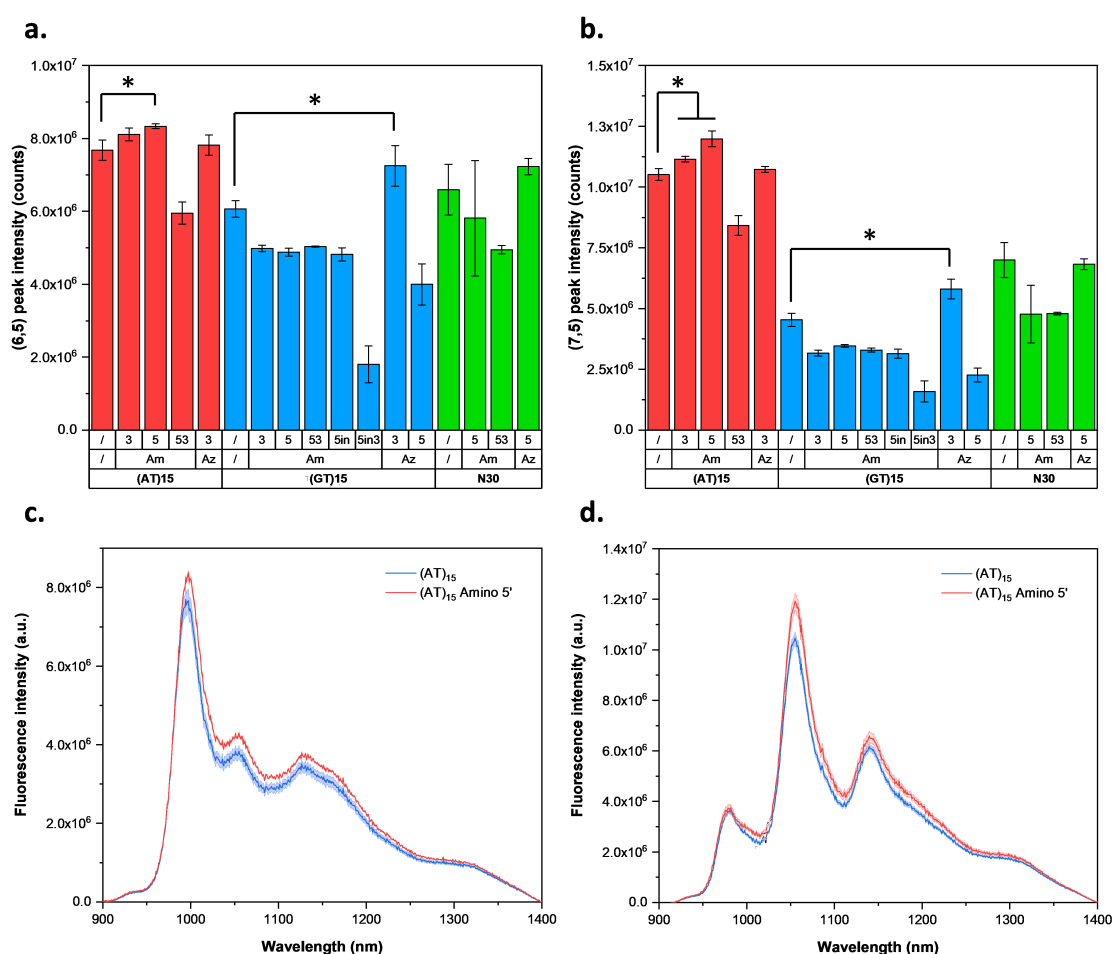


Figure 4.2 – Effect of the modifications on the fluorescence of the DNA-SWCNTs. Intensity of the emission maxima of (a) the (6,5) and (b) the (7,5) chiralities for the unmodified and Amino (“Am”) or Azide (“Az”) -modified (AT)₁₅- (red), (GT)₁₅- (blue) and N₃₀-SWCNT (green) complexes. The numbers above the modification type indicate the position of the modification: 5' (“5”), 3' (“3”), 5' and 3' (“53”), 5' and interior (“5in”) and 5', 3' and interior (“5in3”). The symbol * indicates a significant difference between the means for $p < 0.05$ (two-sample t-test, $n = 3$). Fluorescence spectra under (c) 575 nm and (d) 660 nm excitations for the (AT)₁₅- (blue) and (AT)₁₅ Amino 5'-SWCNT (red) complexes. The error bars and error shadings correspond to 1σ ($n=3$).

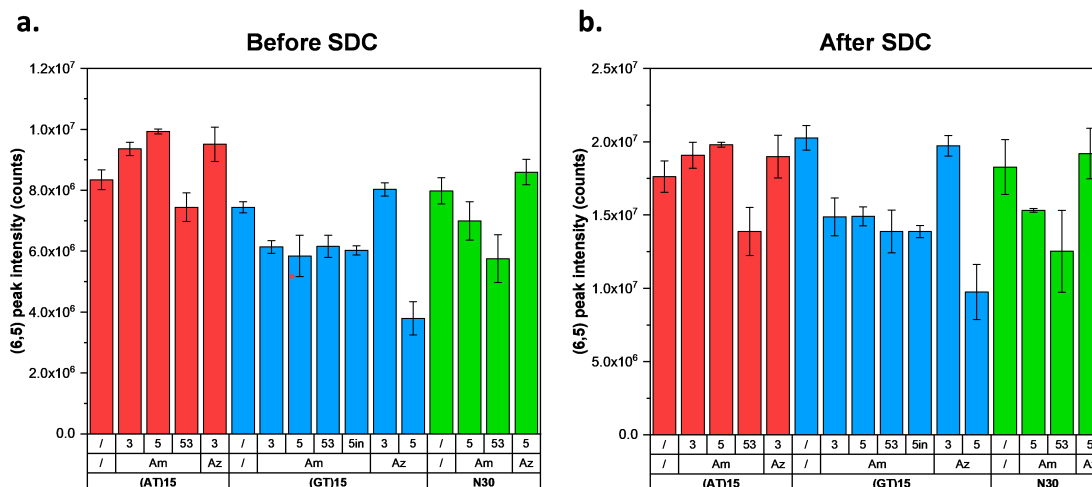


Figure 4.3 – Comparison of the intensities after wrapping replacement with SDC. Intensity of the (6,5) emission peak (a) before and (b) after wrapping replacement with 0.1 % SDC for the unmodified and Amino (“Am”) or Azide (“Az”) -modified (AT)₁₅- (red), (GT)₁₅- (blue) and N₃₀-SWCNT (green) complexes. The numbers above the modification type indicate the position of the modification: 5’ (“5”), 3’ (“3”), 5’ and 3’ (“53”), 5’ and interior (“5in”) and 5’, 3’ and interior (“5in3”). The error bars correspond to 1 σ (n=3).

in fluorescence intensity. Lastly, for the N₃₀-SWCNT complexes, the modifications resulted in either fluorescence intensity decreases, or no significant changes in intensity for the Azide 5’ sample. These findings indicate that the presence of functional groups can significantly enhance the fluorescence intensities of the DNA-SWCNT complexes. Interestingly, all the sequences incorporating more than one modification exhibited fluorescence intensity decreases, hence suggesting that too many modifications could be detrimental to the properties of the complex. Moreover, the improvements in intensity were not specific to a certain type of functional group or position. Indeed, the (AT)₁₅-SWCNT complexes exhibited improvements with the incorporation of one amino group, either on the 3’ or the 5’ end, while the (GT)₁₅-SWCNTs exhibited intensity enhancements with the introduction of one azide group on the 3’ end. The lack of improvement for the N₃₀-SWCNT complexes, combined with the very distinct behaviors observed between the (AT)₁₅- and the (GT)₁₅-SWCNTs, indicates a strong sequence-specificity on the effect of the modifications.

To determine whether the increased fluorescence intensities were due to an increase in quantum yield (QY), we compared the fluorescence intensities of the solutions before and after the addition of 0.1 % (final concentration) sodium deoxycholate (SDC) (**Figure 4.3, Table D.3**), which shows preferential binding to SWCNTs compared to DNA [120]. After SDC addition, the fluorescence intensities of all samples increased and the emission peaks blue-shifted to the same final position, indicative of a total replacement of the DNA wrappings (**Figure D.5**). At the same concentration, SDC-suspended SWCNT complexes should exhibit the same fluorescence intensities as they possess equal QYs [125]. Interestingly, the peak intensities retained the same trends before and after SDC addition, therefore suggesting that the differences in fluorescence

intensities observed for the modified samples are mainly not due to a change in QY effect. The only exception would be the Amino 3'-modified (GT)₁₅-SWCNT complex, for which the intensity before SDC replacement was higher than the unmodified complex and was not significantly different from the unmodified complex post-replacement. The retained changes in intensity after SDC replacement could, instead, indicate a change in the SWCNT chirality distribution. The presence of modifications in the DNA sequence could favor the wrapping of specific chiralities, hence resulting in a greater proportion of (6,5) and (7,5) chiralities for the same overall SWCNT concentration. To verify this hypothesis, we performed photoluminescence emission (PLE) maps in order to analyse the fluorescence intensity distributions for all chiralities (**Figure D.6**, **Figure D.7**, **Figure D.8**). As we showed that the variations in intensities were not due to differences in QY, we considered that it was reasonable to compare the distribution of semiconducting SWCNTs by comparing their intensities on the PLE maps as previously done on surfactant-suspended SWCNTs [70]. We calculated the ratios of the intensities for the (6,5) and (7,5) chiralities with the sum of all intensities across the PLE maps as an estimate for the concentration of (6,5) and (7,5) SWCNTs. As the effect of modifications is sequence-specific, we plotted separately the evolution of peak intensities as a function of the intensity ratios for the (AT)₁₅ and (GT)₁₅ sequences (**Figure D.9**). For the (AT)₁₅-SWCNT complexes, the (6,5) intensity increased along with increasing intensity ratio indicating that the intensity modulation is likely linked to an enrichment in (6,5) chirality. Conversely, the (GT)₁₅-SWCNT complexes exhibited a decrease in (6,5) intensity with increasing intensity ratio, suggesting that the variations in intensity could be caused by another factor. As the (GT)₁₅-SWCNT complexes showed corresponding trends between changes in intensities and dispersion quality (**Figure 4.1**), we therefore believe that the dispersion quality could be the main cause for the observed variations in intensity. We further investigated if the increases in intensity observed could stem from a higher density of defects on the surface of modified DNA-SWCNT samples. We therefore performed Raman spectroscopy on the unmodified and modified DNA-SWCNT complexes (**Figure D.10**) and monitored the ratio of the D and G band intensities, previously used as a measure of the density of defect on the SWCNT surface [252]. With the exception of the Amino 5' modification for the N₃₀-SWCNT complexes, we observed a similar D/G ratio between the unmodified and modified samples, therefore suggesting a similar defect density across all the complexes.

We hypothesized that the modifications could change the interaction between the DNA and the SWCNT, therefore resulting in changes in chirality distribution and dispersion efficiency. To investigate this interaction, we compared the positions of the (6,5) peaks between the various samples (**Figure D.11**). We found that some of the modified complexes exhibited significant red-shifting of the emission, in particular for the (AT)₁₅-SWCNT complexes with Amino 5' and 5'3' modifications as well as for the N₃₀-SWCNT complex with Amino 5' modification. Moreover, we extracted DNA from the SWCNTs and estimated the concentrations of DNA wrapping by monitoring the fluorescence of the Sybr Gold DNA-specific dye (**Figure D.12**). We noted large variations in the fluorescence of the Sybr Gold dye. In particular, we observed a large decrease in Sybr Gold fluorescence for the modified (GT)₁₅ samples, in line with the

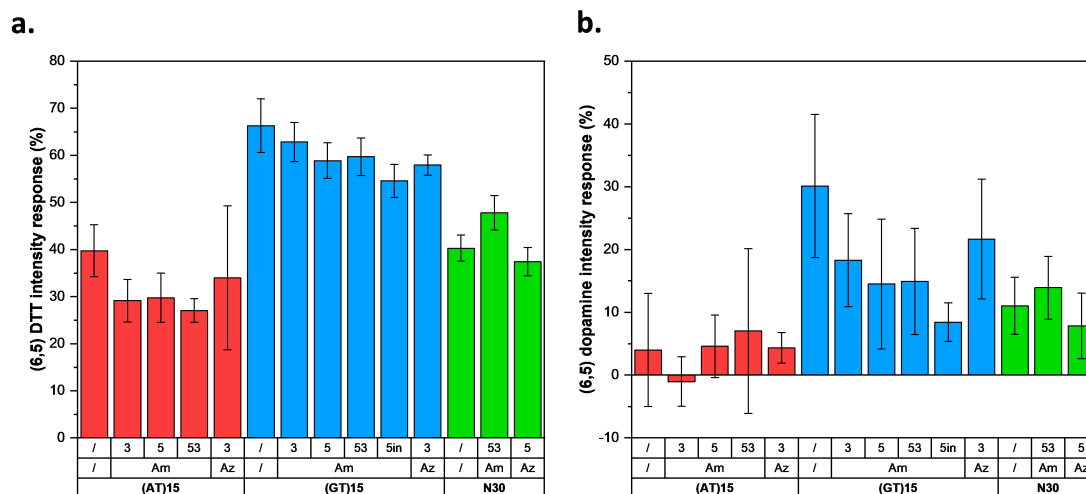


Figure 4.4 – Effect of the modifications on the sensing capabilities of the DNA-SWCNTs. Fluorescence intensity response for the (6,5) chirality upon (a) DTT and (b) dopamine addition for the unmodified and modified (AT)₁₅- (red), (GT)₁₅- (blue) and N₃₀-SWCNT (green) complexes. The response corresponds to $(I-I_0)/I_0$, with I_0 the intensity before addition. The error bars correspond to 1σ ($n=3$).

fluorescence and absorbance data, except for the Azide 3' sample. In addition, we noted increases in Sybr Gold fluorescence between the unmodified (AT)₁₅ sample and the Amino 3', 5'3' and Azide 3' samples. Although these observations do not correlate with the trends obtained for the fluorescence intensities, they show that the modifications can result in a change in the DNA wrapping and the interaction between the wrapping and the SWCNT.

Next, we examined the effects of the modifications on the sensing capabilities of the DNA-SWCNT complexes. We examined the fluorescence of the DNA-SWCNT complexes in the presence of the reducing agent DTT (**Figure 4.4, Table D.4**), which is known to result in a fluorescence intensity increase upon addition [150]. We observed an increase in intensity for all DNA-SWCNT complexes, with a decrease in response for both modified (AT)₁₅- and (GT)₁₅-SWCNT complexes, regardless of the type of functional group and position, compared to their unmodified counterparts (**Figure 4.4, Table D.4**). Interestingly, the decrease in response was not linked to the variations observed in fluorescence intensities. We then examined the effect of the modifications on the selectivity of the sensors by monitoring the response of the various DNA-SWCNT complexes in presence of dopamine (**Figure 4.4, Table D.5**). Multiple studies have previously reported that (GT)₁₅-SWCNT complexes exhibited a large increase in fluorescence intensity upon addition of dopamine [58, 60]. In accordance with these observations, we noted a $30.1 \pm 11.4\%$ increase in fluorescence intensity (**Table D.5**) for the unmodified (GT)₁₅-SWCNT complexes. For the modified (GT)₁₅-SWCNTs, we also observed an increase in fluorescence intensity upon dopamine addition, although lower than for the unmodified complexes (between 8.4 and 21.7 %, **Table D.5**). On the other hand, (AT)₁₅-SWCNT complexes, both modified and unmodified, showed no overall significant intensity change upon dopamine change, in accordance with previous reports [58, 60]. These observations

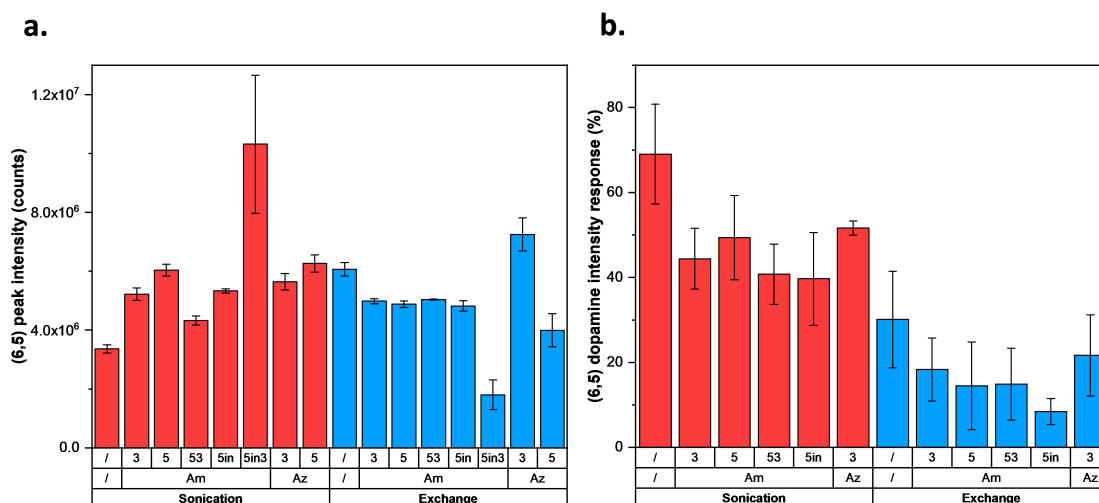


Figure 4.5 – Importance of the preparation procedure on the effect of the modifications. (a) Intensity of the (6,5) emission peak and (b) fluorescence intensity change upon dopamine addition for the unmodified and modified (GT)₁₅-SWCNT complexes prepared by sonication (red) and exchange (blue). The response corresponds to $(I-I_0)/I_0$, with I_0 the intensity before addition. The error bars correspond to 1σ ($n=3$).

indicated that, although a decrease in dopamine response was observed for the modified samples, the modifications did not significantly affect the selectivity of the sensors, with the (GT)₁₅-SWCNT remaining more sensitive to dopamine than the (AT)₁₅-SWCNT complexes. In addition, all the N₃₀-SWCNT complexes exhibited a slightly lower dopamine response than the (GT)₁₅-SWCNT complexes, confirming the greater capability of (GT)₁₅-SWCNT complexes as dopamine sensors.

Finally, we also observed an influence of the preparation technique on the effect of the modifications. We compared the fluorescence intensities (GT)₁₅-SWCNT suspensions prepared by exchange, the approach used for the preparation of the samples discussed previously, and direct sonication (**Figure 4.5**, **Figure D.13**, **Table D.6**). We noted that while the modifications had mostly a negative effect on the intensity for the (GT)₁₅-SWCNTs prepared by exchange, the modified samples prepared by sonication all exhibited an increase in fluorescence intensity compared to the unmodified complex. Although we observed important increases in intensity for the Amino 5'Int3' sample prepared by sonication, this increase was disregarded on account of the low dispersion yield observed for this sample (**Figure D.15**). As for the exchanged samples, we observed that the intensity increases were not due to changes in QY (**Figure D.16**, **Table D.7**) but more related to variations in chirality distribution and dispersion quality (**Figure D.15**). We further tested the responses of the sonicated samples and noted a decrease in response for the modified samples, as was observed for the exchanged samples (**Figure 4.5**, **Figure D.20**, **Table D.9**). We also noted the response of the sonicated samples to be more than two times larger than that of the exchanged samples. We expect the differences in fluorescence intensity and response to stem from variations in DNA conformation, as previously reported

[143]. Although the intensities of the sonicated samples were initially lower than those of the exchanged samples, they could be improved by the introduction of chemical modifications that can retain the higher dopamine response of the sonicated samples. This approach could enable improved monitoring of neurotransmitters *in vivo*, with higher fluorescence intensities before and after dopamine detection compared the unmodified complex (**Figure D.21**).

4.5 Conclusion

In this work we examined the impact of chemically modified DNA sequences on the overall properties of DNA-SWCNT complexes including dispersion efficiency, fluorescence intensity and sensing capabilities. We showed that the effect of the modifications strongly depended on the DNA sequence as we observed distinct trends for the various modifications for the (AT)₁₅, (GT)₁₅ and N₃₀ sequences used in this study. In addition, we noted a strong dependence of the effect of the modifications on the method used for the preparation of the DNA-SWCNT complexes.

We demonstrated that these modifications can be applied to significantly enhance the fluorescence of DNA-SWCNT sensors, while minimally affecting their other properties. In particular, we observed significant increases in fluorescence intensity by up to 13.9 % and 27.9 % for both the Amino 5'-modified (AT)₁₅ and Azide 3'-modified (GT)₁₅-SWCNT sensors prepared by exchange respectively, and up to 136.5 % for Amino 3'-modified (GT)₁₅-SWCNT sensors prepared by sonication. We found that the observed increases in intensity more likely stem from changes in chirality distribution and dispersion quality rather than variations in the optoelectronic properties of the complexes such as QY. Although we observed a small decrease in response for the modified DNA-SWCNT sensors towards both DTT and dopamine, we also noted that the modified complexes retained a similar analyte selectivity with all (GT)₁₅-SWCNT sensors exhibiting a strong intensity increase in presence of dopamine and the (AT)₁₅-SWCNT sensors a lack of response.

Given the dependence on the DNA sequence and preparation technique, we hypothesized that the introduction of chemical modifications in the DNA sequence could alter the interaction between the DNA wrapping and the SWCNT. This hypothesis was further supported by the variations observed in peak positions and DNA wrapping concentrations. These modifications could therefore lead to changes in the DNA wrapping affinity with the SWCNT and the wrapping conformation, potentially justifying the alterations observed in chirality distribution, dispersion quality and analyte response.

In summary, these findings demonstrate a new approach for tuning the properties of specific DNA-SWCNT sensors. Through the introduction of chemical modifications, we demonstrated the ability to significantly enhance the fluorescence intensity of DNA-SWCNT complexes. In addition, this increase in intensity was achieved without losing the sensing capabilities of the sensors towards DTT or dopamine, hence theoretically enabling more efficient sensing *in vivo*. More importantly, these improvements in intensity were achieved without having

to modify the DNA sequence or requiring the addition of any exogenous compounds. The introduction of chemical modifications could therefore be used to further engineer sensors evolved by directed evolution beyond the inherent limits of the DNA-SWCNTs. Finally, future work should be focused on a better understanding of the dependence of the DNA sequence and preparation technique on the effect of the modifications in order to implement these modifications in a more rational manner.

5 Outlook on the directed evolution of DNA-SWCNTs with long oligonucleotides

Portions of this chapter are reproduced from the manuscript in preparation: Lambert B.P; Boghossian, A.A. Directed evolution of DNA-wrapped nanosensors with long oligonucleotides (2021).

5.1 Abstract

The previous chapters focused on the engineering of DNA-wrapped single-walled carbon nanotube (DNA-SWCNT) complexes formed with a specific DNA length. However, numerous studies reported the length, in addition to the sequence, of the DNA wrapping to be critical for engineering various properties of the complex. In this fifth chapter, we demonstrate the advantages of using longer oligonucleotides (up to 60 nucleotides) for improving both the optical and sensing properties of the complexes. Though the directed evolution approaches used in the previous chapter have only been demonstrated on complexes formed with short oligonucleotides (< 40 nucleotides), the extension of this approach to longer oligonucleotides could unlock a previously unexplored space for engineering new sensors. We herein propose a biologically-driven approach for the directed evolution of DNA-SWCNT complexes. We show that this approach could be used to create large libraries of DNA-SWCNT complexes even for long oligonucleotide lengths, which could lead to the discovery of more diverse and better performing sensors.

5.2 Introduction

Single-walled carbon nanotubes (SWCNTs) have attracted particular interest in the field of optical biosensing owing to their peculiar fluorescence properties. As the emission of SWCNTs lies in the near-infrared (NIR) range [23], the fluorescence can be monitored *in vivo* with minimal absorption from biological tissues [27]. In addition, SWCNTs benefit from an indefinitely photostable emission [26], exhibit high sensitivities to changes in their environment [24] and can be readily functionalized with a variety of wrapping molecules to

Chapter 5. Outlook on the directed evolution of DNA-SWCNTs with long oligonucleotides

modulate their optical and colloidal properties [114] as well as their affinity to various targets [78]. Among these wrapping molecules, DNA has been extensively used for the creation of sensors towards a wide range of targets [32, 57–59, 134, 135]. Because the properties of these DNA-wrapped SWCNTs (DNA-SWCNTs) are sequence-dependent, the discovery of new DNA-SWCNT sensors is typically done by screening libraries of complexes with varying sequences. However, the performances of these complexes are limited by the lack of knowledge on how the DNA sequence affects the properties of the complexes.

To overcome this bottleneck, we recently demonstrated the application of directed evolution to engineer DNA-SWCNT complexes [125]. Directed evolution is an approach initially developed for the engineering of proteins that builds on the assumption of a continuous structure-function relationship between the properties of a protein and its amino acid sequence [193]. As a result, directed evolution utilizes iterative mutation, screening, selection steps in order to identify variants of the starting protein sequence that exhibit improved functionality. When applied to DNA-SWCNTs, this approach has been shown to yield sensors with significantly improved optical [125] and sensing properties (see **Chapter 2**).

Although the properties of the DNA-SWCNTs were shown to depend on the sequence of the DNA wrapping, they were additionally shown to depend on the length of the DNA sequence. For example, DNA length has been shown to modulate the dispersion efficiency of the SWCNTs [54, 114, 253], the binding affinity of the DNA to the SWCNTs [120], the specificity towards certain SWCNT lengths [254, 255], the interaction of the complexes with living organisms [256] and the sensing properties of the DNA-SWCNTs [61, 257]. To engineer the properties of DNA-SWCNT complexes, one must therefore consider not only the sequence of the DNA wrapping but also its length. In this work, we demonstrate the use of longer oligonucleotides, up to 60 nucleotides, that can lead to significant improvements in optical and sensing properties. Directed evolution could therefore play a critical role in engineering sequences of this length, especially given the larger sequence space they bring with the increased combinations of possible DNA sequences.

The directed evolution of DNA-SWCNTs requires the creation of a library of DNA variants and the subsequent high-throughput wrapping of this DNA library onto SWCNTs. This strategy is highly effective for oligonucleotides shorter than 40 nucleotides, but impractical for longer sequences due to the low efficiency of the solid-state synthesis procedures that are used to create the DNA library. Namely, these procedures result in increased costs and decreased purity with increasing oligonucleotide length [258]. To address this challenge, we propose the use of a biologically-based approach to generate DNA libraries independently from the length of the DNA sequence, therefore allowing to perform directed evolution on DNA-SWCNTs with long oligonucleotides.

We created libraries of DNA variants *via* polymerase chain reaction (PCR), whose yield is largely independent of the DNA length. In this approach, the polymerase enzyme exponentially generates copies of a DNA template. To create a library of DNA variants, mutations can be

introduced in the sequence through modulation of the replication fidelity of the polymerase enzyme or by performing the PCR reaction on a random DNA template, as we demonstrate in this study. The DNA variants were individually separated by ligation into a plasmid and subsequent transformation into bacterial cells. The individual DNA variants were amplified from the cells by PCR and further purified. The final PCR products were suspended onto SWCNTs using a modified dimethyl sulfoxide (DMSO)-assisted wrapping exchange method. We demonstrated the strength of this approach by comparing the fluorescent properties of resulting DNA-SWCNT complexes suspended with DNA variants amplified from various cell colonies. Although additional work should be performed to improve the reproducibility of this technique, this technique nonetheless provides an important platform for the creation of DNA-SWCNT libraries with longer DNA sequences.

5.3 Materials and methods

5.3.1 Materials

All DNA oligomers were purchased from Microynth AG. Purified HiPco SWCNTs were purchased from NanoIntegris (Batch No. HP29-064). Super-purified HiPco SWCNTs were purchased from NanoIntegris (Batch No. HS37-007). All chemicals were purchased from Sigma-Aldrich, unless otherwise indicated. The Taq polymerase was purchased from Genscript. The pJET plasmid cloning kit (CloneJET) was purchased from Thermo Fisher. The mycotoxins were purchased from Enzo Life Sciences.

5.3.2 Instruments

Absorbance was measured using either a UV-3600 Plus spectrophotometer (Shimadzu) with quartz suprasil cuvettes (Z600393, Hellma Analytics) or a plate reader (Varioskan LUX, Thermo Fisher) with 96- (EIA/RIA, Corning) and 384-well plates (Maxisorp, Nunc). The SWCNT fluorescence was monitored on a previously described custom-made microscope [81]. Briefly, the system is built on a Nikon Ti-E inverted microscope body and illuminated by a super-continuum laser (SuperK Extreme EXR-15 and SuperK VARIA, NKT Photonics) in the 400-830 nm range. The fluorescence light between 900 and 1400 nm is diffracted and measured by an InGaAs detector (NIRvana 640 ST, Princeton Instruments) coupled to a spectrometer (IsoPlane SCT-320, Princeton Instruments) with a 75 lines.mm⁻¹ grating. The measurements are automatized with a custom LabVIEW (15.0f2, National Instruments) code. The individual fluorescence peaks were fitted with individual Lorentzian curves by a custom Matlab code (R2017b, MathWorks).

5.3.3 Preparation of the mutant library

The sequences used for the DNA length comparison were random sequences with length comprised between 6 and 60 nucleotides. The DNA used for the mycotoxin measurement experiments is the S5 sequence previously reported (see **Chapter 2**), 5'-GAG GGG AGG GAG AGG GAG GGG AGA GGA GTG-3'. Experiments were also performed with the longer version of the S5 sequence, the S5L sequence, 5'-GAG GGG AGG GAG AGG GAG GGG AGA GGA GTG GAG GGG AGG GAG AGG GAG GGG AGA GGA GTG -3'. The sequence used for the comparison of the methanol and DMSO denaturation and exchange procedures is the 36 nucleotides-long sequence T-(AT)₁₅: 5'-GAT CCA TAT ATA TAT ATA TAT ATA TAT ATA TAT ATG-3'. This sequence was hybridized before the experiments by first heating at 95°C for 2 min followed by incubation at room temperature for 2 h. The template used for the creation of the colonies and for the comparison of the DNA concentrations is the T-N₃₀ sequence: 5'-AA GAT CGT CGT **GGA TCC** GTA **GAA TTC** NNN NNN NNN NNN NNN NNN NNN NNN NNN **GAA TTC** ATC **GGA TCC** CGT CTC-3', a 30 nucleotides-long random random (N) sequence flanked by two primer binding sites of both 26 and 21 nucleotides for a total length of 77 nucleotides. Each primer binding site contained two restrictions sites, for BamHI (GGA TCC) and EcoRI (GAA TTC), indicated in bold. Unless otherwise indicated, all sequences were dissolved in DI water.

The final DNA samples were created using a total of 2 PCR reactions on the T-N₃₀ template. The first PCR was performed in a 20 μ L volume with each reaction containing 0.2 μ M forward (FP) and reverse (RP) primers (20 μ M stock solutions), 0.2 mM dNTPs, \approx 0.35 ng T-N₃₀ template and 1.5 unit of Taq polymerase. The reaction conditions were: (1) 95°C 2 min, 30 cycles of (2) 95°C 15 s, annealing temperature (T_A) 15 s, 72°C 5 s, (3) 72°C 1 min. Six T_A were tested: 52, 54, 56, 58, 60 and 62°C. The resulting PCR products were run on a denaturing polyacrylamide gel (urea PAGE) to confirm the efficiency of the reaction (**Figure E.1**). The 60°C product was selected and ligated into the pJET 1.2 plasmid vector (CloneJET, Thermo Fisher Scientific). For that, 2 μ L of PCR product was first blunt at 70°C for 5 min with 1 μ L of blunting enzyme (CloneJET, Thermo Fisher Scientific). The reaction mix was then ligated to 1 μ L of pJET vector with 5 units of T4 DNA ligase and incubated overnight at 16°C. 10 μ L of the ligated mixture was cloned into 200 μ L of DH5 α chemically competent cells through heat shock transformation. The cells were grown overnight at 37°C on a carbenicillin-containing agar plate. 96 colonies were hand picked and grown overnight in 1.2 mL LB medium supplemented with carbenicillin in a 96 deep-well plate, and incubated overnight at 37°C and 300 rpm. The DNA was extracted for the cells of the H2 and H3 wells using a Zyppy plasmid kit (ZYMO Research) and subsequently sequenced by Sanger sequencing (SupremeRun, GATC) (**Table E.1**). 15 colonies were selected from the well plate (A6, B3, B10, C5, C9, D1, D2, E12, F3, F7, G4, H2, H3, H9, H11) and a colony PCR was run on each of the samples. The PCR was performed in a 100 μ L volume with each reaction containing 1.25 μ M forward (FP) and reverse (RP) primers (100 μ M stock solutions), 0.4 mM dNTPs, 2 μ L colony and 2.5 unit of Taq polymerase. The reaction conditions were: (1) 95°C 3 min, 35 cycles of (2) 95°C 15 s, 60°C 15 s, 72°C 5 s, (3) 72°C 1 min. The resulting PCR products of the A6, B3 and H3 colonies were run on a urea PAGE to confirm the efficiency of the reaction (**Figure E.2**). 90 μ L of the PCR products were then purified and concentrated to

10 μL with 10 μL silica beads (QIAEX II kit, QIAGEN). As a control, 90 μL of solution containing 1.25 μM of both FP and RP (in DI water) was concentrated to 10 μL with 10 μL silica beads in the same conditions. The 10 μL of concentrated DNA solutions were then used for the preparation of DNA-SWCNT complexes using the DMSO-assisted exchange procedure as previously described. The DNA concentrations were measured by absorbance (Nanodrop 2000, Thermo Fisher). The concentrations of the colony DNA sequences were estimated by subtracting the total DNA concentration of the PCR products by the maximum concentrations of primers and dNTPs.

5.3.4 Gel electrophoresis

We analyzed our various DNA products by denaturing polyacrylamide (PAGE) gel electrophoresis. For that the DNA samples were mixed with equal volumes of 2X formamide loading buffer, further denatured by incubating the mixture at 95°C for 5 min and immediately quenched on ice before loading onto the gel. The samples were run on 15 % urea PAGE gel in 1X Tris-Borate-EDTA (TBE) buffer at 200 V for 1 h (Mini-PROTEAN Tetra Cell, Biorad). The gel was soaked in a staining solution (0.2X Sybr Gold final in 1X TBE) for a total of 30 min and imaged on a blue-light gel image (E-Gel, Thermo Fisher).

5.3.5 DNA quantification

In order to assay the effect of methanol and DMSO on the denaturation of DNA, we recorded the fluorescence of the Sybr Green I dye, which is specific to double-stranded DNA. For that, we first annealed the T-(AT)₁₅ self-complementary sequence by heating at 95°C for 2 min and left to cool down to room temperature for 2 h. The Sybr Green I batch was prepared fresh at a 100X concentration in 1X Tris-Acetate-EDTA (TAE) buffer. The measurements were performed by mixing 99 μL of sample with 1 μL of 100X Sybr Green I dye in a 96-well plate. The dye was excited at 490 nm and the emission between 510 and 560 nm was recorded with an exposure time of 100 ms.

5.3.6 Preparation of the SWCNT suspensions

The DNA-SWCNTs were prepared by wrapping exchange between sodium cholate (SC)-SWCNTs and the DNA as previously depicted [125]. The SC-SWCNT suspension was prepared by mixing 30 mg HiPco SWCNT purified powder with 30 mL 2 % (w/w) SC prepared in DI water. This mixture was homogenized at 5,000 rpm (Polytron PT 1300 D, Kinematica) at room temperature for 20 min, followed by an ultrasonication for 60 min (amplitude 10, 1/4 in. tip, Q700 Sonicator, Qsonica) in an ice bath (the ice was changed after 30 min). The resulting suspension was centrifuged for 4 h at 30,000 rpm at 25°C (SW32 Ti, Optima XPN-80, Beckman Coulter). The supernatant was collected and the concentration measured by absorbance spectroscopy using the extinction coefficient $\epsilon=0.036 \text{ L.cm}^{-1}.\text{mg}^{-1}$ at 632 nm [125]. The

Chapter 5. Outlook on the directed evolution of DNA-SWCNTs with long oligonucleotides

SC-SWCNT used for the preparation of the samples used for the mycotoxin experiments were prepared the same way as previously described using HiPco super purified powder (see **Chapter 3**).

The DNA solutions were dissolved in DI water and mixed to SC-SWCNT and methanol or DMSO at various volume ratios depending on the preparation (the methanol volume being fixed at 60 %), followed by an incubation for at least 1 h at room temperature. The DNA-SWCNTs were further purified to remove the free SC and methanol or DMSO. For that, 1.5 M NaCl was added to the mixture to a final concentration of 0.2 M, followed by the addition of 2.5 volumes of cold ethanol (kept at -20°C) and gentle mixing. The resulting suspension was incubated at -20°C and then centrifuged at 4°C. The supernatant was removed, and the SWCNT-containing pellet was washed with 70 % (v/v) ethanol and further centrifuged. The supernatant was discarded, and the pellet was air-dried at room temperature. The pellet was then resuspended in the desired volume of solvent and finally centrifuged again to remove aggregates. The supernatant of this suspension was collected and its concentration was estimated by measuring the absorbance in 384- or 96-well plates (Varioskan LUX plate reader, Thermo Scientific). Depending on the application, the preparation of the samples was different as indicated below:

- 1) The samples prepared for the DNA length comparison were prepared by using methanol-assisted exchange using a final DNA concentration of 10 μ M (15.5 % volume) and a SC-SWCNT with a final concentration of 31.4 mg/L (24.5 % volume), incubated at room temperature for 90 min, resuspended in DI water and were not further diluted. The sample processing was performed in a 384-well plate, the centrifugation steps were therefore 3,220 x g (5810R, Eppendorf).
- 2) The samples used for the mycotoxin measurements were prepared by using methanol-assisted exchange using a final DNA concentration of 10 μ M (20 % volume) and a SC-SWCNT with a final concentration of 21.6 mg/L (20 % volume), incubated at room temperature for 120 min, resuspended in 0.1 M NaCl and diluted to a final concentration of \approx 7.4 mg/L. The sample processing was performed in 1.5 mL tubes, the centrifugation steps were therefore 21,130 x g (5424R, Eppendorf).
- 3) The samples used for the comparison of the methanol- and DMSO-assisted exchange were prepared by using a final DNA concentration ranging between 0.5 and 3 μ M (15 % volume) and SC-SWCNT with a concentration of 37.5 mg/L (25 % volume), incubated at room temperature overnight, resuspended in DI water and were not further diluted. The sample processing was performed in a 96-well plate, the centrifugation steps were therefore 3,220 x g (5810R, Eppendorf).
- 4) The samples prepared for the colony DNA samples were prepared by using DMSO-assisted exchange using an unknown final DNA concentration (20 % volume) and a SC-SWCNT with a final concentration of 25.6 mg/L (20 % volume), incubated at room temperature for 3 h, resuspended in DI water and were not further diluted. The sample processing was performed

in a 96-well plate, the centrifugation steps were therefore 3,220 x g (5810R, Eppendorf). The SWCNTs exchanged with the primer DNA sequences were prepared in the same way.

5) The samples used for the comparison of the intensities at different DNA concentrations for the DNA template were prepared by DMSO-assisted exchange with a final DNA concentration ranging between 1 and 22 μM (20 % volume) and SC-SWCNT with a concentration of 25.6 mg/L (20 % volume), incubated at room temperature for 3 h, resuspended in DI water and were not further diluted. The sample processing was performed in a 96-well plate, the centrifugation steps were therefore 3,220 x g (5810R, Eppendorf).

5.3.7 Surfactant replacement

The DNA wrapping was replaced using sodium deoxycholate (SDC) surfactant following a previously reported procedure [120]. The SDC was dissolved to a concentration of 1 % (w/w) in DI water. The fluorescence of 45 μL of DNA-SWCNT suspension was first monitored for 10 s with an exposure time of 1 s. The suspension was then mixed with 5 μL of 1 % (w/w) SDC in a 384-well plate and the fluorescence was monitored every 1 s for a total of 110 s at room temperature. The time constants of the wrapping replacement were determined by single the change in peak position by single exponential fits $y(t) = y_0 + A.e^{-\frac{t}{\tau}}$, with τ the time constant of the replacement.

5.3.8 Measurements

Fluorescence measurements were acquired with an exposure time of 5 s (unless otherwise specified), a laser power of 100 % and an excitation bandwidth of 10 nm. The (7,5) and (7,6) chiralities were excited with an illumination of 660 nm and the (9,4) chirality under an illumination of 745 nm. For the mycotoxin experiments, 0.5 μL analyte was added to 49.5 μL of DNA-SWCNT suspension in a 384-well plate. Measurements were performed before and after analyte addition. The photoluminescence emission (PLE) maps were performed with excitations ranging from 500 to 800 nm with a step of 5 nm and the fluorescence was recorded between 900 and 1400 nm.

5.4 Results and discussion

In this study, we investigated the effect of DNA length on the properties of the resulting DNA-SWCNT complexes. Although this investigation has already been explored in several past studies [61, 114, 120, 257], the characterizations were always done with specific sequences, typically (GT)-repeating sequences. As the DNA sequence can have a strong effect on the properties of the sensors [55, 58, 125], we expanded on these studies to explore the effect of DNA length with random sequences to eliminate any contributions from sequence-dependent bias. We wrapped a library of random DNA sequences with lengths between 6 and 60 nucleotides,

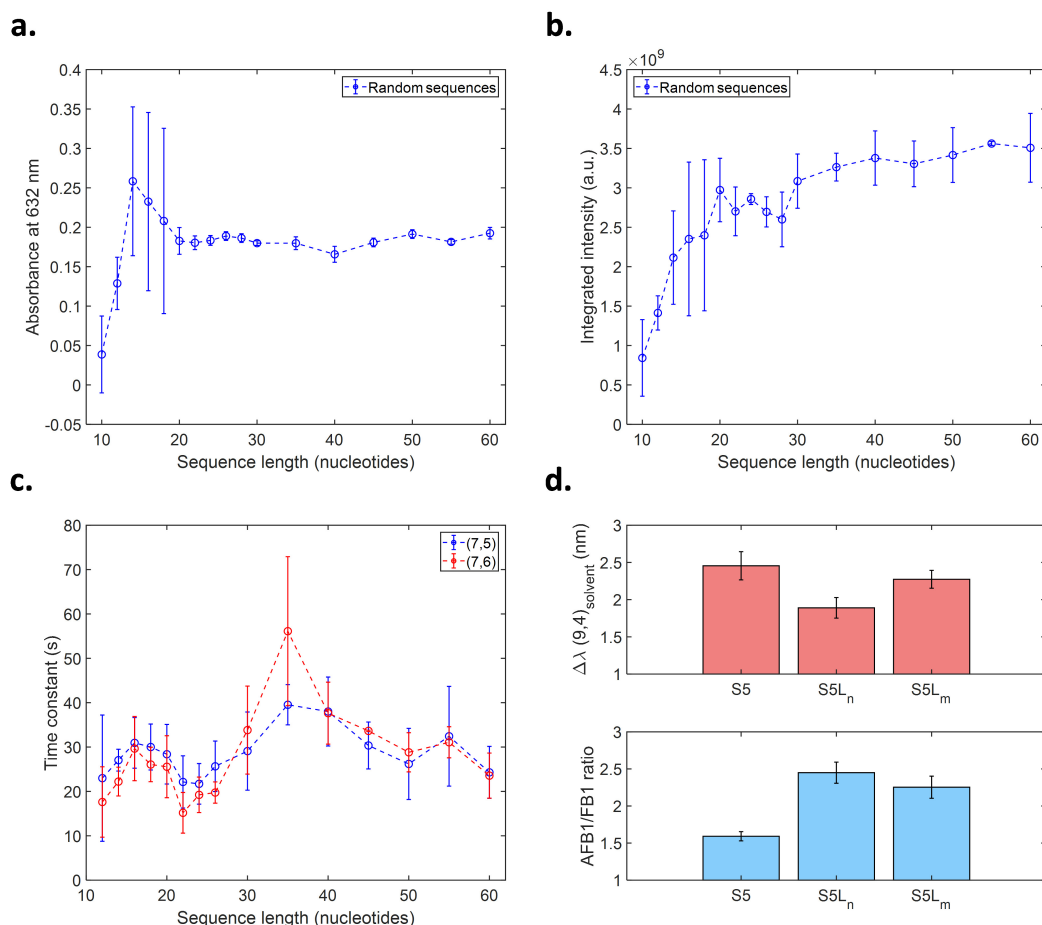


Figure 5.1 – Effect of the DNA length on the properties of DNA-SWCNTs. (a) Absorbance at 632 nm of DNA-SWCNT complexes as a function of sequence length. (b) Integrated fluorescence intensity (under 660 nm excitation) of DNA-SWCNT complexes as a function of sequence length. (c) Time constant of wrapping replacement by SDC surfactant (0.1 % final) for the (7,5) (blue) and (7,6) (red) chiralities as a function of sequence length. The complexes were all formed with random DNA sequences at an equal DNA concentration of 10 μM (final). (d) Response of the S5- and S5L-SWCNT complexes to mycotoxins. (top): Shifting response of the (9,4) chirality towards AFB1. (bottom): Ratio of the responses of the (9,4) chirality towards AFB1 and FB1. The S5L-SWCNT complexes were prepared with the same molar (S5L_n) and mass (S5L_m) concentration of DNA as for the S5-SWCNT complexes. The measurements were performed with a toxin concentration of 10 μM and after an incubation of 200 min post addition. The error bars of all samples correspond to 1 σ (n=3, except for 45 nucleotides-long sequence for which n=2).

denoted as N_X with X indicating the length of the DNA sequence. All the DNA sequences were wrapped with the same final molar concentration of 10 μM using a previously-reported methanol-assisted exchange method [125]. We used the absorbance at 632 nm as a proxy for SWCNT concentration. The N_6 and N_8 oligomers did not result in efficient dispersions of the SWCNTs (**Figure E.3**). We noted an increase in SWCNT concentration for the sequences N_{10} to N_{14} , followed by a plateau in SWCNT concentration (within error) from N_{14} to N_{60} (**Figure 5.1**). This observation therefore indicated that the dispersion efficiency depends on

the DNA length and is likely inefficient for short oligomers, e.g. below 14 nucleotides. This conclusion is in accordance with the findings of Haggemueller *et al.* who found that the wrapping efficiency increased with DNA length for A, C and T-rich sequences [114]. The fluorescence intensities of the resulting DNA-SWCNT complexes were then measured under 660 nm excitation (**Figure 5.1**). We observed an increase in integrated fluorescence intensity along with increasing DNA length, with a more abrupt increase for the lengths between 10 and 20 nucleotides, followed by a subtler increase between 20 and 60 nucleotides. Such an increase in fluorescence intensity with DNA length is also in accordance with previous reports [61, 120]. Next, we examined the effect of DNA length on the binding affinity of the DNA wrapping to the SWCNT by monitoring the kinetics of replacement of DNA with sodium deoxycholate (SDC) surfactant, as previously reported [120]. The binding affinity did not seem to be correlated with the DNA length, the DNA-SWCNT complexes showing an overall similar binding affinity for the (7,6) and (7,5) chiralities regardless of the DNA length, with the exception of the N₃₅-SWCNT complex exhibiting a higher binding affinity. While these findings appear to be in contrast with previous reports [120], we note that the sequences used in our study are random and that the sequence of the DNA wrapping could potentially play an important role in the binding affinity as previously shown [55].

Finally, we investigated the effect of DNA length on the sensing capabilities of DNA-SWCNT sensors. Previous studies reported that the response of the sensors towards dopamine, norepinephrine, riboflavin, hydrogen peroxide and various cancer biomarkers was dependent on DNA length [61, 134, 257]. Herein, we tested the effect of DNA length on fluorescence shifting-based sensors, more specifically the aflatoxin B1 (AFB1) sensors that we developed in previous work (see **Chapter 2**). We therefore tested the performances of the S5 sensor and compared it to the S5L sensor, corresponding to two repeats of the S5 sequence (see **Methods**). The sensors were wrapped both with the same molar concentration (denoted as S5L_n), and with the same mass concentration (denoted as S5L_m) in order to account for changes in the total number of nucleobases due to changes in DNA length. We compared the shifting of the (9,4) chirality upon AFB1 and estimated the selectivity of the sensors by comparing the shifting obtained in presence of AFB1 (the target of interest) and in presence of fumonisin B1 (FB1). The longer sequences did not result in any increase in shifting upon AFB1 addition when compared to the S5 sensor, the S5L_n sensor even exhibiting a decrease in shifting response (**Figure 5.1**). However, when considering the selectivity of the sensor, the longer sequences exhibited a much lower shifting response towards FB1 when compared to the S5 sensor, resulting in a greater AFB1/FB1 response ratio for the (9,4) chirality and therefore increasing drastically the selectivity of the sensors (**Figure 5.1**).

These results demonstrate the interest in using longer oligomers for the creation of DNA-SWCNT sensors. We showed that longer DNA sequence could be used in order to create DNA-SWCNT sensors with increased fluorescence intensities that do not significantly affect the dispersion efficiency and the binding affinity of the complexes. This increase could be of particular interest for sensing applications as the DNA-SWCNT sensors exhibit low quantum yields (QYs) and could strongly benefit from ways to increase their fluorescence intensities

Chapter 5. Outlook on the directed evolution of DNA-SWCNTs with long oligonucleotides

[78]. In addition, the modulation of the DNA length was also shown to result in changes in sensing capabilities. Although, for some sensors, the use of smaller length is preferable [61], we demonstrate here that this is not always the case and that properties, such as selectivity, could be improved by increasing the DNA length.

While using longer DNA sequences could be advantageous in many ways, they are unfortunately more difficult to produce. Typical oligonucleotides used for SWCNT wrapping are created by solid-state oligonucleotide synthesis. This method is, however, efficient only for short oligonucleotides [258]. Indeed, as the coupling efficiency between each nucleotide is lower than 100 %, the DNA synthesis yield decreases with increasing length. For example, if we consider a coupling efficiency of 99.5 % (typical yield given by manufacturers), the yield would go from 90.9 % for a 20 nucleotides-long sequence to 60.9 % for a 100 nucleotides-long sequence. In addition to losses in yield, additional purification needs to be performed in order to only select the length of interest leading to extra losses in yield and increased costs. Such an approach is therefore not viable for the scalable generation of DNA mutants as is required in directed evolution. An alternative way to achieve an efficient synthesis of long DNA oligomers can be to perform polymerase-assisted DNA synthesis.

The polymerase chain reaction (PCR) is a cyclic process in which the polymerase enzyme generate exponentially copies of a DNA template from individual nucleotide components, known as dNTPs [209]. In such process, the polymerase first binds to the hybridized primer site of the DNA sequence and proceeds to replicate the complementary strand for the rest of the sequence, resulting in the creation of double-stranded copies of the template DNA. If a library of DNA sequences is needed, as in the case of directed evolution, it is possible to either perform the PCR reaction with a random DNA template, resulting in a library of random DNA sequences, or to introduce mutations during the PCR process. In the latter case, this can be achieved by a process called error-prone PCR (EP-PCR) in which the polymerase is encouraged to make replication mistakes by alteration of the reaction buffer with salts and unequal amounts of each base in the dNTPs [259]. The mutation rate of the EP-PCR process is usually around 1 mutation per 1000 base pairs (bp), however it is possible to optimize this rate up to 16 mutations per 1000 bp by using kits for example. Upon creation of the DNA library, it is possible to separate all the various DNA mutants by ligating them to a plasmid DNA and transforming the plasmid in competent bacterial strains. Indeed, by using low enough concentrations of plasmid DNA, it is possible to obtain only one plasmid at a time, and therefore only one mutant, per bacteria [260]. It is then possible to separate the various bacteria, containing the various DNA mutants, by plating them on agar plates and carefully selecting single bacterial colonies.

In this work, we are interested in generating a DNA mutant library by PCR and the wrapping of this library for the directed evolution of DNA-SWCNT complexes with long oligomers. We describe the steps of this method in the **Figure 5.2**. Every step is described in further detail in the **Methods** section. As we mentioned, an efficient way to generate DNA mutants is to perform an EP-PCR instead of a classic PCR. However, EP-PCR could result at best in the

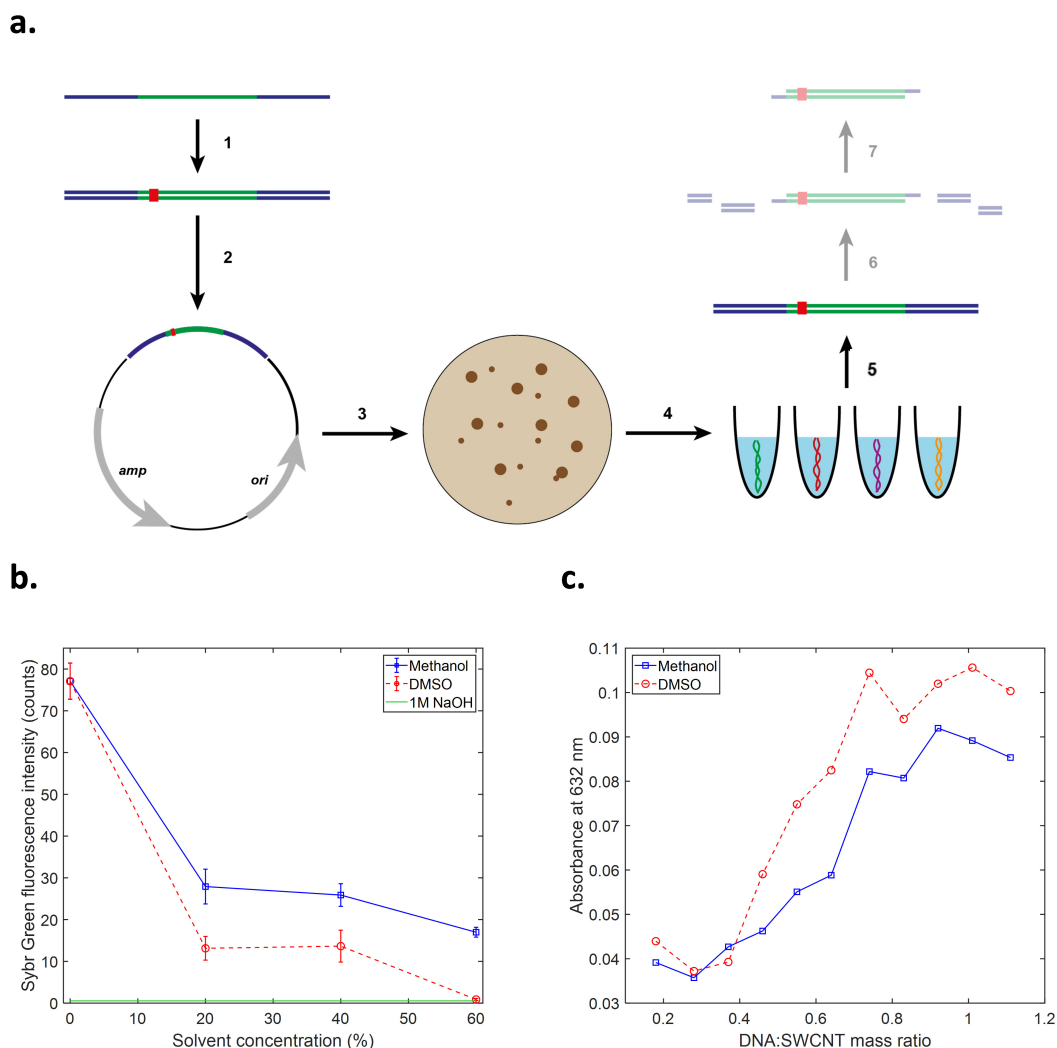


Figure 5.2 – High-throughput generation and wrapping of long DNA oligomers. (a) Schematic of the procedure used for the generation of the DNA mutant library: 1) a template sequence is designed, incorporating the sequence of interest (green) and two primer binding sites (blue), and subsequently amplified *via* PCR. Individual mutations (red) can be inserted in the DNA sequence by performing EP-PCR. 2) The PCR products are ligated in the pJET plasmid. 3) The plasmid is cloned into *E. coli* bacterial cells and the cells subsequently grown on agar plates. 4) The individual cell colonies are picked and the DNA is extracted from the cells. 5) Another PCR reaction is run on the extracted DNA to amplify the individual DNA variants. After this step, the DNA can be purified and wrapped onto SWCNTs. Additional steps (6 and 7) can be performed in order to get rid of the primer binding sites by digesting the restriction sites located within the primer binding sites and further removal of the digested fragments. (b) Intensity of the Sybr Green I fluorescence maximum for a 36 bp double-stranded DNA sequence (T-(AT)₁₅) in presence of 1 M NaOH (green), methanol (blue) and DMSO (red). A decrease in fluorescence indicates a denaturation of the DNA, the NaOH being the control for complete denaturation. The error bars represent 1 σ (n=3). (c) Absorbance at 632 nm for the DNA-SWCNT complexes prepared by wrapping exchange with a 36 bp double-stranded DNA sequence (T-(AT)₁₅) in presence of methanol (blue) and DMSO (red) for various DNA:SWCNT mass ratios.

Chapter 5. Outlook on the directed evolution of DNA-SWCNTs with long oligonucleotides

introduction of 1 or 2 mutations in a 100 nucleotides-long sequence, which may not result in large differences in the final DNA-SWCNT complexes. We therefore decided to generate a library of random DNA mutant by performing a PCR on a random DNA template (T-N₃₀) in order to obtain DNA with very distinct sequences. We first tested the performances of our methodology on a 30 nucleotides-long random template flanked by two primer binding sites of both 26 and 21 nucleotides for a total length of 77 nucleotides. The library generated by the PCR was ligated onto pJET 1.2 plasmid. The plasmid was further transformed into *Escherichia coli* (*E. coli*) chemically competent cells, DH5 α strain, through heat shock transformation. The cells were plated and the colonies were picked individually and grew further in medium overnight. The DNA template could theoretically be recovered at this step through plasmid extraction from the cells and digestion of template from the plasmid. However, we noted that the amount of DNA extracted that way is typically too low to enable further SWCNT wrapping. We therefore performed an additional PCR reaction on the DNA template extracted from the cells. To avoid the multiplication of preparation steps, the plasmid DNA was extracted from the cells during the denaturing step of the PCR, intentionally elongated to facilitate the disruption of the cell walls. The PCR was directly performed on the plasmid DNA with the primers specific to the T-N₃₀ template resulting in an amplification of the DNA template only. After the reaction, we purified the DNA from other contaminants such as proteins, salts and dNTPs using silica beads and subsequently used the purified product for SWCNT wrapping. As the primer binding sites are considered as non-interesting parts of the DNA sequence, we considered the possibility to remove them through first digestion of restriction sites located inside the primer binding sites (BamHI and EcoRI) and subsequent removal of the small, digested DNA fragments at the same time as the DNA purification using silica beads (**Figure E.5**). We did not conduct this step in this experiment as the activity and fidelity of the restriction enzymes was considered too low, resulting in partially digested products. The efficiency of this step could be optimized in future work with the use of restriction enzymes with higher fidelity.

The DNA interacts with the SWCNT *via* π -stacking between the nucleobases and the SWCNT surface, which limits the ability of double-stranded DNA (dsDNA) to wrap SWCNTs compared to single-stranded DNA (ssDNA) [82]. Since the PCR reaction creates dsDNA, the as-synthesized DNA is therefore exceedingly more difficult to wrap onto the SWCNTs. An alternative approach could rely on asymmetric PCR instead of the typical PCR, whereby one primer is used in excess relative to the other, resulting the creation of only single-stranded sequences in the last steps of the reaction. However, the yield of asymmetric PCR is only 60-70 % that of the symmetric PCR [261]. As a result, the wrapping of SWCNTs with products of asymmetric PCR may be efficient for long DNA sequences [262] but would result in too low concentrations for the wrapping of SWCNTs with short oligonucleotides (< 100 nucleotides). Another approach is to denature the dsDNA product before or during the wrapping process. In this work, we propose to replace the methanol by DMSO during the wrapping exchange process in order to allow both the denaturation of the dsDNA product and the initiation of the exchange process. In previous work, high concentrations of DMSO (60 %) have been

shown to completely denature dsDNA [263]. We further verified these findings by monitoring the fluorescence of the dsDNA-specific dye Sybr Green I with a 36 bp hybridized (AT)-rich DNA sequence (T-(AT)₁₅) in presence of various concentrations of methanol, DMSO and 1 M NaOH (**Figure 5.2**). As expected, the NaOH results in complete denaturation of the dsDNA. Although methanol also results in dsDNA denaturation, as reported [264], it does not result in a complete denaturation. DMSO, on the other hand, results in a complete denaturation of dsDNA, similar to the denaturation obtained with 1M NaOH with a concentration of 60 %. In parallel, as for methanol, DMSO has also been shown to increase the critical micelle concentration (CMC) of surfactants [265], which is critical for the exchange process [207]. This was confirmed by the aggregation of sodium cholate (SC)-suspended SWCNTs upon addition of large volumes of DMSO, similarly to what is observed with methanol (**Figure E.6**). We compared the wrapping of the same 36 bp hybridized T-(AT)₁₅ DNA sequence by methanol- and DMSO-assisted exchange procedures with SC-SWCNTs. We noted a better dispersion of the DNA-SWCNTs with the DMSO-assisted exchange procedure, evidenced by the higher absorbance and fluorescence of the final suspensions (**Figure 5.2**, **Figure E.7**). The use of DMSO in the exchange process is therefore an efficient way to denature and suspend dsDNA sequences. Although this approach results in the wrapping of both complementary strands on the SWCNTs, the sequences for a DNA-SWCNT complex of interest can be identified using this approach. If the sequences are known, one can separately order the two strands by solid-state synthesis and wrap them individually onto SWCNTs in order to determine which sequence results in the desired DNA-SWCNT complex, or to determine whether both sequences are needed. In order to identify the sequences of the DNA-SWCNT complexes, the extracted plasmids should be stored during the process for each of the DNA variant, allowing one to sequence the template-containing insert afterwards. We note that that the DNA created by PCR possesses a phosphate group at the 5' end while the DNA synthesized artificially exhibits a hydroxyl group. However, this difference in chemical functionality may not necessarily affect the overall properties of the wrapping, especially for longer DNA sequences.

We selected 15 colonies based on the procedure we described previously, amplified the DNA variants by PCR and purified and subsequently concentrated the DNA using silica beads. The sequence of two colonies, H2 and H3, were determined by sequencing plasmids extracted from the colonies (**Table E.1**). This confirmed that the colonies exhibited distinct sequences for the template part and the same primer binding sites and length, even though the H2 colony presented a deletion in the forward primer binding site. The DNA was not sequenced for all colonies, but we further verified by gel electrophoresis that the DNA from other colonies also presented a similar size (**Figure E.2**). The DNA sequences amplified from the colonies were further wrapped onto SWCNT *via* DMSO-assisted exchange. To prove that the SWCNTs were wrapped by the DNA templates and not the primers, we compared the fluorescence of the SWCNT suspended by the DNA of the H3 colony and suspended by the primers used in the final PCR reaction (**Figure 5.3**). Indeed, the primers were not small enough to be removed by silica bead purification and could potentially wrap onto the SWCNTs. We noted that the SWCNT suspended using the primers resulted in a weak fluorescence signal indicative of a

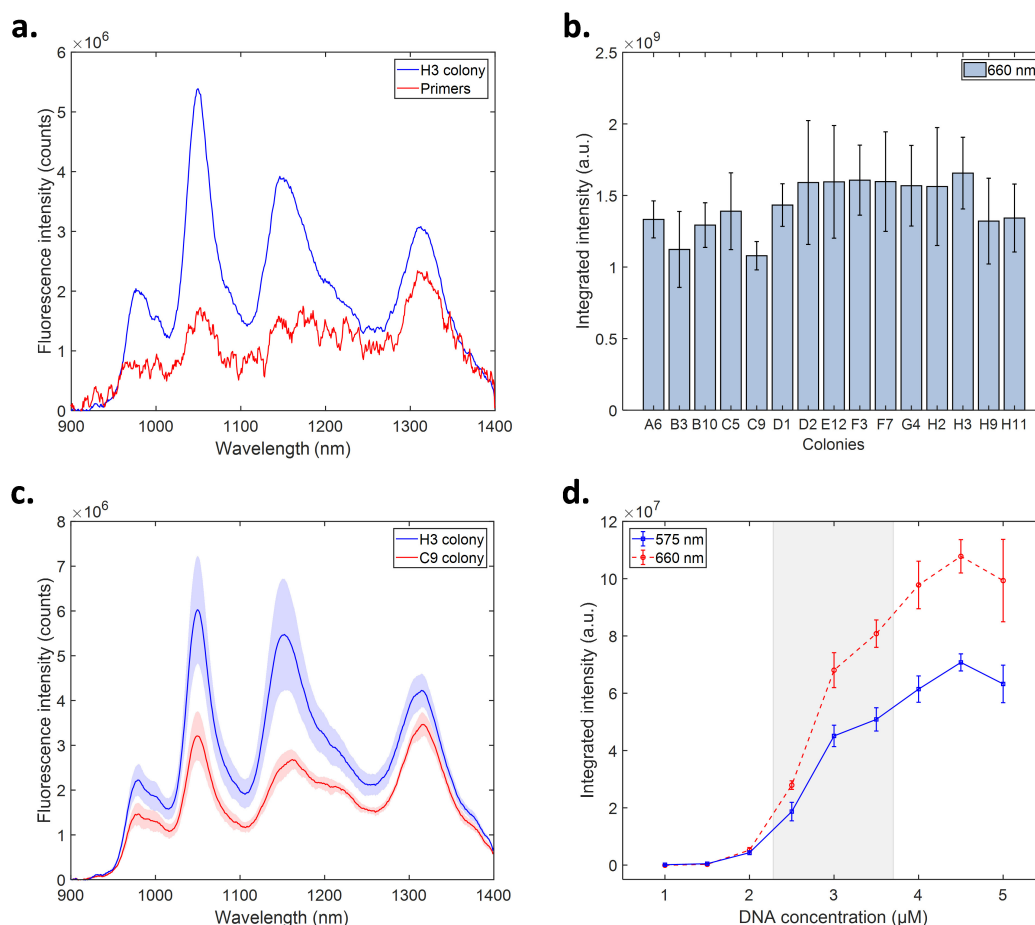


Figure 5.3 – Fluorescence of DNA-SWCNT prepared from amplified colony DNA. (a) Fluorescence spectra (under 660 nm excitation, 10 s exposure) of DNA-SWCNTs prepared with DNA amplified from the H3 colony (blue) and with the primers used for the final PCR reaction (red). (b) Integrated fluorescence intensities (under 660 nm excitation, 10 s exposure) for the DNA-SWCNT complexes prepared with the DNA amplified from 15 individual colonies. (c) Fluorescence spectra (under 660 nm excitation, 10 s exposure) of DNA-SWCNTs prepared with DNA amplified from the H3 (blue) and C9 (red) colonies. (d) Integrated fluorescence intensities (under 575 and 660 nm excitation) for DNA-SWCNT complexes prepared with the DNA template as a function of ssDNA concentration. The shaded grey represents the range of concentrations obtained for the PCR-amplified DNA products. The error bars and error shadings on the curves represent 1σ ($n=3$). For the amplified DNA, the replicates correspond to suspensions prepared with the products of independent PCR reactions.

poorly dispersed SWCNT suspension and a low affinity to SWCNTs. In contrast, the DNA amplified from the H3 colony resulted in a well-defined fluorescence signal, hence confirming the stronger affinity of the DNA template compared to the primers. In addition, the primers are also consumed during the PCR reaction, reducing even more the probability of SWCNT wrapping with the primers. We further compared the integrated fluorescence intensities under 660 nm excitation for all the colony DNA products (**Figure 5.3**). Overall, we noted similar fluorescence intensities (**Figure 5.3**) across all DNA variants but also observed large differences in fluorescence intensity between individual colonies, such as the H3 and C9 colonies.

We also observed differences in fluorescence intensities obtained between various preparations of the same colony sample (**Figure E.8**). We believe these variations could be due to variations in the yield of the PCR reaction across preparations. To verify this, we wrapped SWCNTs with various concentrations of our DNA template, from 1 to 5 μM and compared the integrated fluorescence intensities under both 575 and 660 nm excitations (**Figure 5.3**). The samples prepared by PCR typically exhibited concentrations between 2.3 and 3.7 μM (the shaded grey area in the graph). The variations we observed may therefore have originated from a combination of different DNA sequences and DNA concentrations. Several options are available to minimize these contributions. Although the yield of the PCR reaction cannot be readily controlled, the extracted DNA can be diluted to the same concentration across multiple samples. We note, however, that this approach would greatly limit the throughput of the DNA-SWCNT preparation. Another possibility would be to lower the SWCNT concentration used for the exchange in order to be in the plateau regime observed for DNA:SWCNT mass ratios above 5:1 as shown in **Figure E.9**. This approach would, however, require optimization in order to maintain a high-enough final DNA-SWCNT concentration and a low-enough SWCNT concentration to ensure the sufficient excess of DNA for all reactions.

5.5 Conclusion

In this study, we demonstrated a new approach in order to create DNA libraries for the directed evolution of DNA-SWCNT with long DNA oligomers. We showed that using longer DNA oligomers for the creation of DNA-SWCNT complexes can be advantageous both in terms of fluorescence and sensing properties, therefore catalyzing the need for such an approach.

Because solid-state DNA synthesis is strongly limited for the scalable generation of long oligomers, we proposed the use of polymerase-assisted DNA synthesis. The library creation protocol proposed here was analogous to the approach typically used for the directed evolution of proteins, in which the different variants are separated using bacterial transformation.

Although this protocol resulted in the production of dsDNA, which exhibits low affinity to SWCNT, we demonstrated a new exchange procedure based on the use of DMSO in order to allow the simultaneous denaturation and wrapping of the DNA. We further showed that this procedure is more efficient than the methanol-assisted exchange for the wrapping of dsDNA samples.

Finally, we showcased this procedure by comparing the fluorescence intensities of various DNA sequences originating from a random library and demonstrated that DNA individually separated by bacterial cells could exhibit distinct fluorescence intensities. This therefore confirmed that our approach can be used in order to generate libraries of DNA variants for the directed evolution of DNA-SWCNT sensors, regardless of the length of the DNA sequence.

Future work should be performed in order to fix the additional variability existing due to the inherent variation in yield of the PCR reaction. We suggest to correct such an effect

Chapter 5. Outlook on the directed evolution of DNA-SWCNTs with long oligonucleotides

by optimization of the DNA:SWCNT ratio during the exchange procedure. Furthermore, future experiments could use biotinylated primers during the final PCR in order to enable a purification of the products with streptavidin-coated substrates, hence allowing the removal of the complementary strand and a better purity of the final DNA products.

General conclusion and perspectives

The use of nanomaterial-based complexes is particularly advantageous for a variety of applications. Among these materials, DNA-SWCNT complexes have been extensively used for the creation of optical biosensors because of their peculiar fluorescent properties and high versatility. Yet, despite their advantages, such nanocomplexes can be difficult to design due to uncertainties regarding their structures and structure-function relationship. This is particularly true for DNA-SWCNT complexes as the relationship between the DNA sequence and resulting properties of the complexes is unknown. As a result, the design of these complexes often relies on trial-and-error, leading to the discovery of poorly optimized materials and therefore limiting their performances and applicability.

The field of protein engineering is faced with analogous challenges. Proteins are typically an infinity of possible variants, making it exceedingly difficult to predict how to design them for a specific purpose, in particular if their structure-function relationship is unknown. To overcome this difficulty, approaches such as directed evolution have been developed in order to navigate through the space of protein variants. This approach technique relies on the cyclic succession of mutation, screening and selection steps, enabling to effectively engineer proteins while limiting the size of the screening library to only closely-related protein mutants.

In this thesis, we took inspiration from the techniques developed in the field of protein engineering for the design of DNA-SWCNT complexes. In particular, we took advantage of the sequence-specific properties of the DNA-SWCNTs and demonstrated the possibility to engineer the complexes using directed evolution. Throughout this dissertation, we illustrated the strengths of this approach over current state-of-the-art methods used for the engineering of DNA-SWCNT complexes, enabling faster and greater improvements but also allowing to engineer the complexes on a variety of characteristics simultaneously. We further acknowledged the limitations of the directed evolution approach and proposed alternative ways to engineer the complexes.

The first two chapters were focused on the application of the directed evolution approach for the engineering of DNA-SWCNT complexes. In the **Chapter 1**, we showed that it was possible to improve the fluorescence intensity of the (GT)₁₅-SWCNT complexes *via* the directed evolution approach, by up to 56 % after two cycles of mutation, screening and selection. The directed evolution of the complexes was made possible by the creation of a novel approach

for the high-throughput wrapping of SWCNTs with DNA sequences. We further showed that the observed increase in fluorescence intensity stemmed from an increase in QY of the complexes, resulting from an increase in the coverage of the SWCNT surface by the DNA wrapping. Moreover, we demonstrated that the improvement in QY was dependent on the SWCNT chirality, with the highest increases observed for the (9,4), (10,2) and (8,6) chiralities. Finally, we showed that the improvements observed in fluorescence QY did not significantly impact the overall sensing capabilities of the DNA-SWCNT sensors towards the dopamine neurotransmitter, both in terms of sensitivity and target selectivity. The brighter mutant complexes could therefore be utilized in order to monitor the presence of neurotransmitters *in vivo* at larger penetration depths, while minimally affecting the other properties of the complex.

Next, we showed how the other properties of the DNA-SWCNT complexes, such as sensing capabilities, could be engineered using the directed evolution approach. This was explored in the **Chapter 2** of the thesis, in which we discovered and further engineered DNA-SWCNT sensors for the detection of mycotoxins in food products. For that, we first screened an initial library of random DNA-SWCNT complexes in order to find a sensor responsive to mycotoxins, which would then serve as the starting point of the directed evolution. From this screening, we found the Δ (AG)-SWCNT sensor which exhibited a specific shifting response towards the aflatoxin B1 (AFB1) toxin, mainly for the (9,4) chirality, while reacting minimally to other mycotoxins such as fumonisin B1 (FB1). By performing four rounds of directed evolution on the Δ (AG)-SWCNT sensor, we could improve the AFB1 response by up to 314 %, while simultaneously not losing the SWCNT chirality and target selectivity of the sensor. In parallel, we also demonstrated that DNA shuffling, a synthetic biology technique relying on the combination of multiple positive mutants, could be used in order to achieve a more efficient improvement of the sensors' response. We further demonstrated the possibility to concurrently engineer other properties of the complexes such as fluorescence intensity and SWCNT chirality and target selectivity of the response using additional rounds of directed evolution. Our searches eventually resulted in the discovery of two sensors, Q-3 and F-3, responding selectively to the AFB1 and FB1 toxins on the (9,4) and (7,5) chiralities respectively. Using both sensors, we could perform multimodal sensing of both mycotoxins without the need to separate SWCNT chiralities beforehand. We further tested the performances of our sensors in real conditions by measuring the concentrations of mixed mycotoxins in presence of corn flour. Finally, we investigated the mechanisms for the AFB1 and FB1 interactions. We found that the AFB1 was more prone to interact with the SWCNT surface directly while the FB1 would interact with the DNA wrapping. This had effect on the overall properties of the mycotoxin detection, such as the reversibility of the interaction and the effect of free DNA removal in the sensor samples.

Although we successfully demonstrated the strength of the directed evolution approach for the engineering of DNA-SWCNT complexes in the two first chapters of this thesis, we also acknowledged the limitations of this approach. First, engineering complexes by directed evolution requires an extensive library screening, over 400 complexes in the **Chapter 2**. Then,

as directed evolution concentrates only on variants closely related to the starting sequence, the mutants found by directed evolution may not correspond to the most optimized sequences. To overcome this bottleneck, synthetic biologists have relied on semi-rational approaches, when possible, in order to modify only the parts of the system which are important for the properties of interest. In the **Chapter 3**, the knowledge gathered on the mycotoxin responses in the **Chapter 2** was combined with a systematic investigation of the factors affecting the sensors' characteristics in order to design AFB1 and FB1 sensors in a semi-rational manner. We first found that the AFB1 response was related to the base content, the response increasing with increasing G-content. By optimizing the base content of the DNA sequences, we showed that it was possible to strongly improve the response towards AFB1, up to almost four times more than the Q-3 sensor found by directed evolution. We additionally found that the increase in AFB1 response could be explained by an increase in SWCNT surface coverage. We also demonstrated that, at high G-contents, this effect was even more exacerbated due to the formation of G-quadruplex (G4) secondary structures on the SWCNT surface. The newly found AFB1 sensors were further shown to respond with other targets also interacting with the SWCNT surface, such as zearalenone (ZEN). Next, we selected the F-3 sensor previously demonstrated for FB1 sensing and found that the FB1 response could be improved by mutating bases in a specific location of the DNA sequence, between 7th and 14th bases (from 5' to 3'). We further demonstrated that the maximum improvement in FB1 response was obtained after only one round of mutagenesis on the bases 7 to 14. The FB1 mutants also demonstrated a higher response reversibility compared to the starting F-3 sensor. Finally, we showed that the FB1 mutants could be used to detect other molecules interacting with the DNA wrapping in a similar way as the FB1, such as the ochratoxin A (OTA) and AAL TB toxin. The semi-rational approach demonstrated in the **Chapter 3** therefore enables to evolve DNA-SWCNT even beyond what is achieved by directed evolution. This approach also enabled the discovery of two families of sensors exhibiting specific responses towards targets interacting with either the SWCNT surface or the DNA wrapping.

We showed that the properties of DNA-SWCNT complexes can be optimized through the selective modulation of the DNA sequence using directed evolution or semi-rational design. However, the performances of the complexes remain limited by the inherent limits and performances natural DNA oligonucleotides. To tackle this limitation, we showed in the **Chapter 4** the possibility to chemically modify the DNA wrapping in order to modulate the properties of the DNA-SWCNT complexes. For that, we introduced amino and azide modifications at various positions in different sequences. We demonstrated that the presence of the modifications had a significant effect on the dispersibility of the SWCNTs as well as on the fluorescence intensity of the DNA-SWCNT complexes. In particular, we noted significant increases in intensity for both the modified (AT)₁₅ and (GT)₁₅ sequences, that we attribute to both a selective SWCNT chirality enrichment and increase in dispersion quality. We also noted that the modified complexes retained their selective target sensing capabilities, while exhibiting an overall slightly decreased response. Finally, we showed that the preparation method strongly affected the effect of the modifications on the properties of the complexes. While

the complexes previously compared were prepared by surfactant exchange, we showed that chemically modified samples showed much greater improvements compared to unmodified when prepared by direct sonication. This approach could therefore be used in combination with directed evolution in order to further improve the properties of DNA-SWCNT sensors.

Finally, although the properties of the DNA-SWCNT complexes depend on the DNA sequence, they have also been shown to depend on the length of the DNA sequence. We indeed show that the use of longer oligonucleotides can enable improvements in fluorescence and sensing properties of the complexes. Nonetheless, the directed evolution protocol we developed is highly inefficient for oligonucleotides longer than 40 nucleotides due to the use of solid-state synthesis for the generation of the DNA library. To overcome this challenge, in the **Chapter 5** we demonstrated an alternative method for the generation of DNA-SWCNT libraries based on the biological generation of a library of individual DNA variants and subsequent high-throughput wrapping onto SWCNTs. We showcased this protocol by generating a library of DNA-SWCNT complexes with DNA sequences amplified from individual cell colonies. While this method would require additional refinements in order to become as efficient as the current approach for DNA-SWCNT library generation, it provides an important platform for the generation of libraries of DNA-SWCNTs conjugated with long oligonucleotides and therefore allows for the creation of more diverse libraries.

In conclusion, the work presented in this thesis showed how approaches originally developed in the field of protein engineering can be successfully applied to nanomaterial complexes. In particular, we demonstrated that the properties of the DNA-SWCNT complexes can be significantly improved by using directed evolution. We showed that such approach enabled to engineer DNA-SWCNTs beyond what current state-of-the-art methods allow. While the directed evolution approach has limitations, we presented alternative ways to overcome these challenges, for example by using a semi-rational design, incorporating chemical modifications and using longer DNA sequences.

Nonetheless, the engineering of the DNA-SWCNT complexes remains still faced with various challenges. One of these limitations is the presence of mixed SWCNT chiralities. The presence of these unsorted chiralities complexifies the system as one DNA sequence can interact differently depending on the helicity and handedness of the SWCNT. This would therefore result not only in one type of DNA-SWCNT complex, but in a multitude of DNA-SWCNT complexes mixed altogether. Although, throughout the thesis, we make an analogy between DNA-SWCNT complexes and proteins, the situation is different in protein engineering as one amino acid sequence would correspond to only one possible protein. This limitation could be addressed by performing directed evolution on complexes formed with sorted SWCNT chiralities, therefore a more efficient engineering of the complexes by evolving only one type of complex at a time. Working with separated SWCNT chiralities would also be critical in order to understand better the relationship between structure and function of the DNA-SWCNT complexes. Other challenges, such as limited screening size or the difficulty to obtain optimized sensors, could be overcome through various ways. First, the use of selection

methods, such as SELEX, could replace random library screening in order to find better starting complexes for the directed evolution. Emerging computational techniques, such as machine learning, could also help to narrow down the screening of the mutant library to only a handful of complexes, allowing for a more efficient engineering. Furthermore, while DNA was the nucleic acid studied in this thesis, it could also be possible to create better-performing SWCNT-based sensors by using other types of nucleic acids. Finally, a better characterization of the native DNA-SWCNT structure, through the use of cryo-TEM for instance, could enable a better understanding of the structure-function relationship of DNA-SWCNT complexes, eventually leading to a possible rational design of the complexes with fully optimized characteristics.

We believe the findings presented in this dissertation can have an important impact on the future design of DNA-SWCNT complexes and could help improve the applicability of such complexes in a variety of fields. Although our work was focused on DNA-SWCNT complexes, similar approaches could also be envisioned for other kinds of nanomaterial complexes and would therefore enable to fully explore the possibilities that nanomaterials offer.

A Modulating the optical properties of DNA-SWCNT sensors by directed evolution

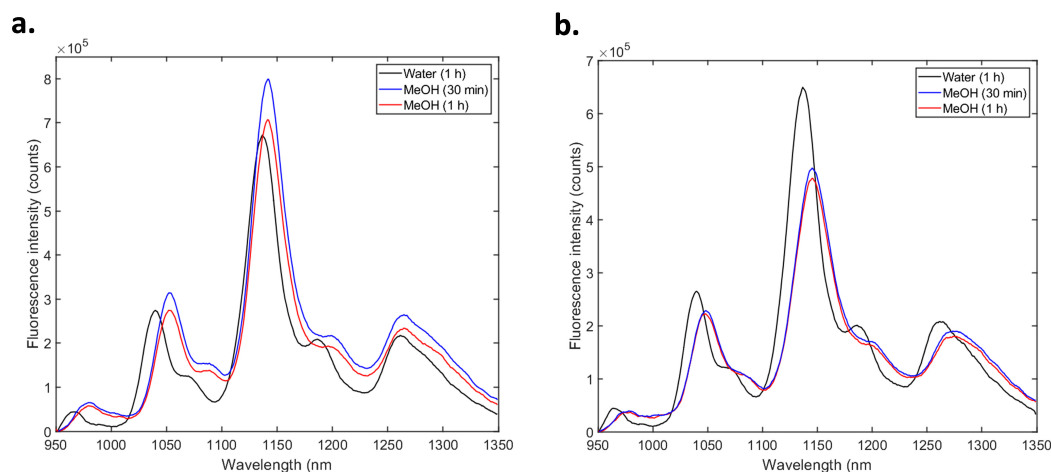


Figure A.1 – Kinetics of wrapping exchange. Fluorescence spectra under 660 nm excitation of SC-SWCNTs exchanged with (a) $(AT)_{15}$ and (b) GT_{15} in the absence (black curves) or presence (blue and red curves) of methanol, necessary to initiate the exchange process. The measurements were taken 30 min (blue) and 1 h (red, black) after methanol (or water) addition.

Appendix A. Modulating the optical properties of DNA-SWCNT sensors by directed evolution

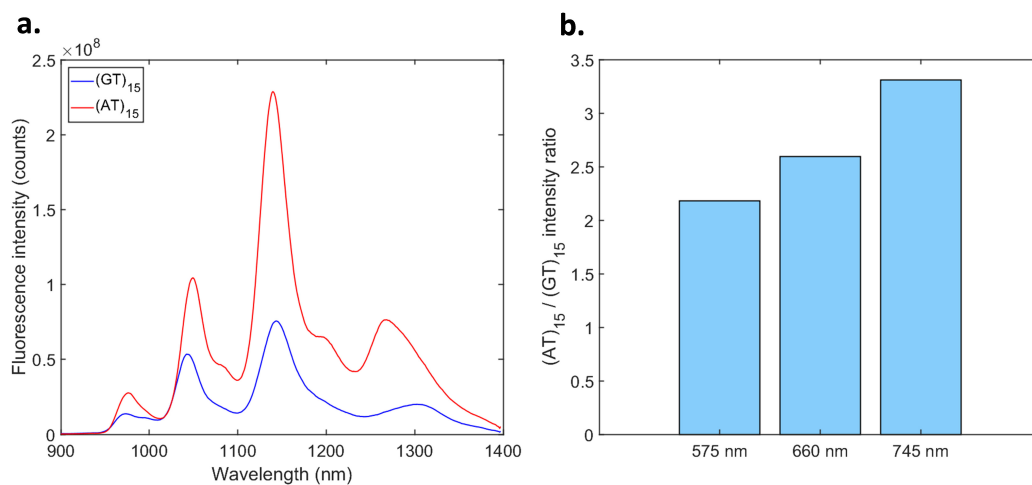


Figure A.2 – Comparison between $(AT)_{15}$ -SWCNT and $(GT)_{15}$ -SWCNT complexes. (a) Comparison of the fluorescence spectra of $(AT)_{15}$ -SWCNT (red curve) and $(GT)_{15}$ -SWCNT (blue curve) complexes under 660 nm excitation. (b) Ratios of the integrated intensities of the $(AT)_{15}$ -SWCNT complexes with the integrated intensities of the $(GT)_{15}$ -SWCNT complexes under 575, 660 and 745 nm excitations.

Appendix A. Modulating the optical properties of DNA-SWCNT sensors by directed evolution

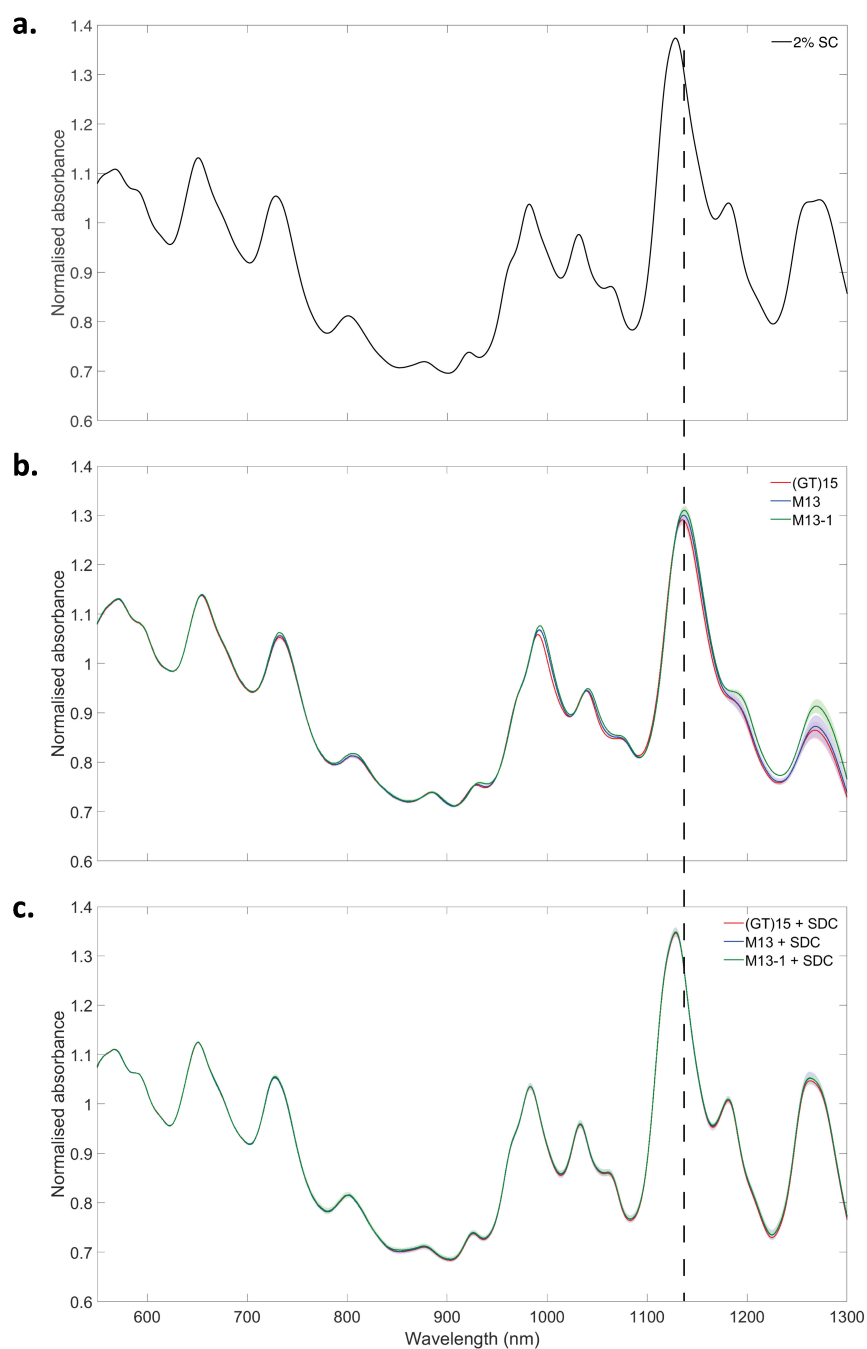


Figure A.4 – Absorbance spectra of the DNA-SWCNT complexes. Absorbance spectra of (a) SC-suspended SWCNT and (b) the DNA-SWCNT complexes before and (c) after wrapping replacement with 0.1 % SDC as a function of the wavelength. All absorbance spectra are normalized to the absorbance at 632 nm, used to determine the SWCNT concentration of HiPco nanotubes. The dotted black line illustrates the peak position of the (7,6) and (9,4) chiralities for the DNA-SWCNT complexes for comparison.

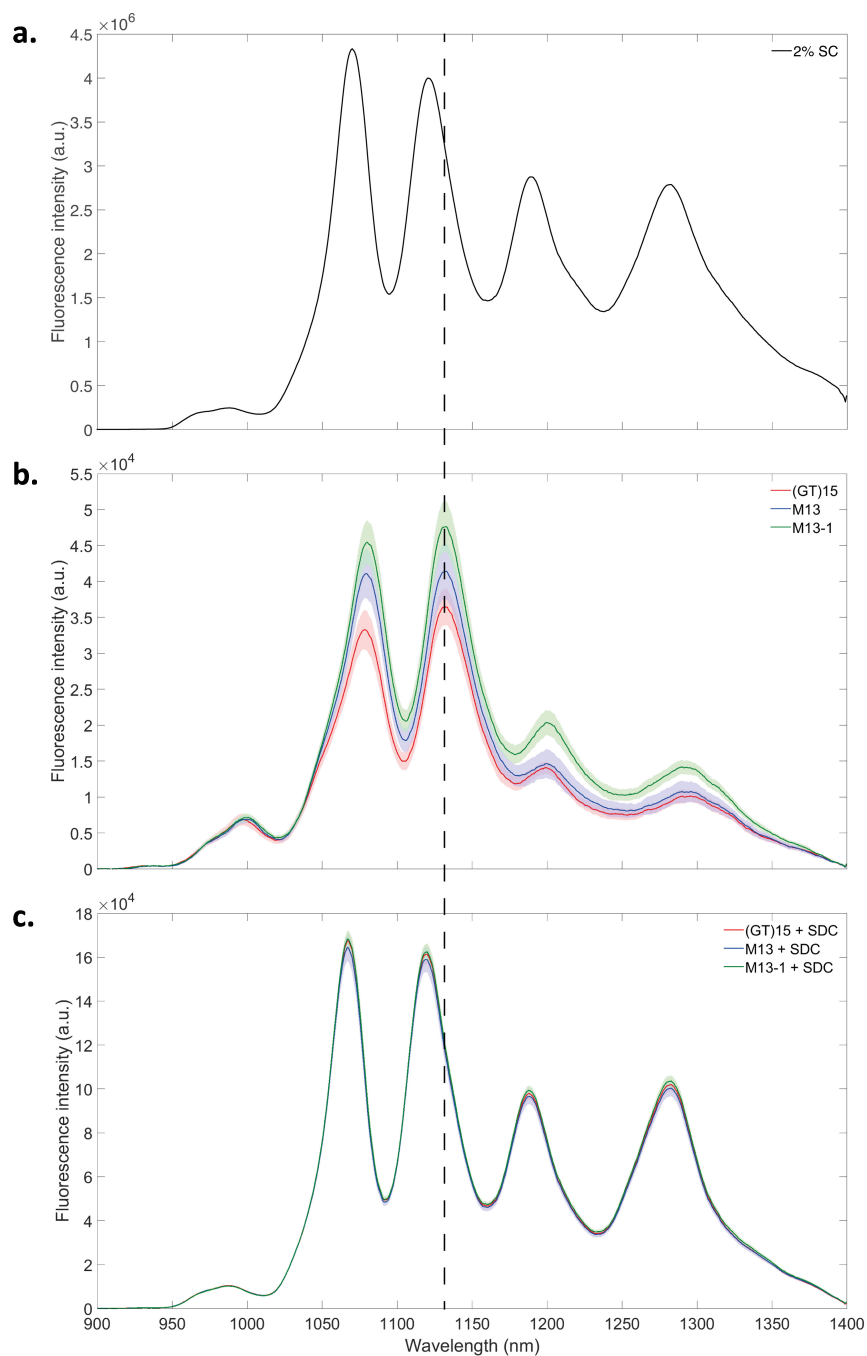


Figure A.5 – Fluorescence spectra of the DNA-SWCNT complexes. Fluorescence spectra of (a) SC-suspended SWCNT and (b) the ssDNA-SWCNT complexes before and (c) after wrapping replacement with 0.1 % SDC as a function of the wavelength. The dotted black line illustrates the peak position of the (9,4) chirality for the DNA-SWCNT complexes for comparison.

Appendix A. Modulating the optical properties of DNA-SWCNT sensors by directed evolution

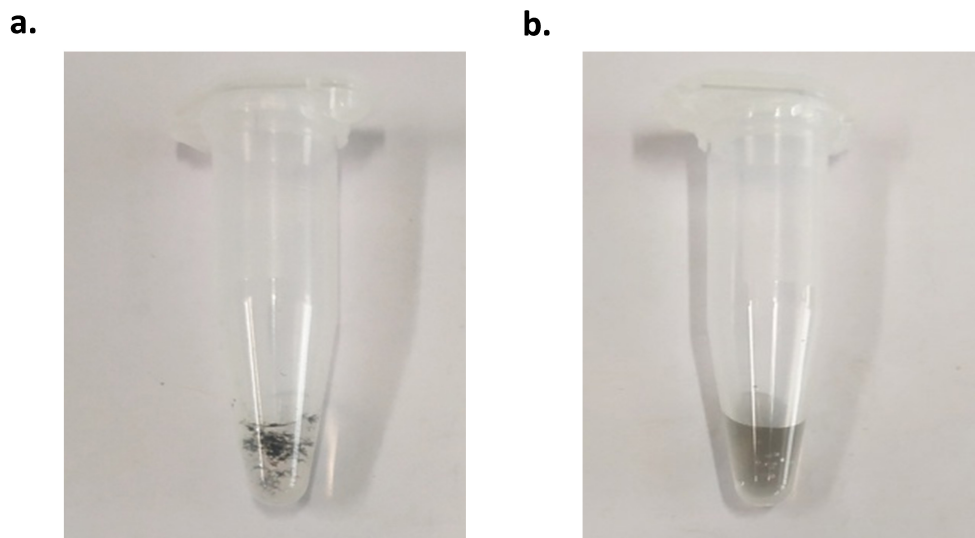


Figure A.6 – Comparison of exchanged SWCNTs without and with DNA. Pictures of the SC-SWCNT suspensions with methanol (a) in the absence of DNA and (b) with the $(GT)_{15}$ DNA sequence. In the absence of DNA, a volume of water equivalent to the volume of DNA is added to the suspension in order to keep a constant final volume for the reaction. In the absence of DNA, we directly observe the formation of SWCNT aggregates, while the suspension remains stable with the $(GT)_{15}$ sequence.

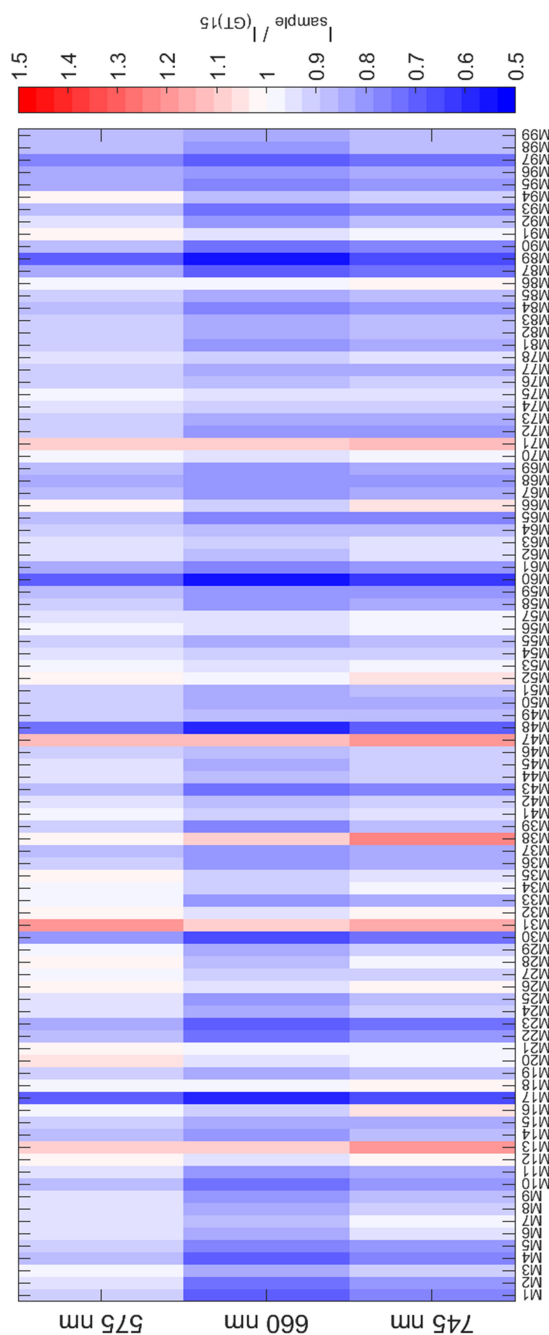


Figure A.7 – Fluorescence response of the first round mutants. Heatmap of the integrated fluorescence intensities of the first round mutants compared to the $(GT)_{15}$ -SWCNT complex under 575, 660 and 745 nm excitations. The M40, M79, M80 and M88 mutants are not shown here as their concentrations were too low to be screened for fluorescence intensity. The M13 and M38 mutants were not selected for further evolution as their errors were larger than for the M13, M47 and M71 mutants (see **Figure A.9**).

Appendix A. Modulating the optical properties of DNA-SWCNT sensors by directed evolution

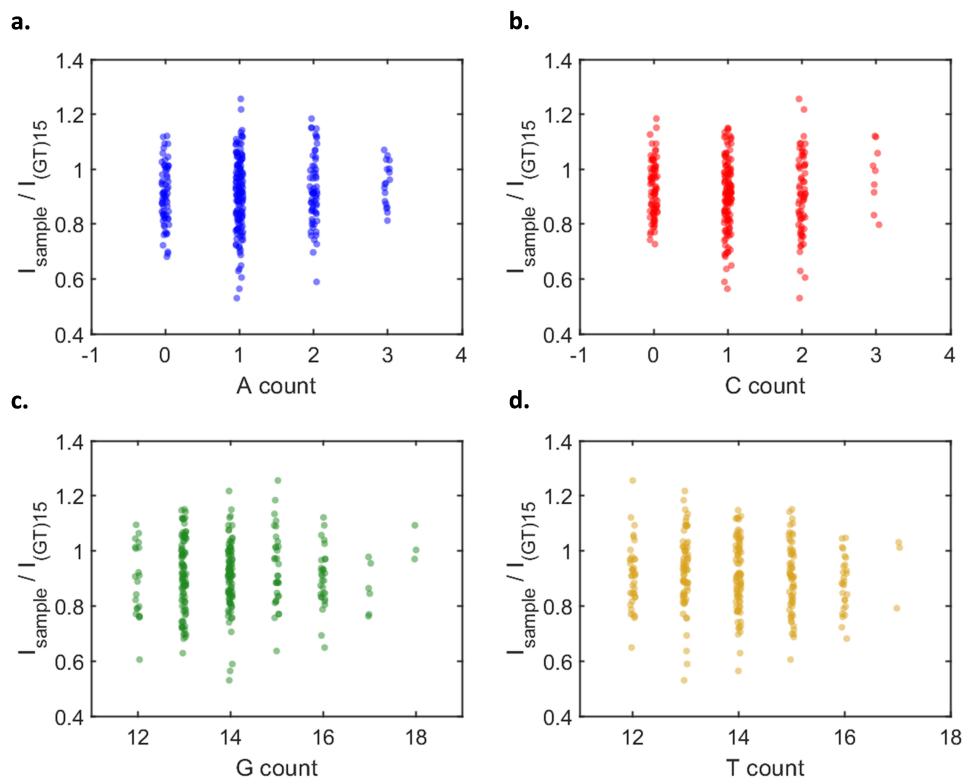


Figure A.8 – Relationship between intensity change and base content. Ratios of the integrated intensities between the first round mutants and the (GT)₁₅-SWCNT complex under 745 nm excitation as a function of the A, C, G, and T content of the sequences. No correlation exist between the ratios of intensities and base content ($p > 0$ for all, Spearman correlation test).

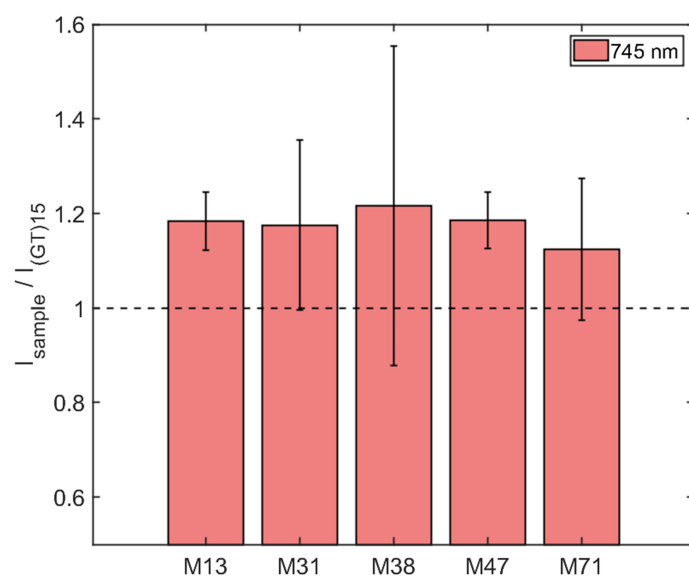


Figure A.9 – Errors in the first round screening. Ratios of the integrated intensities between the best first round mutants and the (GT)₁₅-SWCNT complex under 745 nm excitation.

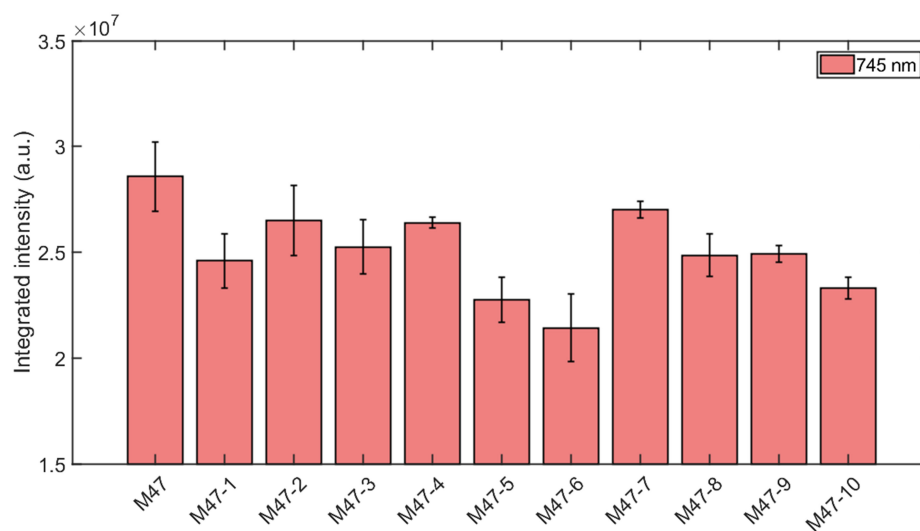


Figure A.10 – Mutants of the M47-SWCNT complex. Integrated intensities for the mutants of the M47 sequence under 745 nm excitation. The error bars represent 1 σ (n=3).

Appendix A. Modulating the optical properties of DNA-SWCNT sensors by directed evolution

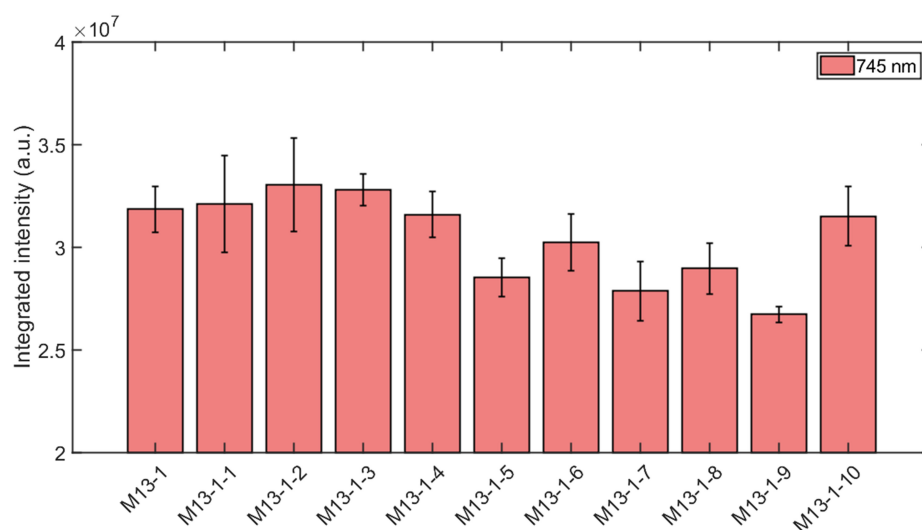
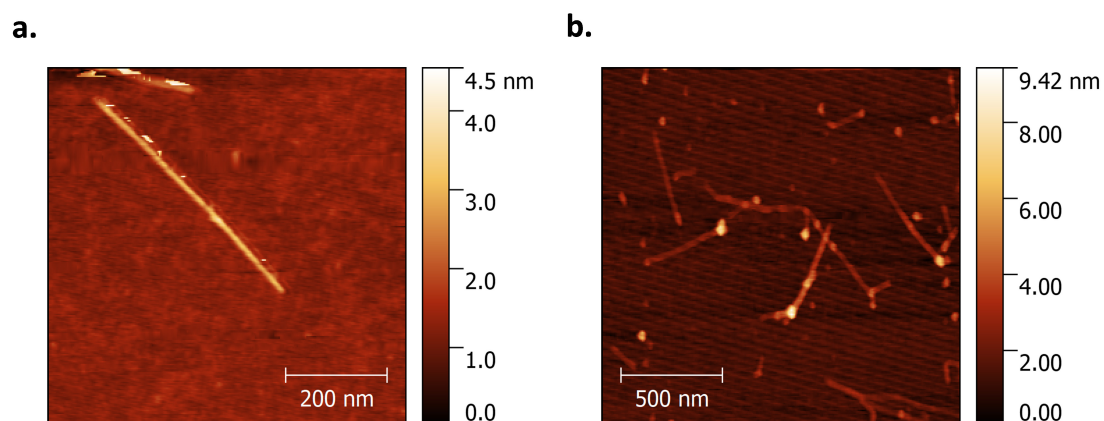


Figure A.11 – Mutants of the M13-1-SWCNT complex. Integrated intensities for the mutants of the M13-1 sequence under 745 nm excitation. The error bars represent 1σ ($n=3$).



| Sequence | Length (nm) | Std (nm) | Number of SWCNTs |
|--------------------|-------------|----------|------------------|
| (GT) ₁₅ | 466.4 | 107.3 | 4 |
| M13 | 467.2 | 59.7 | 4 |

Figure A.12 – AFM characterization of the DNA-SWCNT complexes. (top) AFM images of (a) (GT)₁₅-SWCNT and (b) M13-SWCNT complexes. (bottom) Lengths of the SWCNTs determined from AFM.

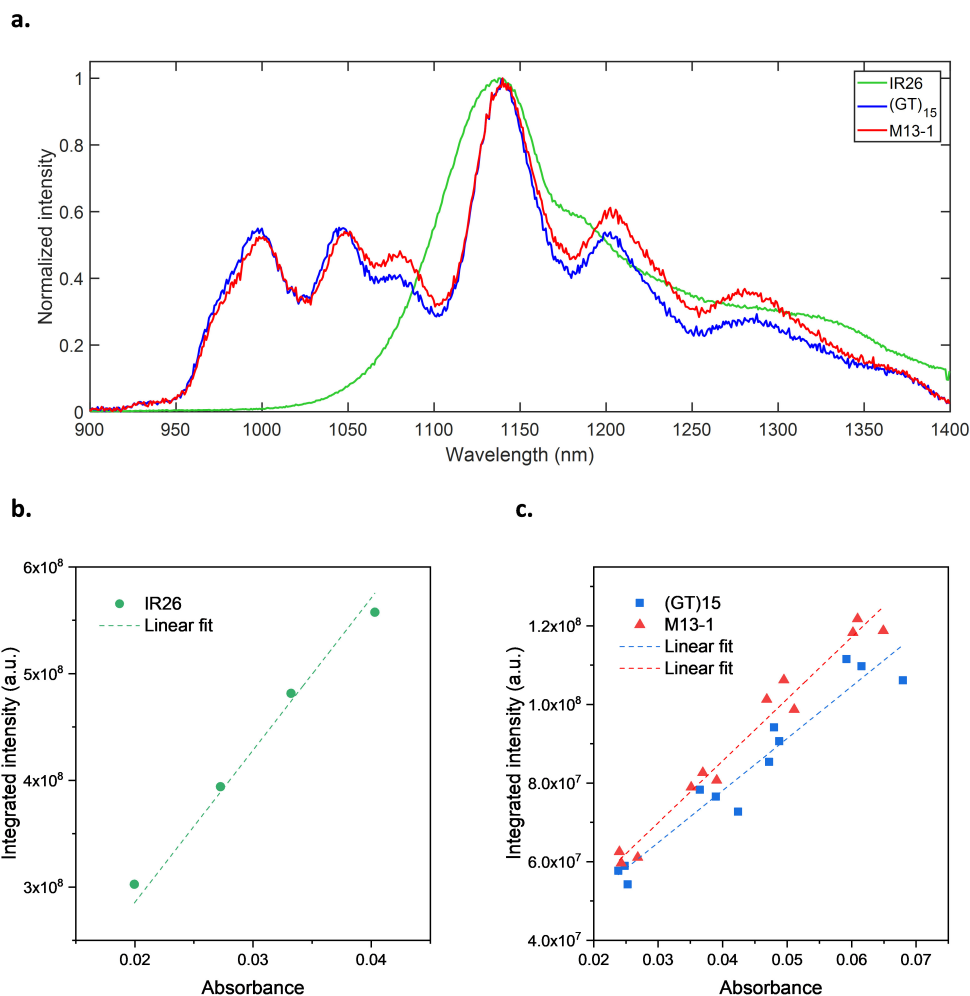


Figure A.13 – Comparison of the fluorescence of the IR-26 dye and the SWCNTs. (a) Normalized fluorescence spectra of the IR-26 dye (green), the (GT)₁₅-SWCNT (blue) and the M13-1-SWCNT (red) complexes under 808 nm excitation. (b) Integrated intensity (under 808 nm excitation) as a function of the absorbance at 808 nm for the IR-26 dye and linear fit. (c) Integrated intensity (under 808 nm excitation) as a function of the absorbance at 808 nm for the (GT)₁₅-SWCNT (blue) and the M13-1-SWCNT (red) complexes and corresponding linear fits.

Table A.2 – Quantum yields (QYs) of DNA-SWCNTs. QYs of DNA-SWCNTs calculated from comparison with IR-26 reference dye (QY = 0.11 %).

| Sequence | QY (%) |
|--------------------|-------------------------------|
| (GT) ₁₅ | $9.7 \pm 0.9 \times 10^{-3}$ |
| M13-1 | $11.5 \pm 0.8 \times 10^{-3}$ |

Appendix A. Modulating the optical properties of DNA-SWCNT sensors by directed evolution

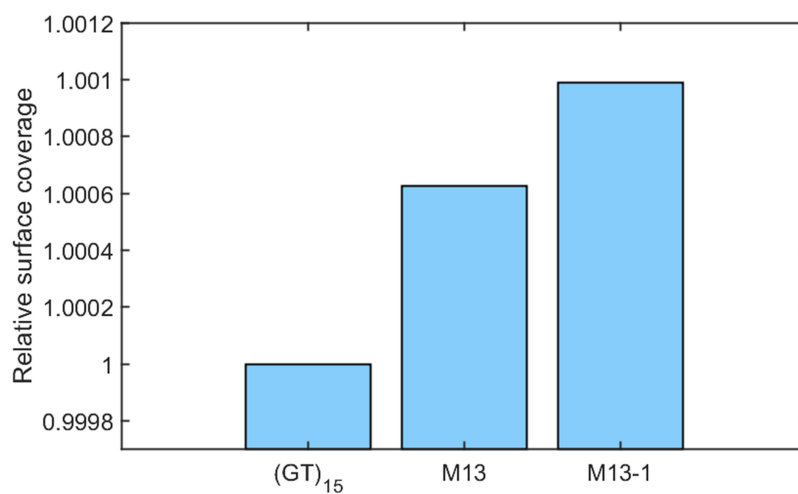


Figure A.14 – Relative surface coverage of the DNA-SWCNTs. Relative surface coverage for the $(GT)_{15}$ -, M13- and M13-1-SWCNT complexes determined from the peak positions of the fitted (6,5), (7,5), (7,6), (10,2), (9,4), (8,4) and (8,6) chiralities. The measurements were performed in 1 replicate.

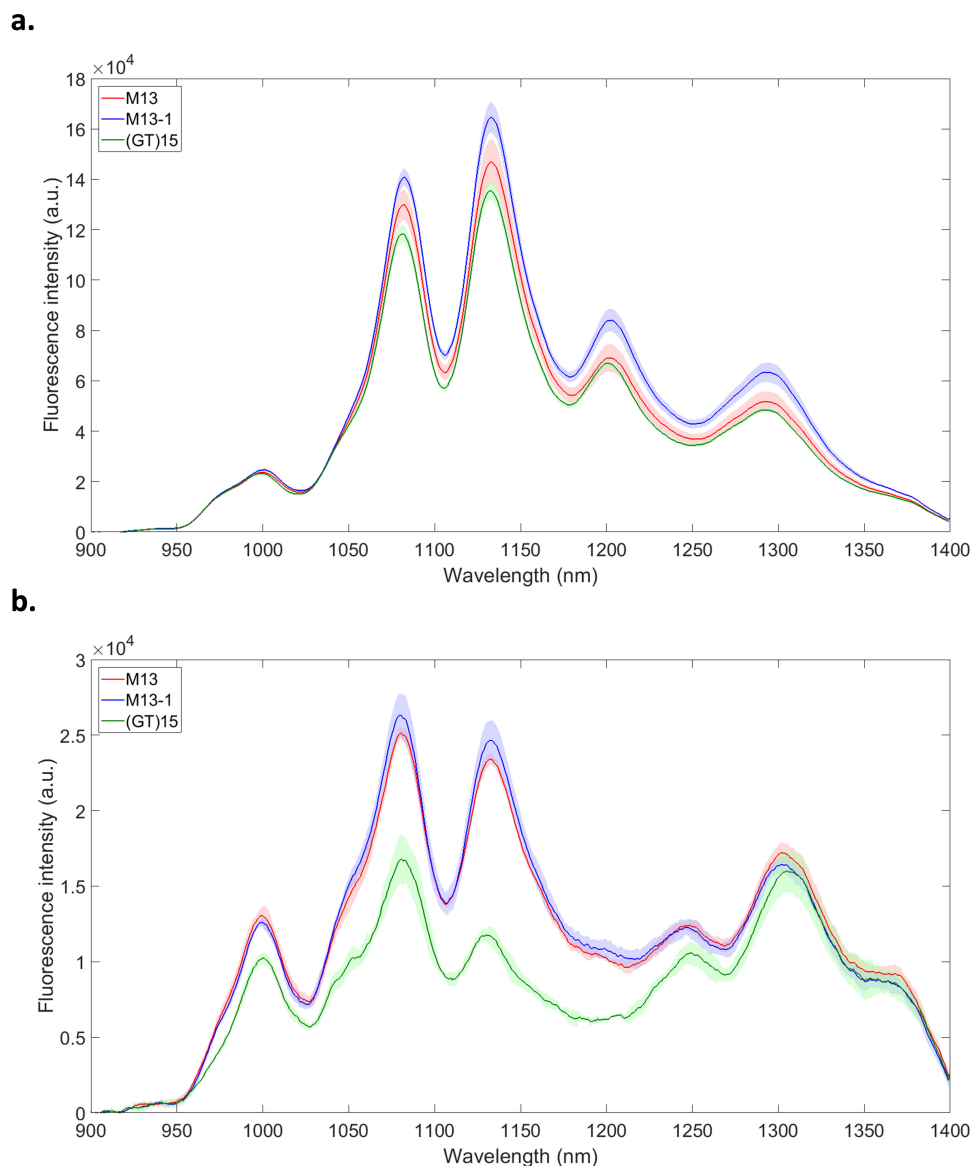


Figure A.15 – Effect of free DNA removal on the fluorescence intensity of DNA-SWCNTs. Effect of the free DNA removal on the fluorescence of the DNA-SWCNT complexes. Fluorescence spectra of the (GT)₁₅- (green), M13- (red) and M13-1 (blue)-SWCNT complexes under 745 nm excitation (a) before and (b) after free DNA removal. The error shading represents 1σ (n=3).

Appendix A. Modulating the optical properties of DNA-SWCNT sensors by directed evolution

Table A.3 – Response of the DNA-SWCNTs towards dopamine and glutamic acid. Response of the DNA-SWCNT complexes towards dopamine and glutamic acid for the (9,4), (10,2), and (8,6) chiralities, as well as the integrated intensity under 745 nm excitation (labelled as “ALL”). The response (in %) corresponds to the ratio $(I-I_0)/I_0$ with I denoting the signal after analyte addition and I_0 denoting the signal before analyte addition. The response is shown with the specified standard deviation ($n=5$). Both values are rounded to the closest integer.

| Labels | Response to dopamine | | | | Response to glutamic acid | | | |
|--------------------|----------------------|---------|----------|---------|---------------------------|--------|-------|-------|
| | (9,4) | (10,2) | (8,6) | ALL | (9,4) | (10,2) | (8,6) | ALL |
| (GT) ₁₅ | 62 ± 8 | 46 ± 8 | 107 ± 12 | 72 ± 8 | 4 ± 5 | 2 ± 5 | 6 ± 5 | 4 ± 4 |
| M13 | 73 ± 10 | 63 ± 9 | 125 ± 18 | 84 ± 11 | 4 ± 4 | 3 ± 4 | 4 ± 5 | 3 ± 4 |
| M13-1 | 58 ± 5 | 58 ± 6 | 90 ± 8 | 70 ± 6 | 1 ± 4 | −1 ± 4 | 3 ± 5 | 1 ± 4 |
| M13-6 | 64 ± 10 | 65 ± 10 | 93 ± 12 | 74 ± 9 | 1 ± 5 | 0 ± 5 | 2 ± 6 | 1 ± 5 |

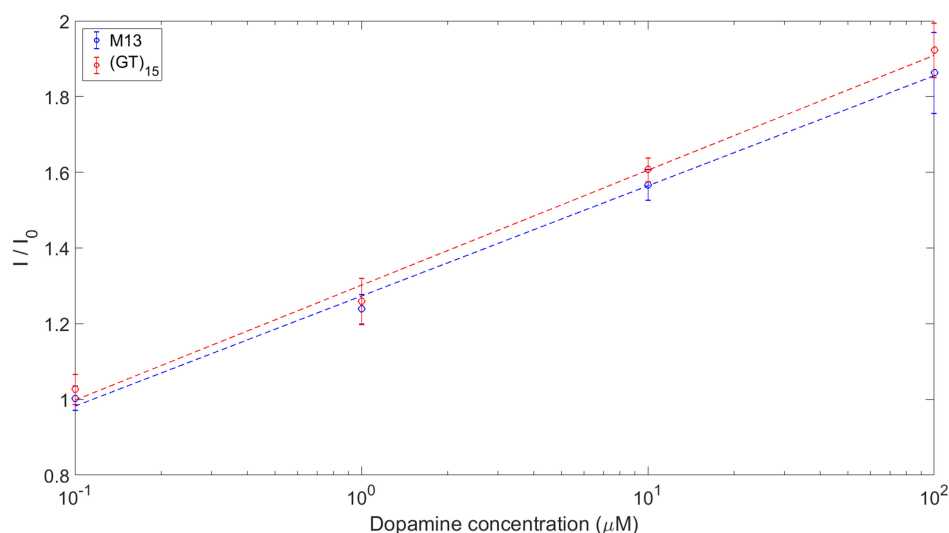


Figure A.16 – Dopamine calibration curves for the (GT)₁₅- and M13-SWCNT complexes. The ratio I/I_0 , with I denoting the integrated fluorescence intensity (under 745 nm excitation) after dopamine detection and I_0 denoting the integrated fluorescence intensity (under 745 nm excitation) before dopamine introduction, is represented as a function of the dopamine concentration in μM (logarithmic scale). The M13-SWCNT complex is shown in blue and the (GT)₁₅-SWCNT complex in red. The error bars represent 1σ ($n=3$).

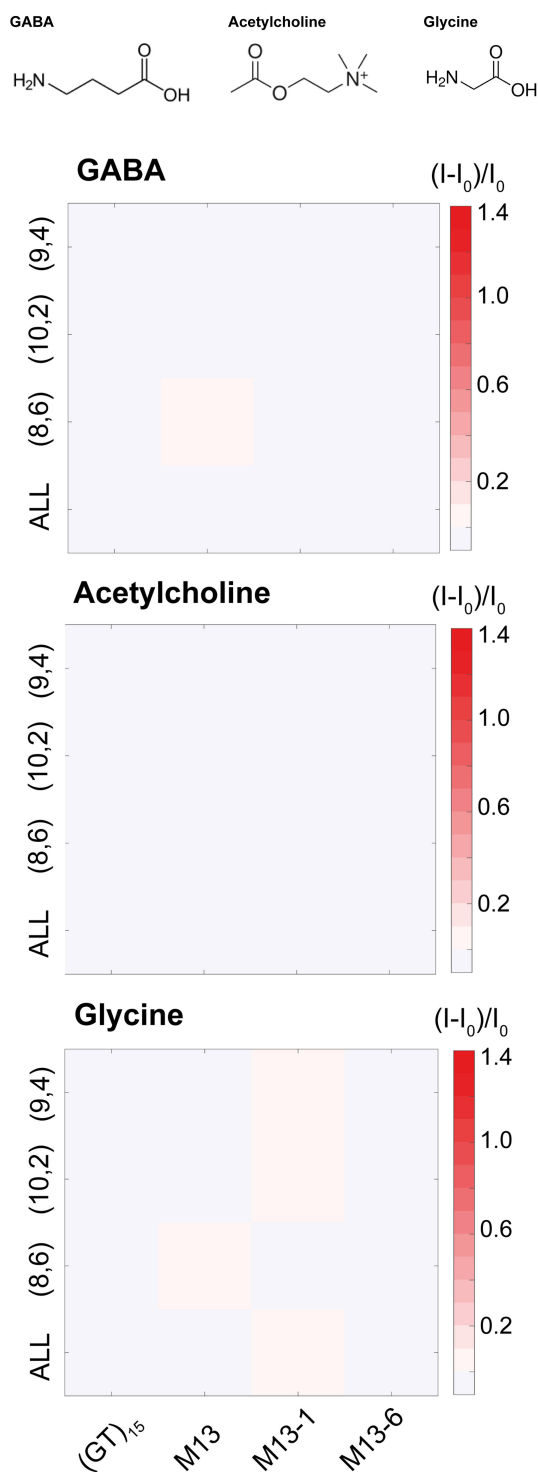


Figure A.17 – Response of the DNA-SWCNT complexes to GABA, acetylcholine, and glycine. Response of the DNA-SWCNT sensors towards γ -aminobutyric acid (GABA), acetylcholine, and glycine (final analyte concentrations of 100 μ M) as a function of the intensity of the (9,4), (10,2), and (8,6) chiralities as well as the integrated intensity under 745 nm excitation (labelled ALL). The response (I) is normalised to the intensity before analyte addition (I_0).

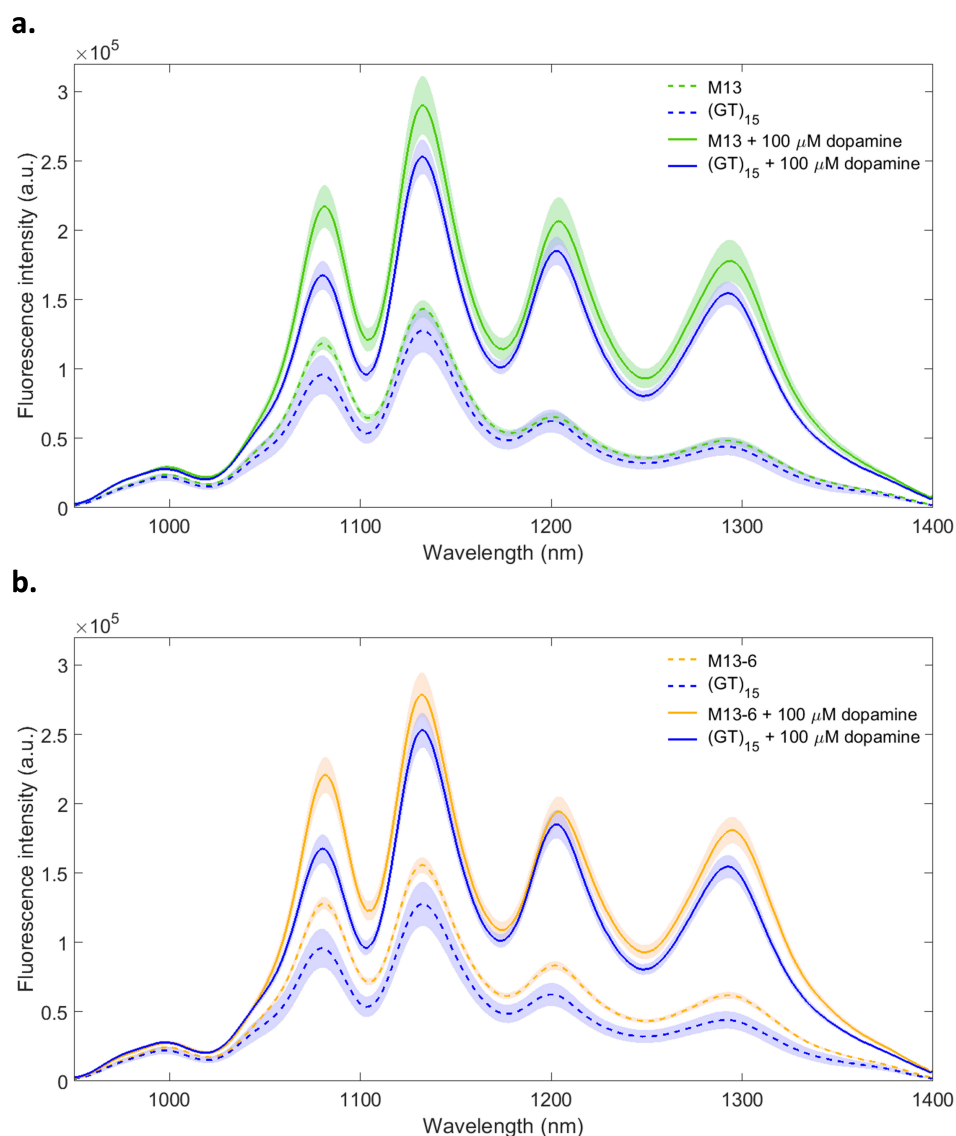


Figure A.18 – Fluorescence spectra for the M13- and M13-6-SWCNT complexes. Fluorescence spectra of the reference and the mutant complexes, before (dotted lines) and after (solid lines) dopamine addition under 745 nm excitation. (a) Fluorescence spectra of the (GT)₁₅-SWCNT (blue curves) and the M13-SWCNT complex (green curves). (b) Fluorescence spectra of the (GT)₁₅-SWCNT (blue curves) and the M13-6-SWCNT complex (orange curves). The shaded areas represent 95 % confidence intervals.

Table A.4 – Increase in imaging depth for the M13-1-SWCNT complex. Increase in penetration depth ($d2 - d1$) in brain cortex tissue ($\gamma_{em} \approx 10 \text{ cm}^{-1}$) by accounting for the increase in intensity (α) observed for the M13-1 mutant for the different SWCNT chiralities as well as the integrated intensity under 745 nm excitation (labelled as “ALL”).

| SWCNT considered | $\gamma_{em} \text{ (cm}^{-1}\text{)}$ | α | $d2 - d1 \text{ (}\mu\text{m)}$ |
|------------------|--|----------|---------------------------------|
| ALL | 10 | 1.41 | 149 |
| (9,4) | 10 | 1.43 | 155 |
| (10,2) | 10 | 1.54 | 188 |
| (8,6) | 10 | 1.56 | 193 |

Appendix A. Modulating the optical properties of DNA-SWCNT sensors by directed evolution

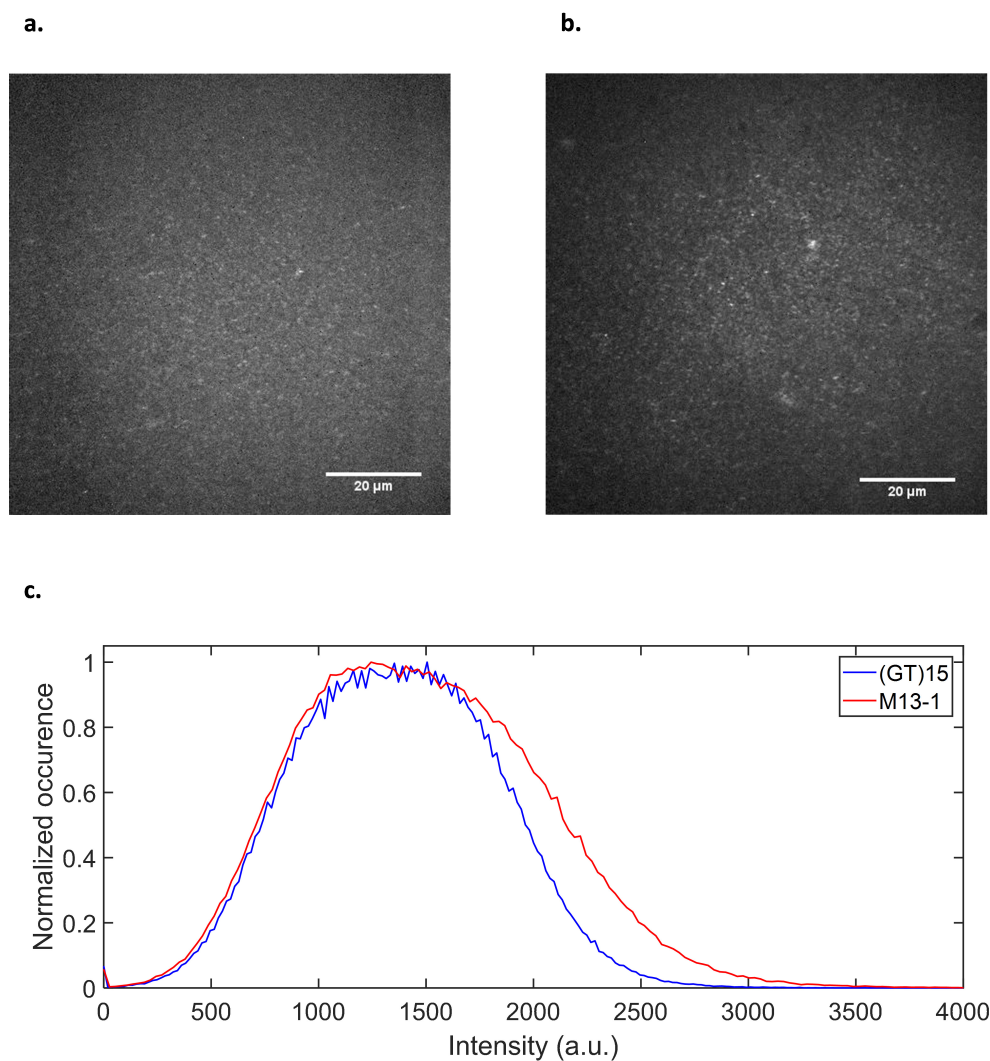


Figure A.19 – Intensity of DNA-SWCNT in NIR confocal microscopy. NIR confocal microscopy images of (a) (GT)₁₅-SWCNT and (b) M13-1-SWCNT complexes. (c) Distribution of the intensity for both the (GT)₁₅-SWCNT (blue) and M13-1-SWCNT (red) complexes imaged by confocal microscopy. Each histogram represents the average of two images taken at different positions.

B Directed evolution of nanosensors for the detection of mycotoxins

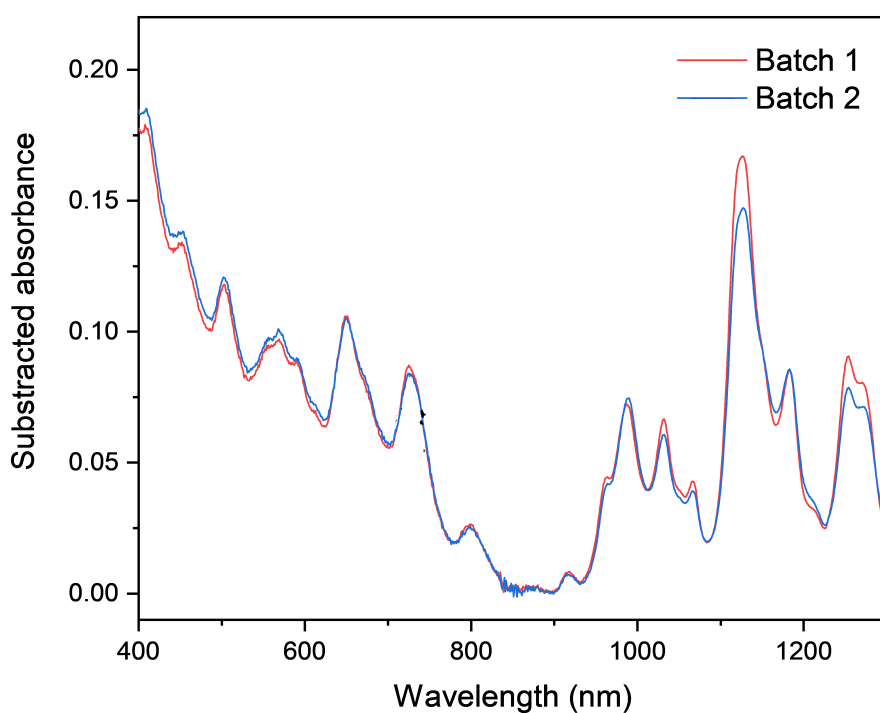


Figure B.1 – Differences between HiPco-SC batches. Absorbance spectra of HiPco-SC (2 % SC) batches. The spectra are both subtracted by the background value at 894 nm.

Appendix B. Directed evolution of nanosensors for the detection of mycotoxins

Table B.1 – Extinction coefficients ϵ for the mycotoxins used in the study. The toxins were diluted in the indicated solvent before UV-VIS measurement.

| Mycotoxin | ϵ (L.cm ⁻¹ .mM ⁻¹) | Wavelength (nm) | Solvent | Reference |
|-----------|--|-----------------|--------------|---------------------------|
| AFB1 | 21.8 | 363 | Ethanol | [266] |
| OTA | 5.5 | 333 | Methanol | [267] |
| ZEN | 6.02 | 316 | Methanol | [268] |
| DON | 5.28 (6.81) | 235 (221) | Acetonitrile | Estimated from [269, 270] |

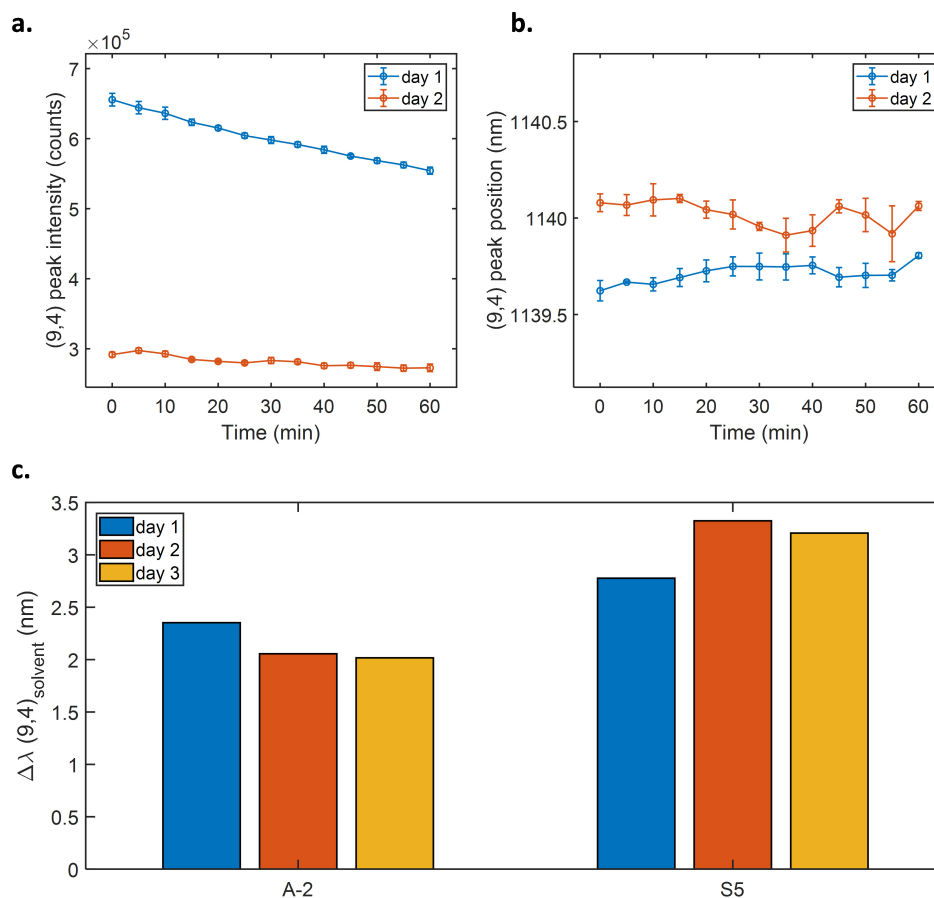


Figure B.2 – Aging of the DNA-SWCNT complexes. Effect of aging on (a) the fluorescence intensity, (b) peak position and (c) AFB1 shifting response of the sensors for the (9,4) chirality. The kinetics (a,b) were performed on the F-3 sensor. The dependence on AFB1 shifting response was performed on the A-2 and S5 sensors after a post-addition time of 200 min and with a AFB1 concentration of 10 μM . Although the aging affects significantly the intensity of the sensors, it does not affect strongly the position of the emission peak or the analyte response.

Appendix B. Directed evolution of nanosensors for the detection of mycotoxins

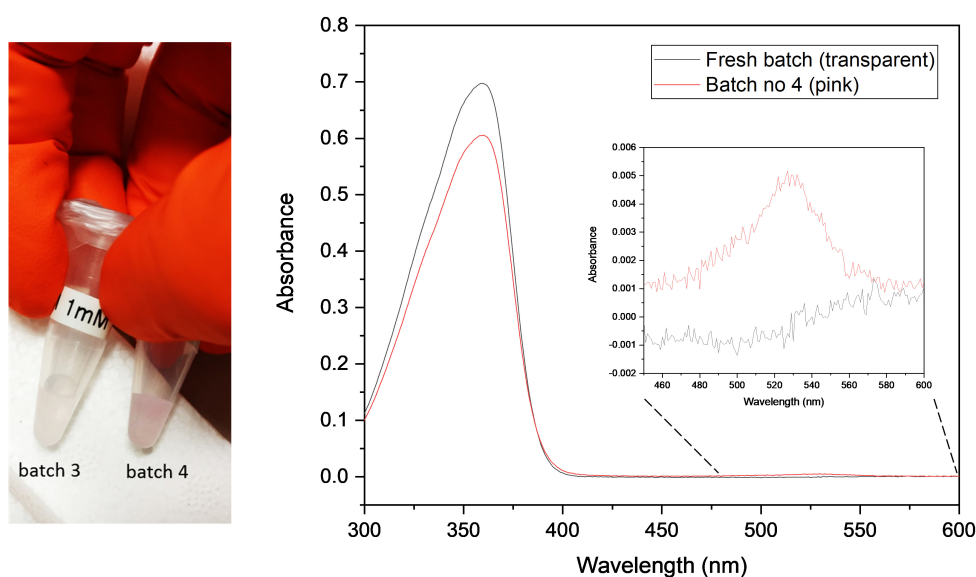


Figure B.3 – Absorbance of the oxidized AFB1. (left) Picture of the fresh ("batch 3") and oxidized ("batch 4") AFB1 stocks. (right) Absorbance spectrum of the fresh and oxidized AFB1 stocks. Both solutions present the 363 nm peak characteristic of AFB1, however the oxidized solution also exhibits a peak around 530 nm in accordance with the visible pink color.

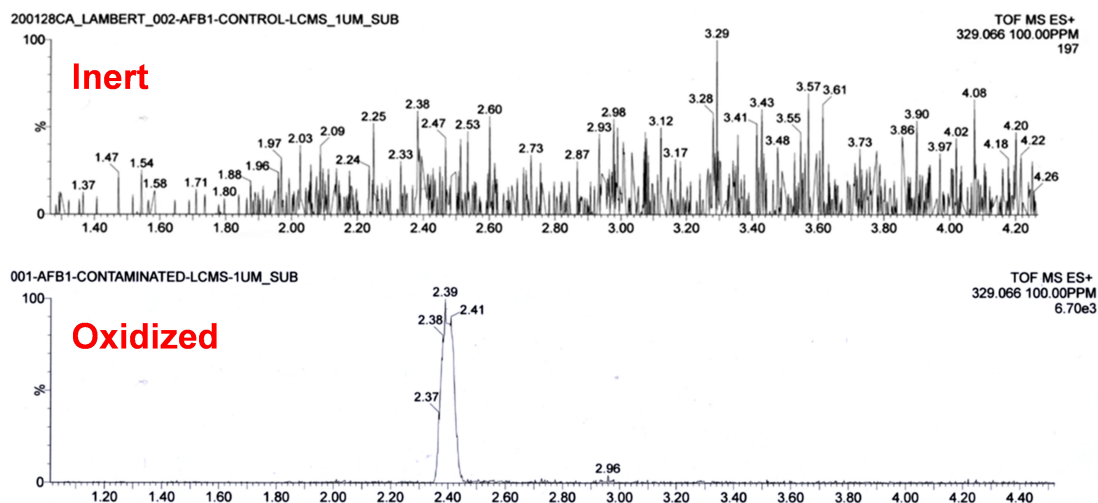


Figure B.4 – HPLC-MS chromatogram of the oxidized AFB1 sample. (left) Picture of the fresh ("batch 3") and oxidized ("batch 4") AFB1 stocks. HPLC-MS chromatograms for the aflatoxin B1 exo-8,9-epoxide ($C_{17}H_{12}O_7$) (m/z equal to 329.066) for (top) inert and (bottom) oxidized batches of AFB1. The HPLC was performed on a C_{18} column and the MS analysis by electrospray in positive mode.

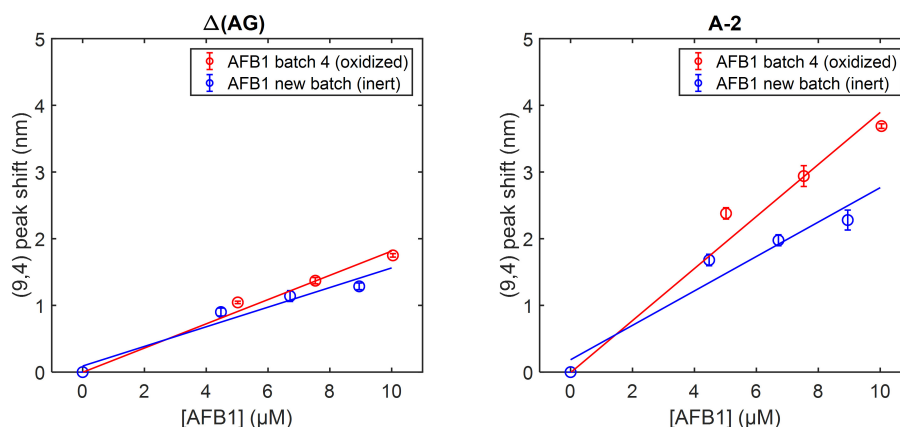


Figure B.5 – Response towards the oxidized AFB1. Peak positions of the (9,4) chirality for (left) the $\Delta(AG)$ and (right) the A-2 sensors in presence of inert (blue) and oxidized (red) AFB1 batches. The final AFB1 concentrations were comprised between 0 and 10 μM . All measurements were performed 200 min post-addition. The error bars represent 1 σ ($n = 3$). The calibration curves were fitted with linear fits.

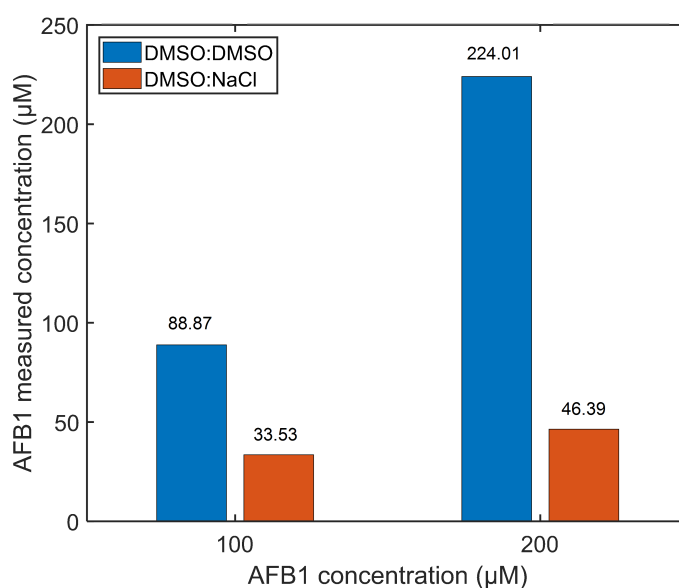


Figure B.6 – Solubility of the AFB1 solutions. Solutions of AFB1 were prepared by mixing 1 μL of AFB1 stock solution (10 or 20 mM in DMSO) in 99 μL of DMSO (blue) or 0.1 M NaCl (orange). The samples were incubated at room temperature for 1 h and centrifuged at 21,130 $\times g$ for 5 min in order to pellet possible aggregates. A small portion of the supernatant (20 μL) was taken, mixed with ethanol (180 μL) and the concentration was measured by absorbance spectroscopy using the extinction coefficient listed in the **Table B.1**. The expected values of concentrations are listed on the X axis and the measured concentrations on the Y axis (and above the bars).

Appendix B. Directed evolution of nanosensors for the detection of mycotoxins

Table B.2 – List of the main sequences discussed in this study. The red underlined letters represent the mutation compared to the parent sequence.

| Name | Parent | Sequence (5' to 3') |
|--------------------|--------------------|--|
| (AG) ₁₅ | / | AGAGAGAGAGAGAGAGAGAGAGAGAGAGAGAG |
| Δ(AG) | (AG) ₁₅ | AGAGAGAGAGAGAG <u>G</u> GAGAGAG <u>C</u> <u>G</u> <u>G</u> GAGAG |
| A-1 | Δ(AG) | AGAGAGAGAGAGAGGGAG <u>T</u> GAGCGGGAGAG |
| A-2 | A-1 | AGAGAGAGAGAGAGGGAGTGAGCGGGAG <u>G</u> <u>G</u> |
| A-3 | A-2 | <u>T</u> GAGAGAGAGAGAGGGAGTGAGCGGGAGGG |
| A-4 | A-3 | TGAGAGAGAGAG <u>G</u> GGGAGTGAGCGGGAGGG |
| B-1 | Δ(AG) | AGAGAGAG <u>G</u> GAGAGGGAGAGAGCGGGAGAG |
| B-2 | B-1 | AGAGAGAGGGAGAGGGAG <u>G</u> GAGCGGGAGAG |
| C-1 | Δ(AG) | AG <u>C</u> GAGAGAGAGAGGGAGAGAGCGGGAGAG |
| C-2 | C-1 | AGCGAGAGAGAGAGGGAGAGAGCGGGAG <u>C</u> <u>G</u> |
| S5 | A-2, B-2 | GAGGGGAGGGAGAGGGAGGGGAGAGGAGTG |
| Q-1 | S5 | GAGGGGAGGGAGAGG <u>T</u> GAGGGGAGAGGAGTG |
| Q-2 | Q-1 | GAGG <u>C</u> GAGGGAGAGGTAGGGGAGAGGAGTG |
| Q-3 | Q-2 | GAGGCC <u>T</u> GGGAGAGGTAGGGGAGAGGAGTG |
| F-1 | S5 | GAGGGGAGG <u>A</u> AGAGGGAGGGGAGAGGAGTG |
| F-2 | F-1 | GAGGGGAG <u>A</u> AAGAGGGAGGGGAGAGGAGTG |
| F-3 | F-2 | GAGGGGAGAAAGAGG <u>A</u> AGGGGAGAGGAGTG |

Table B.3 – Efficiency of toxin removal step by HPLC-MS. The removal of toxin during ethanol precipitation was verified using HPLC-MS for AFB1 and FB1 by calculating the relative concentration of toxin (in %) before and after ethanol precipitation.

| Toxin | Before | After |
|-------|--------|-------|
| AFB1 | 100 | 0.019 |
| FB1 | 100 | 0.025 |

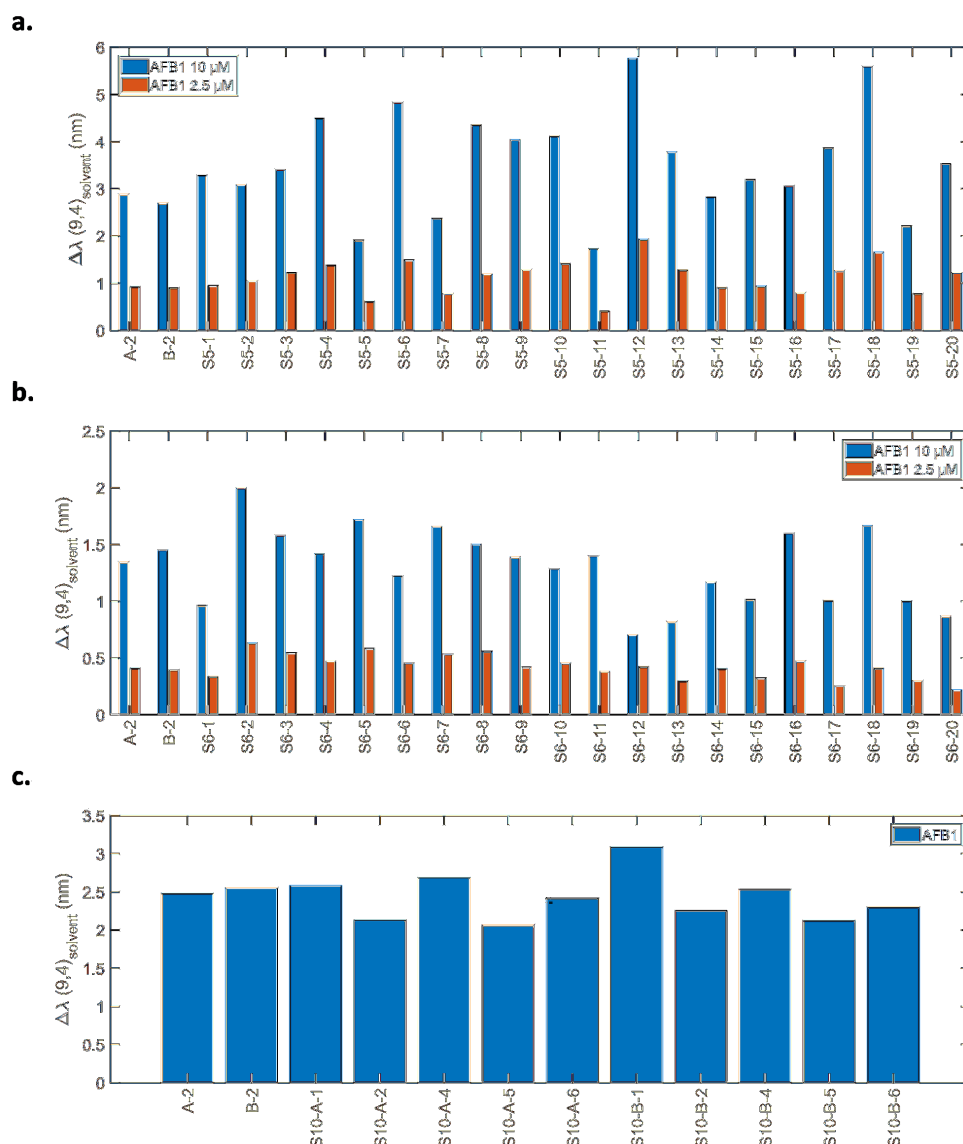


Figure B.7 – Response towards AFB1 for the shuffled mutants. Shifting of the (9,4) peak for the shuffled mutants of the A-2 and B-2 sequences with cut size of (a) 5 and (b) 6 nucleotides. (c) Shuffled mutants of A-2 or B-2 individual sequences with cut size of 10 nucleotides. All measurements were performed 200 min post-addition. The AFB1 was at a final concentration of 10 μ M (blue) or 2.5 μ M (orange). The variations observed for the responses of A-2 and B-2 can be explained by variations of concentration between AFB1 batches. The AFB1 batches prepared under non-inert conditions in DMSO.

Appendix B. Directed evolution of nanosensors for the detection of mycotoxins

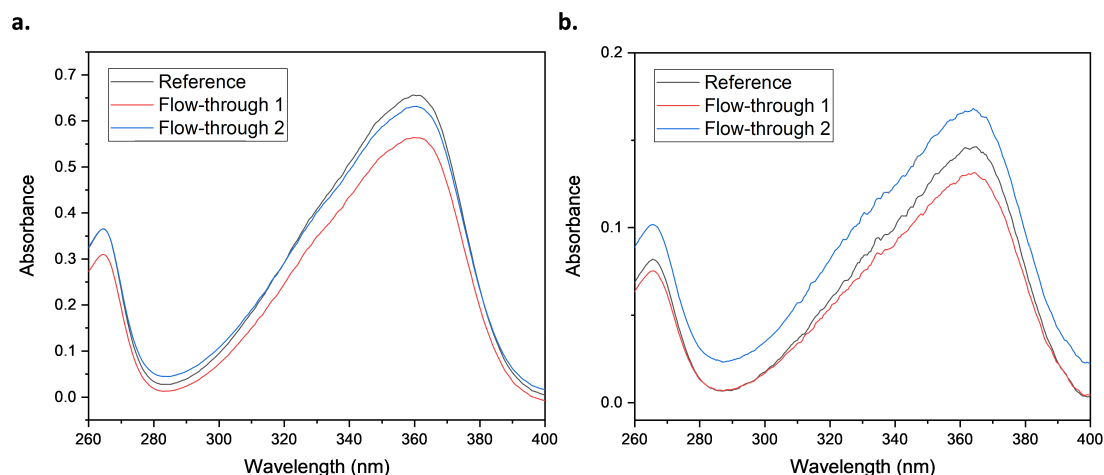


Figure B.8 – Purification of AFB1 samples through PTFE filters. Absorbance spectra of the AFB1 in (a) 100 % methanol and (b) 60 % methanol before (reference) and after filtration through 0.22 μm PTFE filter. This control confirms that the purification of spiked corn samples with PTFE filters does not affect the final concentration of AFB1.

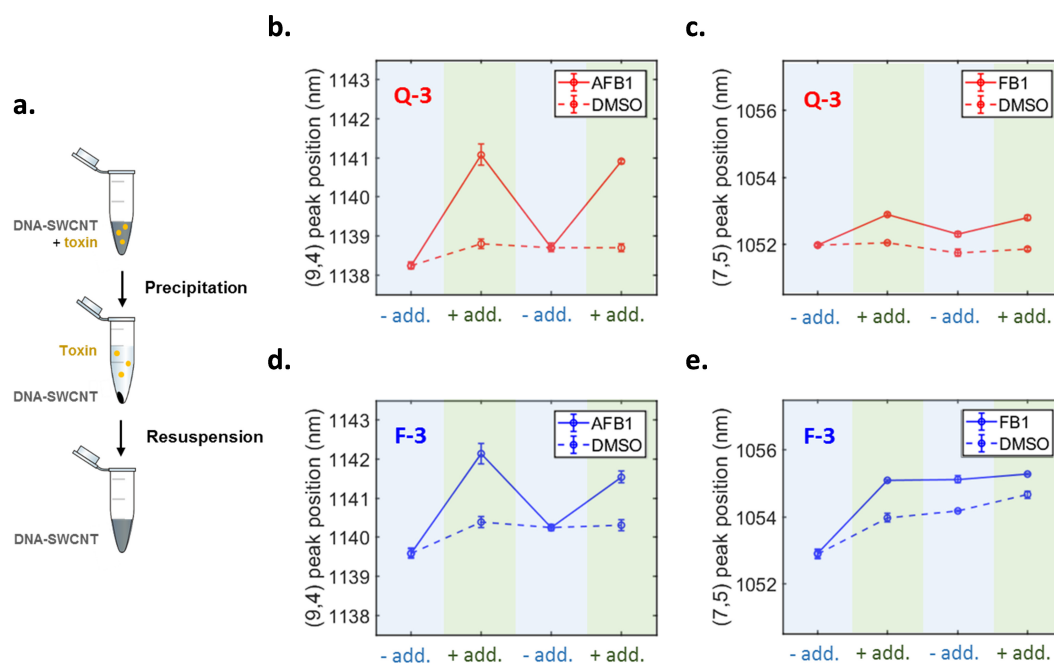


Figure B.9 – Reversibility of the Q-3 and F-3 sensors. (a) Schematic of the simple washing procedure. (b,c) Peak positions of the (9,4) and (7,5) chiralities for the Q-3 sensor, respectively, following the addition of toxin solution (10 μM). (d,e) Peak positions (9,4) and (7,5) chiralities for the F-3 sensor, respectively, following the addition of toxin solution (10 μM). All measurements were performed 200 min post-addition. The error bars represent 1 σ ($n = 3$).

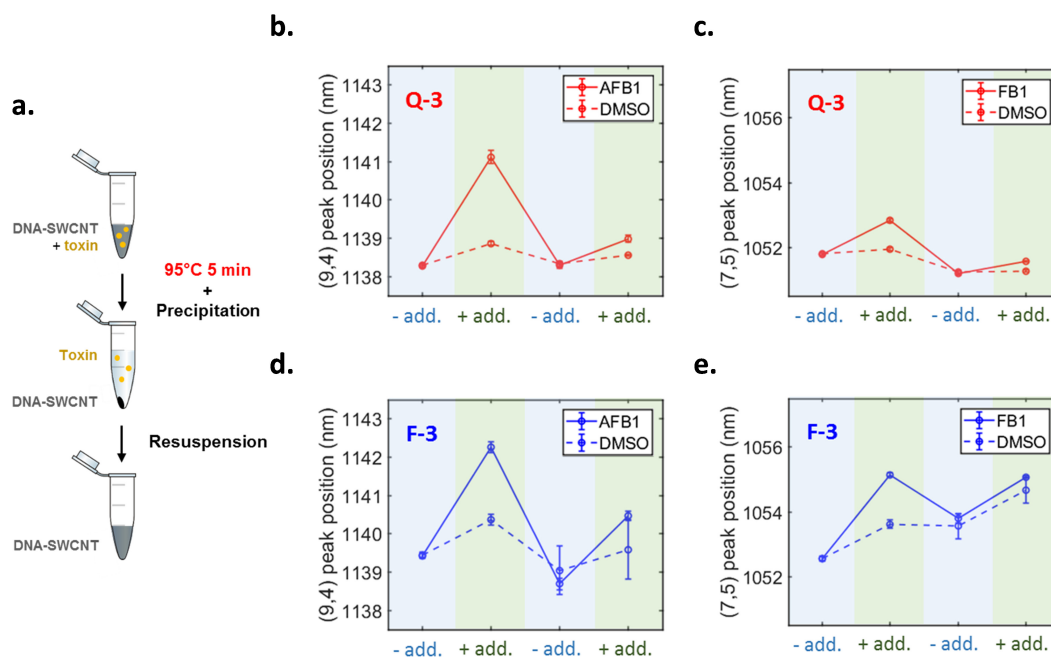


Figure B.10 – Reversibility of the Q-3 and F-3 sensors with an additional denaturation step. (a) Schematic of the modified washing procedure with the additional denaturation step to disrupt the interaction between the toxin and the DNA-SWCNTs. (b,c) Peak positions of the (9,4) and (7,5) chiralities for the Q-3 sensor, respectively, following the addition of toxin solution (10 μ M). (d,e) Peak positions (9,4) and (7,5) chiralities for the F-3 sensor, respectively, following the addition of toxin solution (10 μ M). All measurements were performed 200 min post-addition. The error bars represent 1 σ ($n = 3$).

Appendix B. Directed evolution of nanosensors for the detection of mycotoxins

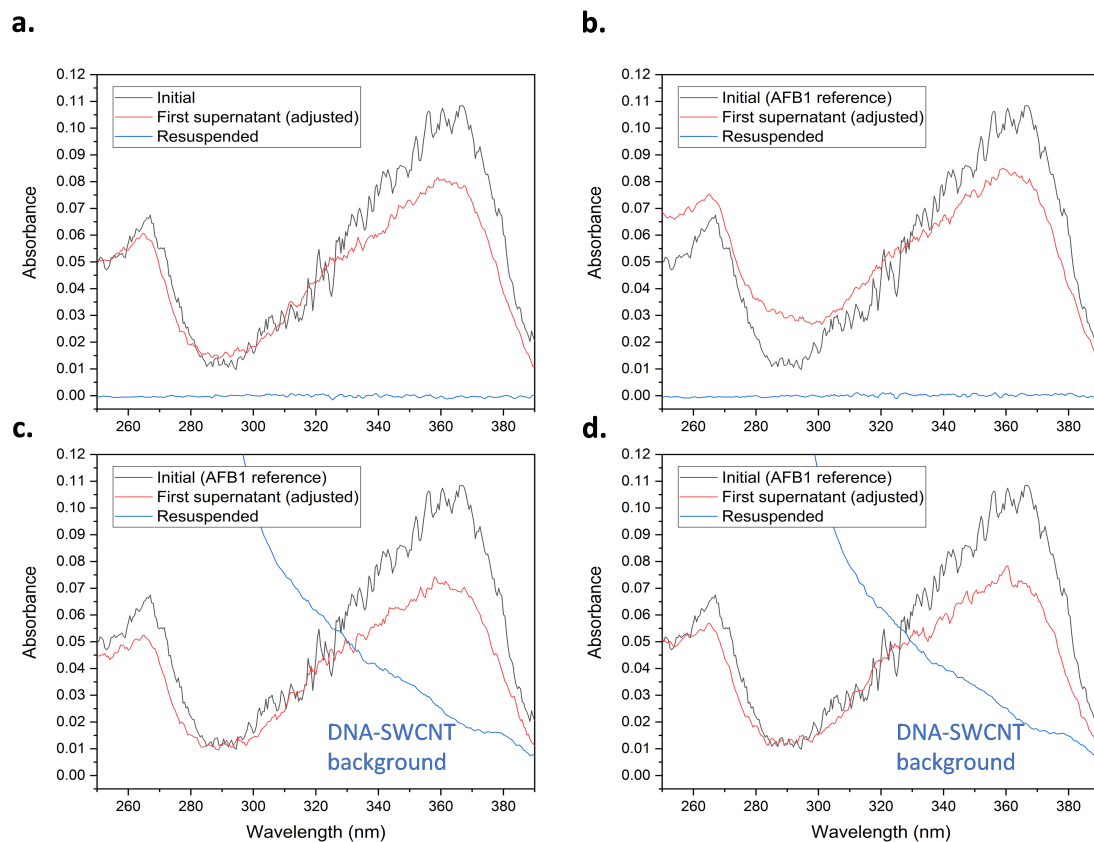


Figure B.11 – Efficiency of toxin removal step by absorbance spectroscopy. The removal of AFB1 during ethanol precipitation verified by absorbance spectroscopy. (a) Without nanotubes. (b) With 2 % SC-SWCNTs. (c) With A-4 DNA-SWCNT. (d) With $\Delta(S5)$ -16 DNA-SWCNT (16th mutant of S5). The first supernatant of the precipitation procedure (ethanol fraction, not containing SWCNTs) is shown here to contain most of the AFB1, hence proving the validity of this technique for the removal of toxins from DNA-SWCNT sensors.

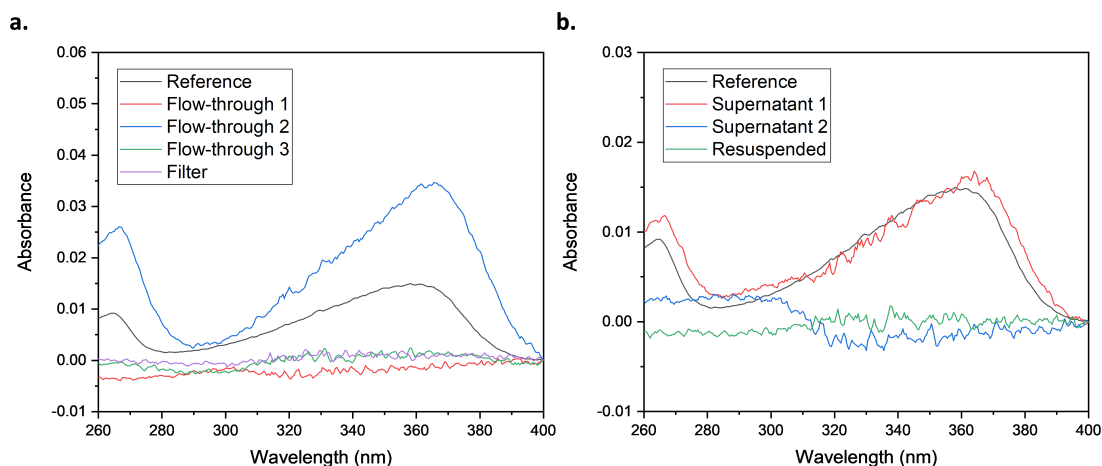


Figure B.12 – Comparison of AFB1 removal with filtering and precipitation. (a) Absorbance spectra of the samples processed by filtering with an Amicon Ultra-0.5 3kDa filter. The reference indicates the initial sample containing AFB1. DI water was added to the sample for the first centrifugation, 50 % ethanol was added for the second and third centrifugations. The filter fraction was washed several times with DI water to remove traces of ethanol and resuspended in 0.1 M NaCl. (b) Absorbance spectra of the samples processed by precipitation. The reference indicates the initial sample containing AFB1. The first precipitation was performed with 100 % ethanol and the second precipitation with 70 % ethanol. The samples were resuspended in 0.1 M NaCl.

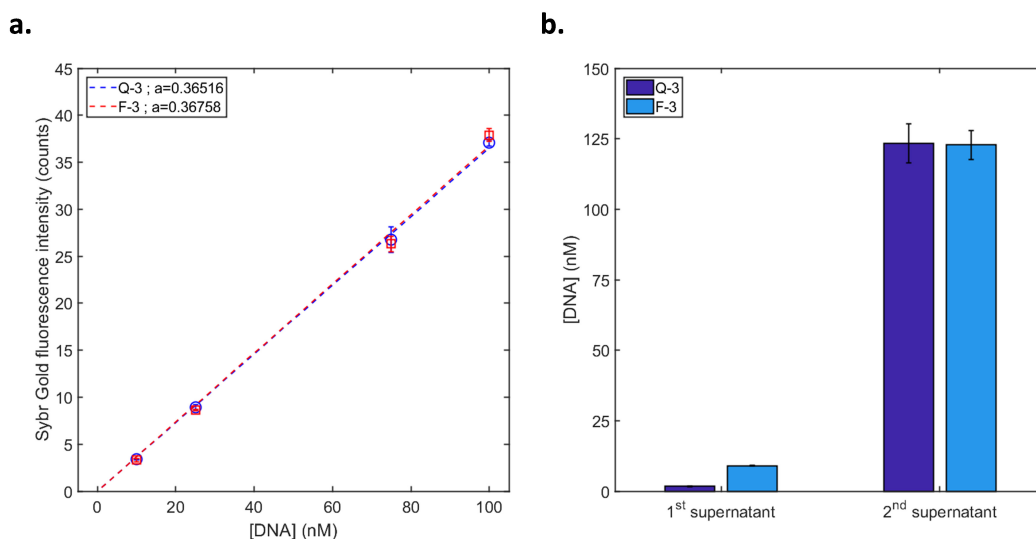


Figure B.13 – Determination of the amount of DNA lost during DNA-SWCNT precipitation. (a) The calibration curve of the Q-3 and F-3 DNA to the fluorescence of the Sybr Gold dye was used to determine the free DNA concentration. (b) Determined concentration of DNA in supernatants from the DNA-SWCNT precipitation protocol. Error bars represent 1 σ (n = 3).

Appendix B. Directed evolution of nanosensors for the detection of mycotoxins

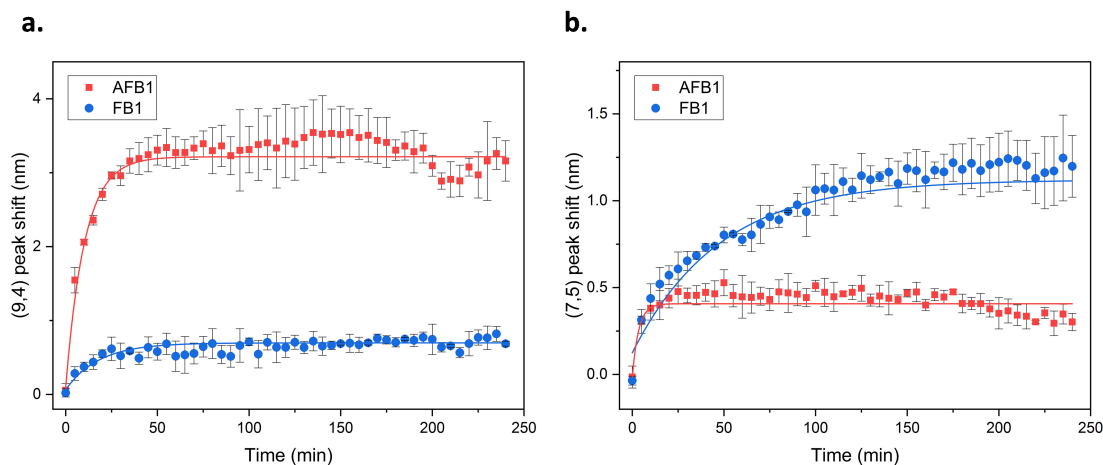


Figure B.14 – Response kinetics for the AFB1 and FB1. Response kinetics for the (a) (9,4) and (b) (7,5) chiralities of the S5 sensor towards AFB1 (5 μ M, red) and FB1 (5 μ M, blue) for the. We noted that for the S5 sensor, the AFB1 response reached its maximum after less than 50 min while the FB1 response took almost 200 min to plateau. All fits are single exponential fits. Error bars represent 1 σ (n = 3). The AFB1 batches were prepared under non-inert conditions in DMSO. The FB1 batches were prepared in methanol.

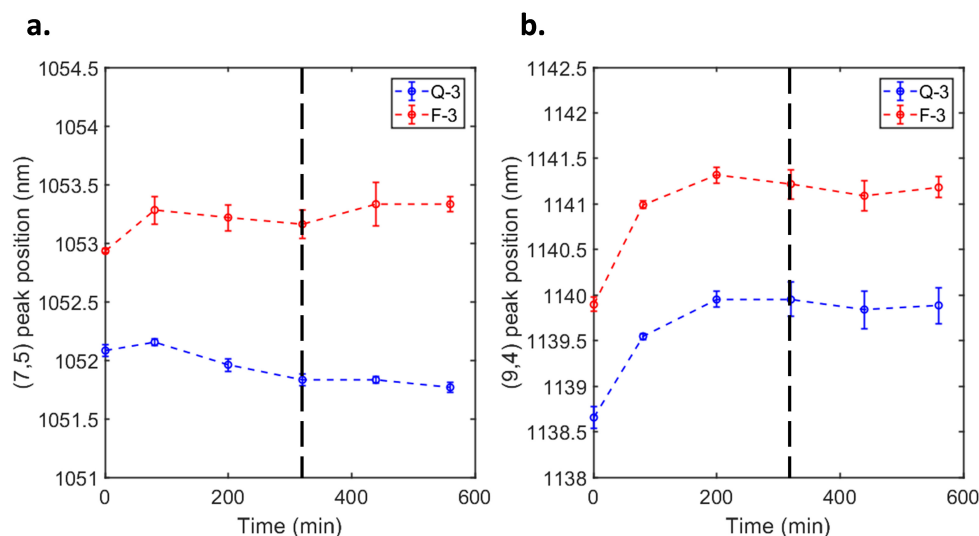


Figure B.15 – Evolution of the peak position with the extracted corn. Evolution of the (a) (7,5) and (b) (9,4) peak positions for the Q-3 (blue) and F-3 (red) sensors as a function of time. The peak position stabilized after 320 min (black horizontal line). The error bars represent 1 σ (n = 3).

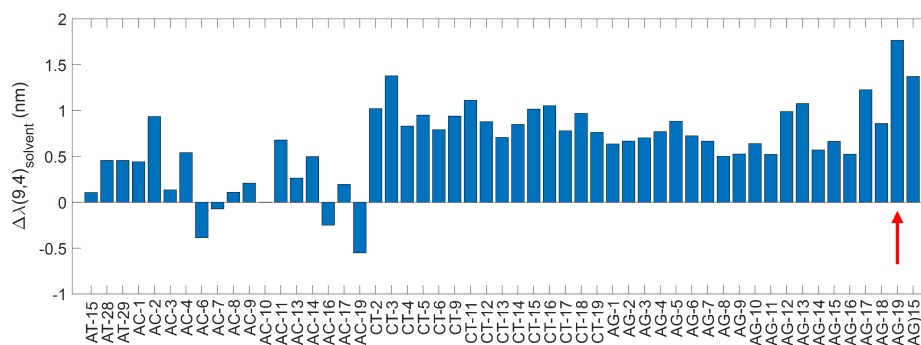


Figure B.16 – Initial screening towards AFB1. Shifting of the (9,4) peak for 53 complexes from the first screening library towards AFB1 (10 μ M final). The Δ (AG) mutant is indicated by the red arrow ("AG-19"). The measurements were taken after 20 min. The AFB1 batches prepared under non-inert conditions in DMSO.

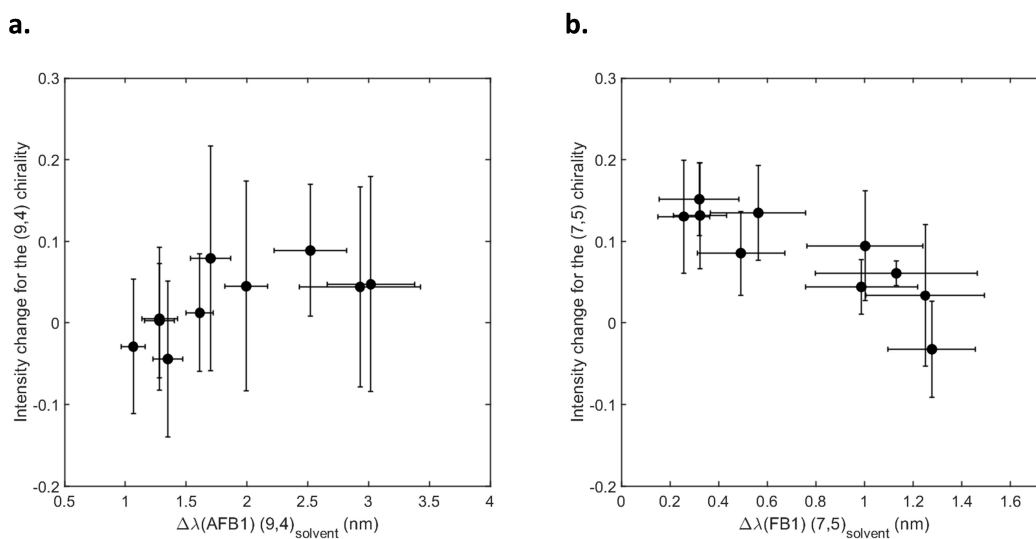


Figure B.17 – Intensity change as a function of the shifting response. Shift in peak position (with respect to the solvent) for (a) the (9,4) chirality in presence of AFB1 and (b) the (7,5) chirality in presence of FB1. The intensity change corresponds to $(I-I_0)/I_0$ with I the intensity of the sensor in presence of toxin and I_0 the intensity of the sensor in the solvent. The toxins are at a final concentration of 5 μ M. The error bars represent 1 σ ($n = 4$). The measurements are performed after a post-addition incubation time of 200 min.

Appendix B. Directed evolution of nanosensors for the detection of mycotoxins

Table B.4 – Summary of the shifting responses of the (9,4) chirality. Mean and standard deviation of the shifting responses in nm in presence of AFB1, FB1, OTA, ZEN and DON (all 10 μM) after a post-addition incubation time of 200 min.

| Name | AFB1 | FB1 | OTA | ZEN | DON |
|--------------------|-----------------|------------------|------------------|-----------------|------------------|
| (AG) ₁₅ | 0.78 \pm 0.09 | −0.46 \pm 0.04 | −0.06 \pm 0.58 | 0.45 \pm 0.03 | 0.02 \pm 0.03 |
| Δ (AG) | 1.65 \pm 0.16 | −0.07 \pm 0.07 | −0.17 \pm 0.05 | 0.69 \pm 0.07 | 0.00 \pm 0.06 |
| A-1 | 2.12 \pm 0.33 | 0.08 \pm 0.11 | −0.06 \pm 0.08 | 0.85 \pm 0.11 | 0.02 \pm 0.04 |
| B-1 | 2.27 \pm 0.26 | 0.18 \pm 0.12 | 0.04 \pm 0.10 | 0.82 \pm 0.10 | 0.03 \pm 0.06 |
| C-1 | 2.01 \pm 0.16 | 0.13 \pm 0.12 | 0.03 \pm 0.04 | 0.85 \pm 0.08 | 0.07 \pm 0.03 |
| A-2 | 3.18 \pm 0.29 | 0.59 \pm 0.28 | 0.38 \pm 0.10 | 1.30 \pm 0.19 | 0.01 \pm 0.07 |
| B-2 | 2.62 \pm 0.24 | 0.23 \pm 0.20 | 0.17 \pm 0.14 | 0.98 \pm 0.12 | 0.00 \pm 0.11 |
| C-2 | 2.56 \pm 0.22 | 0.23 \pm 0.21 | 0.08 \pm 0.17 | 1.10 \pm 0.11 | 0.08 \pm 0.14 |
| A-3 | 4.29 \pm 0.46 | 0.43 \pm 0.19 | 0.35 \pm 0.12 | 1.55 \pm 0.08 | 0.01 \pm 0.13 |
| A-4 | 5.20 \pm 0.71 | 0.39 \pm 0.15 | 0.18 \pm 0.15 | 1.74 \pm 0.17 | −0.06 \pm 0.10 |

Table B.5 – Summary of the shifting responses of the (7,5) chirality. Mean and standard deviation of the shifting responses in nm in presence of AFB1, FB1, OTA, ZEN and DON (all 10 μ M) after a post-addition incubation time of 200 min.

| Name | AFB1 | FB1 | OTA | ZEN | DON |
|--------------------|------------------|------------------|------------------|------------------|------------------|
| (AG) ₁₅ | 0.00 \pm 0.07 | −0.49 \pm 0.06 | −0.27 \pm 0.21 | 0.02 \pm 0.02 | −0.02 \pm 0.02 |
| Δ (AG) | −0.07 \pm 0.03 | 0.22 \pm 0.11 | 0.16 \pm 0.09 | 0.08 \pm 0.02 | 0.03 \pm 0.06 |
| A-1 | −0.19 \pm 0.04 | 0.52 \pm 0.22 | 0.44 \pm 0.22 | 0.09 \pm 0.08 | 0.03 \pm 0.06 |
| B-1 | −0.06 \pm 0.07 | 0.66 \pm 0.27 | 0.52 \pm 0.19 | 0.07 \pm 0.07 | 0.04 \pm 0.07 |
| C-1 | −0.03 \pm 0.03 | 0.36 \pm 0.16 | 0.28 \pm 0.09 | 0.08 \pm 0.03 | 0.03 \pm 0.03 |
| A-2 | 0.17 \pm 0.17 | 1.51 \pm 0.27 | 1.18 \pm 0.18 | 0.01 \pm 0.11 | 0.10 \pm 0.13 |
| B-2 | 0.18 \pm 0.20 | 1.22 \pm 0.28 | 0.95 \pm 0.17 | 0.07 \pm 0.07 | 0.01 \pm 0.15 |
| C-2 | −0.12 \pm 0.05 | 0.38 \pm 0.16 | 0.29 \pm 0.15 | 0.04 \pm 0.03 | −0.01 \pm 0.05 |
| A-3 | 0.20 \pm 0.23 | 1.41 \pm 0.39 | 1.10 \pm 0.29 | −0.28 \pm 0.51 | −0.09 \pm 0.11 |
| A-4 | 0.52 \pm 0.19 | 1.40 \pm 0.23 | 0.93 \pm 0.16 | 0.15 \pm 0.12 | 0.02 \pm 0.15 |

Appendix B. Directed evolution of nanosensors for the detection of mycotoxins

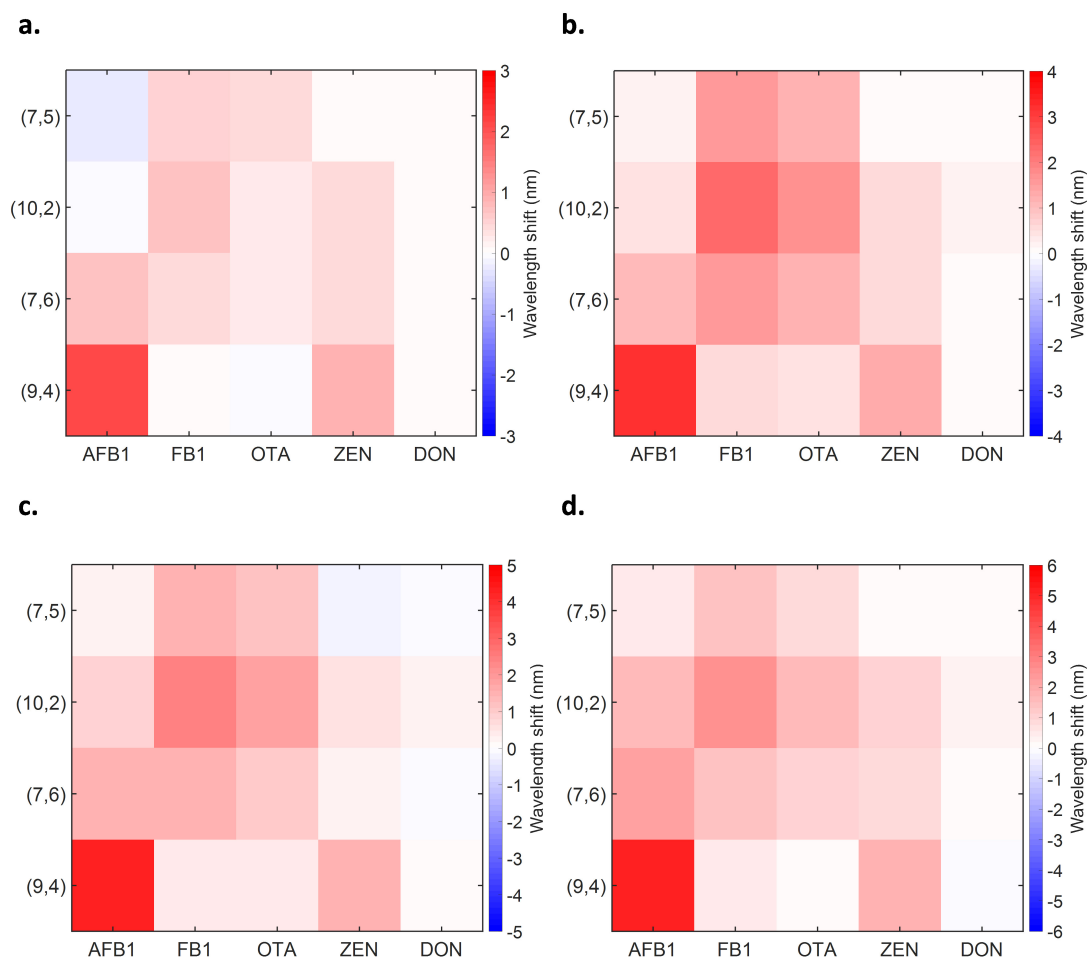


Figure B.18 – Response heatmaps of the mutant sensors. Response of the (a) A-1, (b) A-2, (c) A-3 and (d) A-4 sensors in presence of AFB1, FB1, OTA, ZEN and DON (all 10 μM). The measurements are performed after a post-addition incubation time of 200 min.

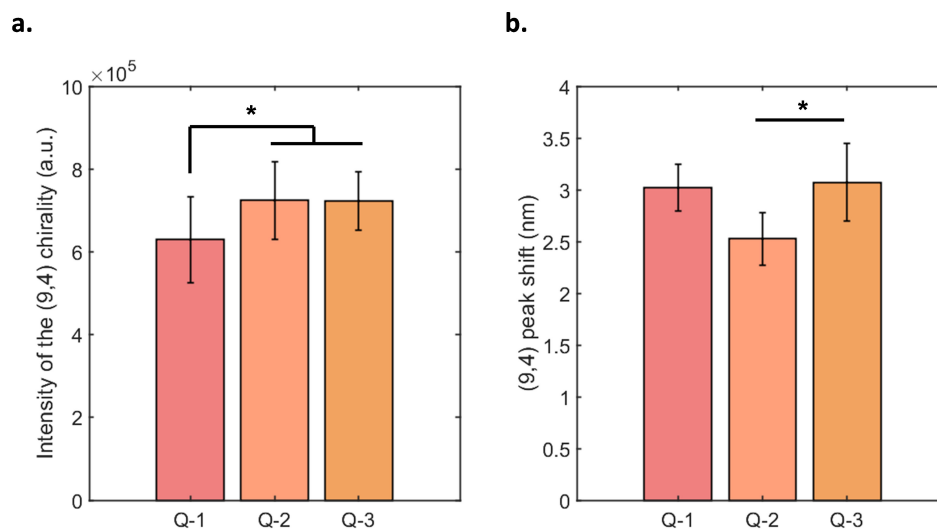


Figure B.19 – Evolution of the intensity and response for the improved intensity mutants. (a) Initial intensity of the (9,4) peak for the Q-1, Q-2 and Q-3 sensors. The symbol * shows a significant difference between the means for $p < 0.05$ (two-sample t-test, $n = 18$). The error bars represent 1σ ($n = 18$). (b) Shift of the (9,4) chirality in presence of AFB1 for the Q-1, Q-2 and Q-3 sensors. The AFB1 is at a final concentration of $10\ \mu\text{M}$. * $p < 0.05$ (two-sample t-test, $n = 3$). The error bars represent 1σ ($n = 3$). The measurements are performed after a post-addition incubation time of 200 min.

Appendix B. Directed evolution of nanosensors for the detection of mycotoxins

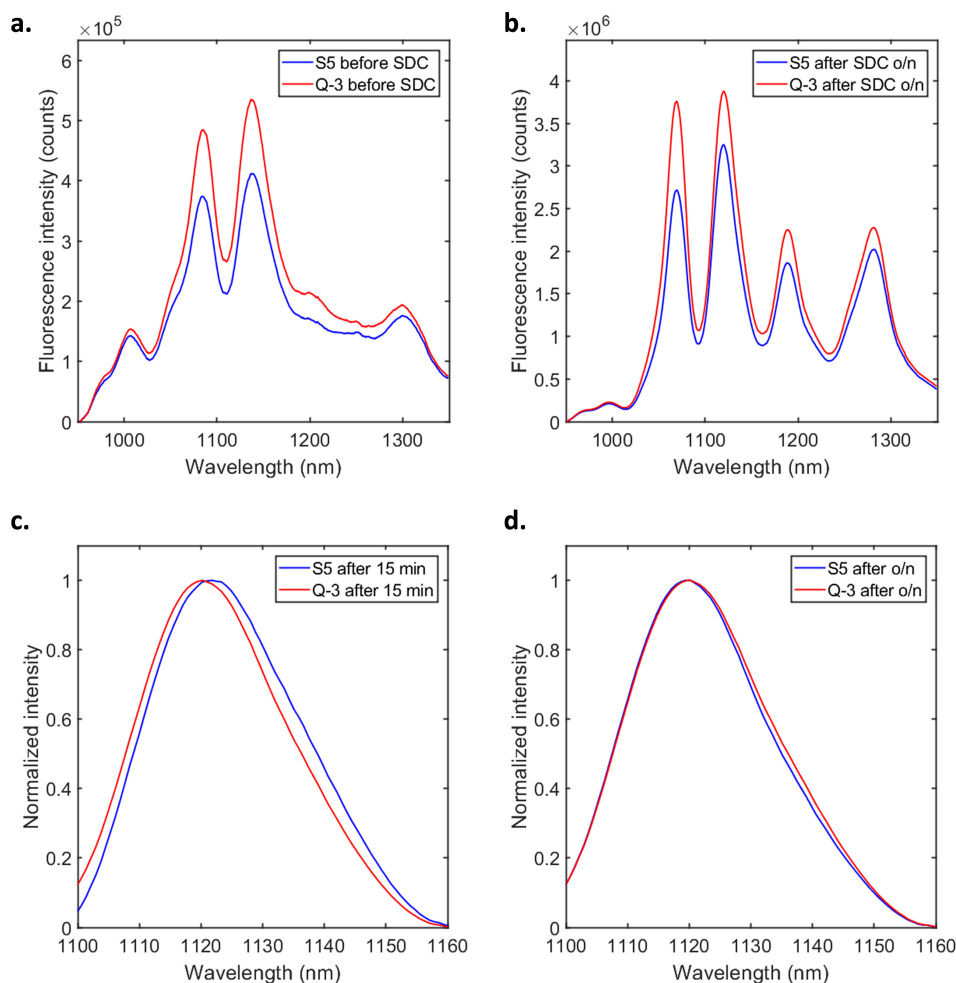


Figure B.20 – Fluorescence of the sensors before and after SDC replacement. Fluorescence spectra for the S5 (blue) and Q-3 (red) sensors (a) before and (b) after wrapping replacement with SDC (final concentration 0.1 %). The "after o/n" measurements are performed after an overnight incubation (> 12 h). Normalized spectra of the (9,4) peak for the S5 (blue) and Q-3 (red) (c) 15 min after SDC addition and (d) after overnight incubation with SDC. The successful completion of the replacement is evidenced by the overlap of the peak positions after overnight incubation. The final concentration of SDC is The lines represent the mean of 3 replicates. The retained differences post-replacement therefore indicate that the differences of fluorescence intensity observed are not due a change in QY but rather a result of changes in chirality distribution.

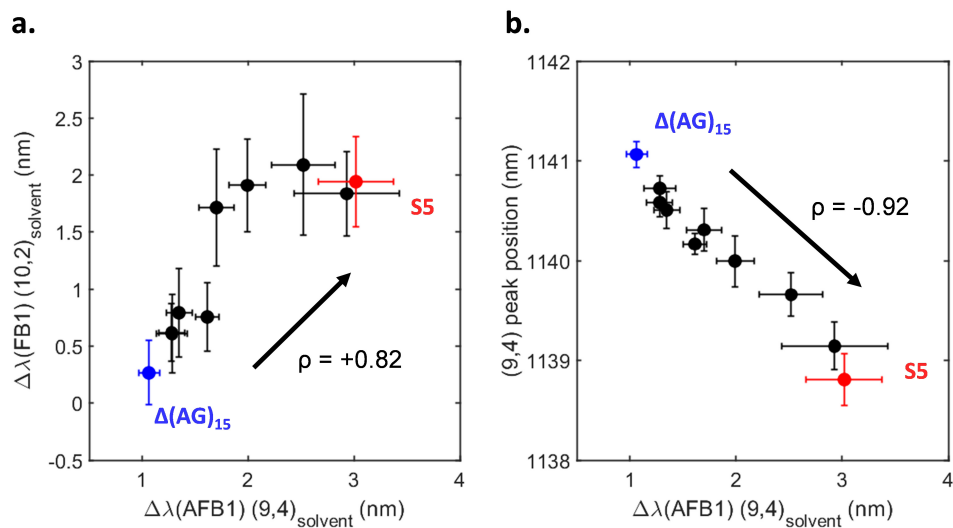


Figure B.21 – Effect of the AFB1 response improvement on the (10,2) FB1 response and peak position. Correlation of the (a) (10,2) FB1 response (b) (9,4) peak position pre-addition with the (9,4) AFB1 response. Spearman correlation tests were done for both datasets revealing a positive ($\rho = +0.82$, $p < 0.05$) and negative ($\rho = -0.92$, $p < 0.05$) correlation for the (a) and (b) panels, respectively. Measurements were taken 200 min post-addition of the relevant toxin (5 μM). Error bars represent 1 σ ($n = 4$).

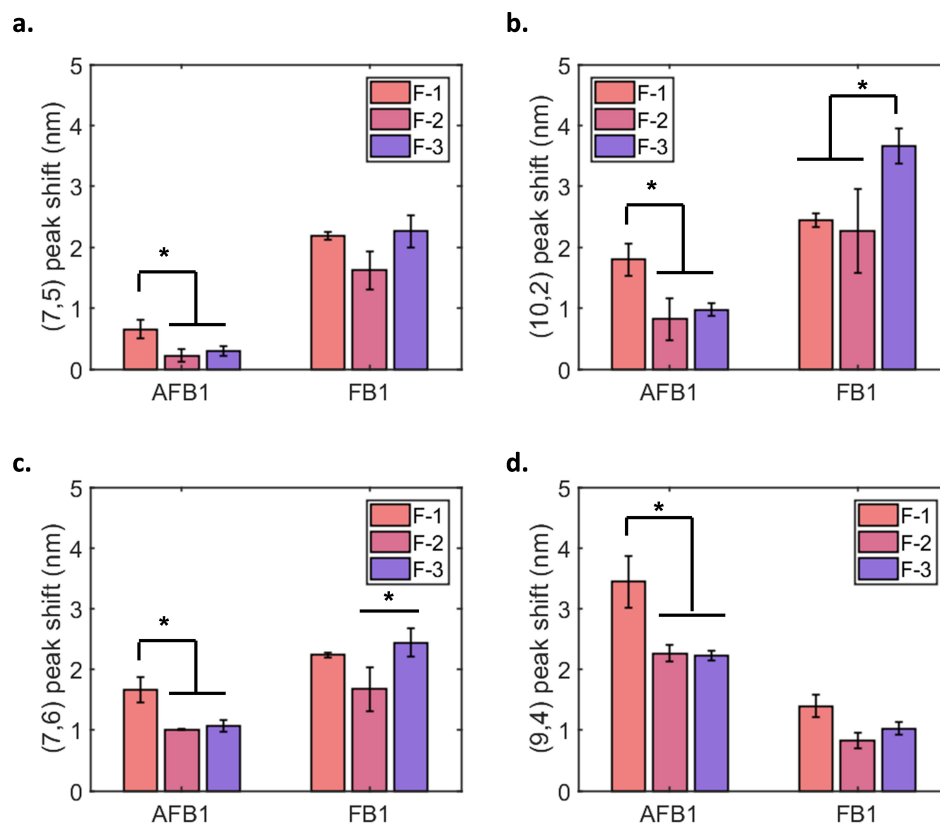


Figure B.22 – Evolution of the response for the improved FB1 mutants. Shifting response of the F-1, F-2, and F-3 mutants in presence of AFB1 (10 μ M) and FB1(10 μ M) for the (a) (7,5), (b) (10,2), (c) (7,6), and (d) (9,4) chiralities. * $p < 0.05$ (two-sample t-test, $n = 3$). Error bars represent 1 σ ($n = 3$). All measurements were performed 200 min post-addition. The FB1 batches were prepared in methanol.

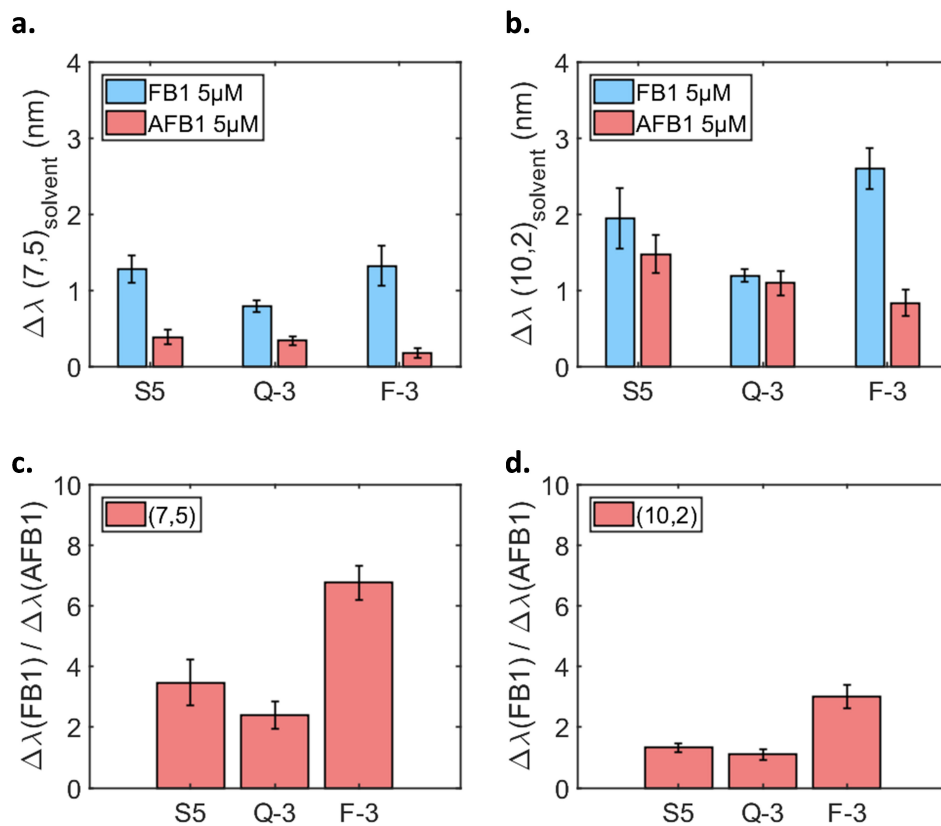


Figure B.23 – Selectivity of the FB1 response. Shifting response of the S5, Q-3, and F-3 sensors in presence of AFB1 (5 μM final concentration) and FB1 (5 μM final concentration) for the (a) (7,5) and (b) (10,2) chiralities. Ratios of the FB1 and AFB1 responses for the (c) (7,5) and (d) (10,2) chiralities. Error bars represent 1 σ ($n = 4$). Measurements were performed 200 min post-addition.

Appendix B. Directed evolution of nanosensors for the detection of mycotoxins

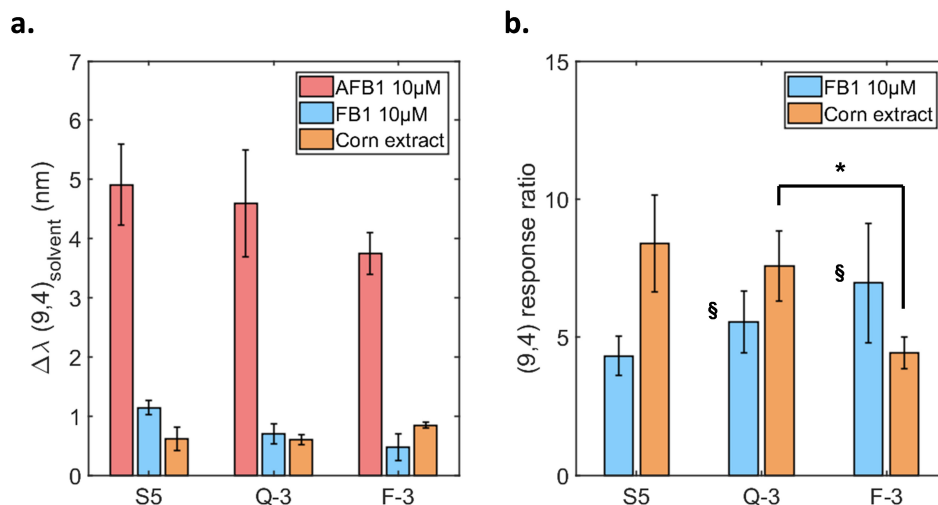


Figure B.24 – Selectivity of the AFB1 response. (a) Shifting response of the (9,4) chirality for the S5, Q-3, and F-3 sensors in presence of AFB1 (5 μM final concentration), FB1 (5 μM final concentration), and corn extract. (b) Ratios of the (9,4) chirality response to AFB1 versus the FB1 and corn extract responses (calculated as $\Delta\lambda(\text{AFB1})/\Delta\lambda(\text{FB1 or corn})$). All measurements were performed 200 min post-addition. * $p < 0.05$ (two-sample t-test, $n = 4$). Error bars represent 1σ ($n = 4$ for all except where § when $n=3$).

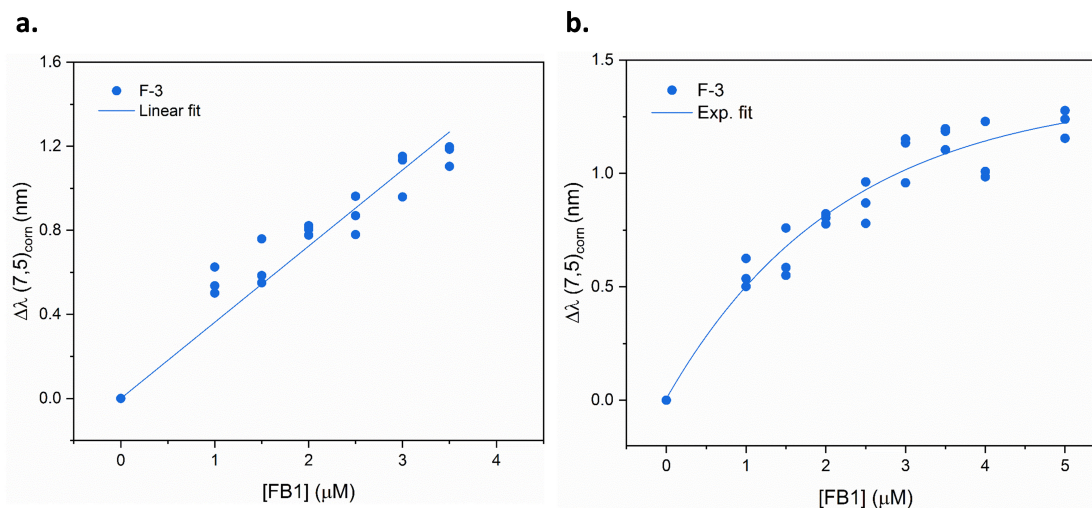


Figure B.25 – Fitting of the FB1 calibration curves. Calibration curves for the (7,5) chirality of the F-3 sensor in presence of FB1 fitted with a (a) linear fit and (b) single exponential fit. All measurements were performed 320 min post-addition in the presence of corn in 60 % methanol.

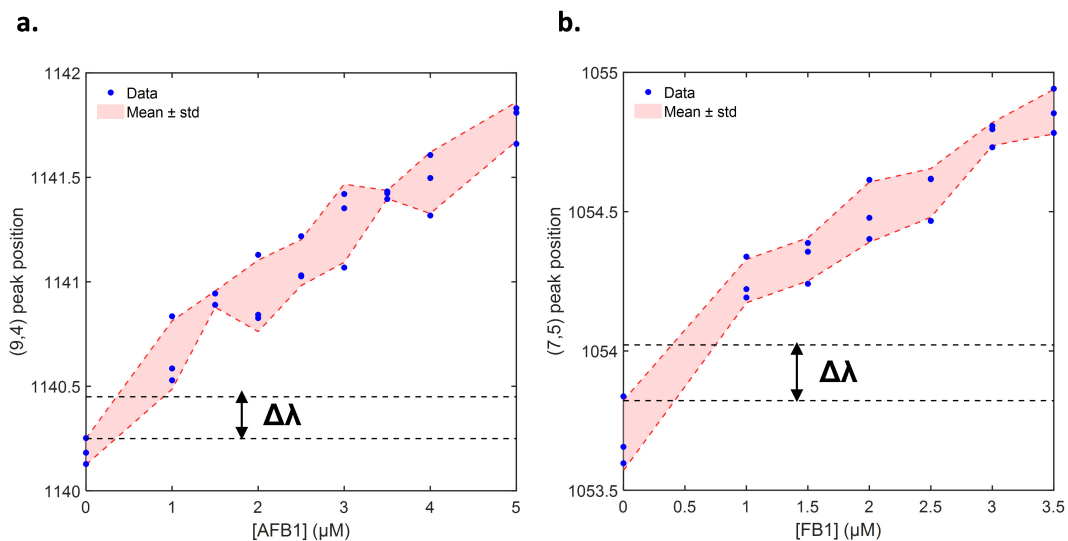


Figure B.26 – Limit of detection for the AFB1 and FB1 sensing. Calibration curves of the (a) (9,4) chirality (Q-3 sensor) towards AFB1 and (b) (7,5) chirality (F-3 sensor) towards FB1. The blue dots represent measured data and the red shaded area represents the mean of the data \pm the standard deviation. Horizontal lines indicate the minimal shift $\Delta\lambda$ necessary to identify a peak shift when compared to the negative control (0.2 nm). At a toxin concentration of 1 μM , the Q-3 sensor exhibits a shift ≥ 0.24 nm towards AFB1 and the F-3 sensor a shift ≥ 0.35 nm towards FB1. All measurements were recorded 320 min post-addition incubation in presence of corn in 60 % methanol.

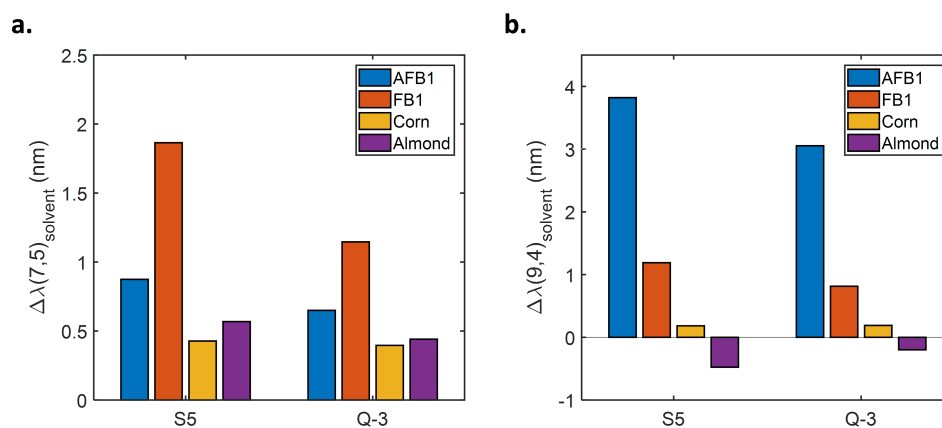


Figure B.27 – Response of the sensors in presence of almond extract. Shifting response of (a) the (7,5) and (b) the (9,4) chiralities in presence of AFB1, FB1, corn flour extract and almond flour extract. The measurements were performed with a toxin concentration of 5 μM and 200 min after addition.

Appendix B. Directed evolution of nanosensors for the detection of mycotoxins

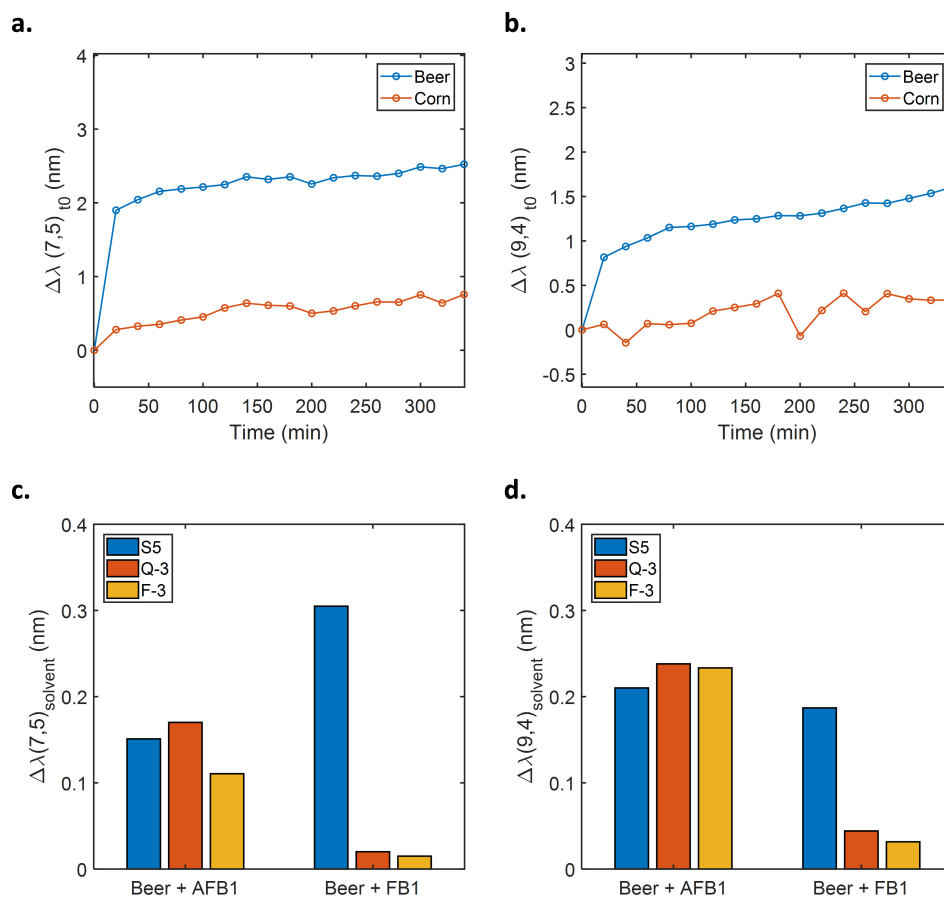
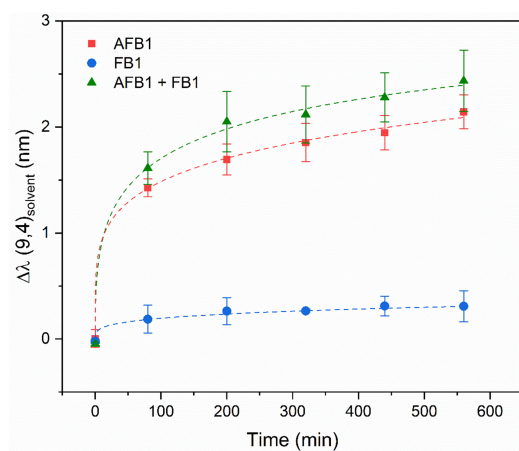


Figure B.28 – Response of the sensors in presence of beer. (a,b) Shifting of the (7,5) and (9,4) chiralities caused by corn extract (red) and beer (blue) as a function of time for the S5 sensor. (c,d) Shifting response of the (7,5) and (9,4) chiralities towards AFB1 and FB1 in presence of beer for the S5, Q-3 and F-3 sensors. The measurements were performed with a toxin concentration of 5 μM and 200 min after addition.

a.



b.

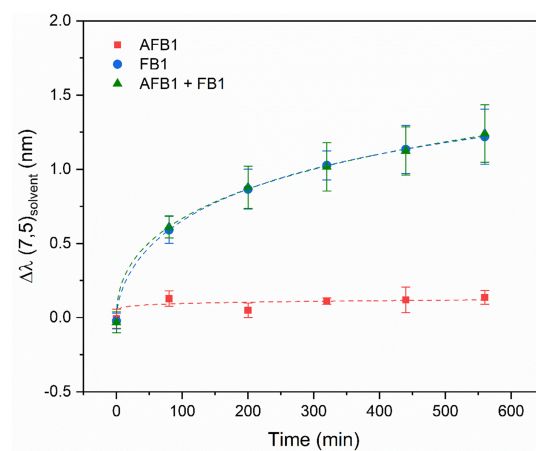


Figure B.29 – Response of the Q-3 and F-3 sensors towards toxin mixtures. The (9,4) and (7,5) chirality response of the (c) Q-3 and (d) F-3 sensors, respectively, towards AFB1 (2.5 μ M, red), FB1 (2.5 μ M, blue), and the toxin mixture (2.5 μ M of each toxin, green). Error bars represent 1 σ (n = 3). All measurements were recorded 320 min post-addition.

Appendix B. Directed evolution of nanosensors for the detection of mycotoxins

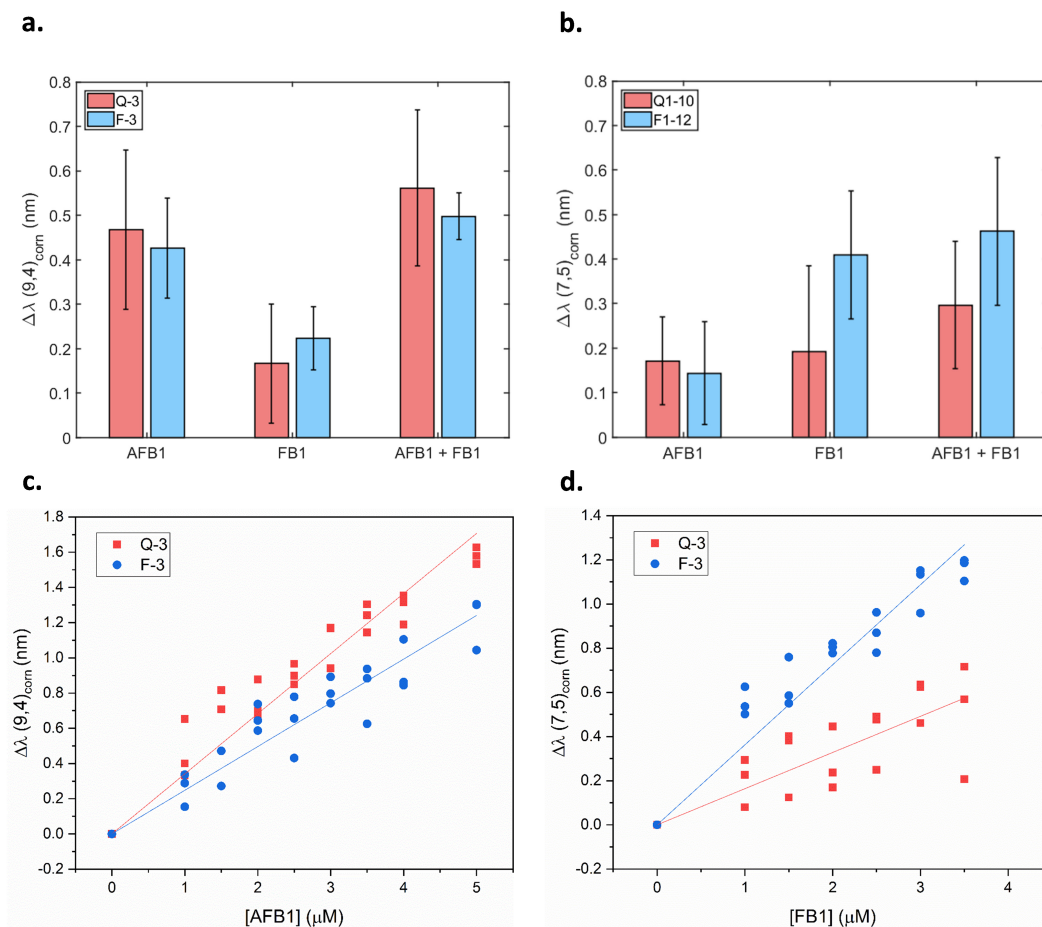


Figure B.30 – Detection of AFB1 and FB1 in spiked corn samples. Wavelength shift of the (a) (9,4) and (b) (7,5) chiralities following the addition of AFB1 (2.5 μM), FB1 (2.5 μM), or AFB1 and FB1 (2.5 μM of each toxin) for the Q-3 (red) and F-3 (blue) sensors. Calibration curves for the (c) (9,4) chirality towards AFB1 and (d) (7,5) chirality towards FB1 for the Q-3 (red) and F-3 (blue) sensors. Error bars represent 1 σ (n = 6). All measurements were performed 320 min post-addition.

Table B.6 – Determination of toxin concentration in corn. The slopes correspond to the linear fits of the calibration curves shown in **Figure B.30**. The shifting response of the sensor is given here for the (9,4) chirality (AFB1) and (7,5) chirality (FB1). The concentration values were calculated from the slope and compared to values measured by HPLC-MS. Red indicates where there was too high error or disagreement between the concentrations measured by fluorescence and HPLC-MS. Green indicates good agreement between the concentrations measured by fluorescence and HPLC-MS.

| Chirality | Sensor | Sample | Slope (nm. μM^{-1}) | Response (nm) | Calculated (μM) | Measured (μM) |
|-----------|--------|----------|---------------------------------|-------------------|------------------------------|----------------------------|
| (9,4) | Q-3 | AFB1 | $a = 0.34 \pm 0.01$ | 0.47 ± 0.18 | 1.37 ± 0.53 | 1.63 ± 0.06 |
| | | AFB1+FB1 | $a = 0.34 \pm 0.01$ | 0.56 ± 0.18 | 1.64 ± 0.52 | 1.53 ± 0.15 |
| | F-3 | AFB1 | $a = 0.25 \pm 0.01$ | 0.43 ± 0.11 | 1.72 ± 0.46 | 1.63 ± 0.06 |
| | | AFB1+FB1 | $a = 0.25 \pm 0.01$ | 0.49 ± 0.05 | 2.01 ± 0.22 | 1.53 ± 0.15 |
| (7,5) | Q-3 | FB1 | $a = 0.16 \pm 0.01$ | 0.19 ± 0.19 | 1.17 ± 1.18 | 1.28 ± 0.12 |
| | | AFB1+FB1 | $a = 0.16 \pm 0.01$ | $0.0.29 \pm 0.14$ | 1.81 ± 0.88 | 1.26 ± 0.12 |
| | F-3 | FB1 | $a = 0.36 \pm 0.01$ | 0.41 ± 0.14 | 1.13 ± 0.53 | 1.28 ± 0.12 |
| | | AFB1+FB1 | $a = 0.36 \pm 0.01$ | 0.46 ± 0.17 | 1.28 ± 0.61 | 1.26 ± 0.12 |

Appendix B. Directed evolution of nanosensors for the detection of mycotoxins

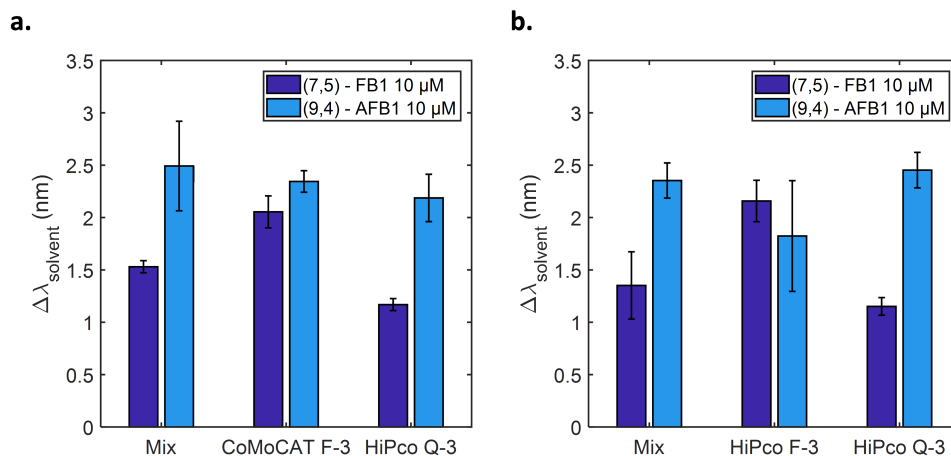


Figure B.31 – Comparison of the mixtures made of HiPco and HiPco-CoMoCAT sensors. Shifting response of the (7,5) (dark blue) and (9,4) (light blue) chiralities for (a) the HiPco-CoMoCAT and (b) the HiPco sensors in presence of FB1 and AFB1. The measurements were performed 200 min after addition and with a toxin concentration of 10 μ M. The use of CoMoCAT for the FB1 sensors does not strongly improve the selectivity of the mixed sensors compared to the individual sensors.

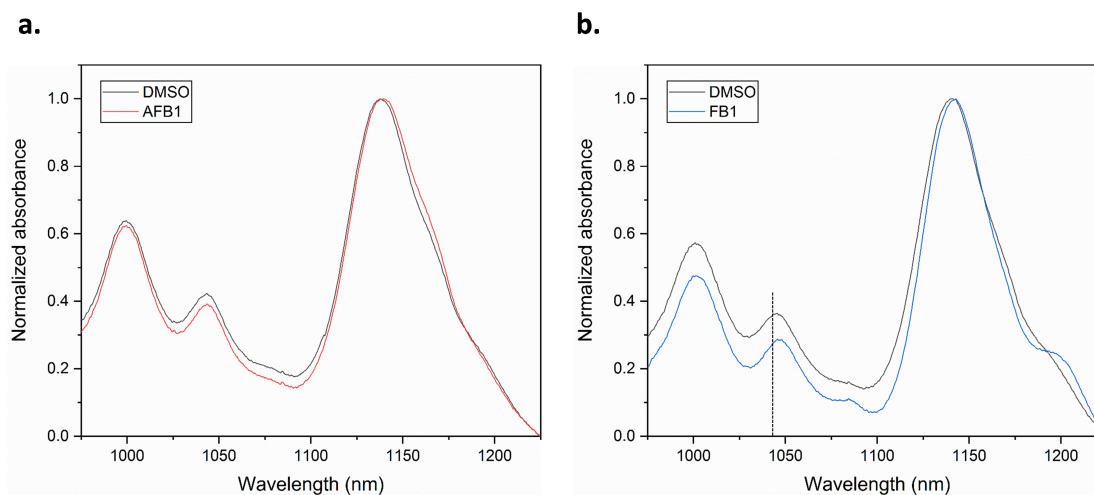


Figure B.32 – Effect of the toxins on the near-infrared DNA-SWCNT absorbance. Absorbance spectra of the (a) Q-3 and (b) F-3 sensors in presence of 10 μ M AFB1 (red) and FB1 (blue), as well as DMSO (black). In the presence of AFB1, the shifting response of the (9,4) peak was convoluted with the (7,6) peak, but we still noted a broadening of the peak at 1150 nm, which could be indicative of the shifting response. In the presence of FB1, a clear shift of the (7,5) peak was observed (indicated by the black dotted line).

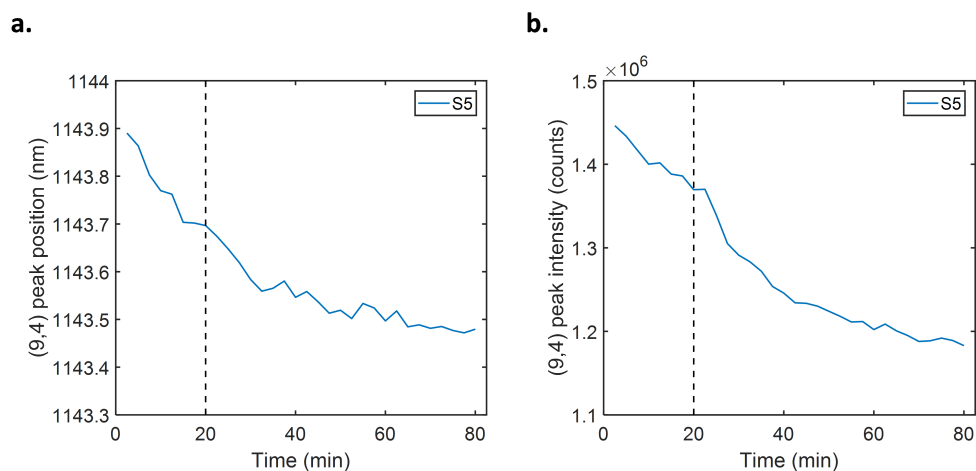


Figure B.33 – Response of immobilized sensors towards AFB1. (a) Peak position and (b) peak intensity of the (9,4) chirality for the immobilized S5 sensor as a function of time in presence of 0.1 M NaCl (0 to 20 min) and in presence of 20 μ M AFB1 (20 to 80 min).

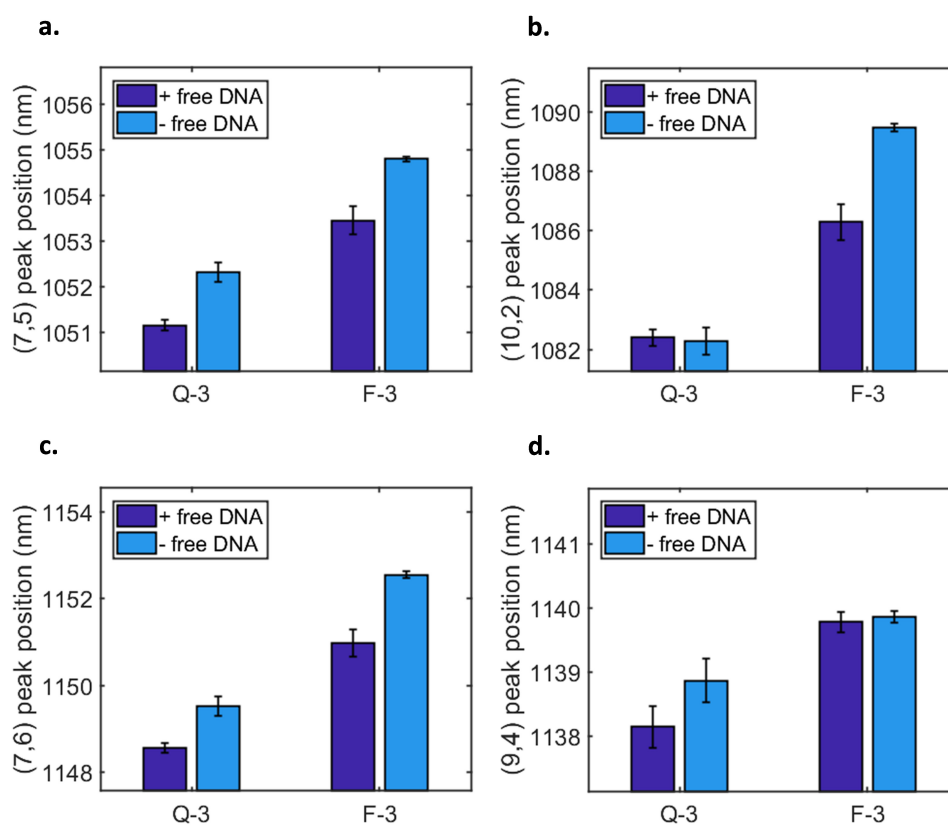


Figure B.34 – Effect of free DNA on the fluorescence peak position. Peak position of the Q-3 and F-3 sensors with and without free DNA for the (a) (7,5), (b) (10,2), (c) (7,6) and (d) (9,4) chiralities. The error bars represent 1 σ (n = 3).

Appendix B. Directed evolution of nanosensors for the detection of mycotoxins

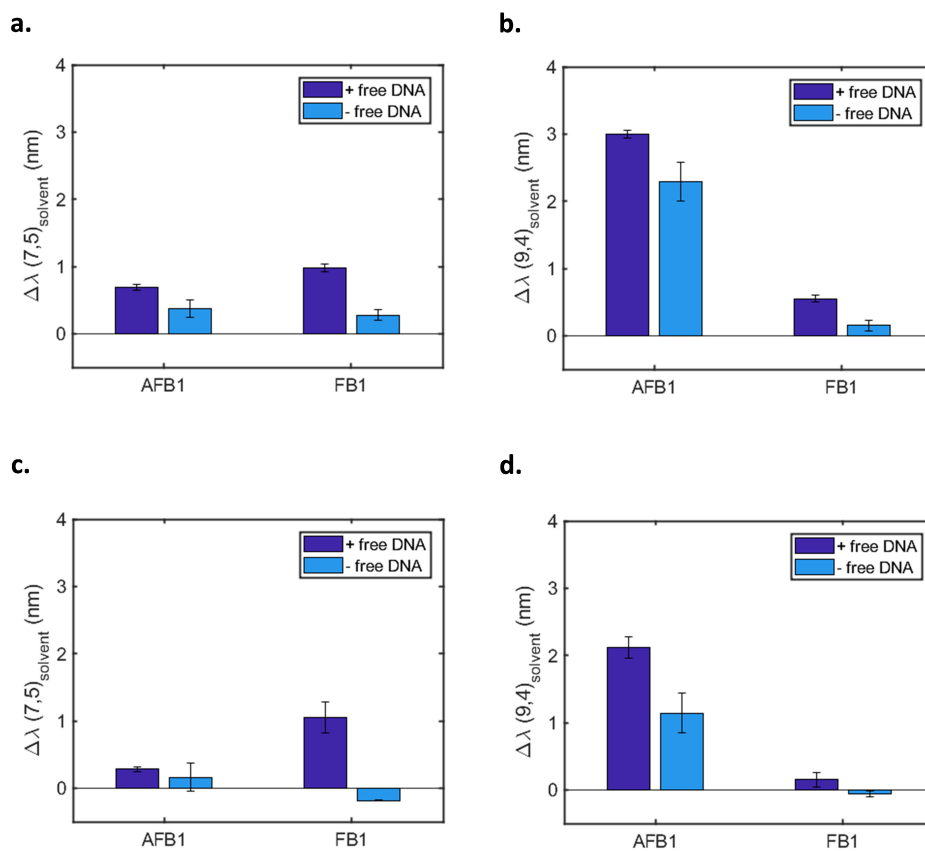


Figure B.35 – Effect of free DNA on the shifting response. Wavelength shifting response of the (a,b) Q-3 and (c,d) F-3 sensors with and without free DNA towards AFB1 (10 μ M) and FB1 (10 μ M) for the (7,5) and (9,4) chiralities. All measurements were performed 200 min post-addition. The error bars represent 1σ (n = 3).

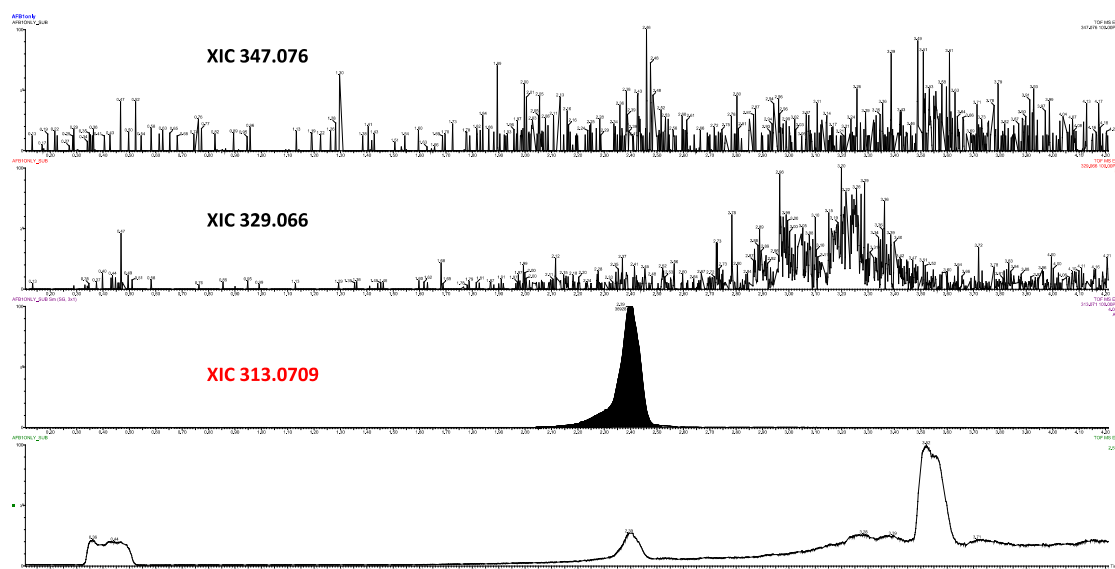


Figure B.36 – HPLC-MS chromatograms of the AFB1 samples. HPLC-MS chromatograms for compounds of m/z equal to (from top to bottom) 347.076, 329.066, 313.0709, and all ions. The m/z of 347.076 corresponds to aflatoxin B1 exo-8,9-dihydrodiol ($C_{17}H_{14}O_8$), the m/z of 329.066 corresponds to aflatoxin B1 exo-8,9-epoxide ($C_{17}H_{12}O_7$), and the m/z of 313.0709 corresponds to aflatoxin B1. The HPLC was performed on a C_{18} column and the MS analysis by electrospray in positive mode.

Appendix B. Directed evolution of nanosensors for the detection of mycotoxins

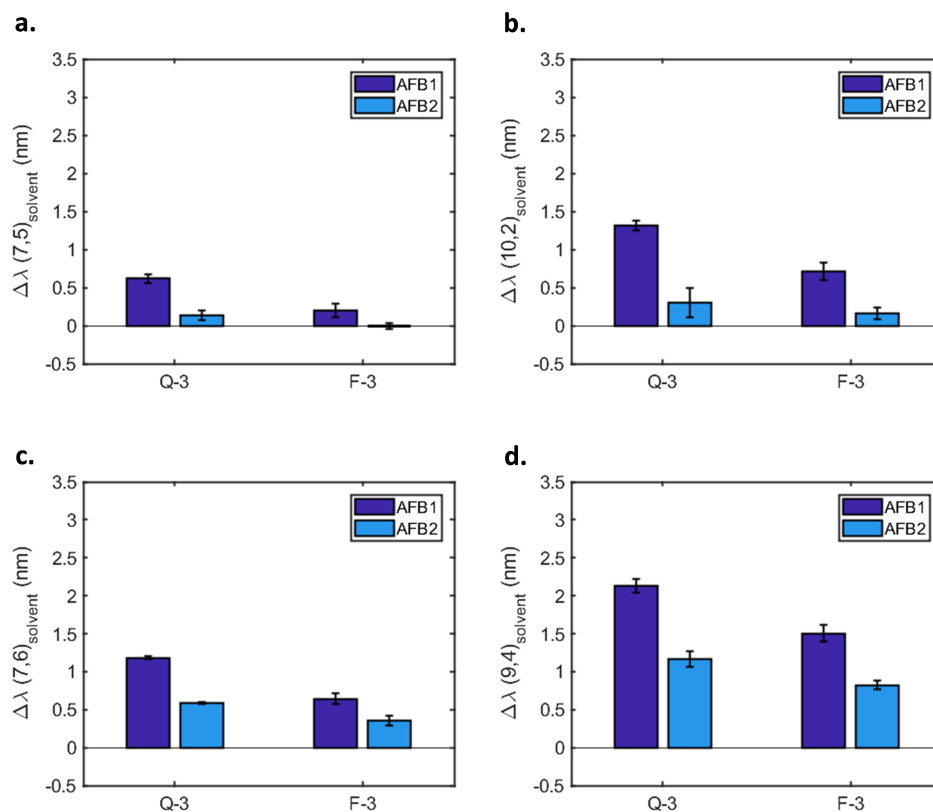


Figure B.37 – Comparison of AFB1 and AFB2 responses. Responses of the Q-3 and F-3 sensors to AFB1 (10 μ M) and AFB2 (10 μ M) for the (a) (7,5), (b) (10,2), (c) (7,6), and (d) (9,4) chiralities. All measurements were performed 200 min post-addition. The error bars represent 1 σ (n = 3).

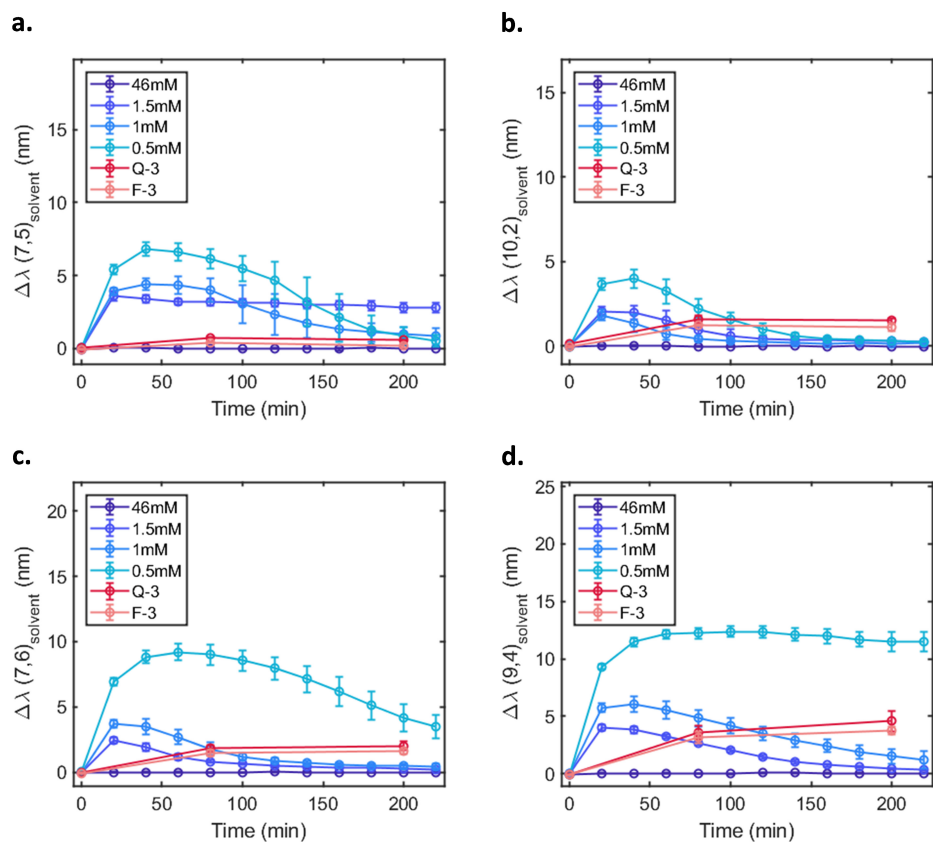


Figure B.38 – Shifting response of surfactant-SWCNTs to AFB1. Comparison of the wavelength shifting response of surfactant-wrapped SWCNTs (blue) and DNA-SWCNTs (red) following the addition of AFB1 (10 μ M) for the (a) (7,5), (b) (10,2), (c) (7,6), and (d) (9,4) chiralities as a function of time. The error bars represent 1 σ (n = 3).

Appendix B. Directed evolution of nanosensors for the detection of mycotoxins

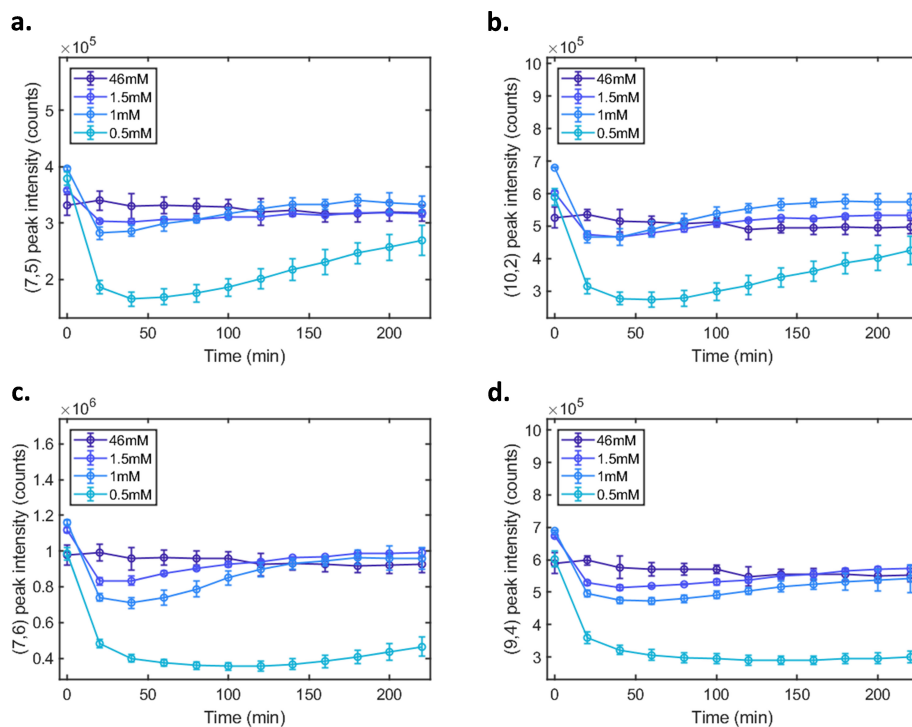


Figure B.39 – Intensity response of surfactant-SWCNTs to AFB1. Comparison of the fluorescence intensity response of surfactant-wrapped SWCNTs (blue) and DNA-SWCNTs (red) following the addition of AFB1 ($10 \mu\text{M}$) for the (a) (7,5), (b) (10,2), (c) (7,6), and (d) (9,4) chiralities as a function of time. The error bars represent 1σ ($n = 3$).

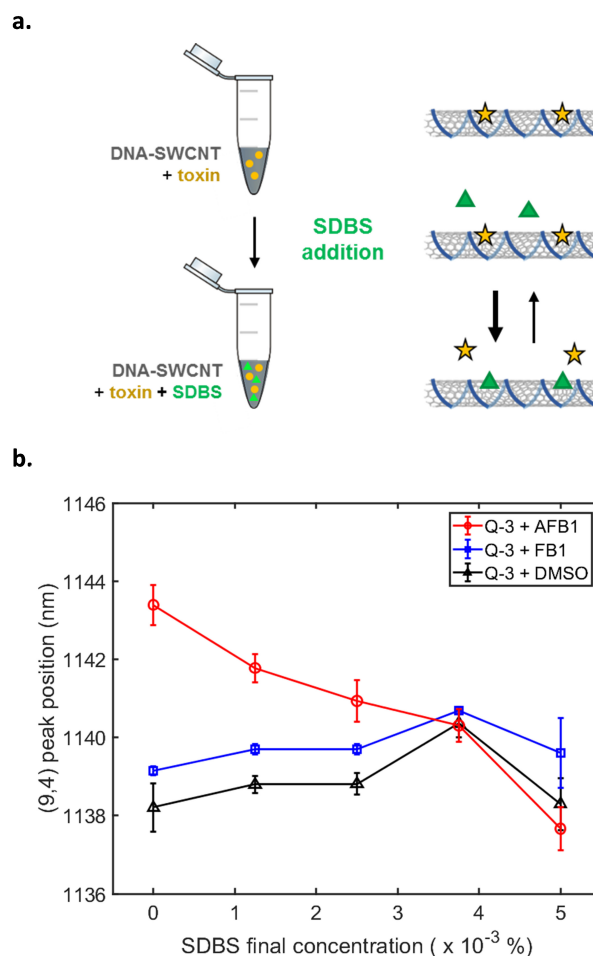


Figure B.40 – Replacement of AFB1 on the surface of DNA-SWCNT sensors. (a) Schematic of the protocol used to remove AFB1 from the surface of the DNA-SWCNTs using SDBS. The SDBS molecules replace the AFB1 molecules on the SWCNT surface, shifting the emission back to its initial position. (b) The position of the (9,4) peak for the Q-3 sensor previously incubated with AFB1 (10 μ M, red), FB1 (10 μ M, blue), or DMSO (black) in presence of varying concentrations of SDBS: 0, 1, 2.5, 3.75, 5 x 10⁻³ % 300 min after addition. The error bars represent 1 σ (n = 3).

Appendix B. Directed evolution of nanosensors for the detection of mycotoxins

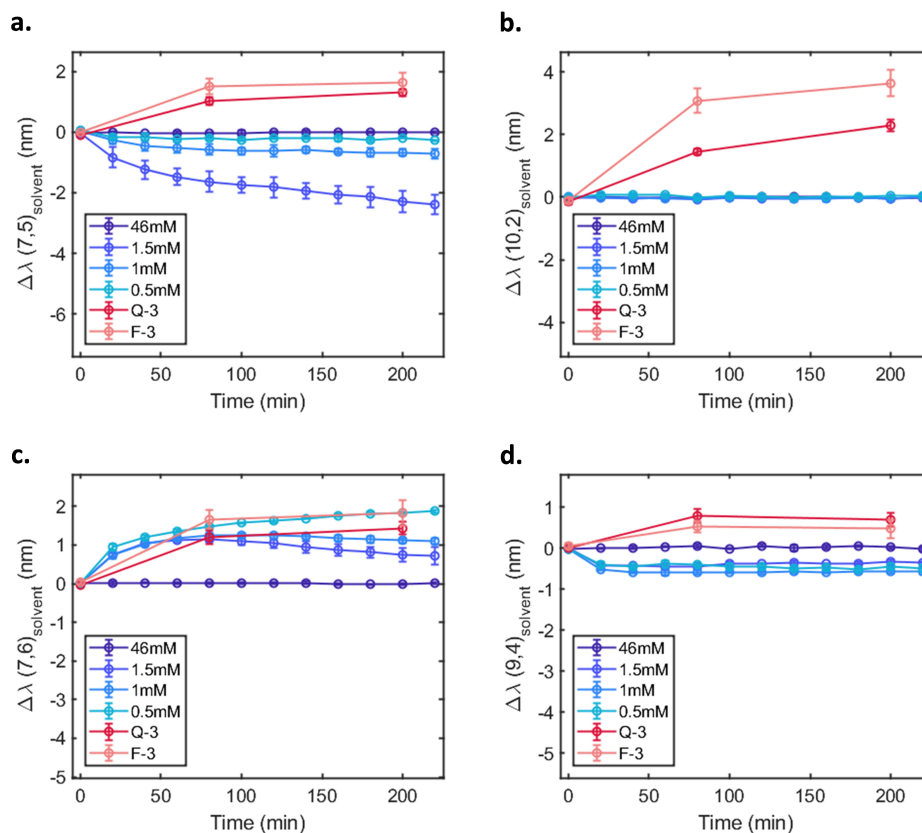


Figure B.41 – Shifting response of surfactant-SWCNTs to FB1. Comparison of the wavelength shifting response of surfactant-wrapped SWCNTs (blue) and DNA-SWCNTs (red) following the addition of FB1 (10 μ M) for the (a) (7,5), (b) (10,2), (c) (7,6), and (d) (9,4) chiralities as a function of time. The error bars represent 1 σ (n = 3).

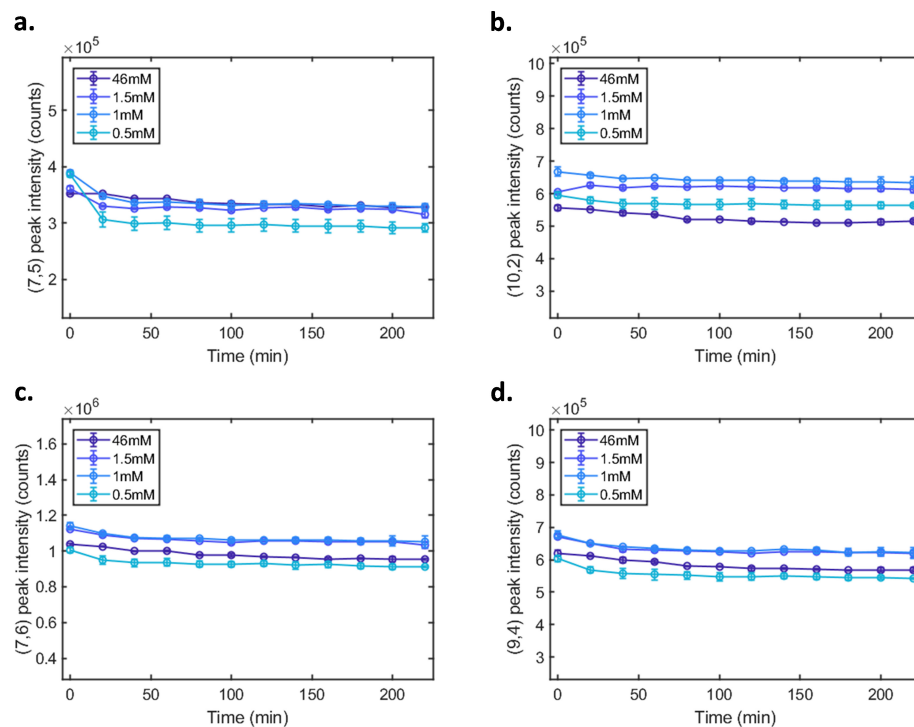


Figure B.42 – Intensity response of surfactant-SWCNTs to FB1. Comparison of the fluorescence intensity response of surfactant-wrapped SWCNTs (blue) and DNA-SWCNTs (red) following the addition of FB1 ($10 \mu\text{M}$) for the (a) (7,5), (b) (10,2), (c) (7,6), and (d) (9,4) chiralities as a function of time. The error bars represent 1σ ($n = 3$).

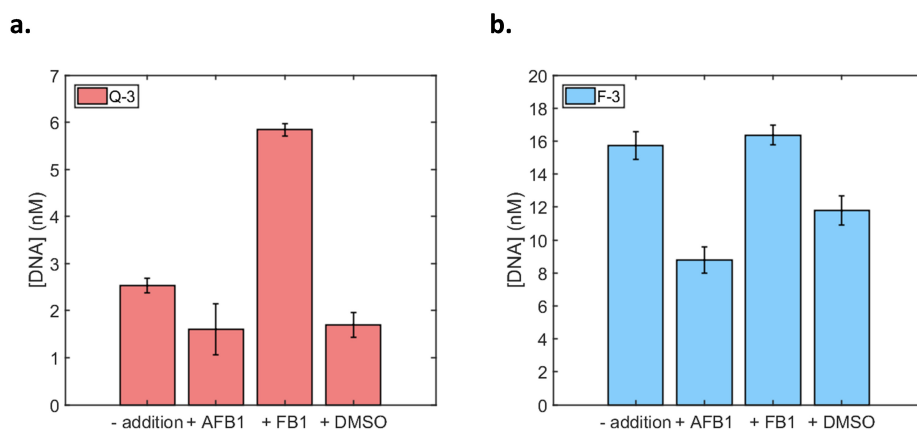


Figure B.43 – Estimation of the DNA concentration after toxin interaction. Concentration of free DNA for (a) the Q-3 and (b) the F-3 sensors before and after addition of AFB1 ($10 \mu\text{M}$), FB1 ($10 \mu\text{M}$), and DMSO. Error bars represent 1σ ($n = 3$).

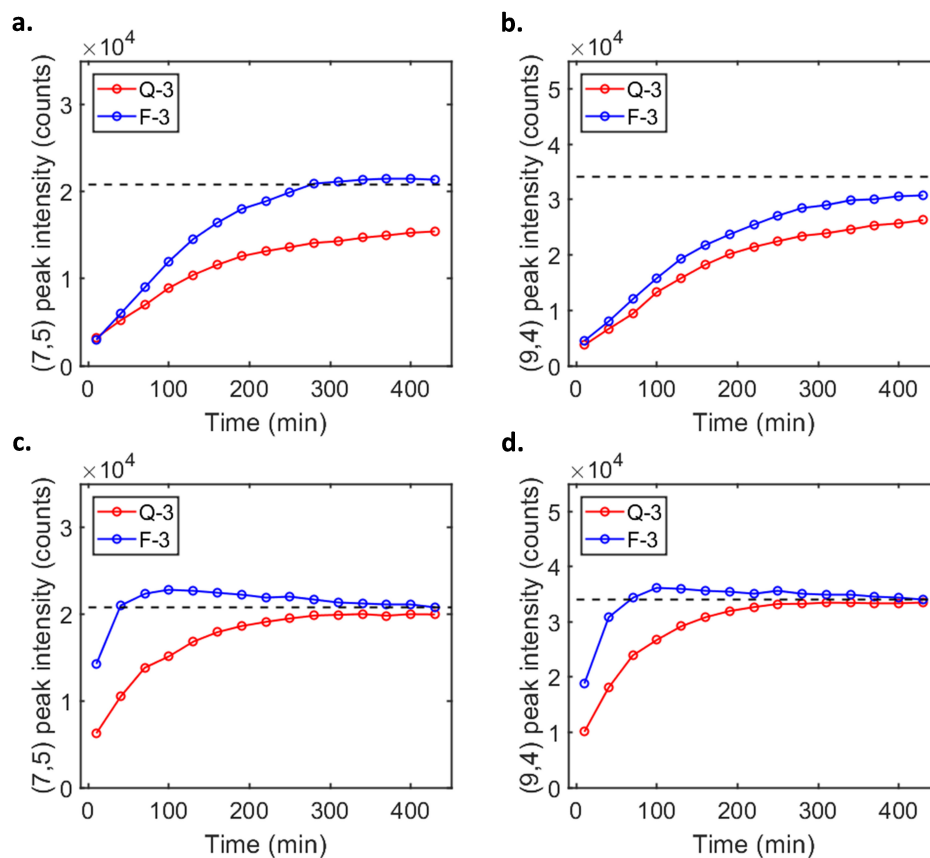


Figure B.44 – SWCNT binding affinity for the Q-3 and F-3 sensors. Replacement kinetics of the DNA for the (7,5) and (9,4) chiralities following the addition of SDBS for the Q-3 (red) and F-3 (blue) sensors. SDBS was added to a final concentration of (a,b) 0.01 % and (c,d) 0.05 % and the fluorescence peak intensities were monitored over time. The intensity corresponds to the maximum intensity at the final position of the (7,5) and (9,4) post-SDBS addition.

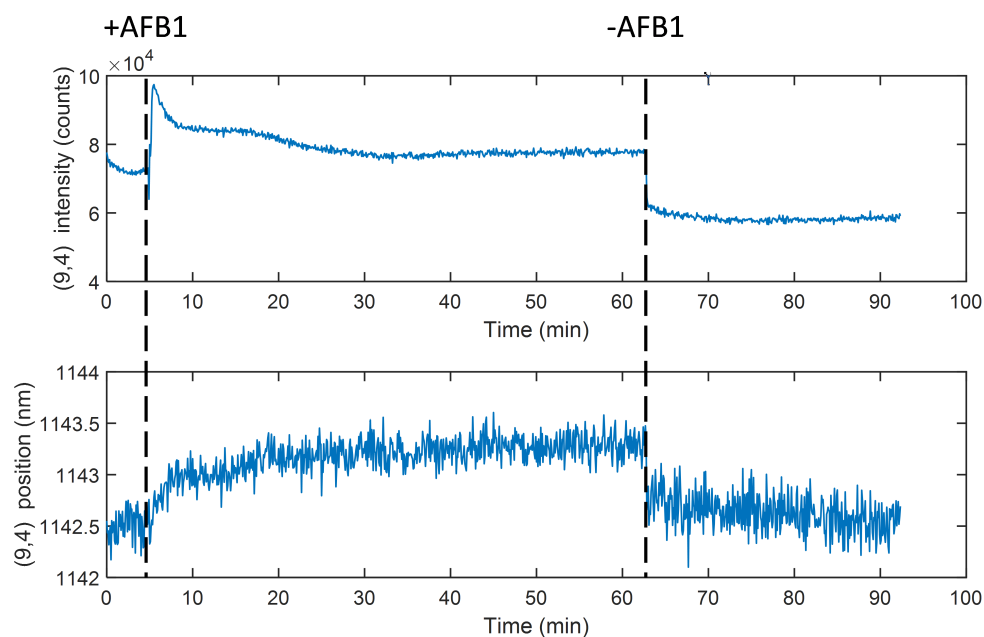


Figure B.45 – Reversibility of the AFB1 sensing in a flow chamber. (top) Peak intensity and (bottom) peak position of the F-3 sensor in presence of 0.1 M NaCl (between 0 and 5 min), 10 μ M AFB1 (between 5 min and 63 min) and washed with 0.1 M NaCl again (after 63 min). The sensors experience a red-shifting of the emission upon addition of AFB1 which is reversed upon washing with buffer. This therefore proves that the sensors could be used in a flow chamber for a practical use.

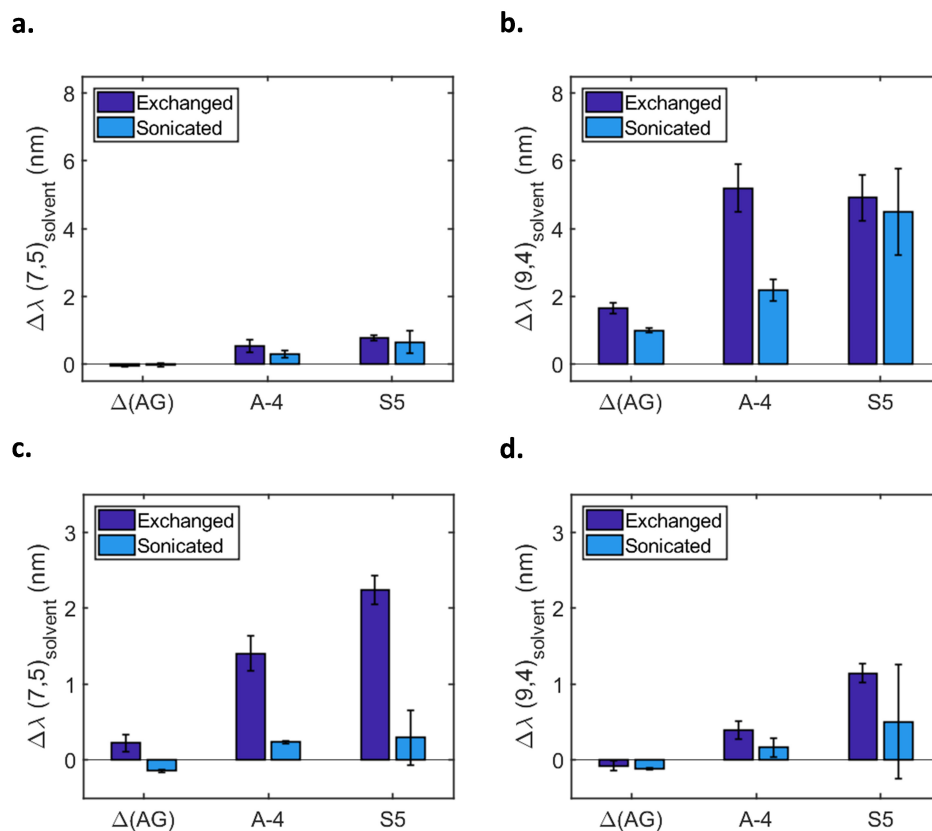


Figure B.46 – Impact of the preparation method on the toxin response. Wavelength shifting response of the (7,5) and (9,4) chiralities for the $\Delta(AG)$, A-4, and S5 sensors prepared by exchange or direct sonication towards (a,b) AFB1 (10 μM) and (c,d) FB1 (10 μM). All measurements were performed 200 min post-addition. The error bars represent 1 σ ($n = 3$). The FB1 batches were prepared in methanol.

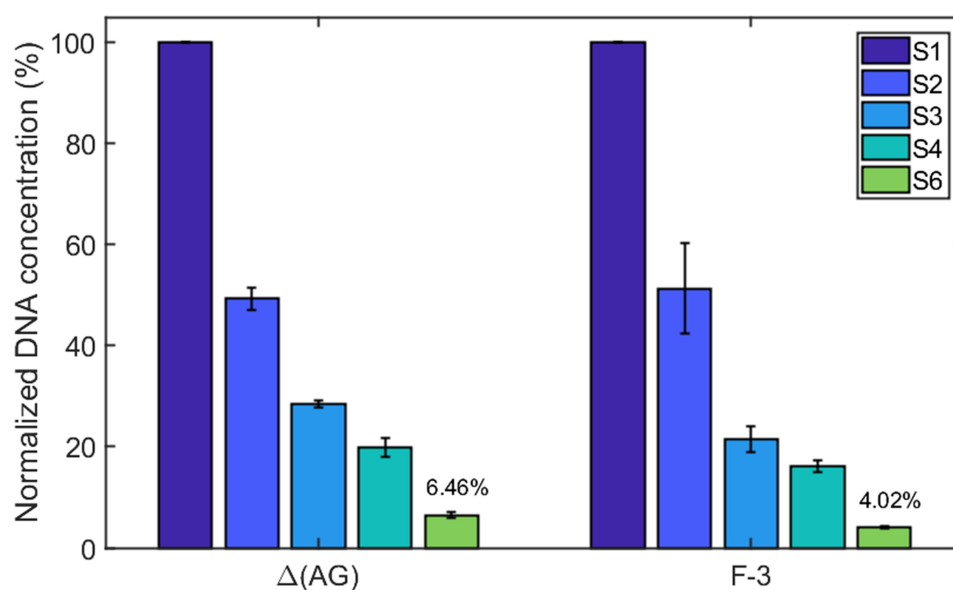


Figure B.47 – Removal of free DNA with a high-throughput procedure. The DNA-SWCNT suspensions are precipitated with salts and ethanol similarly to the toxin removal procedure. Then, the pellet is washed several times with 70 % ethanol in order to wash away the free DNA from the samples. The normalized concentrations of free DNA in the 70 % ethanol supernatants of the Δ (AG) and F-3 DNA-SWCNT sensors are shown here for the first (S1) to the sixth (S6) supernatant fractions. The method effectively removes more than 94 % of the free DNA in 6 washes, allowing for a more scalable approach for free DNA removal and more compatible with directed evolution. Error bars represent 1σ ($n = 3$).

Appendix B. Directed evolution of nanosensors for the detection of mycotoxins

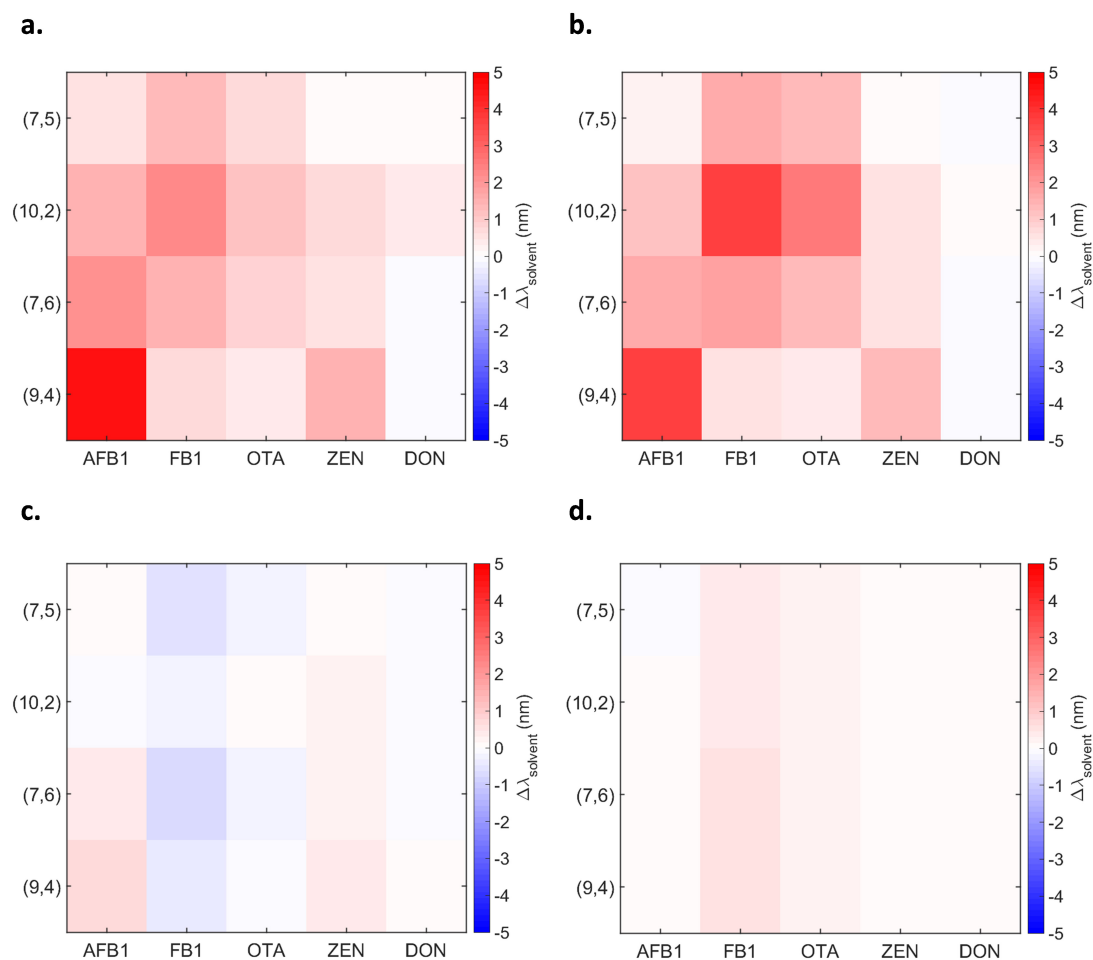


Figure B.48 – Heatmaps for selective and non-selective DNA-SWCNT sensors. Heatmaps of the wavelength shifting response of the (a) Q-3, (b) F-3, (c) (AG)₁₅, and (d) Δ (AT) sensors to the addition of 10 μ M AFB1, FB1, OTA, ZEN or DON. All measurements were recorded 200 min post-addition.

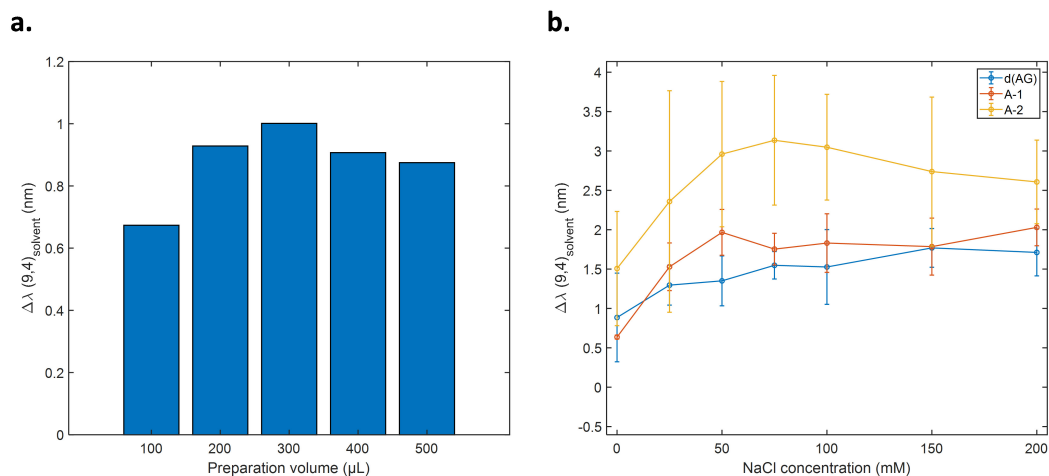


Figure B.49 – Influence of preparation volume and ionic strength on AFB1 response. Shifting response of the (9,4) chirality in presence of AFB1 as a function of (a) the sample preparation volume for the Δ (AG) sensor and (b) the NaCl concentration for the Δ (AG), A-1 and A-2 sensors. The measurements were performed with an AFB1 concentration of 10 μ M and 200 min after addition. The error bars represent 1 σ (n=3). The samples in (a) were resuspended in 0.1 M NaCl and the samples in (b) were prepared in a 300 μ L volume. The AFB1 batches prepared under non-inert conditions in DMSO. These controls show first that, unless prepared in low volume (100 μ L), the behavior of the sensors does not depend on the preparation volume. The controls also show that the response is optimized at a salt concentration of 0.1 M.

C Towards a semi-rational design of DNA-SWCNT sensors

Table C.1 – Extinction coefficients ϵ for the mycotoxins used in the study. The toxins were diluted in the indicated solvent before UV-VIS measurement.

| Mycotoxin | ϵ (L.cm ⁻¹ .mM ⁻¹) | Wavelength (nm) | Solvent | Reference |
|-----------|--|-----------------|----------|-----------|
| AFB1 | 21.8 | 363 | Ethanol | [266] |
| OTA | 5.5 | 333 | Methanol | [267] |
| ZEN | 6.02 | 316 | Methanol | [268] |
| ANG | 8.8 | 301 | Water | [271] |
| COU | 5.7 | 311 | Ethanol | [272] |

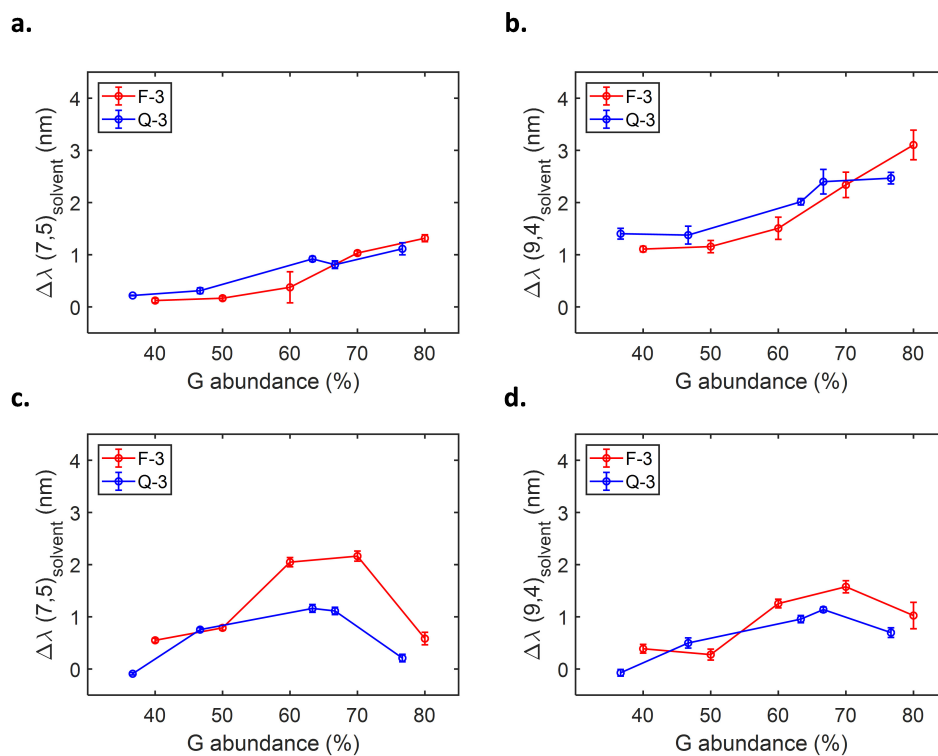


Figure C.1 – Response of the F-3- and Q-3-SWCNT analogues with varying G-content. (a,b) Shifting responses for (a) the (7,5) and (b) the (9,4) chiralities in presence of AFB1 as a function of the G-content. (c,d) Shifting response for (c) the (7,5) and (d) the (9,4) chiralities in presence of FB1 as a function of the G-content. The original F-3 and Q-3 sequences have a G-content of 60 and 63 % respectively, the sequences of the variants are indicated in the **Table C.2**. The measurements were performed with a mycotoxin concentration of 10 μ M and after an incubation time of 200 min post-addition. The error bars represent 1 σ (n=3).

Table C.2 – Sequences of the F-3 and Q-3 G-content variants. The bases changed are indicated in red and underlined.

| Name | G-content (%) | Sequence (5' to 3') |
|--------|---------------|--|
| F-3 | 60 | GAGGGGAGAAAGAGGAAGGGGAGAGGAGTG |
| F-3_G1 | 40 | GAG <u>A</u> GAGAAAGAGGAAG <u>A</u> <u>G</u> AAGAG <u>A</u> AGT <u>A</u> |
| F-3_G2 | 50 | GAG <u>A</u> GGAGAAAGAGGAAG <u>A</u> GGAGAG <u>A</u> AGTG |
| F-3_G3 | 70 | GAGGGGAGAGAGAGG <u>G</u> AGGGGAG <u>G</u> GGAGTG |
| F-3_G4 | 80 | GAGGGG <u>G</u> GA <u>G</u> GAGG <u>G</u> AGGGGAG <u>G</u> GG <u>G</u> GTG |
| Q-3 | 63.3 | GAGGCGTGGGAGAGGTAGGGGAGAGGAGTG |
| Q-3_G1 | 36.7 | GA <u>A</u> GCATGA <u>A</u> GAGAAGTAGAA <u>A</u> GAGAAGAGT <u>A</u> |
| Q-3_G2 | 46.7 | GA <u>A</u> GCGTG <u>A</u> GAGAAGTAGAGGAGAAGAGTG |
| Q-3_G3 | 66.7 | GAGGCGTGGGAGAGGTAGGGGAG <u>G</u> GGAGTG |
| Q-3_G4 | 76.7 | <u>G</u> GGGCGTGGGAGAGGT <u>G</u> GGGGAG <u>G</u> GG <u>G</u> GTG |

Appendix C. Towards a semi-rational design of DNA-SWCNT sensors

Table C.3 – Sequences of the random G-content variants. The H base corresponds to a random mix of the A, C and T bases.

[illegible]

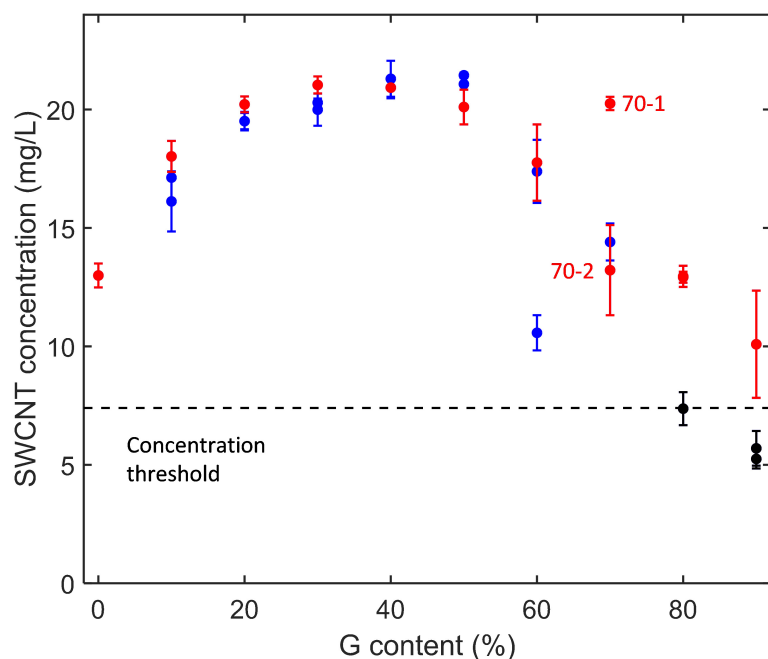


Figure C.2 – SWCNT concentration for the random G-content variants. The SWCNT concentration was estimated by absorbance at 632 nm with 90 μ L solution in a 96-well plate directly after sample resuspension. The black data points are the complexes (G80-1, G90-1 and G90-2) that were discarded because of a too low SWCNT concentration (below the concentration threshold indicated by the black dotted line). The blue and red data points represent the complexes that were used for further characterization. Only the complexes indicated by the red data points were used for the secondary structure characterization (CD, EMSA...). The error bars represent 1 σ (n=3).

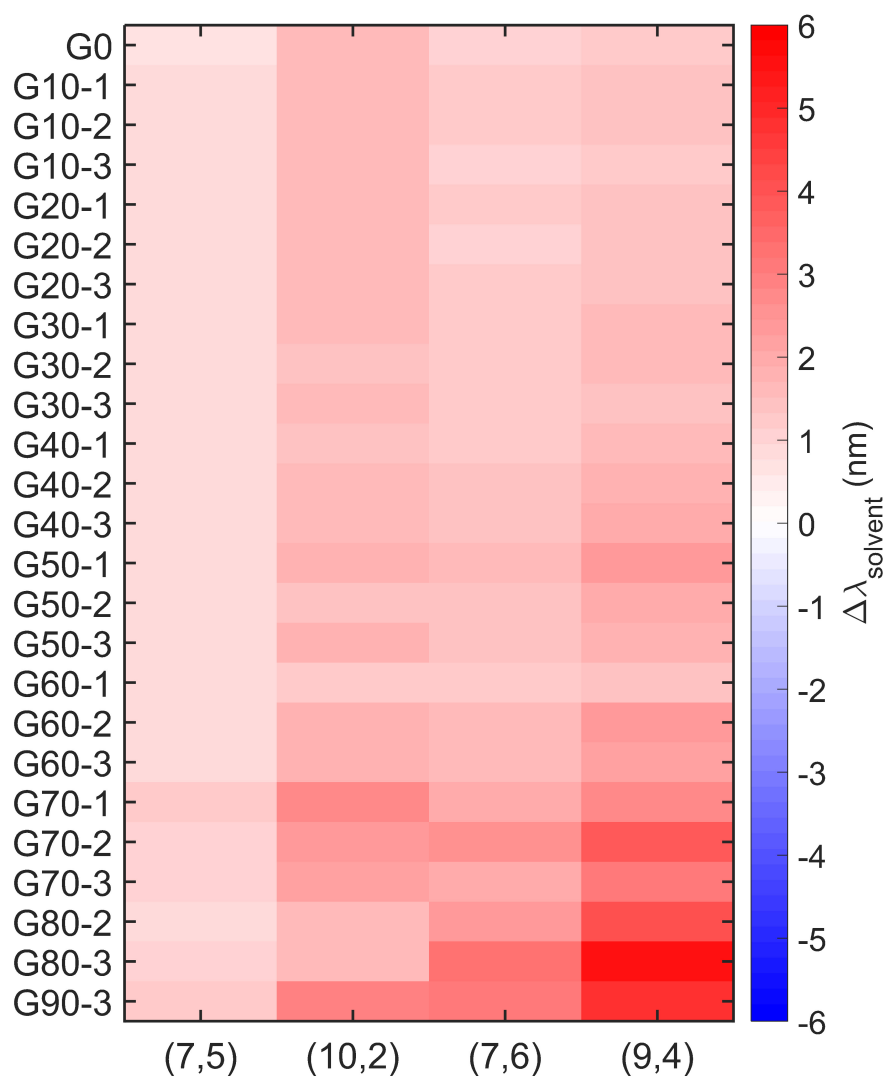
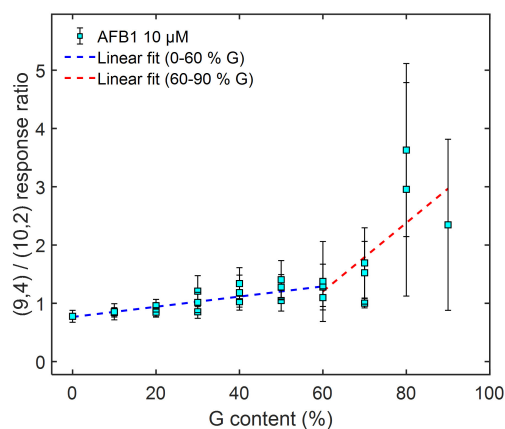


Figure C.3 – Response heatmap of the G-content variants to AFB1. Response of the G-content variants for the (7,5), (10,2), (7,6) and (9,4) chiralities. The measurements were performed with a mycotoxin concentration of 10 μM and after an incubation time of 200 min post-addition.

a.



b.

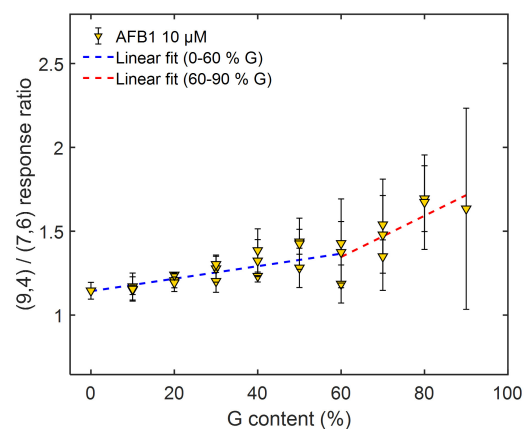


Figure C.4 – Selectivity of the AFB1 response for the G-content variants. Ratios of the shifting responses for the (9,4) and (a) (10,2) or (b) (7,6) chiralities towards AFB1 as a function of G-content. The response ratios are fit with linear fits between 0 and 60 % G-content (blue line), and between 60 and 90 % G-content (red line). The measurements are performed with a toxin concentration of 10 μM and after an incubation time of 200 min post-addition.

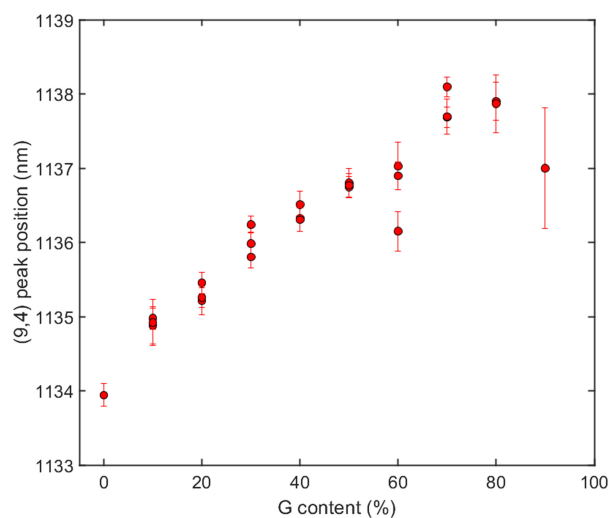


Figure C.5 – Variation in (9,4) peak position for the G-content variants. The error bars represent 1σ ($n=3$).

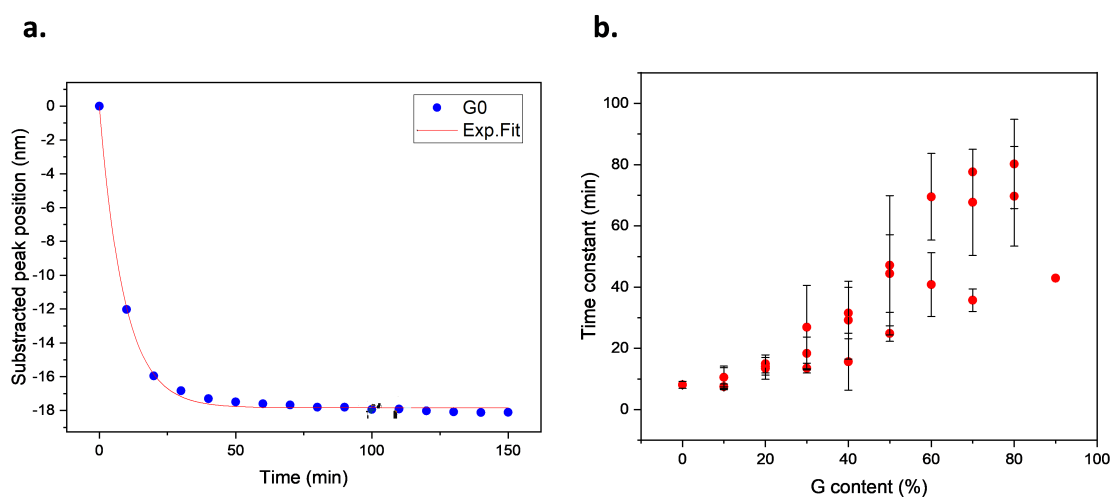


Figure C.6 – Binding affinity of the G-content variants to SWCNTs. (a) Peak position of the (9,4) chirality (subtracted to $t=0$) upon wrapping replacement with SDBS as a function of time. The data (blue) is fit with a single exponential fit (red): $y(t) = y_0 + A.e^{-\frac{t}{\tau}}$, with τ the time constant of the replacement. (b) Time constants of the replacement extracted from the fits as a function of G-content. The higher the time constant, the higher the binding affinity of the DNA wrapping to the SWCNT.

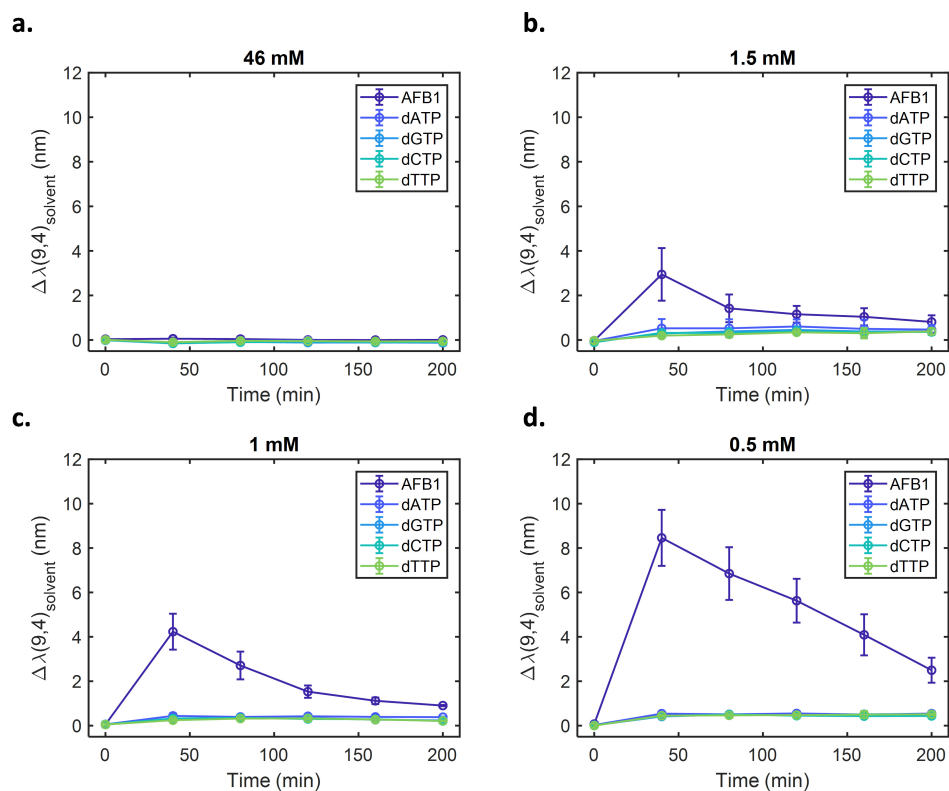


Figure C.7 – Comparison of the SWCNT interaction with AFB1 and nucleobases. Shifting response of the (9,4) chirality for the SC-SWCNTs at (a) 46, (b) 1.5, (c) 1 and (d) 0.5 mM SC in presence of 10 μ M AFB1 and 10 μ M dATP, dGTP, dCTP and dTTP.

Appendix C. Towards a semi-rational design of DNA-SWCNT sensors

Table C.4 – Results of the QGRS Mapper software. For the analysis, the H bases were replaced with A bases. The "position" column denotes the base (from 5' to 3') at which the structure starts. The "length" column designates the length of the structure (in number of bases). The "G-score" column indicates the likelihood of G-quadruplex formation (higher equals to more likely).

| Sequence | Position | Length | QGRS | G- Score |
|----------|----------|--------|--|----------|
| G40-2 | 2 | 23 | <u>GGAGAA</u> <u>GGAAAAA</u> <u>GGAAAGAGG</u> | 19 |
| G50-3 | 1 | 15 | <u>GGAAAGG</u> <u>GAAGGAGGG</u> | 20 |
| G60-3 | 1 | 15 | <u>GGGGG</u> <u>AGAGGAGAGG</u> | 19 |
| G70-1 | 6 | 21 | <u>GGGAAG</u> <u>GGGAGGAAGGG</u> <u>AGGG</u> | 38 |
| G70-2 | 3 | 27 | <u>GGGGAG</u> <u>GGGGAAAGAGGGG</u> <u>GAAGGGGG</u> | 60 |
| G80-2 | 4 | 18 | <u>GGGGAG</u> <u>GGGGGGGG</u> <u>AGGGG</u> | 62 |
| G80-3 | 6 | 22 | <u>GGGGAGG</u> <u>AGGGGGGGGGG</u> <u>GGGGG</u> | 60 |
| G90-3 | 1 | 26 | <u>GGGGGG</u> <u>GGGGGGG</u> <u>GAGGGGG</u> <u>AGGGGGG</u> | 84 |

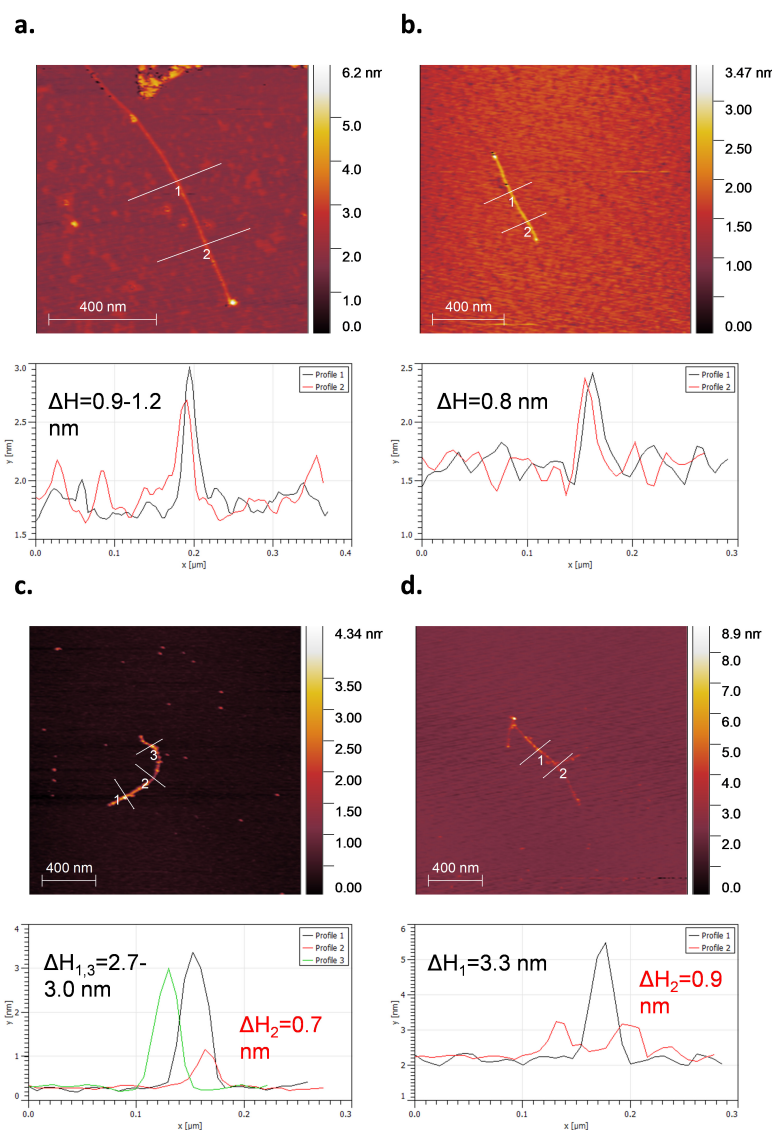


Figure C.8 – AFM height profiles for the G0- and G90-3-SWCNT complexes. (a,b) AFM images (top) and height profiles (bottom) for the G0-SWCNT complexes. The height was determined to be between 0.8 and 1.2 nm on average. (c,d) AFM images (top) and height profiles (bottom) for the G90-3-SWCNT complexes. Two main heights could be observed, one between 0.7 and 0.9 nm (in accordance with the results of the G0-SWCNT complexes) and one between 2.7 and 3.3 nm which we attribute to the formation of secondary structures such as G4 structures.

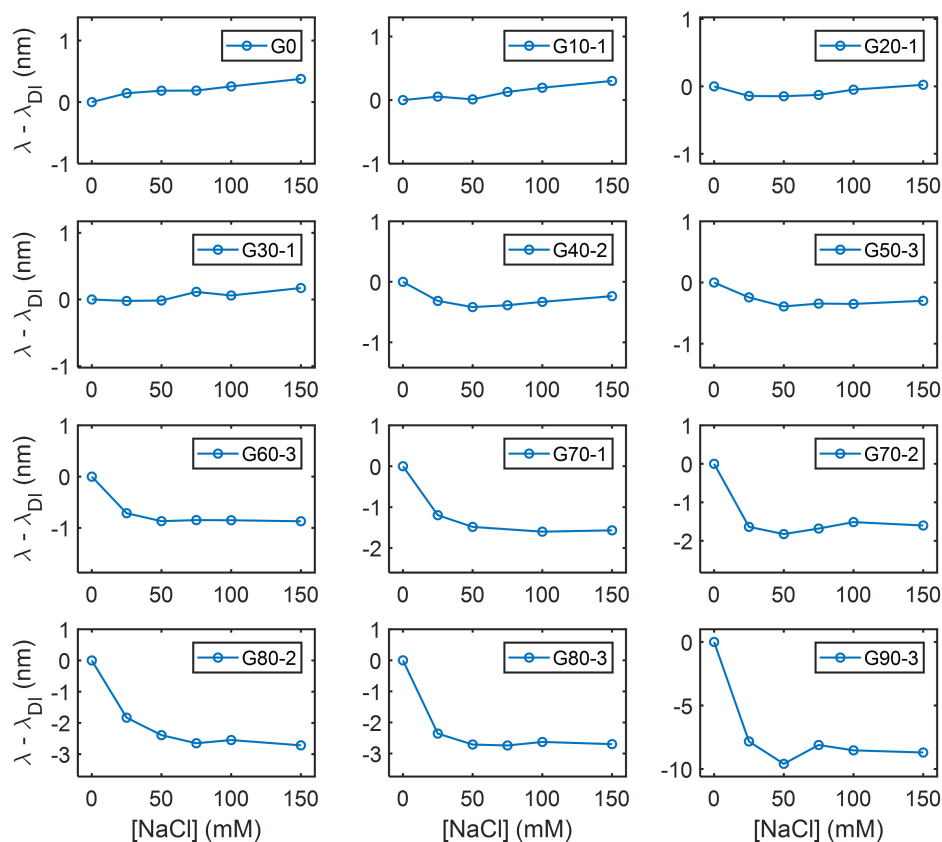


Figure C.9 – Salt dependence of the peak position of the G-content variants. The peak position λ was subtracted by the position of DNA-SWCNTs in DI water λ_{DI} and plotted as a function of the NaCl concentration.

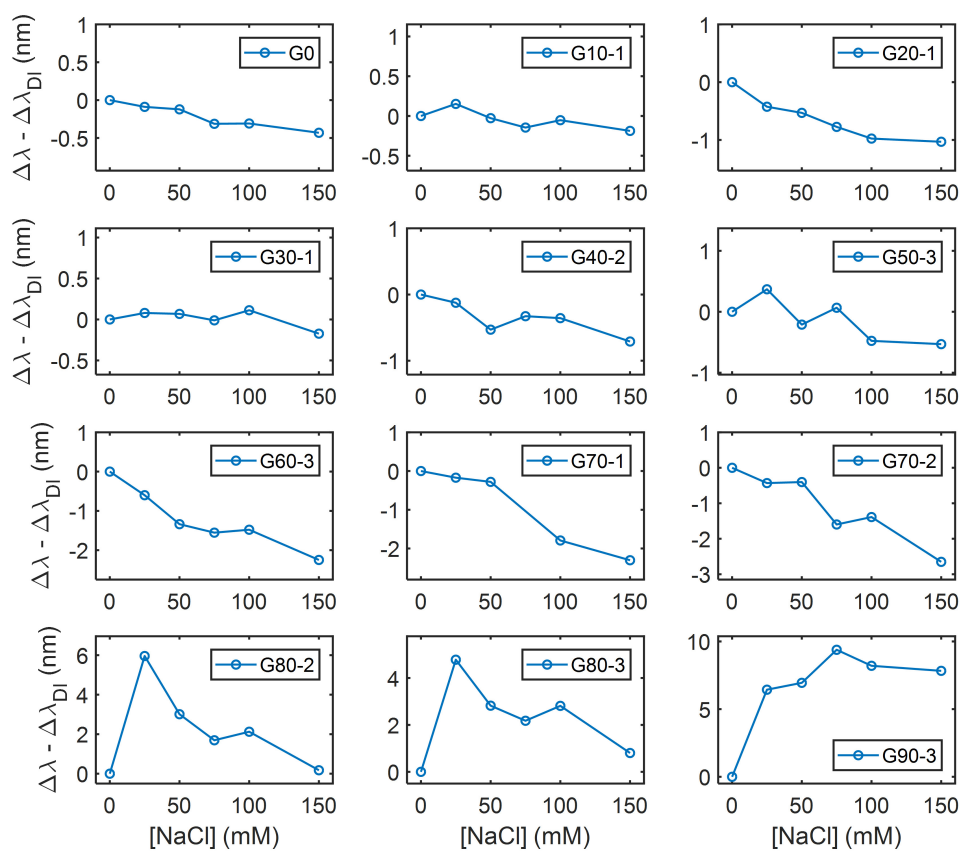
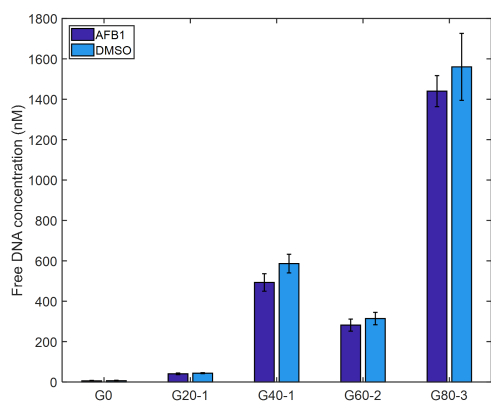


Figure C.10 – Salt dependence of the response of the G-content variants towards AFB1. The response $\Delta\lambda$ was subtracted by the response of DNA-SWCNTs in DI water $\Delta\lambda_{DI}$ and plotted as a function of the NaCl concentration. The response was obtained with a mycotoxin concentration of 10 μ M and after an incubation of 200 min post-addition.

Appendix C. Towards a semi-rational design of DNA-SWCNT sensors

a.



b.

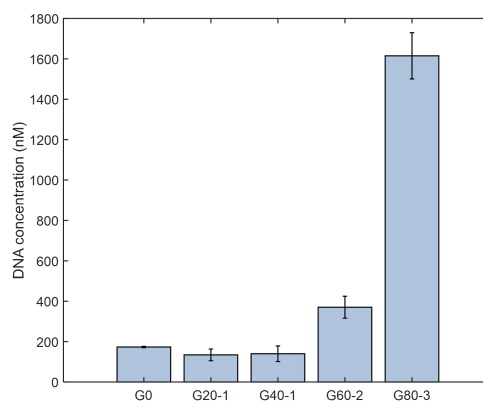
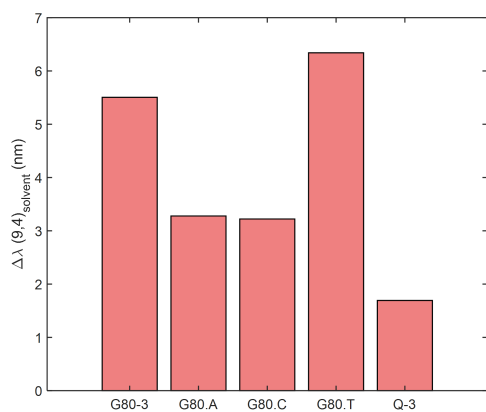


Figure C.11 – DNA quantification for the G-content variants. (a) Concentration of free DNA after interaction with 10 μ M AFB1 or DMSO for the G0-, G20-1-, G40-1-, G60-2- and G80-3-SWCNT complexes. (b) Concentration of extracted DNA wrapping for the G0-, G20-1-, G40-1-, G60-2- and G80-3-SWCNT complexes.

a.



b.

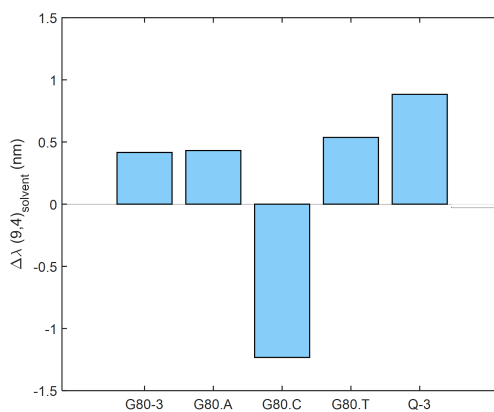


Figure C.12 – Comparison of the G80-3-SWCNT variants and the Q-3-SWCNT sensor. (a) Shifting response of the (9,4) chirality in presence of AFB1. (b) Shifting response of the (9,4) chirality in presence of FB1. The responses were obtained with a mycotoxin concentration of 10 μ M and after an incubation of 200 min post-addition.

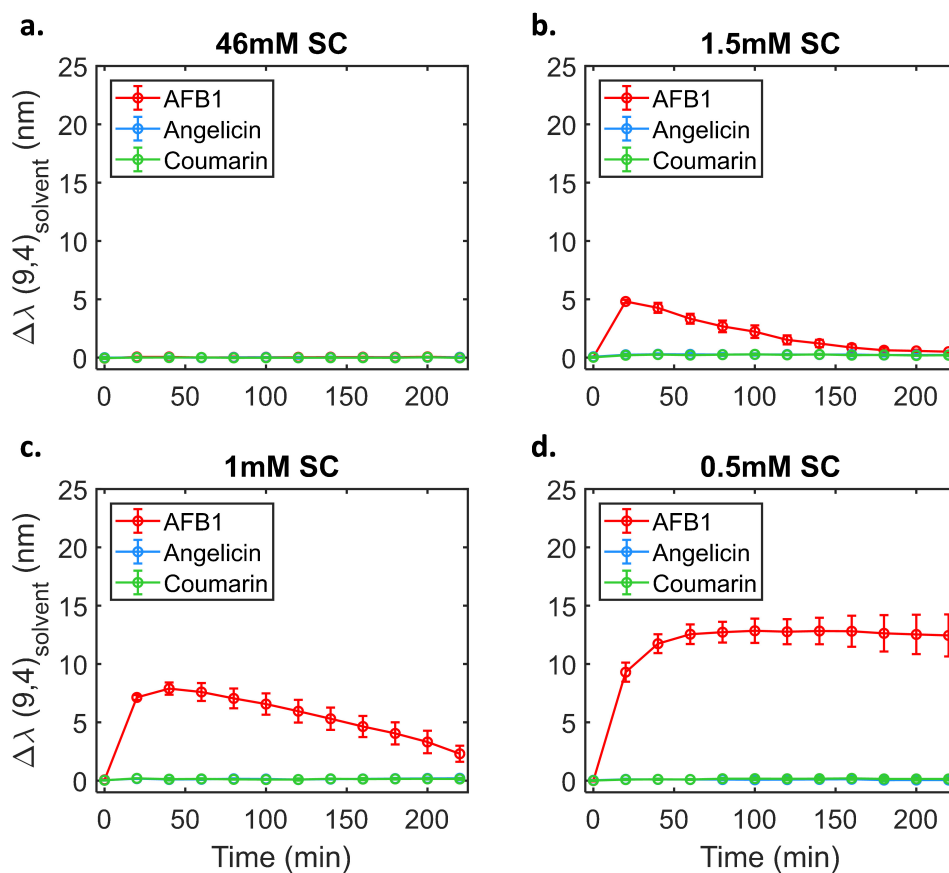


Figure C.13 – Response of SC-SWCNTs towards AFB1, ANG and COU. Kinetics of (9,4) peak shifting for SC-SWCNTs at SC concentrations of (a) 46, (b) 1.5, (c) 1 and (d) 0.5 mM in presence of 10 μM AFB1 (red), ANG (blue) and COU (green).

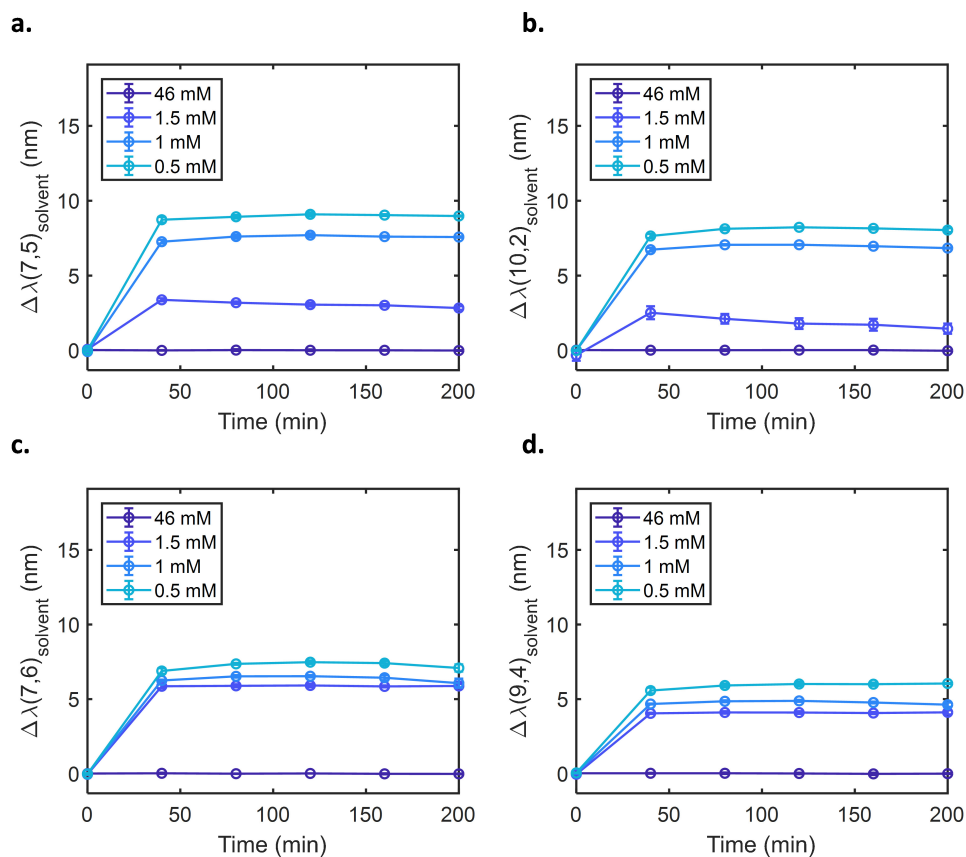


Figure C.14 – Shifting response of SC-SWCNTs towards ZEN. Shifting response of SC-SWCNTs (from 0.6 to 46 mM SC) towards 10 μM ZEN for the (a) (7,5), (b) (10,2), (c) (7,6), (d) (9,4) chiralities.

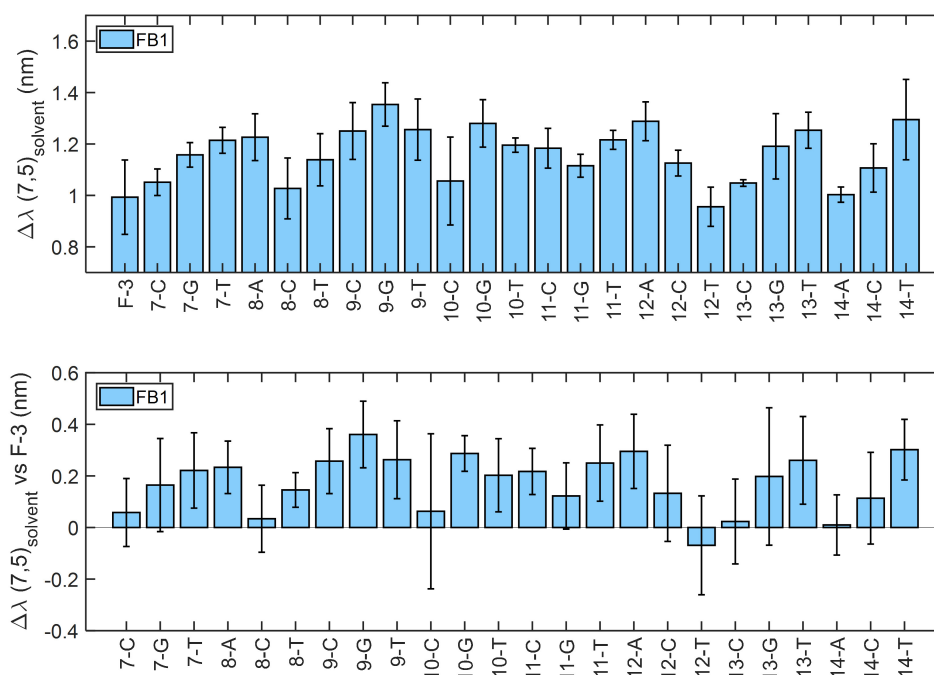


Figure C.15 – Shifting response for the first round of FB1 mutants. (top): Shifting response for the (7,5) chirality for the F-3-SWCNT complex and its mutants. The mutants are labelled as “X-Y” with X the position of the mutated base and Y the base which was used for substitution. (bottom): Shifting response for the (7,5) chirality with respect to the F-3-SWCNT complex. The measurements were performed with a toxin concentration of 5 μM and after an incubation time of 200 min.

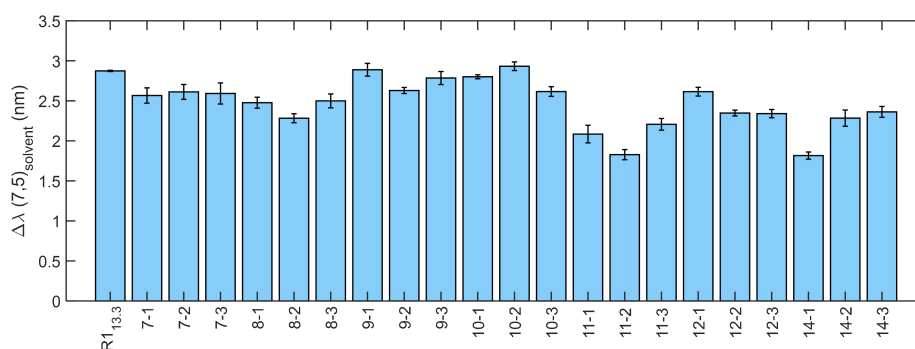
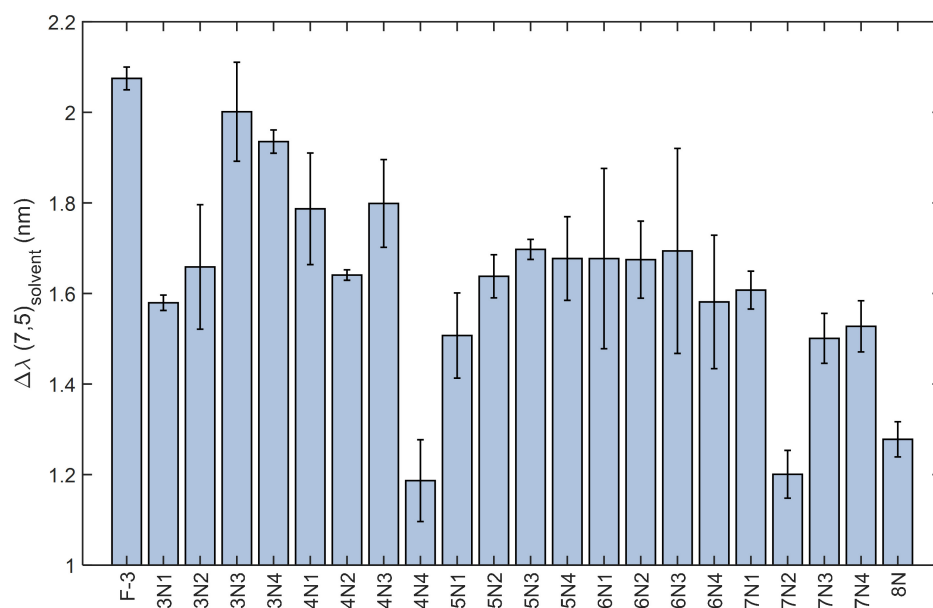


Figure C.16 – Shifting response for the mutants of the R1_{13.3}-SWCNT complex. Shifting response for the (7,5) chirality for the R1_{13.3} and its mutants. The measurements were performed with a toxin concentration of 10 μM and after an incubation time of 200 min.

a.



b.

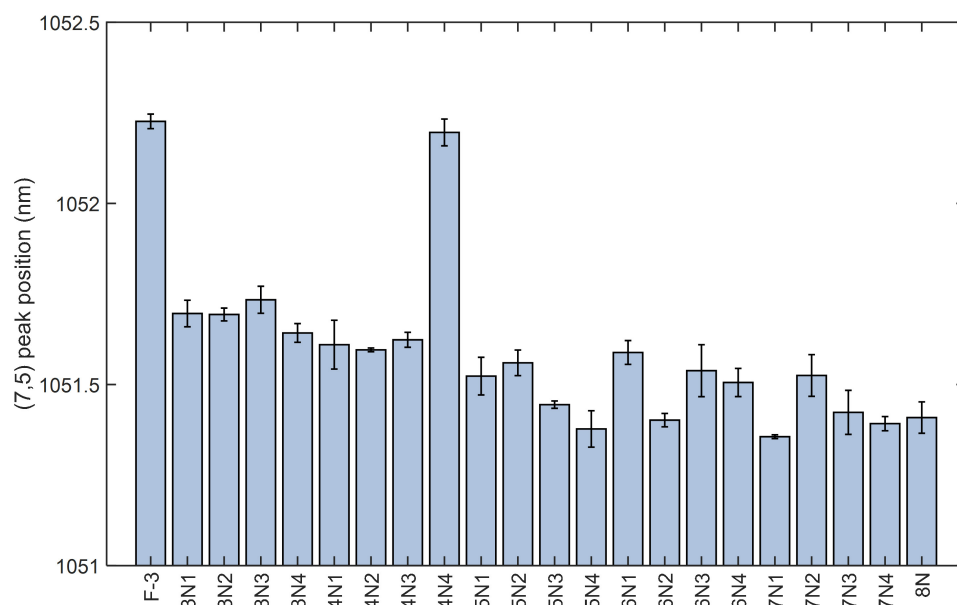


Figure C.17 – Effect of the number of mutations. (a) Shifting response towards FB1 for the (7,5) chirality for the F-3-SWCNT complex and its mutants. (b) Peak position of the (7,5) chirality for the F-3-SWCNT complex and its mutants. The mutants are labelled as “XNY” with X the number of mutations and Y the type of the mutant. The measurements were performed with a toxin concentration of 10 μM and after an incubation time of 200 min.

Table C.5 – Sequences of the FB1 mutants with random mutations. The mutations are indicated in red and underlined, with N indicating a random base (A, C, T or G with equal probability).

| Name | Number of mutations | Sequence (5' to 3') |
|------|---------------------|--|
| F-3 | / | GAGGGGAGAAAAGAGGAAGGGGAGAGGAGTG |
| 3N1 | 3 | GAGGGG <u>NGA</u> <u>NAG</u> <u>NGGA</u> AGGGGAGAGGAGTG |
| 3N2 | 3 | GAGGGGA <u>NA</u> <u>NGA</u> <u>NGA</u> AGGGGAGAGGAGTG |
| 3N3 | 3 | GAGGGGA <u>NNN</u> AGAGGAAGGGGAGAGGAGTG |
| 3N4 | 3 | GAGGGGAGAA <u>NNN</u> GGAAGGGGAGAGGAGTG |
| 4N1 | 4 | GAGGGGA <u>NN</u> <u>ANG</u> <u>NGGA</u> AGGGGAGAGGAGTG |
| 4N2 | 4 | GAGGGG <u>NGA</u> <u>NAN</u> <u>ANGA</u> AGGGGAGAGGAGTG |
| 4N3 | 4 | GAGGGGAGAA <u>NNNN</u> GGAAGGGGAGAGGAGTG |
| 4N4 | 4 | GAGGGG <u>NNNN</u> AGAGGAAGGGGAGAGGAGTG |
| 5N1 | 5 | GAGGGGA <u>NN</u> <u>ANG</u> <u>NNGA</u> AGGGGAGAGGAGTG |
| 5N2 | 5 | GAGGGGA <u>NN</u> <u>ANN</u> <u>NGGA</u> AGGGGAGAGGAGTG |
| 5N3 | 5 | GAGGGG <u>NNN</u> <u>ANG</u> <u>NGGA</u> AGGGGAGAGGAGTG |
| 5N4 | 5 | GAGGGGA <u>NNNN</u> <u>G</u> NGGAAGGGGAGAGGAGTG |
| 6N1 | 6 | GAGGGGA <u>NN</u> <u>ANNNN</u> GGAAGGGGAGAGGAGTG |
| 6N2 | 6 | GAGGGG <u>NNNNN</u> <u>G</u> NGGAAGGGGAGAGGAGTG |
| 6N3 | 6 | GAGGGGA <u>NNNNNN</u> GGAAGGGGAGAGGAGTG |
| 6N4 | 6 | GAGGGG <u>NNN</u> <u>ANG</u> <u>NN</u> GGAAGGGGAGAGGAGTG |
| 7N1 | 7 | GAGGGGA <u>NNNNNNN</u> GGAAGGGGAGAGGAGTG |
| 7N2 | 7 | GAGGGG <u>NNN</u> <u>ANNNN</u> GGAAGGGGAGAGGAGTG |
| 7N3 | 7 | GAGGGG <u>NNNNN</u> <u>GNN</u> GGAAGGGGAGAGGAGTG |
| 7N4 | 7 | GAGGGG <u>NNNNNNN</u> GGAAGGGGAGAGGAGTG |
| 8N | 8 | GAGGGG <u>NNNNNNNN</u> GGAAGGGGAGAGGAGTG |

Appendix C. Towards a semi-rational design of DNA-SWCNT sensors

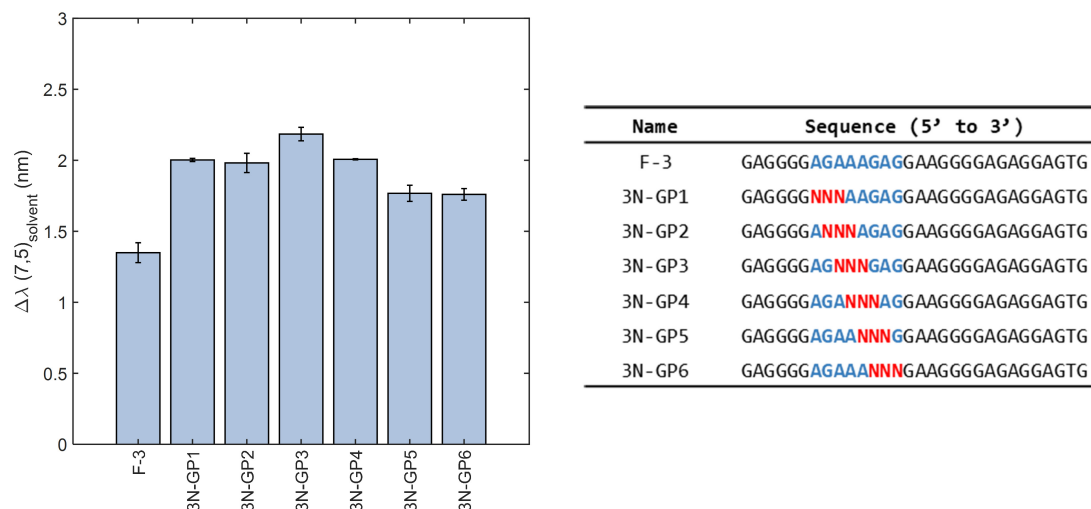


Figure C.18 – Influence of the grouped mutations. (left): Shifting response of the (7,5) chirality towards FB1. (right): Description of the sequences used. The measurements were performed with a toxin concentration of 10 μM and after an incubation time of 200 min.

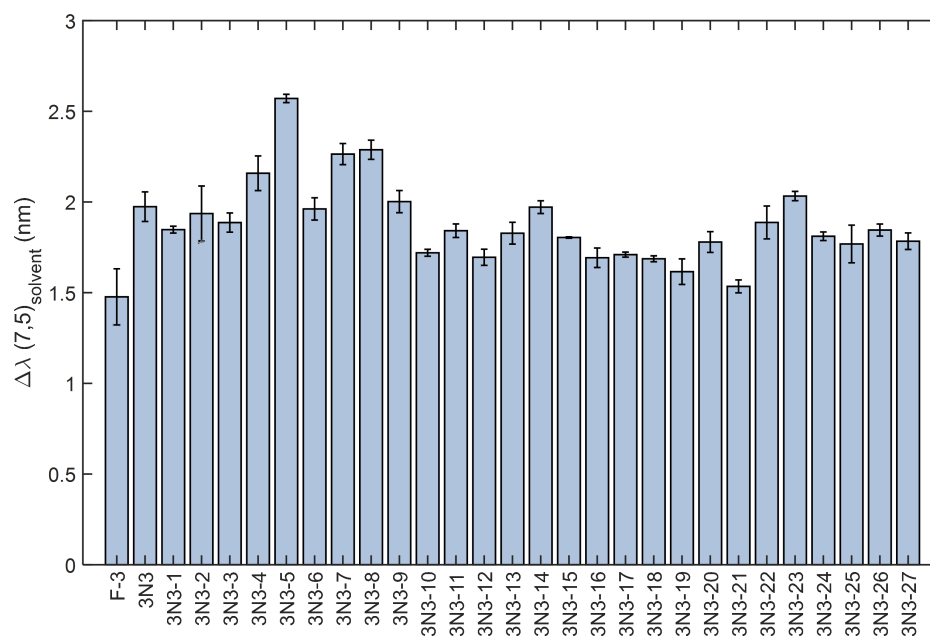


Figure C.19 – Response of the mutants of the 3N3-SWCNT complex. Shifting response for the (7,5) chirality towards FB1. The measurements were performed with a toxin concentration of 10 μM and after an incubation time of 200 min.

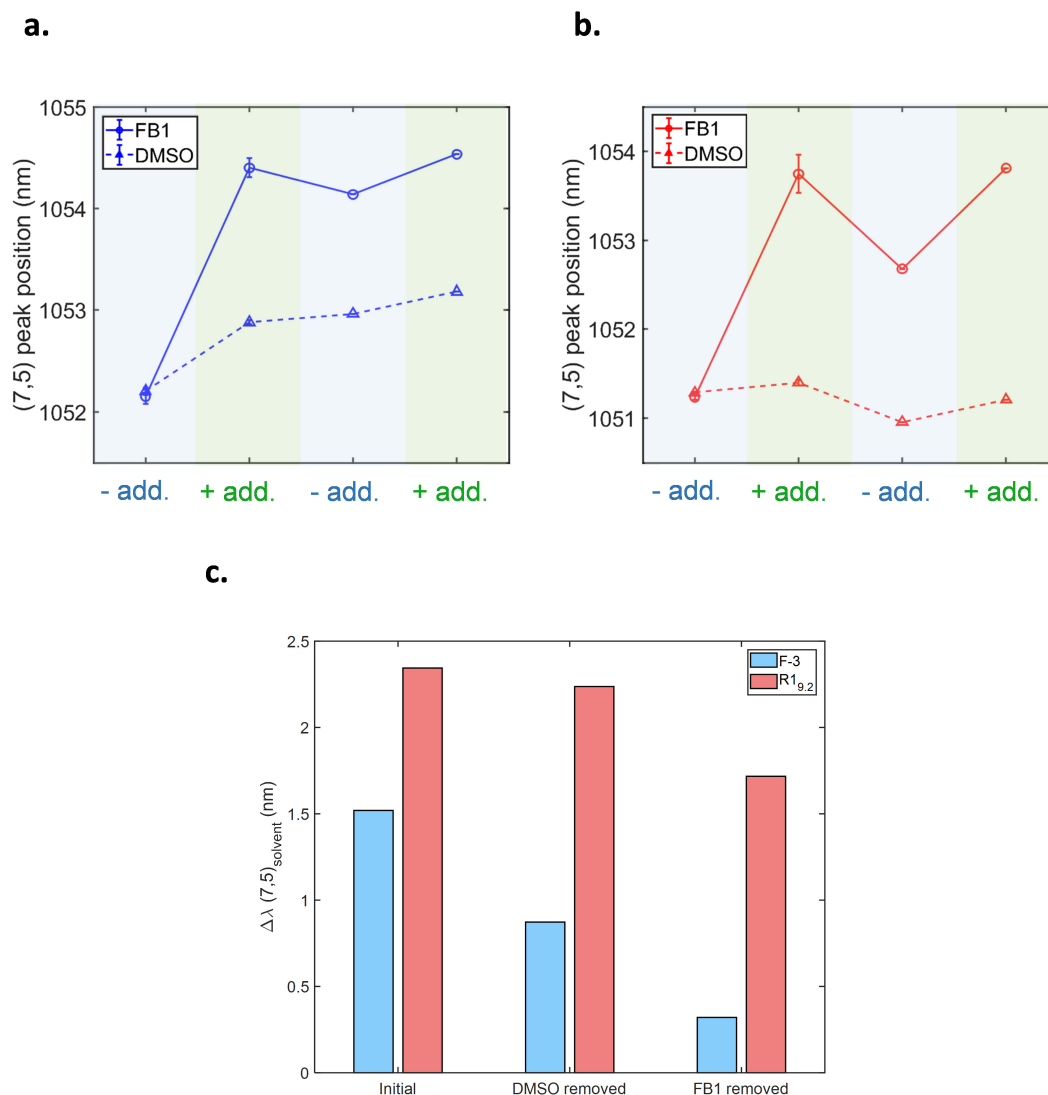


Figure C.20 – Improvement of the FB1 sensor reversibility. (a,b) Peak position of the (7,5) chirality before and after sensor washing for (a) the F-3-SWCNT and (b) the R_{19,2}-SWCNT sensors in presence of FB1 (plain) and DMSO (dotted). (c) Shifting response of the (7,5) chirality towards FB1 before and after sensor washing post-incubation with DMSO or 10 μ M FB1 for the F-3-SWCNT (blue) and R_{19,2}-SWCNT (red). The shifting response were determined with a toxin concentration of 10 μ M and after an incubation time of 200 min. The response post-washing is better retained for the mutant sensor.

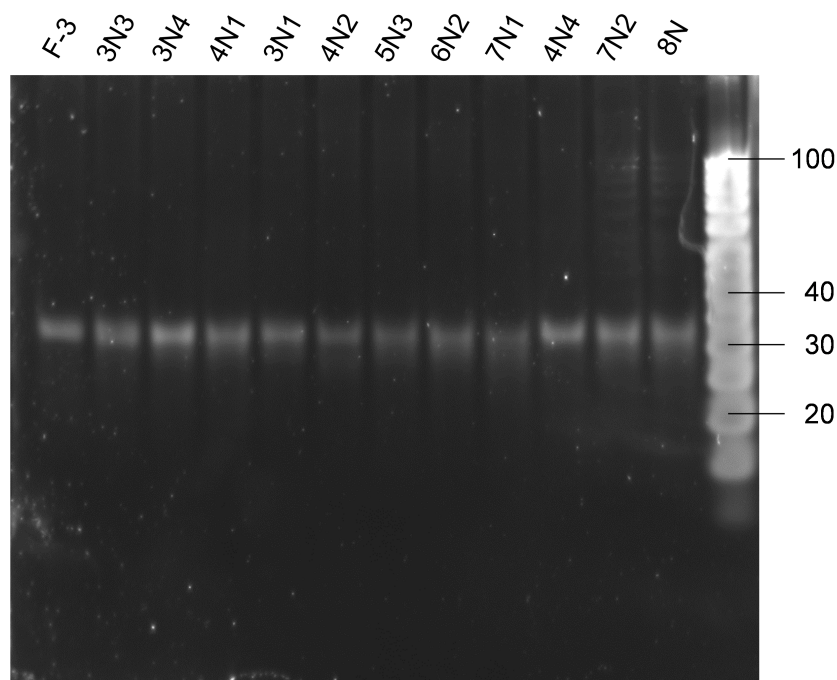


Figure C.21 – Gel electrophoresis of the FB1 sensors. 15 % native polyacrylamide (PAGE) gel electrophoresis of the F-3 and mutant sequences.

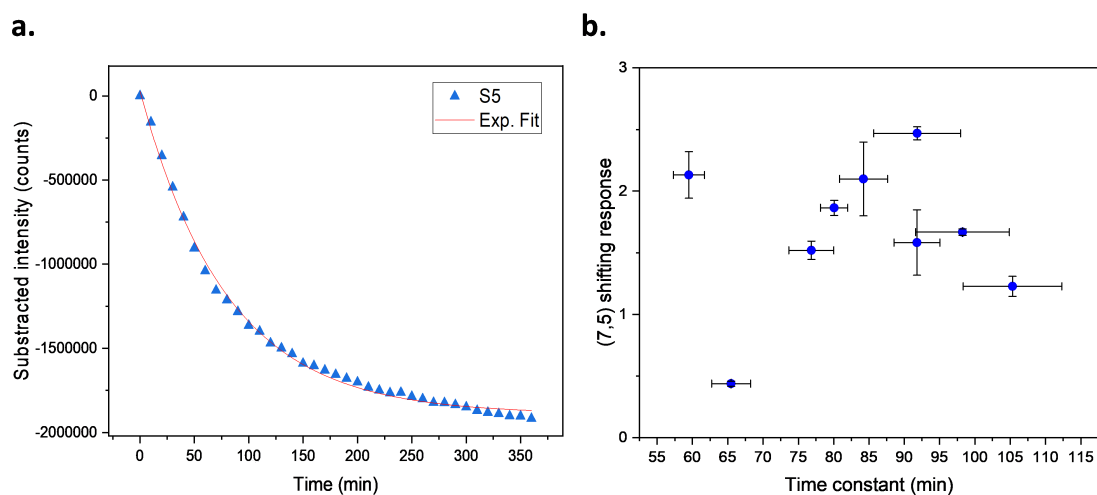


Figure C.22 – Relationship between binding affinity and FB1 sensing. (a) The kinetics of intensity change ($I_0 - I$) upon wrapping replacement with SDBS were fitted with exponential fits $y(t) = y_0 + A \cdot e^{(-\frac{t}{\tau})}$, with τ the time constant of the replacement. (b) Shifting response of the (7,5) chirality towards FB1 as a function of the time constant τ of SDBS replacement extracted from the exponential fits. The shifting response were determined with a toxin concentration of $10 \mu\text{M}$ and after an incubation time of 200 min.

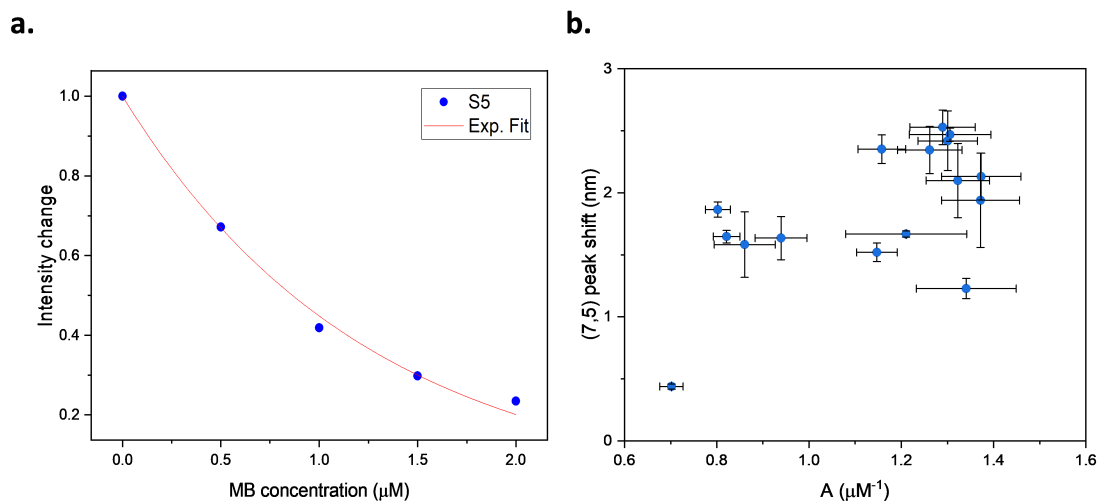


Figure C.23 – Relationship between surface coverage and FB1 sensing. (a) The decrease in fluorescence intensity (I/I_0) as a function of MB concentration. The data was fitted with exponential fits $y(x) = e^{Ax}$. (b) Shifting response of the (7,5) chirality towards FB1 as a function of the parameter A extracted from the exponential fits. The shifting response were determined with a toxin concentration of $10 \mu\text{M}$ and after an incubation time of 200 min.

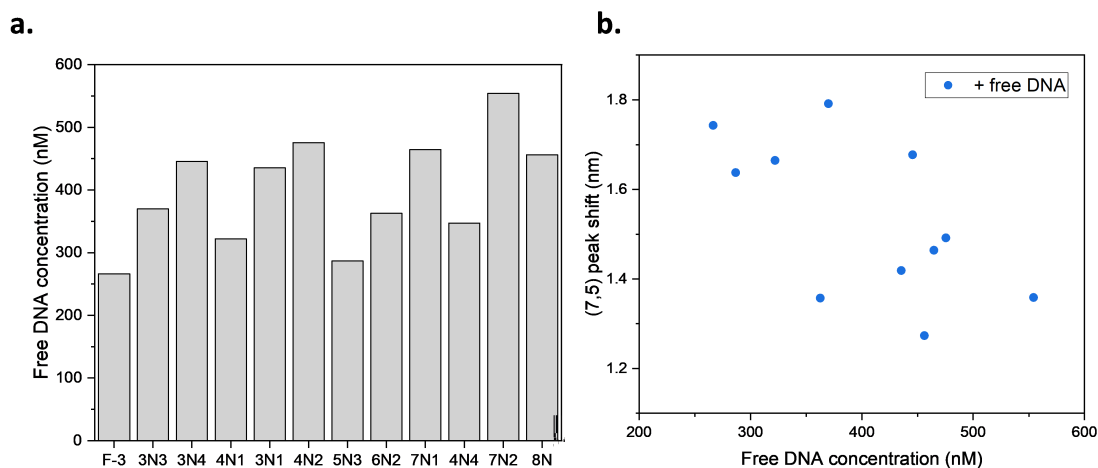


Figure C.24 – Relationship between free DNA concentration and FB1 sensing. (a) The concentration of free DNA for the various sequences used for FB1 sensing. (b) Shifting response of the (7,5) chirality towards FB1 as a function of the concentration of free DNA. The shifting response were determined with a toxin concentration of $10 \mu\text{M}$ and after an incubation time of 200 min.

Appendix C. Towards a semi-rational design of DNA-SWCNT sensors

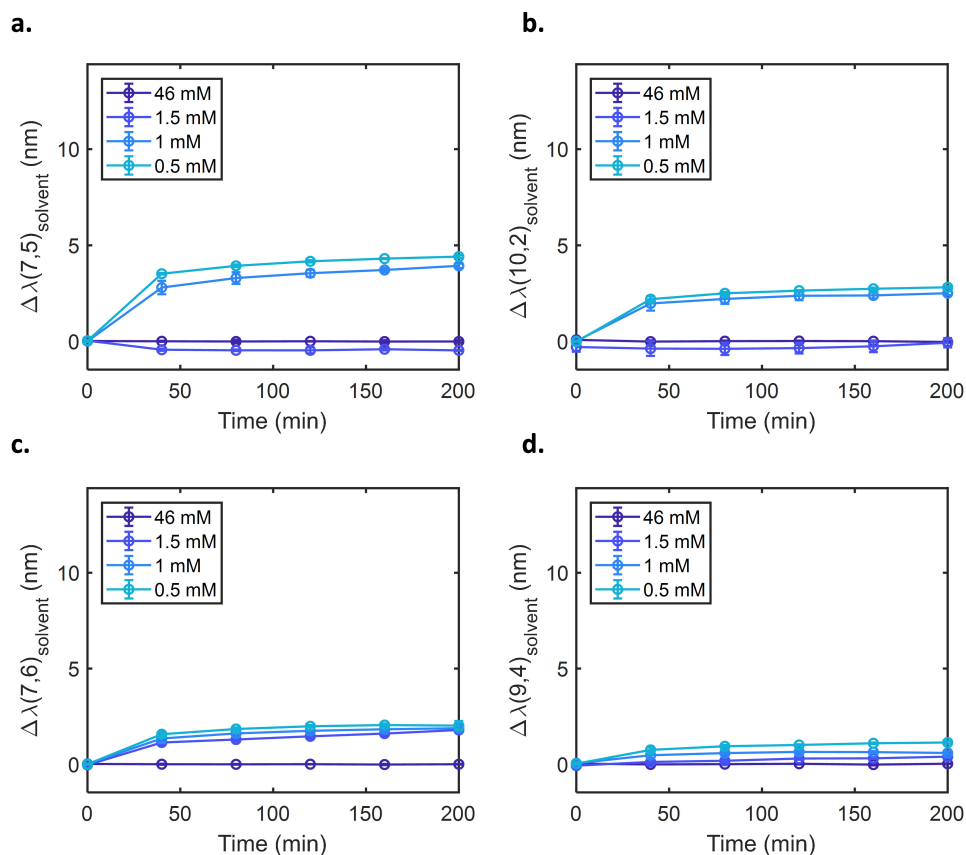


Figure C.25 – Shifting response of SC-SWCNTs towards TB toxin. Shifting response of SC-SWCNTs (from 0.6 to 46 mM SC) towards 10 μ M TB toxin for the (a) (7,5), (b) (10,2), (c) (7,6), (d) (9,4) chiralities.

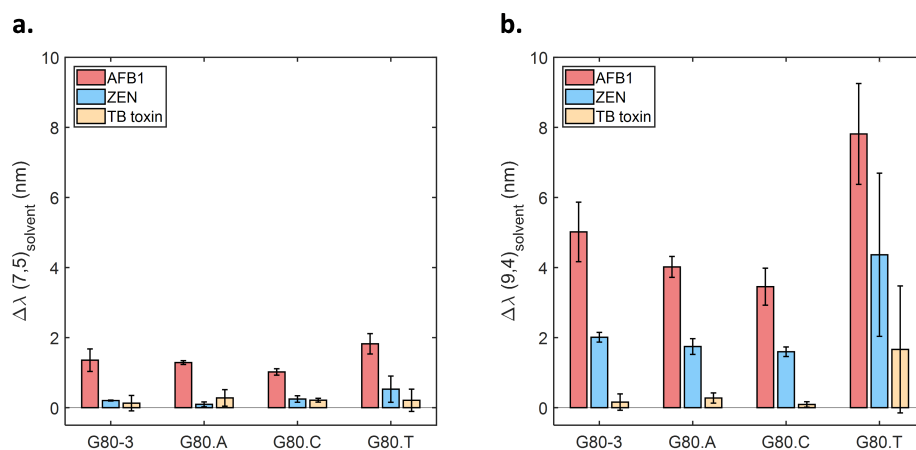


Figure C.26 – Response of the G80-3-SWCNT variants to TB toxin. Shifting response of the G80-3-SWCNT variants to AFB1 (red), ZEN (blue) and TB toxin (yellow) for (a) the (7,5) and (b) the (9,4) chiralities. The shifting response were determined with a toxin concentration of 10 μ M and after an incubation time of 200 min.

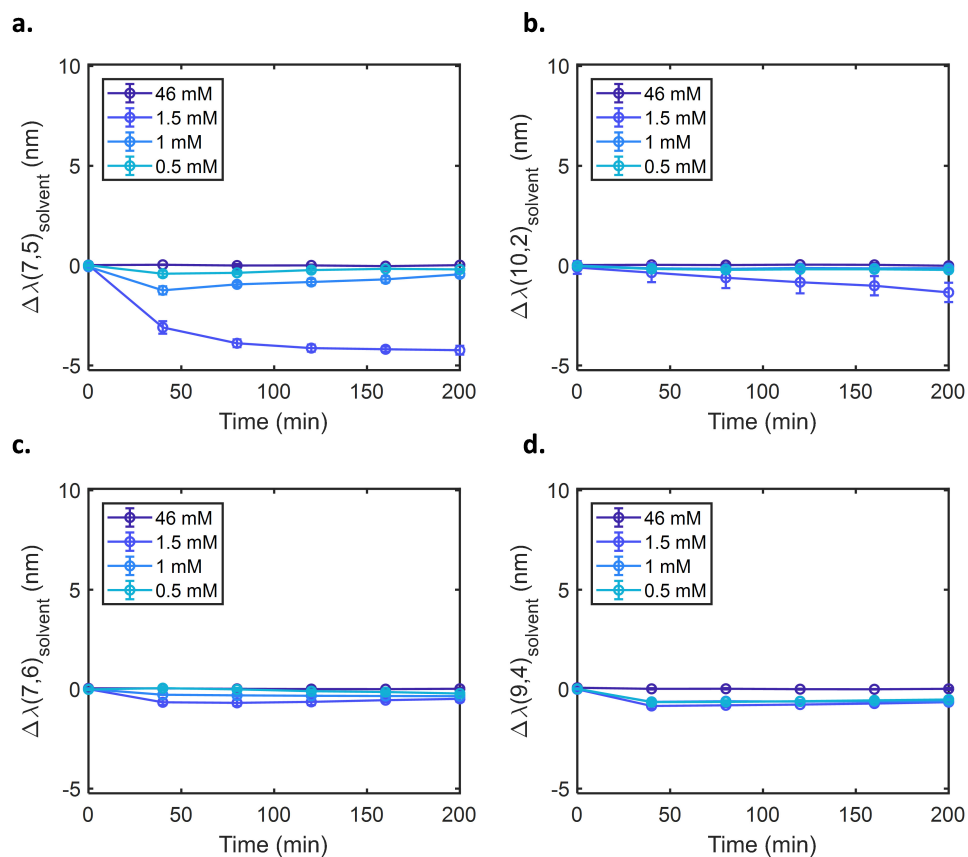


Figure C.27 – Shifting response of SC-SWCNTs towards OTA. Shifting response of SC-SWCNTs (from 0.6 to 46 mM SC) towards 10 μ M OTA for the (a) (7,5), (b) (10,2), (c) (7,6), (d) (9,4) chiralities.

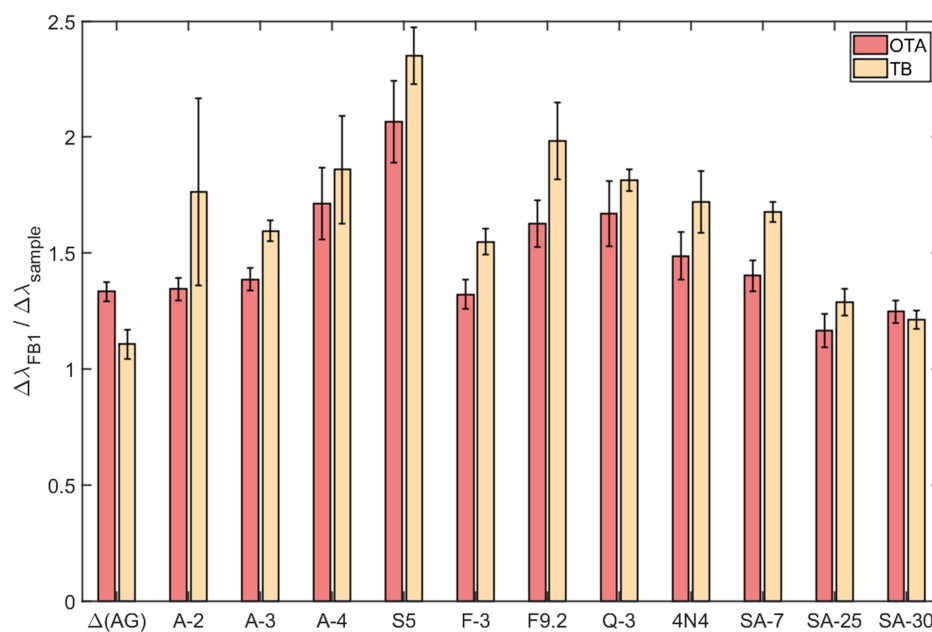


Figure C.28 – Sequence-dependent selectivity of the analyte response. Ratio of the shifting responses between FB1 and OTA (red) or TB toxin (yellow), representing the selectivity of the FB1 response with respect to the OTA and TB toxin. The selectivity of the response is dependent on the DNA sequence. The shifting response were determined with a toxin concentration of 10 μ M and after an incubation time of 200 min.

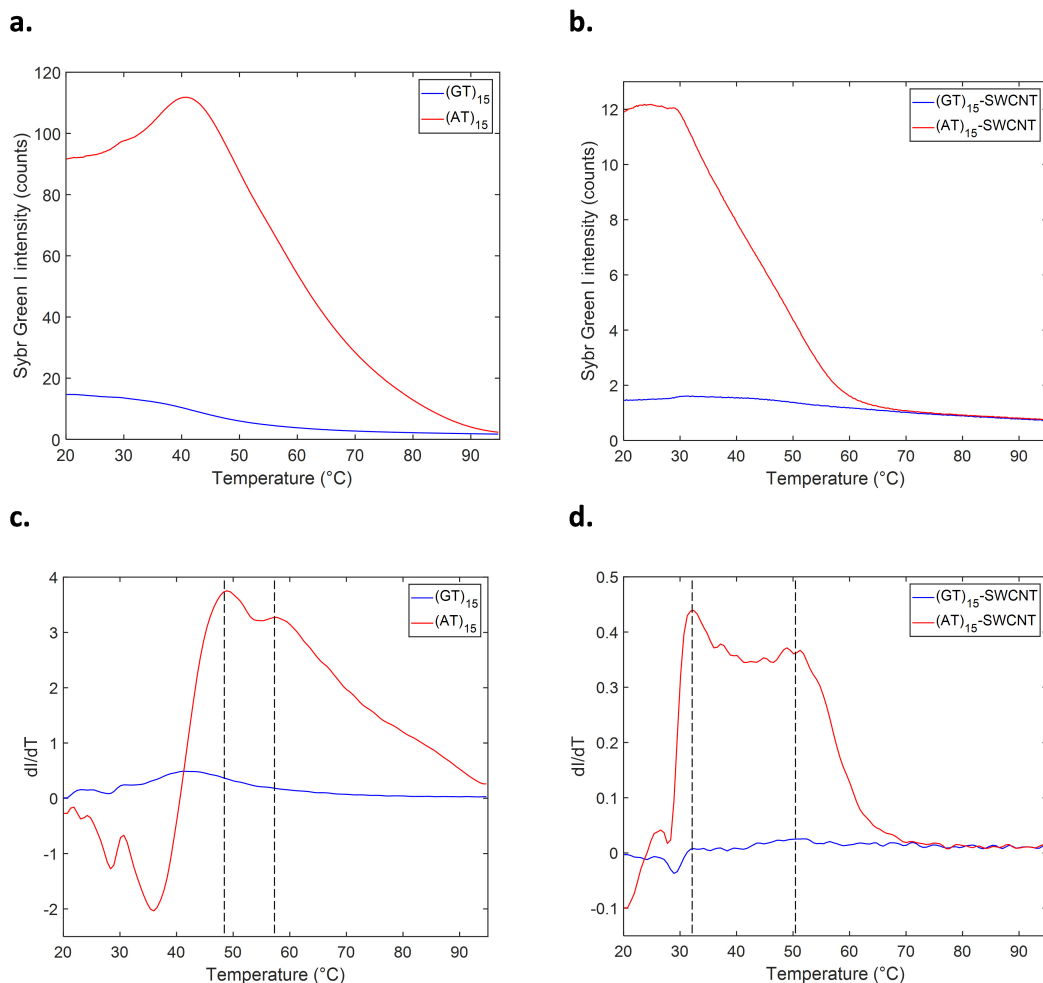


Figure C.29 – Melting curves of DNA and DNA-SWCNT complexes. Melting curves of (a) (AT)₁₅ and (GT)₁₅ sequences and (b) (AT)₁₅- and (GT)₁₅-SWCNT complexes. First derivative of the melting curves of (a) (AT)₁₅ and (GT)₁₅ sequences and (b) (AT)₁₅- and (GT)₁₅-SWCNT complexes. The horizontal dotted lines represent the melting temperatures of the (AT)₁₅ sequence and (AT)₁₅-SWCNT complex.

D Modulating the properties of DNA-SWCNTs through DNA chemical modification

Table D.1 – List of the modified sequences studied in this work. This list includes the DNA sequence, the type of modification (functional groups), the position where the modification is located in the sequence, the kind of linker used in the modification and the label used to describe the modification in the main text.

| Sequence | Modification | Position | Linker | Label |
|--------------------|---------------------------|--------------------|---------------------------------------|---------------|
| (AT) ₁₅ | Amino (-NH ₂) | 3' | C ₆ | Amino 3' |
| (AT) ₁₅ | Amino (-NH ₂) | 5' | C ₆ | Amino 5' |
| (AT) ₁₅ | Amino (-NH ₂) | 5' + 3' | C ₆ | Amino 5'3' |
| (AT) ₁₅ | Azide (-N ₃) | 3' | NHS Ester | Azide 3' |
| (AT) ₁₅ | Azide (-N ₃) | 5' | C ₆ Amide + C ₃ | Azide 5' |
| (GT) ₁₅ | Amino (-NH ₂) | 3' | C ₆ | Amino 3' |
| (GT) ₁₅ | Amino (-NH ₂) | 5' | C ₆ | Amino 5' |
| (GT) ₁₅ | Amino (-NH ₂) | 5' + 3' | C ₆ | Amino 5'3' |
| (GT) ₁₅ | Amino (-NH ₂) | 5' + Interior | dT + C ₆ | Amino 5'Int |
| (GT) ₁₅ | Amino (-NH ₂) | 5' + 3' + Interior | dT + C ₆ | Amino 5'Int3' |
| (GT) ₁₅ | Azide (-N ₃) | 3' | NHS Ester | Azide 3' |
| (GT) ₁₅ | Azide (-N ₃) | 5' | C ₆ Amide + C ₃ | Azide 5' |
| N ₃₀ | Amino (-NH ₂) | 5' | C ₆ | Amino 5' |
| N ₃₀ | Amino (-NH ₂) | 5' + 3' | C ₆ | Amino 5'3' |
| N ₃₀ | Azide (-N ₃) | 5' | C ₆ Amide + C ₃ | Azide 5' |

Appendix D. Modulating the properties of DNA-SWCNTs through DNA chemical modification

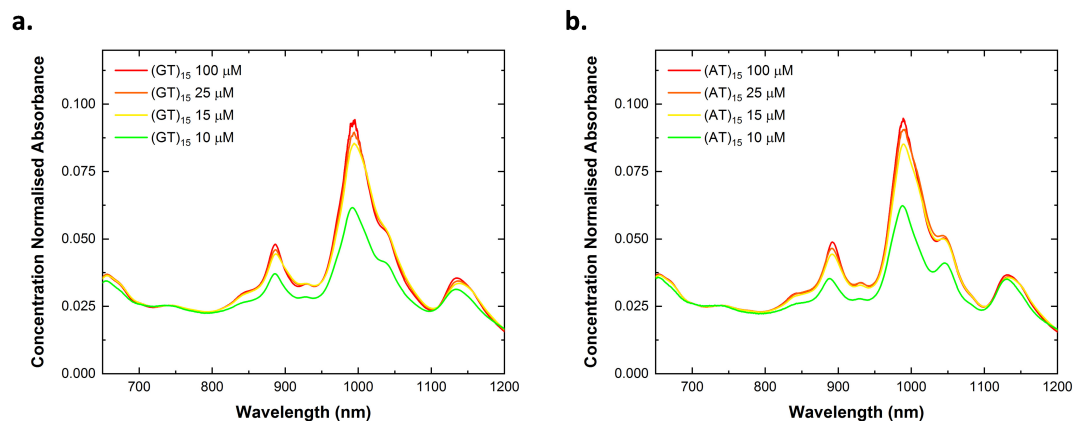


Figure D.1 – Optimization of the DNA concentration used for exchange. Absorbance spectra for SWCNT prepared by exchange with (a) (GT)₁₅ and (b) (AT)₁₅ oligonucleotides at 10 μM (green), 15 μM (yellow), 25 μM (orange) and 100 μM (red) final DNA concentrations. A large increase in peak-to-valley ratio was observed for the (6,5) absorption peak between the 10 and 15 μM DNA batches for both (GT)₁₅ and (AT)₁₅ sequences, but only small variations were observed between the concentrations ranging from 15 to 100 μM. Based on this observation, a DNA concentration of 15 μM was considered as optimal for the dispersion of SWCNTs.

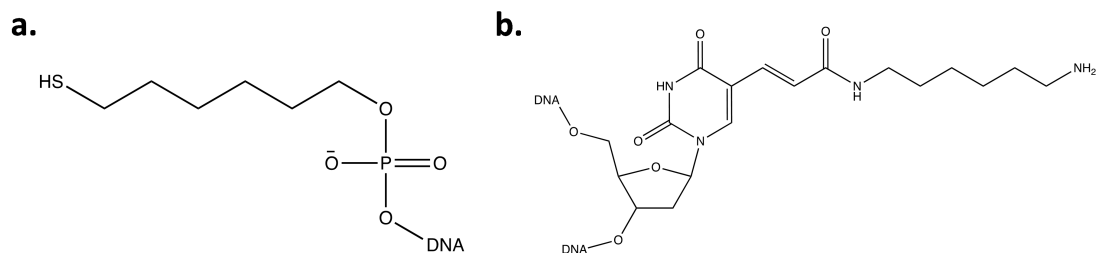


Figure D.2 – Chemical structures of the thiol and internal amino modifications. The internal amino modification is attached to a thymidine (dT) base.

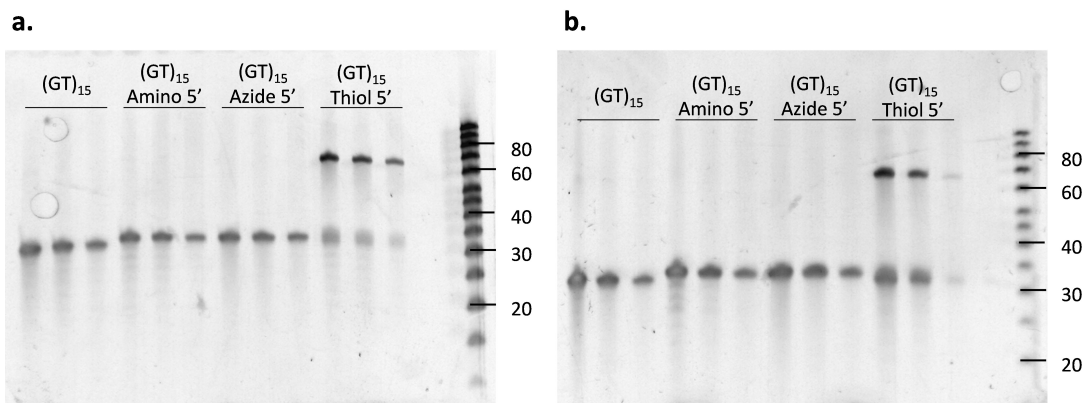


Figure D.3 – Gel electrophoresis of unmodified and modified (GT)₁₅. Denaturing 15 % PAGE gels of DNA extracted from (a) sonicated and (b) exchanged DNA-SWCNT samples. DNA samples were run at three concentrations for each sequence: 1X, 0.5X, and 0.2X in the first, second, and third lanes, respectively. As expected, a band around 30 nucleotides is observed for every sequence. An additional band at ≈ 60 nucleotides is also present for the thiol-modified DNA sequence, indicating the presence of dimers.

Appendix D. Modulating the properties of DNA-SWCNTs through DNA chemical modification

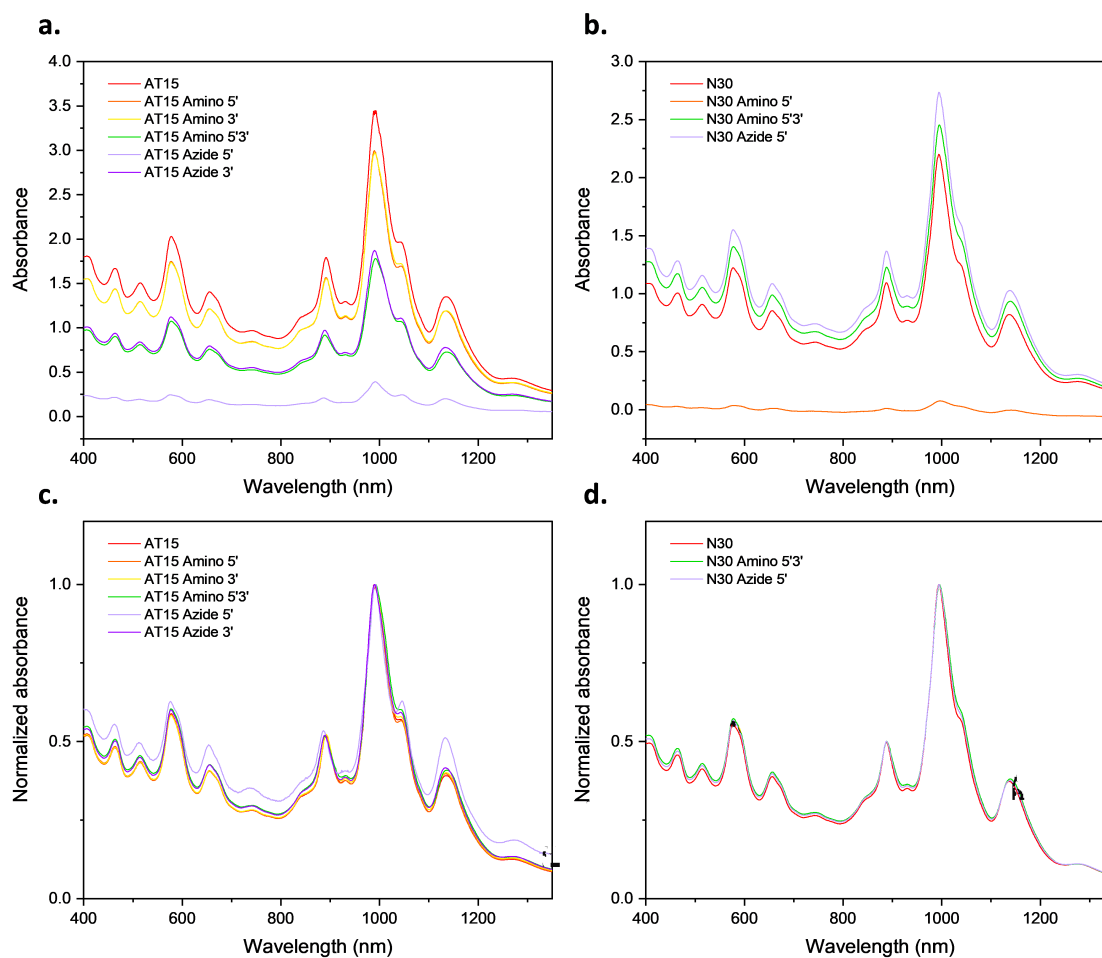


Figure D.4 – Absorbance of the (AT)₁₅- and N₃₀-SWCNT complexes. (a,b) Absorbance spectra and (c,d) absorbance spectra normalized to the (6,5) E₁₁ absorption peak. The spectra are represented for the unmodified and Amino or Azide-modified (a,c) (AT)₁₅-SWCNT and (b,d) N₃₀-SWCNT complexes.

Table D.2 – Summary of the intensity changes compared to the unmodified samples. Intensity changes $(I-I_0)/I_0$ of the modified samples (I) with respect to unmodified samples (I_0) for the (6,5) and (7,5) emission maxima and for the (AT)₁₅-, (GT)₁₅- and N₃₀-based samples. The error corresponds to 1 σ (n=3).

| Sample | (6,5) intensity change (%) | (7,5) intensity change (%) |
|----------------------------------|----------------------------|----------------------------|
| (AT) ₁₅ Amino 3' | 5.6 ± 5.9 | 6.0 ± 3.3 |
| (AT) ₁₅ Amino 5' | 8.6 ± 4.5 | 13.9 ± 5.5 |
| (AT) ₁₅ Amino 5'3' | -22.5 ± 7.7 | -19.9 ± 6.2 |
| (AT) ₁₅ Azide 3' | 1.8 ± 7.3 | 1.9 ± 3.4 |
| (GT) ₁₅ Amino 3' | -17.8 ± 5.2 | -30.2 ± 8.7 |
| (GT) ₁₅ Amino 5' | -19.6 ± 5.6 | -23.6 ± 7.3 |
| (GT) ₁₅ Amino 5'3' | -16.9 ± 4.1 | -27.4 ± 7.8 |
| (GT) ₁₅ Amino 5'Int | -20.6 ± 6.8 | -30.6 ± 10.2 |
| (GT) ₁₅ Amino 5'Int3' | -70.3 ± 12.4 | -64.9 ± 15.9 |
| (GT) ₁₅ Azide 3' | 19.5 ± 12.9 | 27.9 ± 14.9 |
| (GT) ₁₅ Azide 5' | -34.1 ± 13.1 | -50.0 ± 12.6 |
| N ₃₀ Amino 3' | -11.8 ± 34.6 | -31.8 ± 27.3 |
| N ₃₀ Amino 5'3' | -24.9 ± 12.6 | -31.5 ± 11.4 |
| N ₃₀ Azide 5' | 9.6 ± 14.0 | -2.4 ± 13.4 |

Appendix D. Modulating the properties of DNA-SWCNTs through DNA chemical modification

Table D.3 – Summary of the intensities after SDC replacement. Intensity changes $(I-I_0)/I_0$ of the SDC-replaced samples with respect to unmodified samples or to the intensities before SDC replacement for the (6,5) emission maximum and for the $(AT)_{15}$ -, $(GT)_{15}$ - and N_{30} -based samples. The error corresponds to 1σ ($n=3$).

| Sample | $(I-I_0)/I_0$ vs unmodified (%) | $(I-I_0)/I_0$ vs before SDC (%) |
|-------------------------|---------------------------------|---------------------------------|
| $(AT)_{15}$ | / | 111.1 ± 17.3 |
| $(AT)_{15}$ Amino 3' | 8.3 ± 11.2 | 103.8 ± 12.1 |
| $(AT)_{15}$ Amino 5' | 12.4 ± 7.1 | 99.4 ± 2.6 |
| $(AT)_{15}$ Amino 5'3' | -21.2 ± 15.5 | 86.6 ± 28.9 |
| $(AT)_{15}$ Azide 3' | 7.8 ± 14.4 | 99.7 ± 22.0 |
| $(GT)_{15}$ | / | 172.3 ± 14.3 |
| $(GT)_{15}$ Amino 3' | -26.6 ± 10.5 | 142.2 ± 24.8 |
| $(GT)_{15}$ Amino 5' | -26.4 ± 7.4 | 155.2 ± 28.9 |
| $(GT)_{15}$ Amino 5'3' | -31.5 ± 11.4 | 125.2 ± 30.6 |
| $(GT)_{15}$ Amino 5'Int | -31.6 ± 6.3 | 130.2 ± 10.1 |
| $(GT)_{15}$ Azide 3' | -2.7 ± 7.6 | 145.6 ± 12.1 |
| $(GT)_{15}$ Azide 5' | -51.9 ± 13.5 | 157.1 ± 67.7 |
| N_{30} | / | 129.1 ± 29.7 |
| N_{30} Amino 3' | -16.2 ± 11.1 | 119.1 ± 15.3 |
| N_{30} Amino 5'3' | -31.5 ± 25.7 | 117.8 ± 64.2 |
| N_{30} Azide 5' | 4.9 ± 19.7 | 123.2 ± 25.6 |

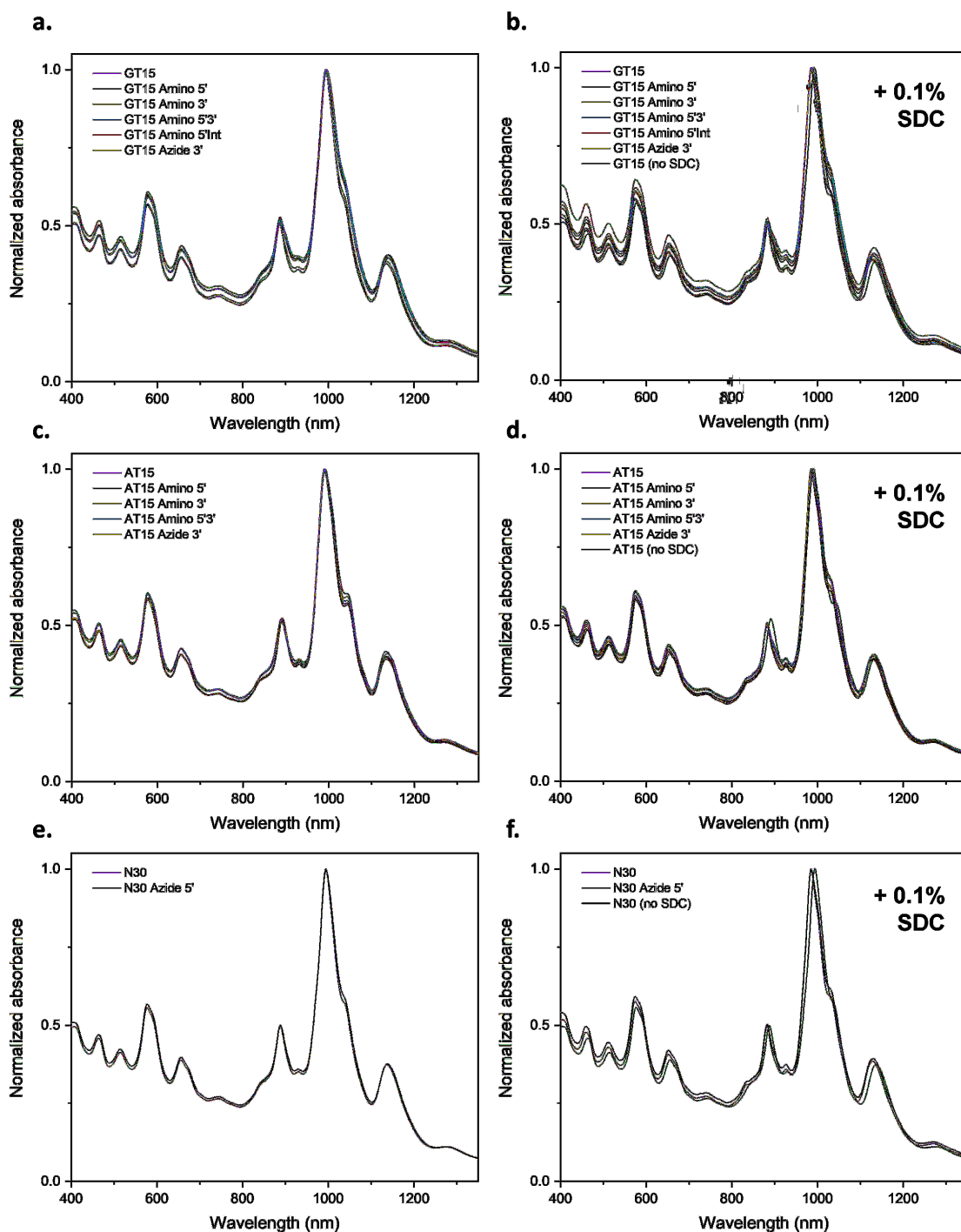


Figure D.5 – Comparison of the absorbance spectra after wrapping replacement with SDC. Absorbance spectra normalized to the (6,5) E_{11} absorption peak for the unmodified and Amino-, Azide-modified (a,b) (GT)₁₅-SWCNT, (c,d) (AT)₁₅-SWCNT and (e,f) N₃₀-SWCNT complexes (a,c,e) before and (b,d,f) after wrapping replacement with 0.1 % SDC.

Appendix D. Modulating the properties of DNA-SWCNTs through DNA chemical modification

Table D.4 – Summary of the DTT responses. Intensity response $(I-I_0)/I_0$ in presence of 10 mM DTT, with I_0 the intensity before addition, and final intensities of the samples after DTT addition for the (6,5) emission maximum and for the (AT)₁₅-, (GT)₁₅- and N₃₀-based samples. The error corresponds to 1 σ (n=3).

| Sample | Intensity response (%) | Intensity after DTT (x 10 ⁶ counts) |
|--------------------------------|------------------------|--|
| (AT) ₁₅ | 39.7 ± 5.5 | 10.2 ± 0.3 |
| (AT) ₁₅ Amino 3' | 29.1 ± 4.5 | 10.1 ± 0.4 |
| (AT) ₁₅ Amino 5' | 29.7 ± 5.2 | 10.9 ± 0.5 |
| (AT) ₁₅ Amino 5'3' | 27.0 ± 2.5 | 7.8 ± 0.1 |
| (AT) ₁₅ Azide 3' | 34.0 ± 15.3 | 9.7 ± 0.9 |
| (GT) ₁₅ | 66.3 ± 5.7 | 10.2 ± 0.4 |
| (GT) ₁₅ Amino 3' | 62.8 ± 4.2 | 8.7 ± 0.3 |
| (GT) ₁₅ Amino 5' | 58.9 ± 3.8 | 8.6 ± 0.3 |
| (GT) ₁₅ Amino 5'3' | 59.7 ± 4.0 | 8.4 ± 0.2 |
| (GT) ₁₅ Amino 5'Int | 54.6 ± 3.5 | 8.3 ± 0.2 |
| (GT) ₁₅ Azide 3' | 57.9 ± 2.2 | 10.8 ± 0.1 |
| N ₃₀ | 40.3 ± 2.8 | 9.8 ± 0.1 |
| N ₃₀ Amino 5'3' | 47.8 ± 3.6 | 7.6 ± 0.2 |
| N ₃₀ Azide 5' | 37.4 ± 3.0 | 10.1 ± 0.3 |

Table D.5 – Summary of the dopamine responses. Intensity response $(I-I_0)/I_0$ in presence of 100 μ M dopamine, with I_0 the intensity before addition, and final intensities of the samples after dopamine addition for the (6,5) emission maximum and for the (AT)₁₅-, (GT)₁₅- and N₃₀-based samples. The error corresponds to 1 σ (n=3).

| Sample | Intensity response (%) | Intensity after dopamine (x 10 ⁶ counts) |
|--------------------------------|------------------------|---|
| (AT) ₁₅ | 4.0 ± 9.0 | 7.7 ± 0.5 |
| (AT) ₁₅ Amino 3' | -1.0 ± 4.0 | 8.3 ± 0.2 |
| (AT) ₁₅ Amino 5' | 4.6 ± 5.0 | 8.9 ± 0.4 |
| (AT) ₁₅ Amino 5'3' | 7.0 ± 13.1 | 5.8 ± 0.7 |
| (AT) ₁₅ Azide 3' | 4.3 ± 2.4 | 4.9 ± 0.1 |
| (GT) ₁₅ | 30.1 ± 11.4 | 7.6 ± 0.9 |
| (GT) ₁₅ Amino 3' | 18.3 ± 7.4 | 5.9 ± 0.4 |
| (GT) ₁₅ Amino 5' | 14.5 ± 10.3 | 5.6 ± 0.6 |
| (GT) ₁₅ Amino 5'3' | 14.9 ± 8.5 | 5.8 ± 0.4 |
| (GT) ₁₅ Amino 5'Int | 8.4 ± 3.1 | 5.2 ± 0.1 |
| (GT) ₁₅ Azide 3' | 21.7 ± 9.5 | 7.7 ± 0.5 |
| N ₃₀ | 11.0 ± 4.5 | 7.3 ± 0.2 |
| N ₃₀ Amino 5'3' | 13.9 ± 5.0 | 5.0 ± 0.2 |
| N ₃₀ Azide 5' | 7.8 ± 5.2 | 7.2 ± 0.3 |

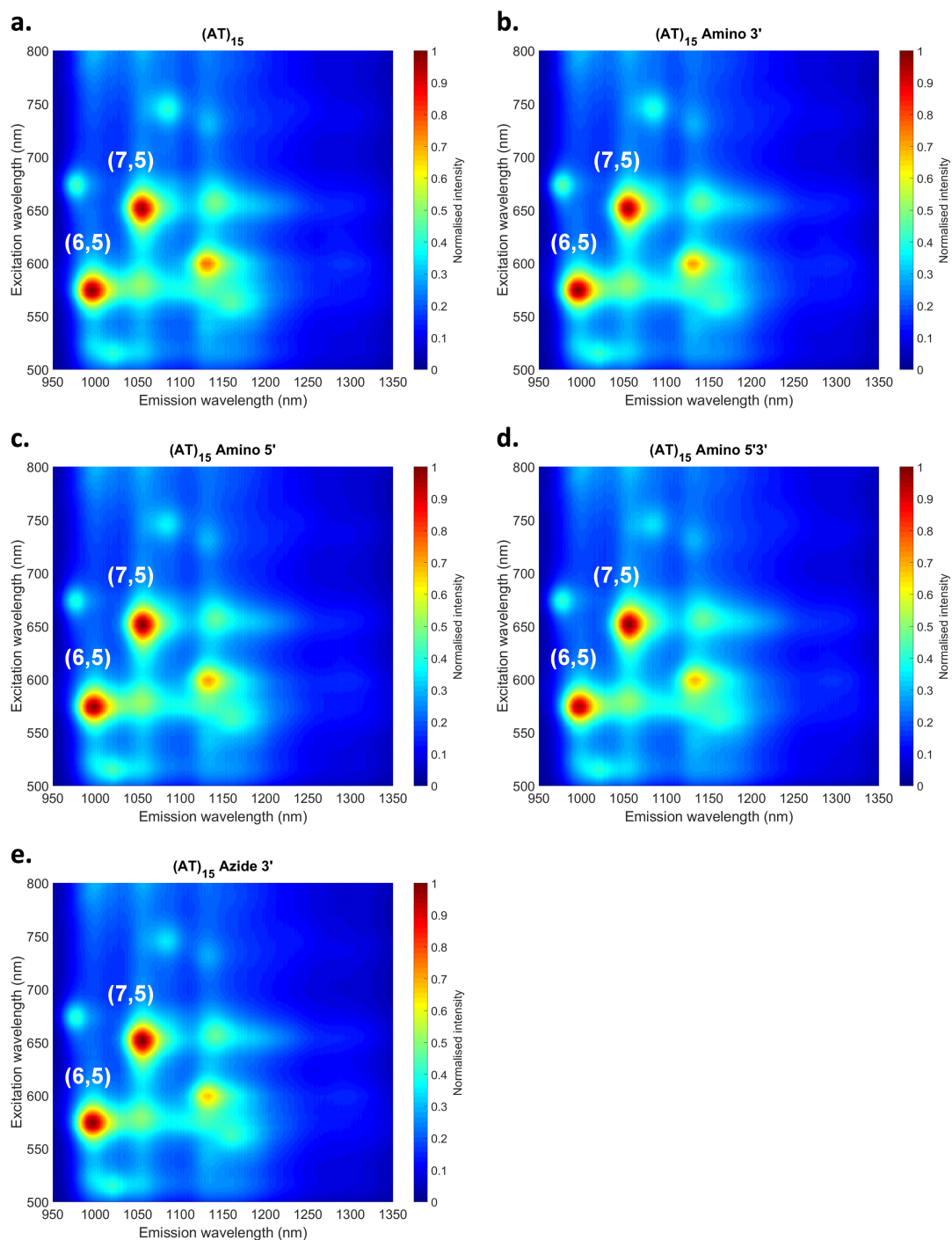


Figure D.6 – PLE maps of the unmodified and modified $(AT)_{15}$ -SWCNT complexes. Photoluminescence excitation (PLE) maps for the (a) unmodified and (b) Amino 3'-, (c) Amino 5'-, (d) Amino 5'3'-, (e) Azide 3'-modified $(AT)_{15}$ -SWCNT complexes. The intensity is normalized between 0 and 1.

Appendix D. Modulating the properties of DNA-SWCNTs through DNA chemical modification

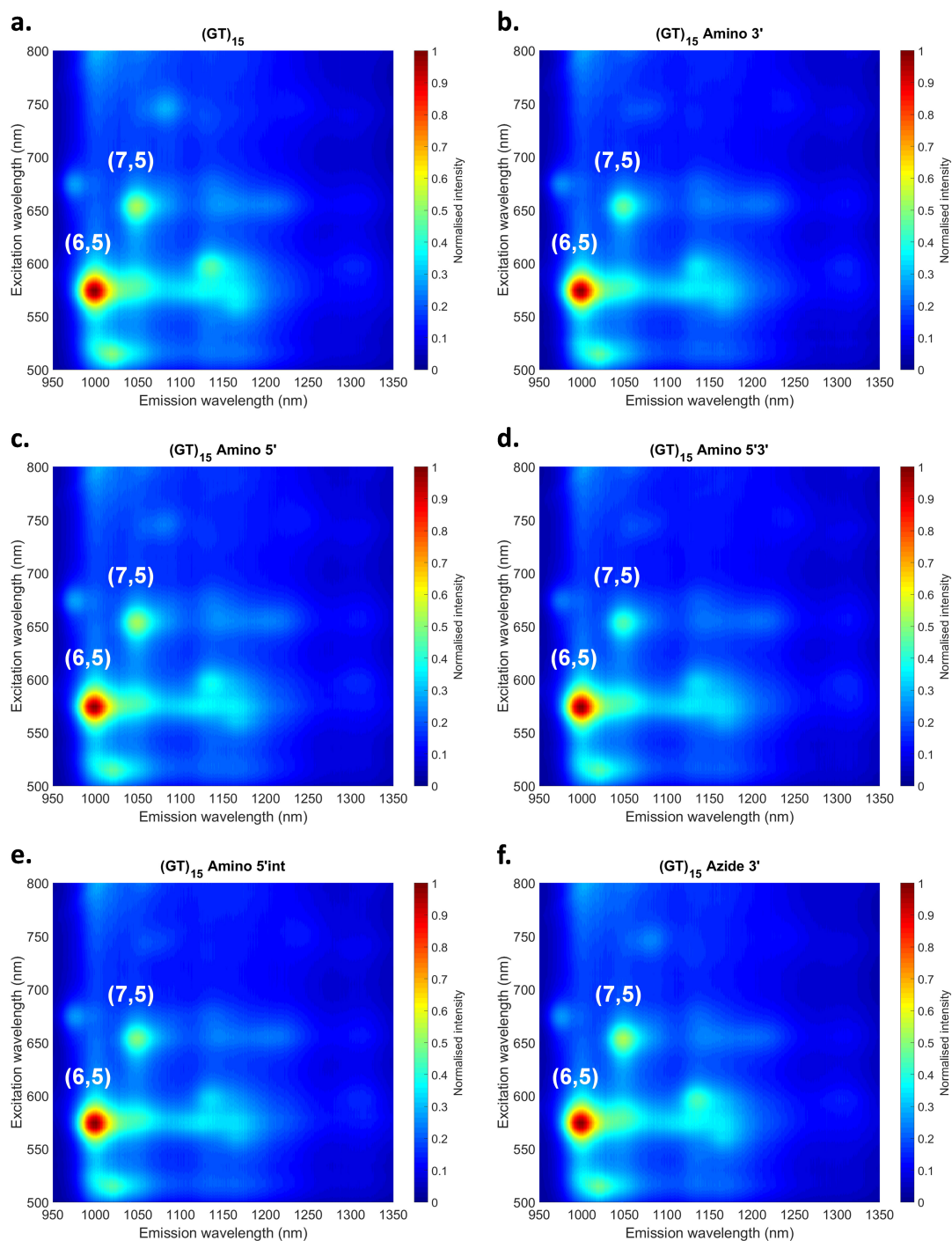


Figure D.7 – PLE maps of the unmodified and modified $(GT)_{15}$ -SWCNT complexes. Photoluminescence excitation (PLE) maps for the (a) unmodified and (b) Amino 3'-, (c) Amino 5'-, (d) Amino 5'3'-, (e) Amino 5'Int-, (f) Azide 3'-modified $(GT)_{15}$ -SWCNT complexes. The intensity is normalized between 0 and 1.

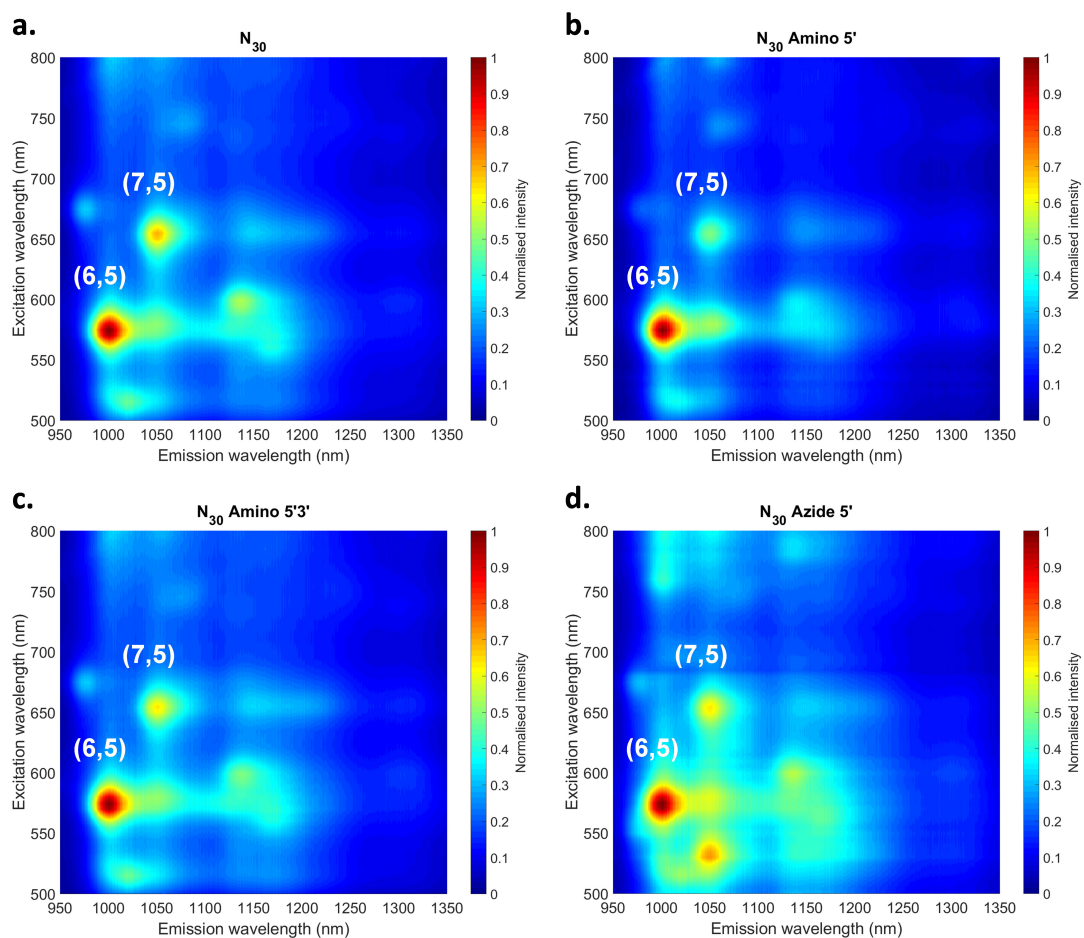


Figure D.8 – PLE maps of the unmodified and modified N_{30} -SWCNT complexes. Photoluminescence excitation (PLE) maps for the (a) unmodified and (b) Amino 5'-, (c) Amino 5'3'-, (d) Azide 5'-modified N_{30} -SWCNT complexes. The intensity is normalized between 0 and 1.

Appendix D. Modulating the properties of DNA-SWCNTs through DNA chemical modification

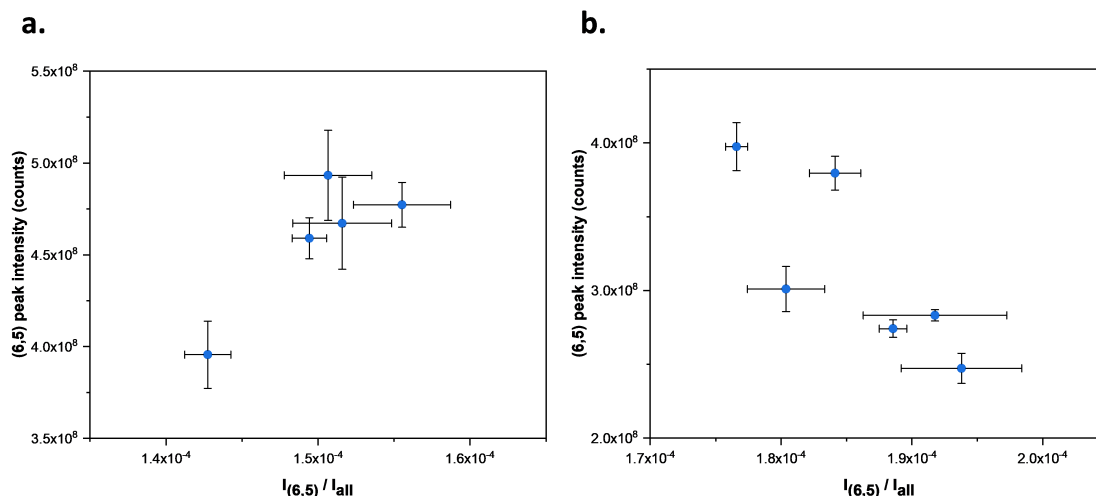


Figure D.9 – Relationship between peak intensity change and peak intensity prevalence. Intensities of the emission maxima of the (6,5) chirality as a function of the ratios of the (6,5) chirality with the summed integrated emissions excited from 500 to 800 nm (see PLE maps conditions in **Methods**) for (a) the (AT)₁₅-SWCNT complexes and (b) the (GT)₁₅-SWCNT complexes. The error bars correspond to 1σ ($n=3$).

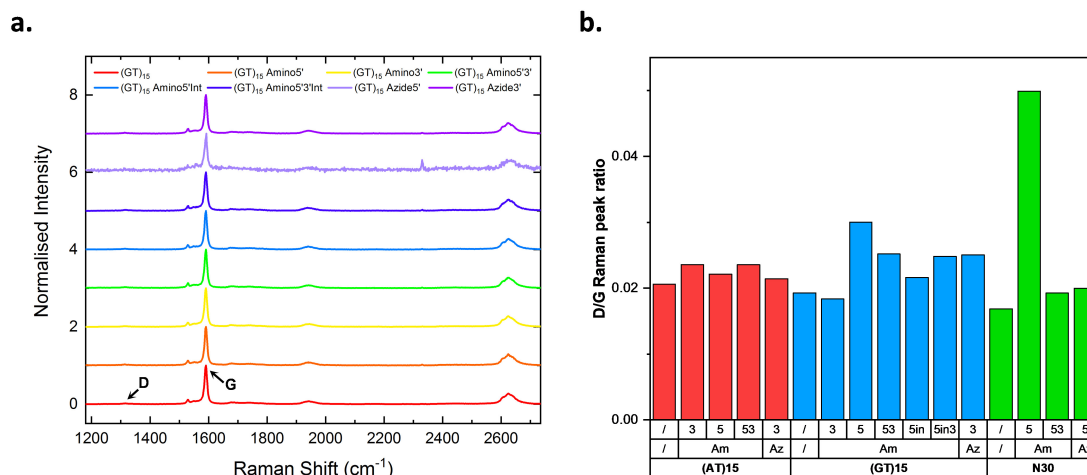


Figure D.10 – Effect of the modifications on the D/G Raman peak ratio. (a) Normalized Raman spectra for the unmodified and modified (GT)₁₅-SWCNT complexes. The D and G peaks, around 1310 and 1590 cm^{-1} respectively, are indicated by arrows on the graph. (b) Ratios of the D and G peaks for the unmodified and Amino ("Am") or Azide ("Az") -modified (AT)₁₅- (red), (GT)₁₅- (blue) and N₃₀-SWCNT (green) complexes. The numbers above the modification type indicate the position of the modification: 5' ("5"), 3' ("3"), 5' and 3' ("53"), 5' and interior ("5in") and 5', 3' and interior ("5in3"). The D/G ratio can be used to probe the density of defects on the SWCNT surface, a higher ratio indicating a ratio density of defects.

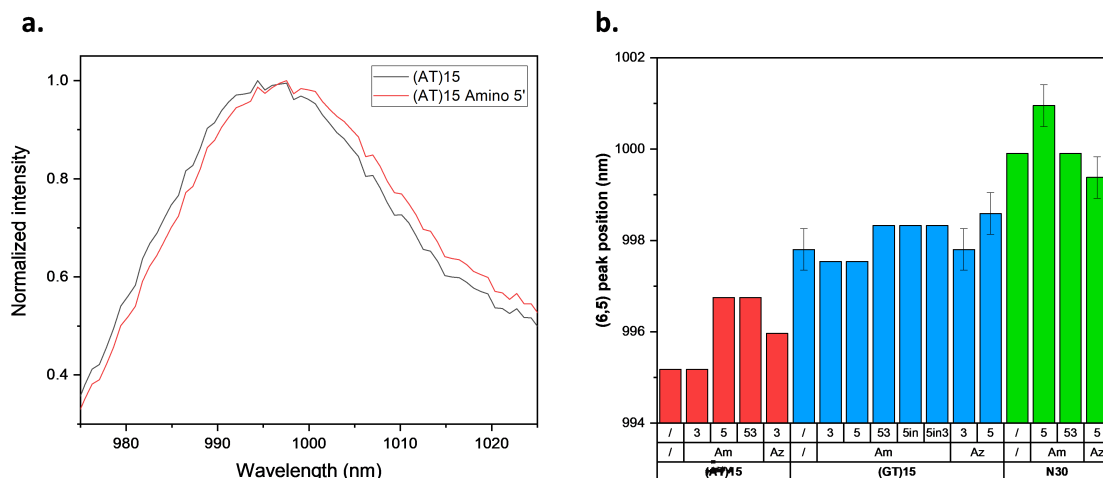


Figure D.11 – Effect of the modifications on the peak position of the DNA-SWCNTs. (a) Normalized fluorescence spectra of the (6,5) emission peak for the unmodified (black) and Amino 5' (red) (AT)₁₅-SWCNT complexes. (b) Position of the emission maximum of the (6,5) chirality for the unmodified and Amino (“Am”) or Azide (“Az”) -modified (AT)₁₅- (red), (GT)₁₅- (blue) and N₃₀-SWCNT (green) complexes. The numbers above the modification type indicate the position of the modification: 5' (“5”), 3' (“3”), 5' and 3' (“53”), 5' and interior (“5in”) and 5', 3' and interior (“5in3”). The error bars correspond to 1 σ (n=3).

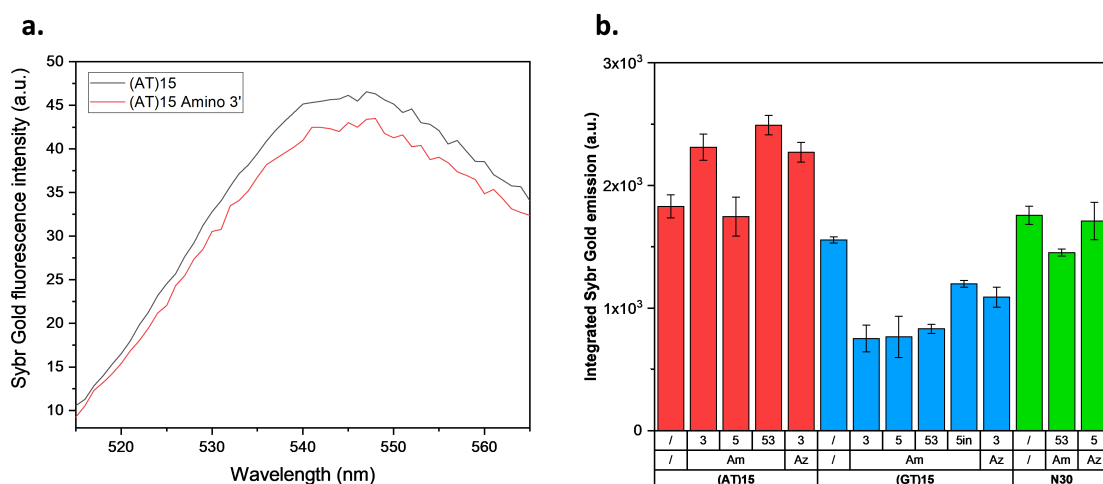


Figure D.12 – Effect of the modifications on the concentration of DNA on the SWCNT surface. (a) Fluorescence spectra of the Sybr Gold dye (under 495 nm excitation) in presence of DNA extracted from unmodified (black) and Amino 3' (red) (AT)₁₅-SWCNT complexes. (b) Integrated fluorescence (between 515 and 565 nm) of the Sybr Gold dye in presence of DNA extracted from the unmodified and Amino (“Am”) or Azide (“Az”) -modified (AT)₁₅- (red), (GT)₁₅- (blue) and N₃₀-SWCNT (green) complexes. The numbers above the modification type indicate the position of the modification: 5' (“5”), 3' (“3”), 5' and 3' (“53”), 5' and interior (“5in”) and 5', 3' and interior (“5in3”). The fluorescence of the dye is proportional to the concentration of DNA and depends on the DNA sequence. It is therefore possible to estimate changes in DNA wrapping concentrations by comparing the intensity of the dye between samples of the same DNA sequence. The error bars correspond to 1 σ (n=2).

Appendix D. Modulating the properties of DNA-SWCNTs through DNA chemical modification

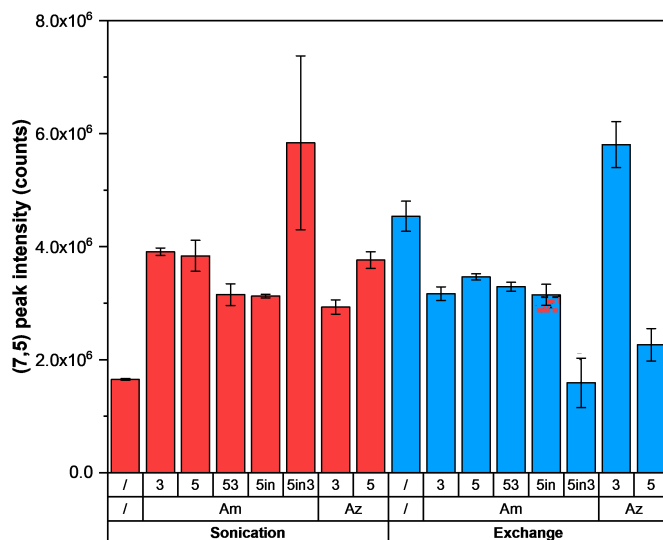


Figure D.13 – Effect of the modification on the (7,5) intensity for sonicated and exchanged samples. Intensities of the maximum of the (7,5) emission for the unmodified and Amino (“Am”) or Azide (“Az”) -modified (GT)₁₅-SWCNT complexes prepared by sonication (red) and exchange (blue). The numbers above the modification type indicate the position of the modification: 5’ (“5”), 3’ (“3”), 5’ and 3’ (“53”), 5’ and interior (“5in”) and 5’, 3’ and interior (“5in3”). The error bars correspond to 1 σ (n=3).

Table D.6 – Summary of the intensity changes for the sonicated samples. Intensity changes $(I-I_0)/I_0$ of the modified samples (I) with respect to unmodified samples (I_0) for the (6,5) and (7,5) emission maxima and for the sonicated (GT)₁₅-SWCNT complexes. The error corresponds to 1 σ (n=3).

| Sample | (6,5) intensity change (%) | (7,5) intensity change (%) |
|----------------------------------|-----------------------------------|-----------------------------------|
| (GT) ₁₅ Amino 3' | 55.4 ± 10.8 | 136.5 ± 5.3 |
| (GT) ₁₅ Amino 5' | 79.6 ± 10.6 | 132.1 ± 17.6 |
| (GT) ₁₅ Amino 5'3' | 28.7 ± 8.8 | 90.6 ± 12.7 |
| (GT) ₁₅ Amino 5'Int | 58.7 ± 6.8 | 89.1 ± 3.0 |
| (GT) ₁₅ Amino 5'Int3' | 207.1 ± 74.4 | 253.0 ± 94.0 |
| (GT) ₁₅ Azide 3' | 67.9 ± 12.7 | 77.3 ± 8.8 |
| (GT) ₁₅ Azide 5' | 86.5 ± 13.3 | 127.6 ± 10.0 |

Appendix D. Modulating the properties of DNA-SWCNTs through DNA chemical modification

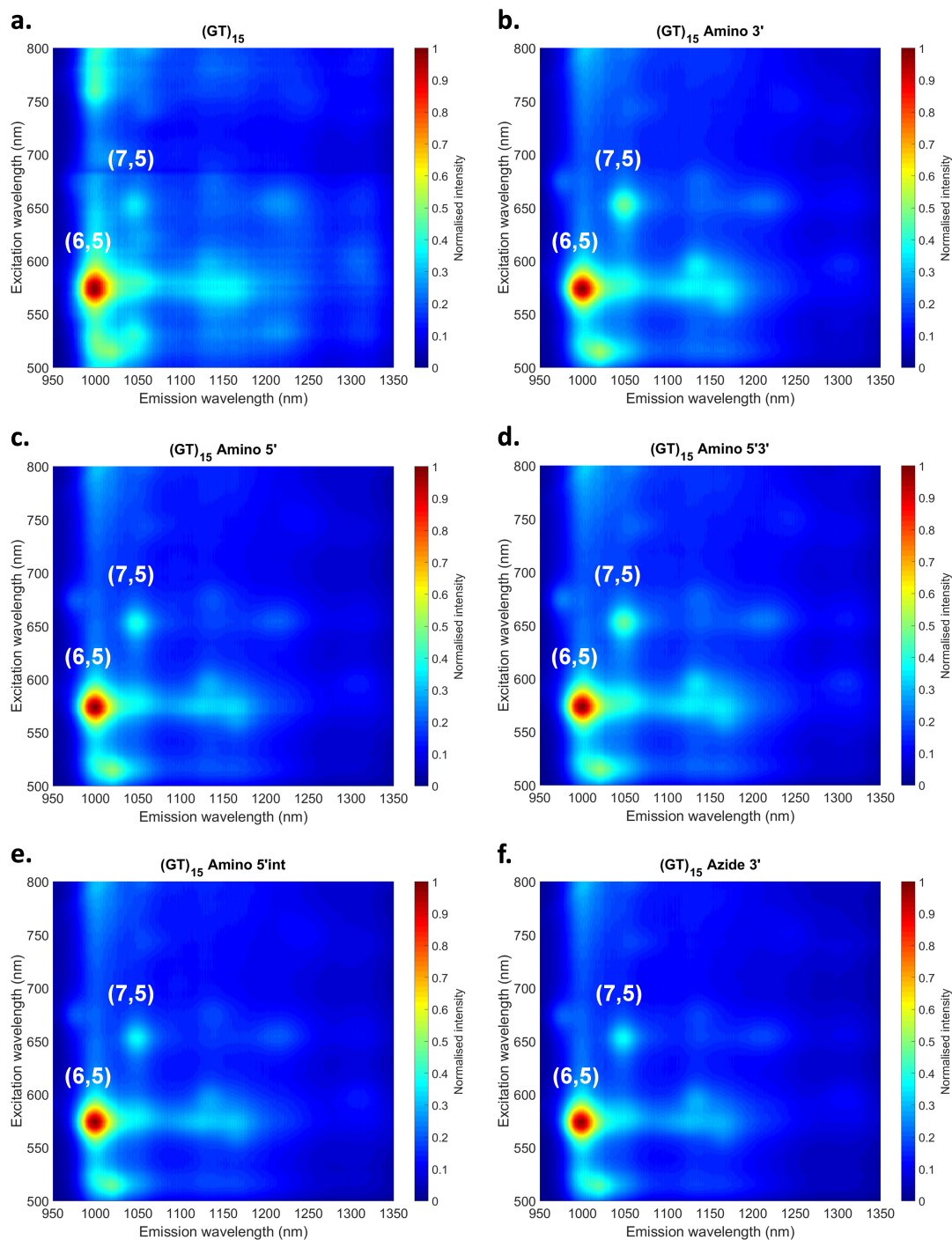


Figure D.14 – PLE maps of the sonicated $(GT)_{15}$ -SWCNT complexes. Photoluminescence excitation (PLE) maps for the (a) unmodified and (b) Amino 3', (c) Amino 5', (d) Amino 5'3', (e) Amino 5'Int-, (f) Azide 3'-modified $(GT)_{15}$ -SWCNT complexes prepared by sonication. The intensity is normalized between 0 and 1.

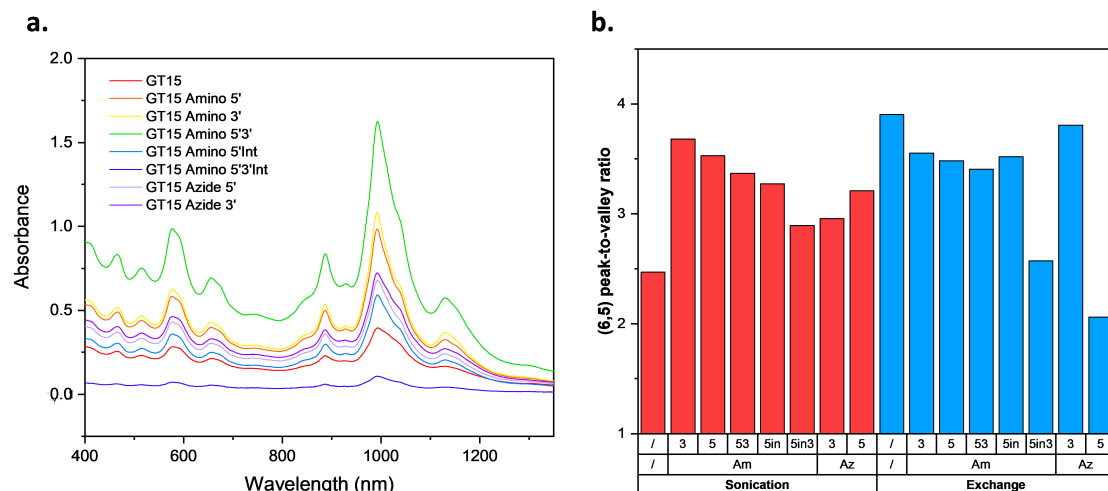


Figure D.15 – Effect of the modifications on the dispersibility of sonicated samples. (a) Absorbance spectra of unmodified and modified (GT)₁₅-SWCNT complexes. (b) Peak-to-valley ratio for the (6,5) E₁₁ absorption peak for the unmodified and Amino (“Am”) or Azide (“Az”) -modified (GT)₁₅-SWCNT complexes prepared by sonication (red) and exchange (blue). The numbers above the modification type indicate the position of the modification: 5’ (“5”), 3’ (“3”), 5’ and 3’ (“53”), 5’ and interior (“5in”) and 5’, 3’ and interior (“5in3”). We define the valley as the minimum in absorbance around 1100 nm.

Appendix D. Modulating the properties of DNA-SWCNTs through DNA chemical modification

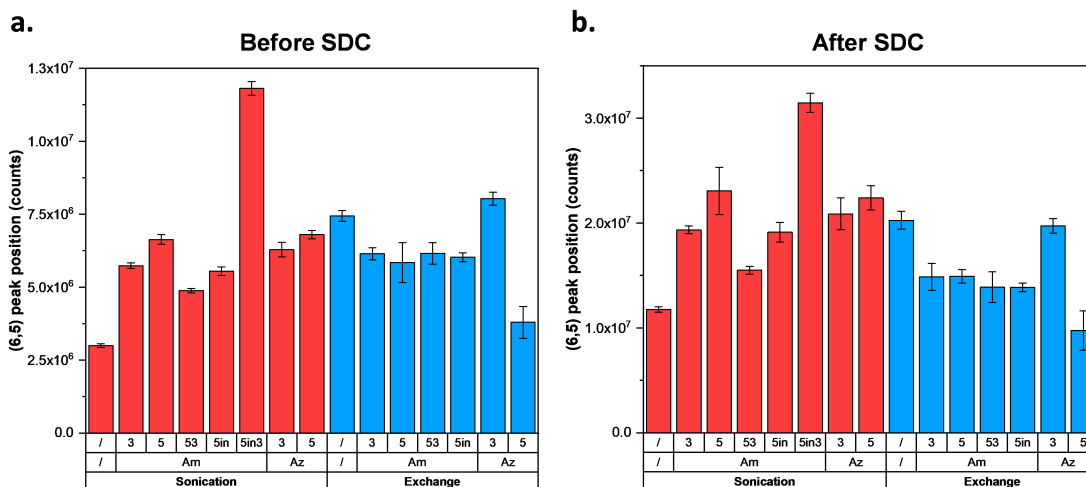


Figure D.16 – Wrapping replacement of the sonicated and exchanged samples. Intensity of the (6,5) emission peak (a) before and (b) after wrapping replacement with 0.1 % SDC for the unmodified and Amino (“Am”) or Azide (“Az”) -modified (GT)₁₅-SWCNT complexes prepared by sonication (red) and exchange (blue). The numbers above the modification type indicate the position of the modification: 5’ (“5”), 3’ (“3”), 5’ and 3’ (“53”), 5’ and interior (“5in”). The error bars correspond to 1 σ (n=3).

Table D.7 – Summary of the intensities after SDC replacement for the sonicated samples. Intensity changes $(I-I_0)/I_0$ of the SDC-replaced samples with respect to unmodified samples or to the intensities before SDC replacement for the (6,5) emission maximum and for the sonicated (GT)₁₅-SWCNT complexes. The error corresponds to 1 σ (n=3).

| Sample | $(I-I_0)/I_0$ vs unmodified (%) | $(I-I_0)/I_0$ vs before SDC (%) |
|----------------------------------|---------------------------------|---------------------------------|
| (GT) ₁₅ | / | 291.9 ± 12.5 |
| (GT) ₁₅ Amino 3’ | 64.6 ± 5.5 | 237.4 ± 9.0 |
| (GT) ₁₅ Amino 5’ | 96.2 ± 21.5 | 247.6 ± 37.1 |
| (GT) ₁₅ Amino 5’3’ | 31.9 ± 5.4 | 217.5 ± 9.7 |
| (GT) ₁₅ Amino 5’Int | 62.7 ± 10.1 | 244.7 ± 20.3 |
| (GT) ₁₅ Amino 5’Int3’ | 167.6 ± 10.5 | 166.5 ± 10.2 |
| (GT) ₁₅ Azide 3’ | 77.5 ± 15.1 | 232.0 ± 29.5 |
| (GT) ₁₅ Azide 5’ | 90.5 ± 12.2 | 229.4 ± 19.7 |

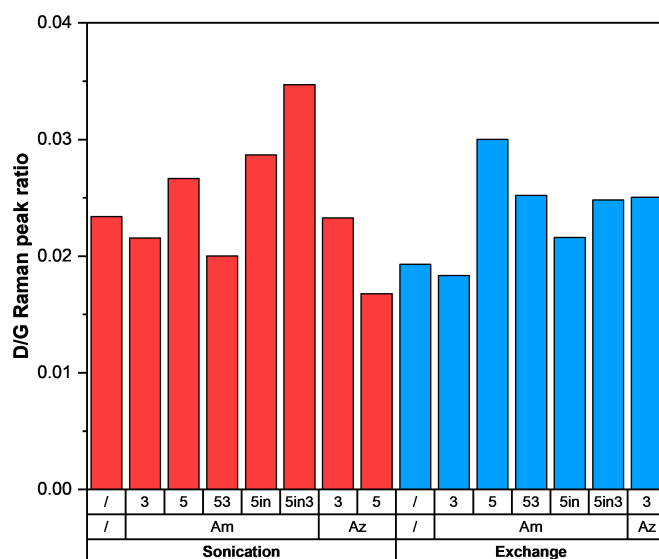


Figure D.17 – Effect on the D/G Raman peak ratio for the sonicated and exchanged samples. Ratios of the D and G peaks for the unmodified and Amino (“Am”) or Azide (“Az”) -modified (GT)₁₅-SWCNT complexes prepared by sonication (red) and exchange (blue). The numbers above the modification type indicate the position of the modification: 5’ (“5”), 3’ (“3”), 5’ and 3’ (“53”), 5’ and interior (“5in”) and 5’, 3’ and interior (“5in3”).

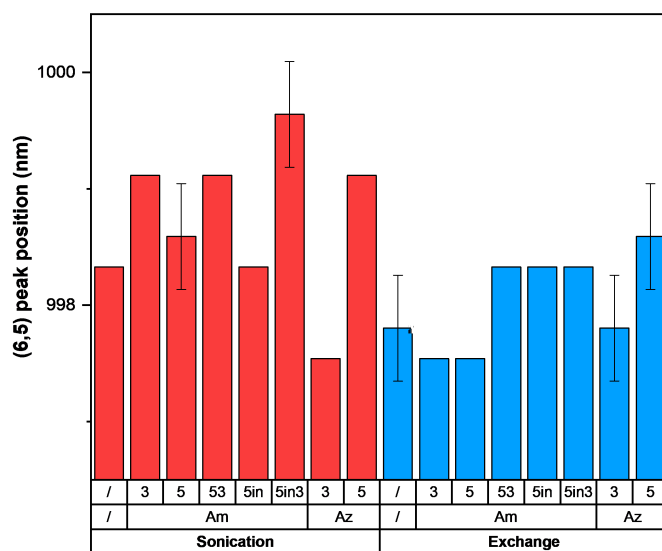


Figure D.18 – Effect on the peak position for the sonicated and exchanged samples. Position of the emission maximum of the (6,5) chirality for the unmodified and Amino (“Am”) or Azide (“Az”) -modified (GT)₁₅-SWCNT complexes prepared by sonication (red) and exchange (blue). The numbers above the modification type indicate the position of the modification: 5’ (“5”), 3’ (“3”), 5’ and 3’ (“53”), 5’ and interior (“5in”) and 5’, 3’ and interior (“5in3”). The error bars correspond to 1 σ (n=3).

Appendix D. Modulating the properties of DNA-SWCNTs through DNA chemical modification

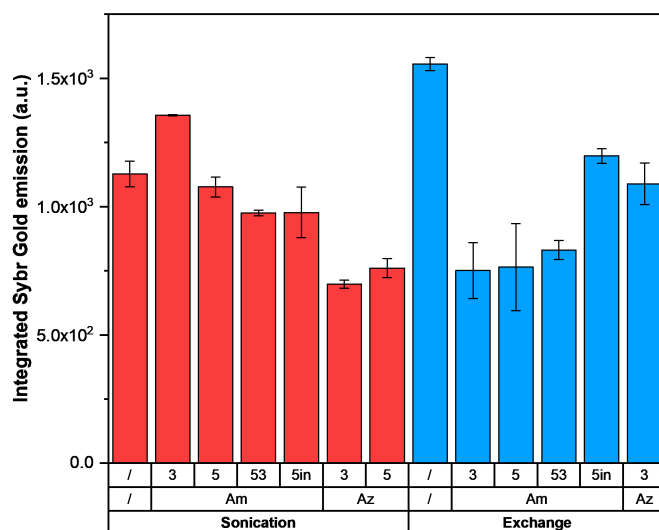


Figure D.19 – Effect on the concentration of DNA wrapping for the sonicated and exchanged samples. Integrated fluorescence (between 515 and 565 nm) of the Sybr Gold dye in presence of DNA extracted from the unmodified and Amino (“Am”) or Azide (“Az”) -modified (GT)₁₅-SWCNT complexes prepared by sonication (red) and exchange (blue). The numbers above the modification type indicate the position of the modification: 5’ (“5”), 3’ (“3”), 5’ and 3’ (“53”), 5’ and interior (“5in”). The error bars correspond to 1 σ (n=2).

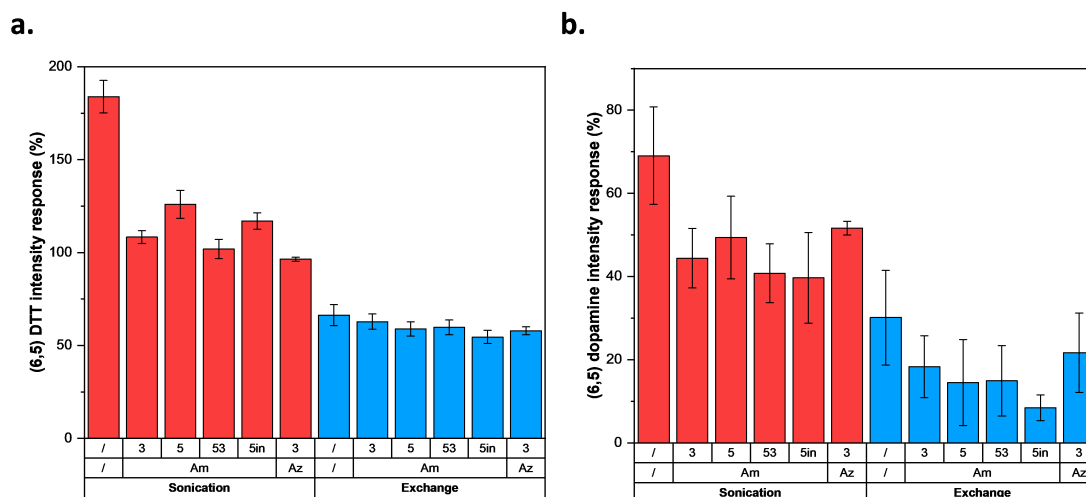


Figure D.20 – Sensing capabilities of the sonicated and exchanged samples. Fluorescence intensity response for the (6,5) chirality upon (a) DTT and (b) dopamine addition for the unmodified and Amino (“Am”) or Azide (“Az”) -modified (GT)₁₅-SWCNT complexes prepared by sonication (red) and exchange (blue). The numbers above the modification type indicate the position of the modification: 5’ (“5”), 3’ (“3”), 5’ and 3’ (“53”), 5’ and interior (“5in”). The response corresponds to (I/I_0) , with I_0 the intensity before addition. The error bars correspond to 1 σ (n=3).

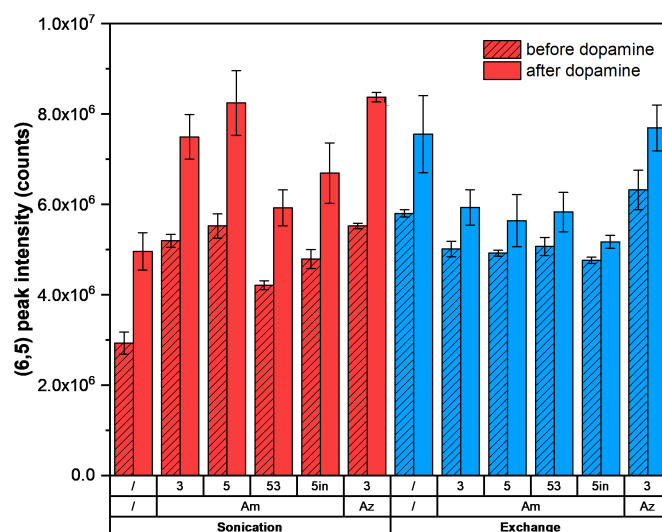


Figure D.21 – Intensities after dopamine addition for the sonicated and exchanged samples. Intensity of the maximum emission of the (6,5) chirality before and after (dashed) dopamine addition for the unmodified and Amino (“Am”) or Azide (“Az”) -modified (GT)₁₅-SWCNT complexes prepared by sonication (red) and exchange (blue). The numbers above the modification type indicate the position of the modification: 5’ (“5”), 3’ (“3”), 5’ and 3’ (“53”), 5’ and interior (“5in”). The error bars correspond to 1 σ (n=3).

Table D.8 – Summary of the DTT responses for the sonicated samples. Intensity response $(I-I_0)/I_0$ in presence of 10 mM DTT, with I_0 the intensity before addition, and final intensities of the samples after DTT addition for the (6,5) emission maximum and for sonicated (GT)₁₅-SWCNT complexes. The error corresponds to 1 σ (n=3).

| Sample | Intensity response (%) | Intensity after DTT (x 10 ⁶ counts) |
|--------------------------------|------------------------|--|
| (GT) ₁₅ | 183.9 ± 8.7 | 7.4 ± 0.4 |
| (GT) ₁₅ Amino 3’ | 108.3 ± 3.5 | 10.8 ± 0.3 |
| (GT) ₁₅ Amino 5’ | 126.0 ± 7.5 | 13.1 ± 0.4 |
| (GT) ₁₅ Amino 5’3’ | 101.9 ± 5.1 | 8.7 ± 0.4 |
| (GT) ₁₅ Amino 5’Int | 116.9 ± 4.4 | 10.9 ± 0.4 |
| (GT) ₁₅ Azide 3’ | 96.4 ± 1.1 | 11.7 ± 0.1 |

Appendix D. Modulating the properties of DNA-SWCNTs through DNA chemical modification

Table D.9 – Summary of the dopamine responses for the sonicated samples. Intensity response $(I-I_0)/I_0$ in presence of 100 μM dopamine, with I_0 the intensity before addition, and final intensities of the samples after dopamine addition for the (6,5) emission maximum and for sonicated $(\text{GT})_{15}$ -SWCNT complexes. The error corresponds to 1 σ ($n=3$).

| Sample | Intensity response (%) | Intensity after dopamine ($\times 10^6$ counts) |
|--------------------------------|------------------------|--|
| $(\text{GT})_{15}$ | 69.0 ± 11.7 | 4.9 ± 0.4 |
| $(\text{GT})_{15}$ Amino 3' | 44.4 ± 7.2 | 7.5 ± 0.5 |
| $(\text{GT})_{15}$ Amino 5' | 49.4 ± 9.9 | 8.2 ± 0.7 |
| $(\text{GT})_{15}$ Amino 5'3' | 40.8 ± 7.1 | 5.9 ± 0.4 |
| $(\text{GT})_{15}$ Amino 5'Int | 39.7 ± 10.9 | 6.7 ± 0.7 |
| $(\text{GT})_{15}$ Azide 3' | 51.6 ± 1.7 | 8.4 ± 0.1 |

E Outlook on the directed evolution of DNA-SWCNTs with long oligonucleotides

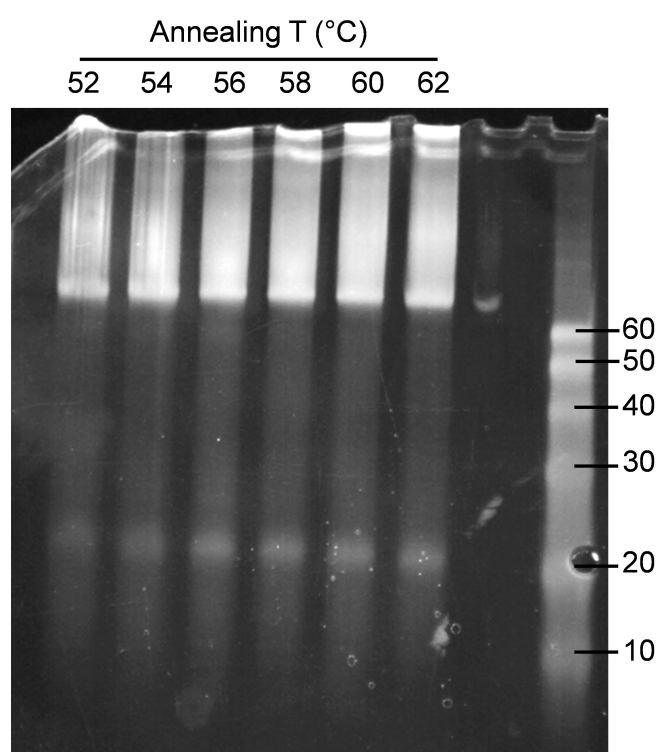


Figure E.1 – Gel electrophoresis of the products from the first PCR. 15 % urea PAGE gel of the products resulting from the PCR of the T-N₃₀ template. The different lanes correspond to the products resulting from the reaction at the different annealing temperatures, from 52 to 62°C. The lane on the right side is a DNA ladder indicating the size of the fragments between 10 and 60 nucleotides. We can observe two main bands in the PCR products, a first intense band above 60 nucleotides corresponding to our 77 nucleotides-long product, and a second band around 20 nucleotides corresponding to the primers.

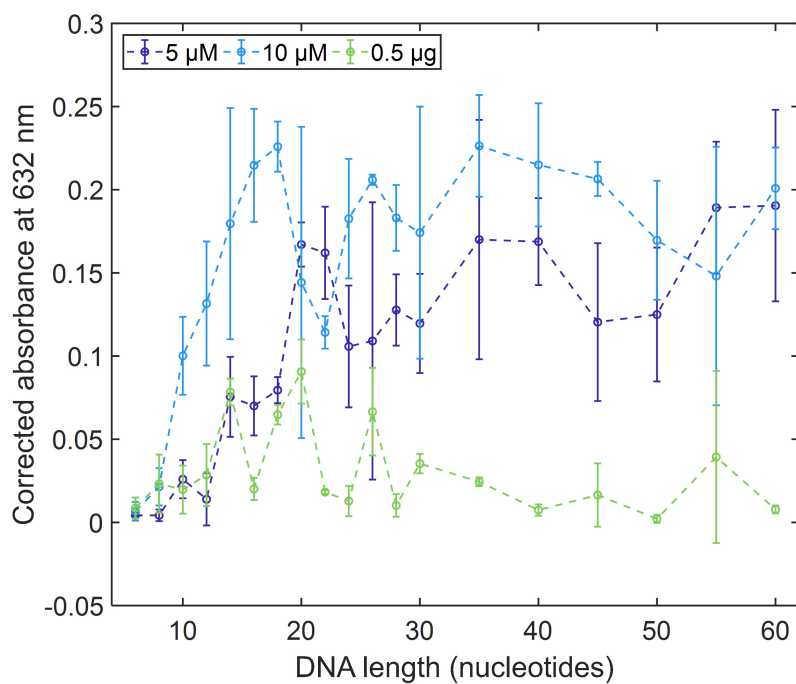


Figure E.3 – Effect of the DNA concentration on the dispersibility of DNA-SWCNTs. Blank-subtracted absorbance at 632 nm of DNA-SWCNT complexes prepared with random DNA sequences with length varying from 6 to 60 nucleotides at same molar concentration, 5 μ M (dark blue) and 10 μ M (light blue), and at same mass concentration (0.5 μ g).

Appendix E. Outlook on the directed evolution of DNA-SWCNTs with long oligonucleotides

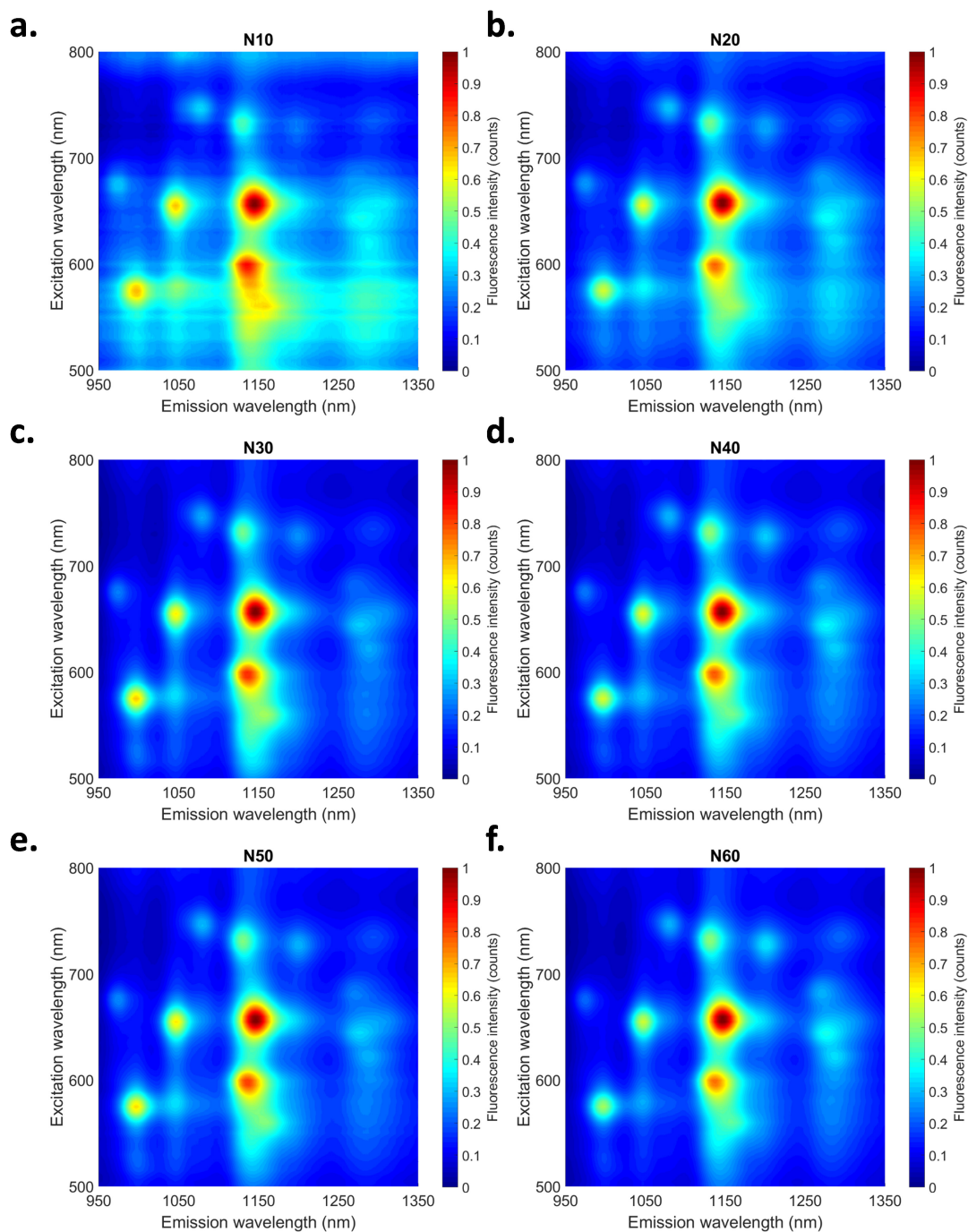


Figure E.4 – PLE maps of the DNA-SWCNTs prepared with DNA of varying lengths. PLE maps with excitation ranging from 500 to 800 nm and emission from 900 to 1400 nm for DNA-SWCNT complexes prepared with the (a) N₁₀, (b) N₂₀, (c) N₃₀, (d) N₄₀, (e) N₅₀, (f) N₆₀ sequences. The fluorescence intensities are normalized between 0 and 1.

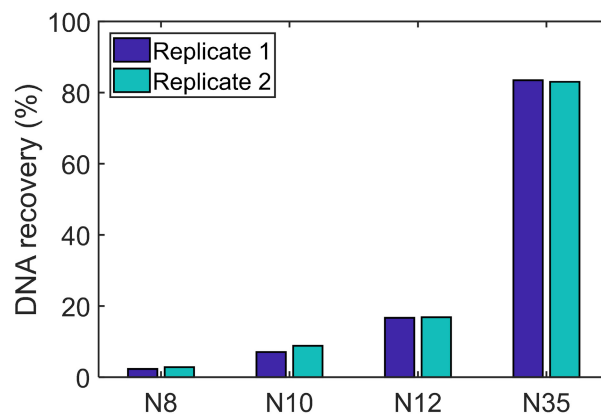


Figure E.5 – DNA recovery with silica beads as a function of length. The DNA recovery is defined as the concentration of DNA after silica bead purification compared to the DNA concentration before purification. The DNA concentrations were measured by UV absorption (Nanodrop 2000). The number after the “N” letter indicates the length of the random DNA sequence in nucleotides.

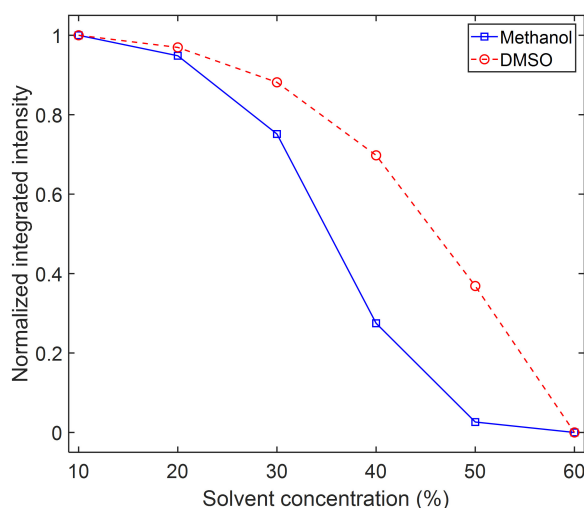


Figure E.6 – Aggregation of SC-SWCNTs with methanol and DMSO. Normalized integrated intensity (under 660 nm excitation, 1 s exposure) for SC-SWCNTs in presence of various concentrations of methanol (blue) and DMSO (red), between 10 and 60 % (v/v). The intensity is quenched for both solvent at a concentration of 60 %, indicating a complete aggregation of the SWCNTs.

Appendix E. Outlook on the directed evolution of DNA-SWCNTs with long oligonucleotides

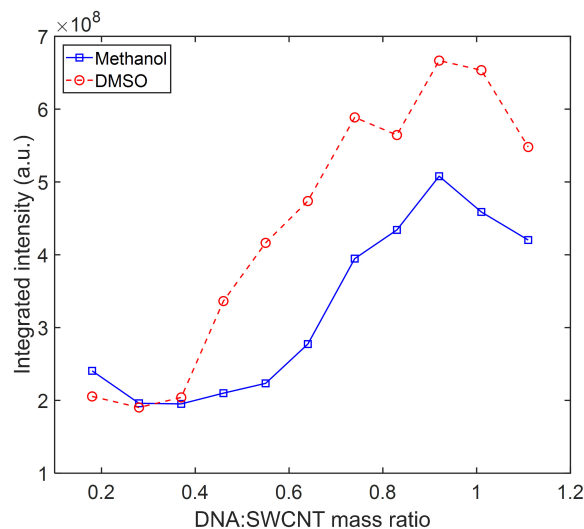


Figure E.7 – Fluorescence of DNA-SWCNT complexes prepared by methanol- and DMSO-assisted exchange. Integrated fluorescence intensities (under 660 nm excitation, 10 s exposure) for the DNA-SWCNT complexes prepared by wrapping exchange with a 36 bp double-stranded DNA sequence (T-(AT)₁₅) in presence of methanol (blue) and DMSO (red) for various DNA:SWCNT mass ratios.

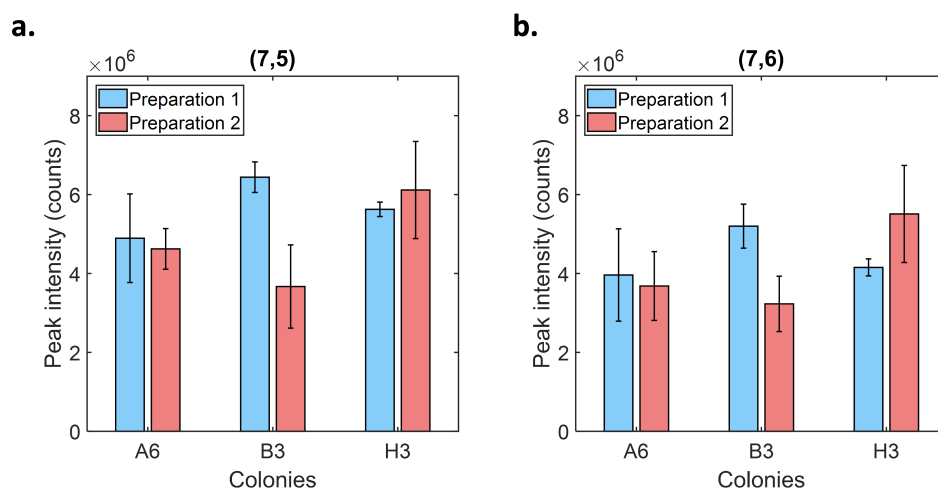


Figure E.8 – Reproducibility of the properties of the DNA-SWCNT prepared from colonies. Peak intensities for the (a) (7,5) and (b) (7,6) chiralities for the DNA-SWCNT complexes prepared with the DNA amplified from the A6, B3 and H3 colonies for two independent preparations done on two different days (10 s exposure). The two preparations involved two independent PCR reactions from the colonies and two independent DNA-SWCNT complexes preparations. The error bars correspond to 1σ (n=3).

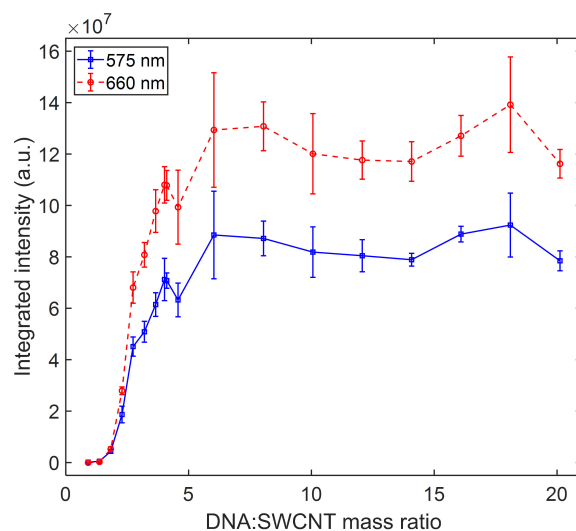


Figure E.9 – Optimization of the DNA:SWCNT mass ratio based on fluorescence intensity. Integrated fluorescence intensities (under 575 and 660 nm excitation) for DNA-SWCNT complexes prepared with the DNA template as a function of the DNA:SWCNT mass ratio used for the exchange procedure. The intensities reach a plateau for ratios higher than 5:1 DNA:SWCNT, it could therefore be possible to optimize the SWCNT concentrations in order to avoid variations in intensities upon variations in DNA concentration. The error bars represent 1σ ($n=3$).

Bibliography

1. Lambert, B. P., Gillen, A. J. & Boghossian, A. A. Synthetic Biology: A Solution for Tackling Nanomaterial Challenges. *J. Phys. Chem. Lett.* **11**, 4791–4802 (2020).
2. Binning, G., Rohrer, H., Gerber, C. & Weibel, E. Surface Studies by Scanning Tunneling Microscopy. *Phys. Rev. Lett.* **49**, 57–61 (1982).
3. Meyer, G. & Amer, N. M. Novel optical approach to atomic force microscopy. *Appl. Phys. Lett.* **53**, 1045–1047 (1998).
4. Crommie, M. F., Lutz, C. P., Eigler, D. M. & Heller, E. J. Quantum corrals. *Phys. D Nonlinear Phenom.* **83**, 98–108 (1995).
5. Collet, J. & Vuillaume, D. Nano-field effect transistor with an organic self-assembled monolayer as gate insulator. *Appl. Phys. Lett.* **73**, 2681–2683 (1998).
6. Klemens, F. *et al.* The Ballistic Nano-transistor. *IEDM*, 55–58 (1999).
7. Barenholz, Y. C. Doxil® — The first FDA-approved nano-drug : Lessons learned. *J. Control. Release* **160**, 117–134 (2012).
8. Dawidczyk, C. M. *et al.* State-of-the-art in design rules for drug delivery platforms : Lessons learned from FDA-approved nanomedicines. *J. Control. Release* **187**, 133–144 (2014).
9. Jun, Y.-w., Lee, J.-h. & Cheon, J. Chemical Design of Nanoparticle Probes for High-Performance Magnetic Resonance Imaging Angewandte. *Angew. Chemie - Int. Ed.* **47**, 5122–5135 (2008).
10. Park, J. Y. & Kricka, L. J. Prospects for nano- and microtechnologies in clinical point-of-care testing. *Lab Chip* **7**, 547–549 (2007).
11. Faridi, A. & Mahdi, S. Biopolymer nano-particles and natural nano-carriers for nano-encapsulation of phenolic compounds. *Colloids Surfaces B Biointerfaces* **146**, 532–543 (2016).
12. Rashidi, L. & Khosravi-darani, K. The Applications of Nanotechnology in Food Industry The Applications of Nanotechnology. *Crit. Rev. Food Sci. Nutr.* **51**, 723–730 (2011).
13. Sekhon, B. S. Food nanotechnology – an overview. *Nanotechnol. Sci. Appl.* **3**, 1–15 (2010).

Bibliography

14. Grätzel, M. Dye-sensitized solar cells. *J. Photochem. Photobiol. C Photochem. Rev.* **4**, 145–153 (2003).
15. Law, M., Greene, L. E., Johnson, J. C. & Saykally, R. Nanowire dye-sensitized solar cells. *Nat. Mater.* **4**, 455–459 (2005).
16. Zaluska, A., Zaluski, L. & Ström-Olsen, J. Structure , catalysis and atomic reactions on the nano-scale : a systematic approach to metal hydrides for hydrogen storage. *Appl. Phys. A* **72**, 157–165 (2001).
17. Tikhomirov, V. K., Driesen, K., Görrler-Walrand, C. & Mortier, M. Broadband telecommunication wavelength emission in Yb³⁺ - Er³⁺ - Tm³⁺ co-doped nano-glass- ceramics. *Opt. Express* **15**, 9535–9540 (2007).
18. Yardimci, N. T., Lu, H. & Jarrahi, M. High power telecommunication-compatible photoconductive terahertz emitters based on plasmonic nano-antenna arrays. *Appl. Phys. Lett.* **109**, 1–4 (2016).
19. Gutiérrez, J. M. *et al.* Nano-emulsions : New applications and optimization of their preparation. *Curr. Opin. Colloid Interface Sci.* **13**, 245–251 (2008).
20. Jacobs, J. E., Poel, I. V. D. & Osseweijer, P. Sunscreens with Titanium Dioxide (TiO₂) Nano-Particles: A Societal Experiment. *Nanoethics* **4**, 103–113 (2010).
21. Bernholc, J., Brenner, D., Nardelli, M. B., Meunier, V. & Roland, C. Mechanical and electrical properties of nanotubes. *Annu. Rev. Mater. Res.* **2002**, **32**, 347–75 (2002).
22. Kataura, H. *et al.* Optical properties of single-wall carbon nanotubes. *Synth. Met.* **103**, 2555–2558 (1999).
23. O'Connell, M. J. *et al.* Band Gap Fluorescence from Individual Single-Walled Carbon Nanotubes. *Science (80-.)*. **297**, 593–596 (2002).
24. Cognet, L. *et al.* Stepwise Quenching of Exciton Fluorescence in Carbon Nanotubes by Single-Molecule Reactions. *Science (80-.)*. **316**, 1465–1469 (2007).
25. Jin, H., Heller, D. A., Kim, J. H. & Strano, M. S. Stochastic analysis of stepwise fluorescence quenching reactions on single-walled carbon nanotubes: Single molecule sensors. *Nano Lett.* **8**, 4299–4304 (2008).
26. Heller, D. A., Baik, S., Eurell, T. E. & Strano, M. S. Single-walled carbon nanotube spectroscopy in live cells: Towards long-term labels and optical sensors. *Adv. Mater.* **17**, 2793–2799 (2005).
27. Hemmer, E., Benayas, A., Légaré, F. & Vetrone, F. Exploiting the biological windows: Current perspectives on fluorescent bioprobes emitting above 1000 nm. *Nanoscale Horizons* **1**, 168–184 (2016).
28. Kruss, S. *et al.* High-resolution imaging of cellular dopamine efflux using a fluorescent nanosensor array. *PNAS* **114**, 1789–1794 (2017).

29. Landry, M. P. *et al.* Single-molecule detection of protein efflux from microorganisms using fluorescent single-walled carbon nanotube sensor arrays. *Nat. Nanotechnol.* **12**, 368–377 (2017).
30. Welsher, K., Sherlock, S. P. & Dai, H. Deep-tissue anatomical imaging of mice using carbon nanotube fluorophores in the second near-infrared window. *Proc. Natl. Acad. Sci.* **108**, 8943–8948. arXiv: 1105.3536 (2011).
31. Diao, S. *et al.* Fluorescence Imaging In Vivo at Wavelengths beyond 1500 nm. *Angew. Chemie Int. Ed.* **54**, 14758–14762. arXiv: 1502.02775 (2015).
32. Jena, P. V. *et al.* A Carbon Nanotube Optical Reporter Maps Endolysosomal Lipid Flux. *ACS Nano* **11**, 10689–10703 (2017).
33. Galassi, T. V. *et al.* An optical nanoreporter of endolysosomal lipid accumulation reveals enduring effects of diet on hepatic macrophages in vivo. *Sci. Transl. Med.* **10**, 1–11 (2018).
34. Bonis-O'Donnell, J. T. *et al.* Dual Near-Infrared Two-Photon Microscopy for Deep-Tissue Dopamine Nanosensor Imaging. *Adv. Funct. Mater.* **27**, 1–10 (2017).
35. Galassi, T. V. *et al.* Long-term in vivo biocompatibility of single-walled carbon nanotubes. *PLoS One* **15**, 1–22 (2020).
36. Baskoutas, S. & Terzis, A. F. Size-dependent band gap of colloidal quantum dots. *J. Appl. Phys.* **99**, 013708 (2006).
37. Koumura, N., Zijlstra, R. W. J., Delden, R. A., Harada, N. & Feringa, B. L. Light-driven monodirectional molecular rotor. *Nature* **401**, 1997–2000 (1999).
38. Sauvage, J.-p. Transition Metal-Containing Rotaxanes and Catenanes in Motion : Toward Molecular Machines and Motors Introduction : Recent Development of. *Acc. Chem. Res.* **31**, 611–619 (1998).
39. Kay, E. R. & Leigh, D. A. Rise of the Molecular Machines. *Angew. Chemie - Int. Ed.* **54**, 10080–10088 (2015).
40. Allen, C., Maysinger, D. & Eisenberg, A. Nano-engineering block copolymer aggregates for drug delivery. *Colloids Surfaces B Biointerfaces* **16**, 3–27 (1999).
41. Rodriguez-Hernandez, J., Checot, F., Gnanou, Y. & Lecommandoux, S. Toward 'smart' nano-objects by self-assembly of block copolymers in solution. *Prog. Polym. Sci.* **30**, 691–724 (2005).
42. Rothemund, P. W. K. Folding DNA to create nanoscale shapes and patterns. *Nature* **440**, 297–302 (2006).
43. Maune, H. T. *et al.* Self-assembly of carbon nanotubes into two-dimensional geometries using DNA origami templates. *Nat. Nanotechnol.* **5**, 61–66 (2010).
44. Moates, F. C. *et al.* Infrared Thermographic Screening of Combinatorial Libraries of Heterogeneous Catalysts. *Ind. Eng. Chem. Res.* **35**, 4801–4803 (1996).

Bibliography

45. He, T., Kreidler, E., Xiong, L. & Ding, E. Combinatorial screening and nano-synthesis of platinum binary alloys for oxygen electroreduction. *J. Power Sources* **165**, 87–91 (2007).
46. Yazaydin, A. O. *et al.* Screening of Metal - Organic Frameworks for Carbon Dioxide Capture from Flue Gas Using a Combined Experimental and Modeling Approach. *J. Am. Chem. Soc.* **131**, 18198–18199 (2009).
47. Wilmer, C. E. *et al.* Large-scale screening of hypothetical metal–organic frameworks. *Nat. Chem.* **4**, 83–89 (2012).
48. Naha, P. C., Chhour, P. & Cormode, D. P. Systematic in vitro toxicological screening of gold nanoparticles designed for nanomedicine applications. *Toxicol. Vitro* **29**, 1445–1453 (2015).
49. Hogemann, D., Ntziachristos, V., Josephson, L. & Weissleder, R. High Throughput Magnetic Resonance Imaging for Evaluating Targeted Nanoparticle Probes. *Bioconjug. Chem.* **13**, 116–121 (2002).
50. Weissleder, R., Kelly, K., Sun, E. Y., Shtatland, T. & Josephson, L. Cell-specific targeting of nanoparticles by multivalent attachment of small molecules. *Nat. Biotechnol.* **23**, 1418–1423 (2005).
51. Weisman, R. B. & Bachilo, S. M. Dependence of Optical Transition Energies on Structure for Single-Walled Carbon Nanotubes in Aqueous Suspension : An Empirical Kataura Plot. *Nano Lett.* **3**, 1235–1238 (2003).
52. Antonucci, A., Kupis-Rozmyslowicz, J. & Boghossian, A. A. Noncovalent Protein and Peptide Functionalization of Single-Walled Carbon Nanotubes for Bodelivery and Optical Sensing Applications. *ACS Appl. Mater. Interfaces* **9**, 11321–11331 (2017).
53. Umemura, K. Hybrids of Nucleic Acids and Carbon Nanotubes for Nanobiotechnology. *Nanomaterials* **5**, 321–350 (2015).
54. Vogel, S. R., Kappes, M. M., Hennrich, F. & Richert, C. An unexpected new optimum in the structure space of DNA solubilizing single-walled carbon nanotubes. *Chem. - A Eur. J.* **13**, 1815–1820 (2007).
55. Albertorio, F., Hughes, M. E., Golovchenko, J. A. & Branton, D. Base dependent DNA-carbon nanotube interactions: activation enthalpies and assembly-disassembly control. *Nanotechnology* **48**, 1–6. arXiv: NIHMS150003 (2009).
56. Yamamoto, Y., Fujigaya, T., Niidome, Y. & Nakashima, N. Fundamental properties of oligo double-stranded DNA/single-walled carbon nanotube nanobiohybrids. *Nanoscale* **2**, 1767–72 (2010).
57. Zhang, J. *et al.* Single molecule detection of nitric oxide enabled by d(AT)₁₅ DNA adsorbed to near infrared fluorescent single-walled carbon nanotubes. *J. Am. Chem. Soc.* **133**, 567–581 (2011).
58. Kruss, S. *et al.* Neurotransmitter detection using corona phase molecular recognition on fluorescent single-walled carbon nanotube sensors. *J. Am. Chem. Soc.* **136**, 713–724 (2014).

59. Harvey, J. D., Baker, H. A., Mercer, E., Budhathoki-Uprety, J. & Heller, D. A. Control of Carbon Nanotube Solvatochromic Response to Chemotherapeutic Agents. *ACS Appl. Mater. Interfaces* **9**, 37947–37953 (2017).
60. Mann, F. A., Herrmann, N., Meyer, D. & Kruss, S. Tuning selectivity of fluorescent carbon nanotube-based neurotransmitter sensors. *Sensors (Switzerland)* **17** (2017).
61. Beyene, A. G. *et al.* Ultralarge Modulation of Fluorescence by Neuromodulators in Carbon Nanotubes Functionalized with Self-assembled Oligonucleotide Rings. *Nano Lett.* **18**, 6995–7003 (2018).
62. Dresselhaus, M. S., Dresselhaus, G. & Eklund, P. C. *Science of Fullerenes and Carbon Nanotubes* (1996).
63. Saito, R., Fujita, M., Dresselhaus, G. & Dresselhaus, M. S. Electronic structure of chiral graphene tubules. *Appl. Phys. Lett.* **60**, 2204–2206 (1992).
64. Kasha, M. Characterization of electronic transitions in complex molecules. *Discuss. Faraday Soc.* **9**, 14–19 (1950).
65. Boghossian, A. A. *et al.* Near-infrared fluorescent sensors based on single-walled carbon nanotubes for life sciences applications. *ChemSusChem* **4**, 848–863 (2011).
66. Choi, J. H. & Strano, M. S. Solvatochromism in single-walled carbon nanotubes. *Appl. Phys. Lett.* **90**, 88–91 (2007).
67. Wang, F. *et al.* Observation of Excitons in One-Dimensional Metallic Single-Walled Carbon Nanotubes. **227401**, 1–4 (2007).
68. Backes, C. *Noncovalent Functionalization of Carbon Nanotubes* PhD thesis (2012).
69. Naumov, A. V., Ghosh, S., Tsyboulski, D. A., Bachilo, S. M. & Weisman, R. B. Analyzing absorption backgrounds in single-walled carbon nanotube spectra. *ACS Nano* **5**, 1639–1648 (2011).
70. Rocha, J. D. R., Bachilo, S. M., Ghosh, S., Arepalli, S. & Weisman, R. B. Efficient spectrofluorimetric analysis of single-walled carbon nanotube samples. *Anal. Chem.* **83**, 7431–7437 (2011).
71. Martinić, I., Eliseeva, S. V. & Petoud, S. Near-infrared emitting probes for biological imaging: Organic fluorophores, quantum dots, fluorescent proteins, lanthanide(III) complexes and nanomaterials. *J. Lumin.* **189**, 19–43 (2017).
72. Kingston, C. T. & Simard, B. Fabrication of Carbon Nanotubes. *Anal. Lett.* **36**, 3119–3145 (2003).
73. Crochet, J., Clemens, M. & Hertel, T. Optical properties of structurally sorted single-wall carbon nanotube ensembles. *Phys. Status Solidi Basic Res.* **244**, 3964–3968 (2007).
74. Crochet, J. J., Sau, J. D., Duque, J. G., Doorn, S. K. & Cohen, M. L. Electrodynamic and excitonic intertube interactions in semiconducting carbon nanotube aggregates. *ACS Nano* **5**, 2611–2618 (2011).

Bibliography

75. Hagen, A. *et al.* Exponential decay lifetimes of excitons in individual single-walled carbon nanotubes. *Phys. Rev. Lett.* **95**, 1–4 (2005).
76. Harrah, D. M. & Swan, A. K. The role of length and defects on optical quantum efficiency and exciton decay dynamics in single-walled carbon nanotubes. *ACS Nano* **5**, 647–655 (2011).
77. Liu, T. & Xiao, Z. Exact and closed form solutions for the quantum yield, exciton diffusion length, and lifetime to reveal the universal behaviors of the photoluminescence of defective single-walled carbon nanotubes. *J. Phys. Chem. C* **115**, 16920–16927 (2011).
78. Gillen, A. J. & Boghossian, A. A. Non-covalent Methods of Engineering Optical Sensors Based on Single-Walled Carbon Nanotubes. *Front. Chem.* **7**, 1–13 (2019).
79. Heller, D. a. *et al.* Peptide secondary structure modulates single-walled carbon nanotube fluorescence as a chaperone sensor for nitroaromatics. *Proc. Natl. Acad. Sci. U. S. A.* **108**, 8544–8549 (2011).
80. Bisker, G. *et al.* Protein-targeted corona phase molecular recognition. *Nat. Commun.* **7**, 10241 (2016).
81. Zubkovs, V., Schuergers, N., Lambert, B., Ahunbay, E. & Boghossian, A. A. Mediatorless, Reversible Optical Nanosensor Enabled through Enzymatic Pocket Doping. *Small* **13**, 1–10 (2017).
82. Zheng, M. *et al.* DNA-assisted dispersion and separation of carbon nanotubes. *Nat. Mater.* **2**, 338–342 (2003).
83. Crick, F. & Watson, J. Molecular Structure of Nucleic Acids: A Structure for Deoxyribose Nucleic Acid. *Nature* **171**, 737–738 (1953).
84. Ussery, D. W. DNA Structure: A-, B- and Z-DNA Helix Families. *Encycl. Life Sci.* (2002).
85. Varani, G. Exceptionally Stable Nucleic Acid Hairpins. *Annu. Rev. Biophys. Biomol. Struct.* **24**, 379–404 (1995).
86. Antao, V. P. & Tinoco, I. Thermodynamic parameters for loop formation in RNA and DNA hairpin tetraloops. *Nucleic Acids Res.* **20**, 819–824 (1992).
87. Turner, D. H. Bulges in nucleic acids. *Curr. Opin. Struct. Biol.* **2**, 334–337 (1992).
88. Gilbert, D. E. & Feigon, J. Multistranded DNA structures. *Curr. Opin. Struct. Biol.* **9**, 305–314 (1999).
89. Tuerk, C. & Gold, L. Systematic evolution of ligands by exponential enrichment: RNA ligands to bacteriophage T4 DNA polymerase. *Science (80-.)*. **249**, 505–510 (1990).
90. Sakamoto, K. *et al.* Molecular computation by DNA hairpin formation. *Science (80-.)*. **288**, 1223–1226 (2000).
91. Petty, J. T. *et al.* Optically enhanced, near-IR, silver cluster emission altered by single base changes in the DNA template. *J. Phys. Chem. B* **115**, 7996–8003 (2011).
92. Li, N., Larson, T., Nguyen, H. H., Sokolov, K. V. & Ellington, A. D. Directed evolution of gold nanoparticle delivery to cells. *Chem. Commun.* **46**, 392–394 (2010).

93. Nakashima, N., Okuzono, S., Murakami, H., Nakai, T. & Yoshikawa, K. DNA Dissolves Single-walled Carbon Nanotubes in Water. *Chem. Lett.* **32**, 456–457 (2003).
94. Johnson, R. R., Johnson, A. T. C. & Klein, M. L. Probing the structure of DNA-carbon nanotube hybrids with molecular dynamics. *Nano Lett.* **8**, 69–75 (2008).
95. Zhao, X. & Johnson, J. K. Simulation of adsorption of DNA on carbon nanotubes. *J. Am. Chem. Soc.* **129**, 10438–10445 (2007).
96. Cathcart, H. *et al.* Ordered DNA wrapping switches on luminescence in single-walled nanotube dispersions. *J. Am. Chem. Soc.* **130**, 12734–12744 (2008).
97. Kilina, S. *et al.* Unveiling Stability Criteria of DNA-Carbon Nanotubes Constructs by Scanning Tunneling Microscopy and Computational Modeling. *J. Drug Deliv.* **2011**, 1–9 (2011).
98. Mayo, M. L., Chen, Z. Q. & Kilina, S. V. Computational studies of nucleotide selectivity in DNA-carbon nanotube hybrids. *J. Phys. Chem. Lett.* **3**, 1–9 (2012).
99. Lee, O. S. How does ss-DNA recognize the chirality of carbon nanotubes? *J. Comput. Sci.* **15**, 60–64 (2016).
100. Roxbury, D., Mittal, J. & Jagota, A. Molecular-basis of single-walled carbon nanotube recognition by single-stranded DNA. *Nano Lett.* **12**, 1464–1469 (2012).
101. Tu, X., Manohar, S., Jagota, A. & Zheng, M. DNA sequence motifs for structure-specific recognition and separation of carbon nanotubes. *Nature* **460**, 250–253 (2009).
102. Zheng, M. *et al.* Structure-Based Carbon Nanotube Sorting by Sequence-Dependent DNA Assembly. *Science (80-.)*. **302**, 1545–1548 (2003).
103. Campbell, J. F., Tessmer, I., Thorp, H. H. & Erie, D. A. Atomic force microscopy studies of DNA-wrapped carbon nanotube structure and binding to quantum dots. *J. Am. Chem. Soc.* **130**, 10648–10655 (2008).
104. He, W. *et al.* Novel Strategy for the Investigation on Chirality Selection of Single-Walled Carbon Nanotubes with DNA by Electrochemical Characterization. *Anal. Chem.* **90**, 12810–12814 (2018).
105. Snyder, S. E. & Rotkin, S. V. Optical identification of a DNA-wrapped carbon nanotube: Signs of helically broken symmetry. *Small* **4**, 1284–1286. arXiv: arXiv:0803.3802v1 (2008).
106. Roxbury, D., Jagota, A. & Mittal, J. Structural characteristics of oligomeric DNA strands adsorbed onto single-walled carbon nanotubes. *J. Phys. Chem. B* **117**, 132–140 (2013).
107. Johnson, R., Kohlmeyer, A. & Johnson, A. Free Energy Landscape of a DNA- Carbon Nanotube Hybrid Using Replica Exchange Molecular Dynamics. *Nano Lett.* (2009).
108. Alizadehmojarad, A. A. *et al.* Binding Affinity and Conformational Preferences Influence Kinetic Stability of Short Oligonucleotides on Carbon Nanotubes. *Adv. Mater. Interfaces* **7**, 1–10 (2020).
109. Martin, W., Zhu, W. & Krilov, G. Simulation study of noncovalent hybridization of carbon nanotubes by single-stranded DNA in water. *J. Phys. Chem. B* **112**, 16076–16089 (2008).

Bibliography

110. Heller, D. A. *et al.* Optical Detection of DNA Conformational Polymorphism on Single-Walled Carbon Nanotubes. *Science* (80-.). **311**, 508–511 (2006).
111. Jin, H. *et al.* Divalent ion and thermally induced DNA conformational polymorphism on single-walled carbon nanotubes. *Macromolecules* **40**, 6731–6739 (2007).
112. Salem, D. P. *et al.* Ionic strength mediated phase transitions of surface adsorbed DNA on single-walled carbon nanotubes. *J. Am. Chem. Soc.* **139**, 16791–16802 (2017).
113. Gillen, A. J., Kupis-Rozmysłowicz, J., Gigli, C., Schuergers, N. & Boghossian, A. A. Xeno Nucleic Acid Nanosensors for Enhanced Stability Against Ion-Induced Perturbations. *J. Phys. Chem. Lett.* **9**, 4336–4343 (2018).
114. Haggemueller, R. *et al.* Comparison of the Quality of Aqueous Dispersions of Single Wall Carbon Nanotubes Using Surfactants and Biomolecules. *Langmuir* **24**, 5070–5078 (2008).
115. Roxbury, D., Tu, X., Zheng, M. & Jagota, A. Recognition ability of DNA for carbon nanotubes correlates with their binding affinity. *Langmuir* **27**, 8282–8293 (2011).
116. Kato, Y., Niidome, Y. & Nakashima, N. Thermodynamics of the Exchange of Solubilizers on Single-walled Carbon Nanotubes. *Chem. Lett.* **40**, 730–732 (2011).
117. Kato, Y., Inoue, A., Niidome, Y. & Nakashima, N. Thermodynamics on Soluble Carbon Nanotubes: How Do DNA Molecules Replace Surfactants on Carbon Nanotubes? *Sci. Rep.* **2**, 1–7 (2012).
118. Iliafar, S., Mittal, J., Vezenov, D. & Jagota, A. Interaction of single-stranded DNA with curved carbon nanotube is much stronger than with flat graphite. *J. Am. Chem. Soc.* **136**, 12947–12957 (2014).
119. Shankar, A., Mittal, J. & Jagota, A. Binding between DNA and carbon nanotubes strongly depends upon sequence and chirality. *Langmuir* **30**, 3176–3183 (2014).
120. Jena, P. V., Safaee, M. M., Heller, D. A. & Roxbury, D. DNA-Carbon Nanotube Complexation Affinity and Photoluminescence Modulation Are Independent. *ACS Appl. Mater. Interfaces* **9**, 21397–21405. arXiv: 15334406 (2017).
121. Chehel Amirani, M. & Tang, T. Binding of nucleobases with graphene and carbon nanotube: A review of computational studies. *J. Biomol. Struct. Dyn.* **33**, 1567–1597 (2015).
122. Ao, G., Khripin, C. Y. & Zheng, M. DNA-Controlled Partition of Carbon Nanotubes in Polymer Aqueous Two-Phase Systems. *J. Am. Chem. Soc.* **136**, 10383–10392 (2014).
123. Ao, G., Streit, J. K., Fagan, J. A. & Zheng, M. Differentiating Left- and Right-Handed Carbon Nanotubes by DNA. *J. Am. Chem. Soc.* **138**, 16677–16685 (2016).
124. Zheng, Y., Bachilo, S. M. & Weisman, R. B. Quenching of Single-Walled Carbon Nanotube Fluorescence by Dissolved Oxygen Reveals Selective Single-Stranded DNA Affinities. *J. Phys. Chem. Lett.* **8**, 1952–1955 (2017).

125. Lambert, B., Gillen, A. J., Schuergers, N., Wu, S.-J. & Boghossian, A. A. Directed evolution of the optoelectronic properties of synthetic nanomaterials. *ChemComm* **55**, 3239–3242 (2019).
126. Zheng, Y., Alizadehmojarad, A. A., Bachilo, S. M., Kolomeisky, A. B. & Weisman, R. B. Dye Quenching of Carbon Nanotube Fluorescence Reveals Structure-Selective Coating Coverage. *ACS Nano* **14**, 12148–12158 (2020).
127. Ito, M. *et al.* The Effect of DNA Adsorption on Optical Transitions in Single Walled Carbon Nanotubes. *J. Phys. Chem. C*, 150828160259001 (2015).
128. Ke, F., Chen, J., Wu, R. & Chen, Y. Dispersion quality of single-walled carbon nanotubes reveals the recognition sequence of DNA. *Nanotechnology* **31** (2020).
129. Jeng, E. S., Moll, A. E., Roy, A. C., Gastala, J. B. & Strano, M. S. Detection of DNA hybridization using the near-infrared band-gap fluorescence of single-walled carbon nanotubes. *Nano Lett.* **6**, 371–375 (2006).
130. Harvey, J. D. *et al.* A carbon nanotube reporter of microRNA hybridization events in vivo. *Nat. Biomed. Eng.* **1**, 1–11 (2017).
131. Lee, K., Nojoomi, A., Jeon, J., Lee, C. Y. & Yum, K. Near-Infrared Fluorescence Modulation of Refolded DNA Aptamer-Functionalized Single-Walled Carbon Nanotubes for Optical Sensing. *ACS Appl. Nano Mater.* **1**, 5327–5336 (2018).
132. Yoo, C. H. *et al.* DNA aptamer release from the DNA-SWNT hybrid by protein recognition. *Chem. Commun.* **52**, 2784–2787 (2016).
133. Salem, D. P. *et al.* Chirality dependent corona phase molecular recognition of DNA-wrapped carbon nanotubes. *Carbon N. Y.* **97**, 147–153 (2016).
134. Yaari, Z. *et al.* Machine-Perception Nanosensor Platform to Detect Biomarkers of Ovarian Cancer. *bioRxiv* (2021).
135. Polo, E. & Kruss, S. Impact of Redox-Active Molecules on the Fluorescence of Polymer-Wrapped Carbon Nanotubes. *J. Phys. Chem. C* **120**, 3061–3070 (2016).
136. Ozawa, H., Ide, N., Fujigaya, T., Niidome, Y. & Nakashima, N. One-pot separation of highly enriched (6,5)-single-walled carbon nanotubes using a fluorene-based copolymer. *Chem. Lett.* **40**, 239–241 (2011).
137. Vichchulada, P. *et al.* Sonication power for length control of single-walled carbon nanotubes in aqueous suspensions used for 2-dimensional network formation. *J. Phys. Chem. C* **114**, 12490–12495 (2010).
138. Yu, H. *et al.* Optimizing sonication parameters for dispersion of single-walled carbon nanotubes. *Chem. Phys.* **408**, 11–16 (2012).
139. Graf, A. *et al.* Large scale, selective dispersion of long single-walled carbon nanotubes with high photoluminescence quantum yield by shear force mixing. *Carbon N. Y.* **105**, 593–599 (2016).

Bibliography

140. Kurnosov, N. V., Leontiev, V. S. & Karachevtsev, V. A. Enhancement of Photoluminescence from Semiconducting Nanotubes in Aqueous Suspensions due to Cysteine and Dithiothreitol Doping: Influence of the Sonication Treatment. *Nanoscale Res. Lett.* **11**, 1–7 (2016).
141. Koh, B. & Cheng, W. The Impact of Sonication on the Surface Quality of Single-Walled Carbon Nanotubes. *J. Pharm. Sci.* **104**, 2594–2599 (2015).
142. Jin, S., Wijesekara, P., Boyer, P. D., Dahl, K. N. & Islam, M. F. Length-dependent intracellular bundling of single-walled carbon nanotubes influences retention. *J. Mater. Chem. B* **5**, 6657–6665 (2017).
143. Yang, Y., Sharma, A., Noetinger, G., Zheng, M. & Jagota, A. Pathway-Dependent Structures of DNA-Wrapped Carbon Nanotubes: Direct Sonication vs. Surfactant/DNA Exchange. *J. Phys. Chem. C* (2020).
144. Gillen, A. J., Lambert, B. P., Antonucci, A., Molina-Romero, D. & Boghossian, A. A. Modulating the properties of DNA-SWCNT sensors using chemically modified DNA. *bioRxiv* (2021).
145. Setaro, A. *et al.* Preserving π -conjugation in covalently functionalized carbon nanotubes for optoelectronic applications. *Nat. Commun.* **8**, 14281 (2017).
146. Berger, F. J. *et al.* Interaction of Luminescent Defects in Carbon Nanotubes with Covalently Attached Stable Organic Radicals. *ACS Nano* **15**, 5147–5157 (2021).
147. Piao, Y. *et al.* Brightening of carbon nanotube photoluminescence through the incorporation of sp³ defects. *Nat. Chem.* **5**, 840–5. arXiv: NIHMS150003 (2013).
148. Berger, F. J. *et al.* Brightening of Long, Polymer-Wrapped Carbon Nanotubes by sp³ Functionalization in Organic Solvents. *ACS Nano* **13**, 9259–9269 (2019).
149. Spreinat, A. *et al.* Quantum defects in fluorescent carbon nanotubes for sensing and mechanistic studies. *chemrxiv*, 1–39 (2021).
150. Sen, F. *et al.* Observation of oscillatory surface reactions of riboflavin, trolox, and singlet oxygen using single carbon nanotube fluorescence spectroscopy. *ACS Nano* **6**, 10632–10645 (2012).
151. Kurnosov, N. V., Leontiev, V. S., Linnik, A. S., Lytvyn, O. S. & Karachevtsev, V. A. Photoluminescence intensity enhancement in SWNT aqueous suspensions due to reducing agent doping: Influence of adsorbed biopolymer. *Chem. Phys.* **438**, 23–30 (2014).
152. Hou, Z. & Krauss, T. D. Photoluminescence brightening of isolated single-walled carbon nanotubes. *J. Phys. Chem. Lett.* **8**, 4954–4959 (2017).
153. Yang, J. *et al.* Chirality-Selective Photoluminescence Enhancement of ssDNA-Wrapped Single-Walled Carbon Nanotubes Modified with Gold Nanoparticles. *Small* **12**, 3164–3171 (2016).
154. Lutsyk, P. *et al.* A sensing mechanism for the detection of carbon nanotubes using selective photoluminescent probes based on ionic complexes with organic dyes. *Light Sci. Appl.* **5** (2016).

155. Ignatova, T. *et al.* Significant FRET between SWNT/DNA and rare earth ions: A signature of their spatial correlations. *ACS Nano* **5**, 6052–6059 (2011).
156. Sen, S., Sen, F., Boghossian, A. A., Zhang, J. & Strano, M. S. Effect of reductive dithiothreitol and trolox on nitric oxide quenching of single-walled carbon nanotubes. *J. Phys. Chem. C* **117**, 593–602 (2013).
157. Held, K. D. & Melder, D. C. Toxicity of the Sulfhydryl-Containing Radioprotector Dithiothreitol. *Radiat. Res.* **112**, 544–554 (1987).
158. Hirano, S. & Suzuki, K. T. Exposure, metabolism, and toxicity of rare earths and related compounds. *Environ. Health Perspect.* **104**, 85–95 (1996).
159. Jeong, S. *et al.* High-throughput evolution of near-infrared serotonin nanosensors. *Sci. Adv.* **5**, 1–13 (2019).
160. Yang, K. K., Wu, Z. & Arnold, F. H. Machine-learning-guided directed evolution for protein engineering. *Nat. Methods* **16**, 687–694. arXiv: 1811.10775 (2019).
161. Lin, Y. R. *et al.* Control over overall shape and size in de novo designed proteins. *Proc. Natl. Acad. Sci. U. S. A.* **112**, E5478–E5485 (2015).
162. Bravaya, K. B., Grigorenko, B. L., Nemukhin, A. V. & Krylov, A. I. Quantum chemistry behind bioimaging: insights from ab initio studies of fluorescent proteins and their chromophores. *Acc. Chem. Res.* **45**, 265–275 (2012).
163. Ormo, M. *et al.* Crystal structure of the Aequorea victoria green fluorescent protein. *Science* (80-.). **273**, 1392–1395 (1996).
164. Chen, K. & Arnold, F. H. Tuning the activity of an enzyme for unusual environments: Sequential random mutagenesis of subtilisin E for catalysis in dimethylformamide. *Proc. Natl. Acad. Sci. U. S. A.* **90**, 5618–5622 (1993).
165. Jain, S. C., Shinde, U., Li, Y., Inouye, M. & Berman, H. M. The crystal structure of an autoprocessed Ser221Cys-subtilisin E-propeptide complex at 2.0 Å resolution. *J. Mol. Biol.* **284**, 137–144 (1998).
166. Bhardwaj, G. *et al.* Accurate de novo design of hyperstable constrained peptides. *Nature* **538**, 329–335 (2016).
167. Oresic, M. & Shalloway, D. Specific Correlations between Relative Synonymous Codon Usage and Protein Secondary Structure. *J. Mol. Biol.* **281**, 31–48 (1998).
168. Planck Collaboration. Astrophysics Special feature Planck 2015 results. *Astron. Astrophys.* **594**. arXiv: 1502.01589 (2016).
169. Shih, Y.-p. *et al.* High-throughput screening of soluble recombinant proteins. *Protein Sci.* **11**, 1714–1719 (2002).
170. Walter, G., Konrad, B. & Lueking, A. High-throughput protein arrays : prospects for molecular diagnostics. *Trends Mol. Med.* **8**, 250–253 (2002).

Bibliography

171. Wildt, R. M. T. D., Mundy, C. R., Gorick, B. D. & Tomlinson, I. M. Antibody arrays for high-throughput screening of antibody – antigen interactions. *Nat. Biotechnol.* **18**, 989–994 (2000).
172. Yang, G. & Withers, S. G. Ultrahigh-Throughput FACS-Based Screening for Directed Enzyme Evolution. *ChemBioChem* **10**, 2704–2715 (2009).
173. Dou, J. *et al.* De novo design of a fluorescence-activating β -barrel. *Nature* **561**, 485–491 (2018).
174. Heim, R., Prashert, D. C. & Tsien, R. Y. Wavelength mutations and posttranslational autooxidation of green fluorescent protein. *Proc. Natl. Acad. Sci.* **91**, 12501–12504 (1994).
175. Heim, R. & Tsien, R. Y. Engineering green fluorescent protein for improved brightness , longer wavelengths and fluorescence resonance energy transfer. *Curr. Biol.* **6**, 178–182 (1995).
176. Wachter, R. M., Elsliger, M.-a., Kallio, K., Hanson, G. T. & Remington, S. J. Structural basis of spectral shifts in the yellow-emission variants of green fluorescent protein. *Structure* **6**, 1267–1277 (1998).
177. Cormack, B. P., Valdivia, R. H. & Falkow, S. FACS-optimized mutants of the green fluorescent protein (GFP). *Gene* **173**, 33–38 (1996).
178. Banáš, P., Otyepka, M., Jeřábek, P., Petřek, M. & Damborský, J. Mechanism of enhanced conversion of 1,2,3-Trichloropropane by mutant Haloalkane dehalogenase revealed by molecular modeling. *J. Comput. Aided. Mol. Des.* **20**, 375–383 (2006).
179. Siloto, R. M. & Weselake, R. J. Site saturation mutagenesis: Methods and applications in protein engineering. *Biocatal. Agric. Biotechnol.* **1**, 181–189 (2012).
180. Miyazaki, K. & Arnold, F. H. Exploring nonnatural evolutionary pathways by saturation mutagenesis: Rapid improvement of protein function. *J. Mol. Evol.* **49**, 716–720 (1999).
181. Bloom, J. D., Labthavikul, S. T., Otey, C. R. & Arnold, F. H. Protein stability promotes evolvability. *Proc. Natl. Acad. Sci. U. S. A.* **103**, 5869–5874 (2006).
182. Meyer, M. M., Hochrein, L. & Arnold, F. H. Structure-guided SCHEMA recombination of distantly related β -lactamases. *Protein Eng. Des. Sel.* **19**, 563–570 (2006).
183. Smith, M. A., Romero, P. A., Wu, T., Brustad, E. M. & Arnold, F. H. Chimeragenesis of distantly-related proteins by noncontiguous recombination. *Protein Sci.* **22**, 231–238 (2013).
184. Saito, Y. *et al.* Machine-Learning-Guided Mutagenesis for Directed Evolution of Fluorescent Proteins. *ACS Synth. Biol.* **7**, 2014–2022 (2018).
185. Pavelka, A., Chovancova, E. & Damborsky, J. HotSpot Wizard: A web server for identification of hot spots in protein engineering. *Nucleic Acids Res.* **37**, 376–383 (2009).
186. Kuipers, R. K. *et al.* 3DM: Systematic analysis of heterogeneous superfamily data to discover protein functionalities. *Proteins Struct. Funct. Bioinforma.* **78**, 2101–2113 (2010).

187. Moore, J. C. & Arnold, F. H. Directed evolution of a para-nitrobenzyl esterase for aqueous-organic solvents. *Nat. Biotechnol.* **14**, 303–308 (1996).
188. Socha, R. D. & Tokuriki, N. Modulating protein stability - Directed evolution strategies for improved protein function. *FEBS J.* **280**, 5582–5595 (2013).
189. Arnold, F. H. & Georgiou, G. Directed Enzyme Evolution: Screening and Selection Methods. *Methods Mol. Biol.* **230**. arXiv: arXiv:1011.1669v3 (2003).
190. Xiao, H., Bao, Z. & Zhao, H. High throughput screening and selection methods for directed enzyme evolution. *Ind. Eng. Chem. Res.* **54**, 4011–4020 (2015).
191. Van Rossum, T., Kengen, S. W. & Van Der Oost, J. Reporter-based screening and selection of enzymes. *FEBS J.* **280**, 2979–2996 (2013).
192. Bloom, J. D., Romero, P. A., Lu, Z. & Arnold, F. H. Neutral genetic drift can alter promiscuous protein functions, potentially aiding functional evolution. *Biol. Direct* **2**, 7–10. arXiv: 0705.0201 (2007).
193. Romero, P. A. & Arnold, F. H. Exploring protein fitness landscapes by directed evolution. *Nat. Rev. Mol. Cell Biol.* **10**, 866–876 (2009).
194. Wang, Y., De, S. & Yan, N. Rational control of nano-scale metal-catalysts for biomass conversion. *Chem. Commun.* **52**, 6210–6224 (2016).
195. Albanese, A., Tang, P. S. & Chan, W. C. The Effect of Nanoparticle Size, Shape, and Surface Chemistry on Biological Systems. *Annu. Rev. Biomed. Eng.* **14**, 1–16 (2012).
196. Kinnear, C., Moore, T. L., Rodriguez-Lorenzo, L., Rothen-Rutishauser, B. & Petri-Fink, A. Form Follows Function: Nanoparticle Shape and Its Implications for Nanomedicine. *Chem. Rev.* **117**, 11476–11521 (2017).
197. Arnold, F. H. Design by Directed Evolution. *Acc. Chem. Res.* **31**, 125–131 (1998).
198. Tsyboulski, D. A., Rocha, J.-d. D. R., Bachilo, S. M., Cognet, L. & Weisman, R. B. Structure-dependent fluorescence efficiencies of individual single-walled carbon nanotubes. *Nano Lett.* **7**, 3080–3085. arXiv: 0709.0196 (2007).
199. Wei, X. *et al.* Photoluminescence Quantum Yield of Single-Wall Carbon Nanotubes Corrected for the Photon Reabsorption Effect. *Nano Lett.* **20**, 410–417 (2020).
200. Hong, G., Antaris, A. L. & Dai, H. Near-infrared fluorophores for biomedical imaging. *Nat. Biomed. Eng.* **1** (2017).
201. Hatami, S. *et al.* Absolute photoluminescence quantum yields of IR26 and IR-emissive Cd1-xHg_xTe and PbS quantum dots – method- and material-inherent challenges. *Nanoscale* **7**, 133–143 (2015).
202. Crochet, J., Clemens, M. & Hertel, T. Quantum yield heterogeneities of aqueous single-wall carbon nanotube suspensions. *J. Am. Chem. Soc.* **129**, 8058–8059 (2007).
203. Lebedkin, S. *et al.* FTIR-luminescence mapping of dispersed single-walled carbon nanotubes. *New J. Phys.* **5**, 140.1–140.11 (2003).

Bibliography

204. Jones, M. *et al.* Analysis of photoluminescence from solubilized single-walled carbon nanotubes. *Phys. Rev. B - Condens. Matter Mater. Phys.* **71**, 1–9 (2005).
205. Dong, L., Joseph, K. L., Witkowski, C. M. & Craig, M. M. Cytotoxicity of single-walled carbon nanotubes suspended in various surfactants. *Nanotechnology* **19** (2008).
206. Park, M. *et al.* Measuring the Accessible Surface Area within the Nanoparticle Corona Using Molecular Probe Adsorption. *Nano Lett.* **19**, 7712–7724 (2019).
207. Giraldo, J. P. *et al.* A Ratiometric Sensor Using Single Chirality Near-Infrared Fluorescent Carbon Nanotubes: Application to in Vivo Monitoring. *Small* **11**, 3973–3984 (2015).
208. Zhang, J. *et al.* Molecular recognition using corona phase complexes made of synthetic polymers adsorbed on carbon nanotubes. *Nat. Nanotechnol.*, 959–968 (2014).
209. Green, M. R. & Sambrook, J. *Molecular cloning: A Laboratory Manual* arXiv: arXiv: 1011.1669v3 (2012).
210. Lee, M. A. *et al.* Implanted Nanosensors in Marine Organisms for Physiological Biologging: Design, Feasibility, and Species Variability. *ACS Sensors* **4**, 32–43 (2019).
211. Golovynskyi, S. *et al.* Optical windows for head tissues in near-infrared and short-wave infrared regions: Approaching transcranial light applications. *J. Biophotonics* **11**, 1–12 (2018).
212. Lee, A. J. *et al.* Bright fluorescence from individual single-walled carbon nanotubes. *Nano Lett.* **11**, 1636–1640 (2011).
213. Mousavi, S. M., Hashemi, S. A., Zarei, M., Amani, A. M. & Babapoor, A. Nanosensors for Chemical and Biological and Medical Applications. *Med. Chem. (Los. Angeles)*. **08** (2018).
214. Riu, J., Maroto, A. & Rius, F. X. Nanosensors in environmental analysis. *Talanta* **69**, 288–301 (2006).
215. Srivastava, A. K., Dev, A. & Karmakar, S. Nanosensors and nanobiosensors in food and agriculture. *Environ. Chem. Lett.* **16**, 161–182 (2018).
216. Soares, R. R. *et al.* Advances, challenges and opportunities for point-of-need screening of mycotoxins in foods and feeds. *Analyst* **143**, 1015–1035 (2018).
217. Singh, J. & Mehta, A. Rapid and sensitive detection of mycotoxins by advanced and emerging analytical methods: A review. *Food Sci. Nutr.* **8**, 2183–2204 (2020).
218. Eskola, M. *et al.* Worldwide contamination of food-crops with mycotoxins: Validity of the widely cited ‘FAO estimate’ of 25%. *Crit. Rev. Food Sci. Nutr.* **60**, 2773–2789 (2020).
219. Tola, M. & Kebede, B. Occurrence, importance and control of mycotoxins: A review. *Cogent Food Agric.* **2** (2016).
220. Rasch, C., Kumke, M. & Löhmannsröben, H. G. Sensing of Mycotoxin Producing Fungi in the Processing of Grains. *Food Bioprocess Technol.* **3**, 908–916 (2010).

221. Babu, D. & Muriana, P. M. Sensitive quantification of aflatoxin B1 in animal feeds, corn feed grain, and yellow corn meal using immunomagnetic bead-based recovery and real-time immunoquantitative-pcr. *Toxins (Basel)*. **6**, 3223–3237 (2014).
222. Cramer, A., Raillard, S. A., Bermudez, E. & Stemmer, W. P. DNA shuffling of a family of genes from diverse species accelerates directed evolution. *Nature* **391**, 288–291 (1998).
223. Anukul, N., Vangnai, K. & Mahakarnchandkul, W. Significance of regulation limits in mycotoxin contamination in Asia and risk management programs at the national level. *J. Food Drug Anal.* **21**, 227–241 (2013).
224. Rodrigues, I. & Naehrer, K. A three-year survey on the worldwide occurrence of mycotoxins in feedstuffs and feed. *Toxins (Basel)*. **4**, 663–675 (2012).
225. Nißler, R. *et al.* Sensing with Chirality-Pure Near-Infrared Fluorescent Carbon Nanotubes. *Anal. Chem.* **93**, 6446–6455 (2021).
226. Muga, F. C., Workneh, T. S. & Marennya, M. O. Electrical properties of maize kernels contaminated with aflatoxin. *Agric. Eng. Int. CIGR J.* **20**, 197–205 (2018).
227. Gillen, A. J. *et al.* Templating colloidal sieves for tuning nanotube surface interactions and optical sensor responses. *J. Colloid Interface Sci.* **565**, 55–62 (2020).
228. Johnson, W. W. & Guengerich, F. P. Reaction of aflatoxin B1 exo-8,9-epoxide with DNA: Kinetic analysis of covalent binding and DNA-induced hydrolysis. *Proc. Natl. Acad. Sci. U. S. A.* **94**, 6121–6125 (1997).
229. McLean, M. & Dutton, M. F. Cellular interactions and metabolism of aflatoxin: An update. *Pharmacol. Ther.* **65**, 163–192 (1995).
230. Shieh, J. C. & Song, P. S. Photochemically Induced Binding of Aflatoxins to DNA and its Effects on Template Activity. *Cancer Res.* **40**, 689–695 (1980).
231. Misra, R. P., Muench, K. F. & Humayun, M. Z. Covalent and Noncovalent Interactions of Aflatoxin with Defined Deoxyribonucleic Acid Sequences. *Biochemistry* **22**, 3351–3359 (1983).
232. Stone, M. P., Gopalakrishnan, S., Harris, T. M. & Graves, D. E. Carcinogen-nucleic acid interactions: Equilibrium binding studies of aflatoxins b1 and b2. *J. Biomol. Struct. Dyn.* **5**, 1025–1041 (1988).
233. Ma, L., Wang, J. & Zhang, Y. Probing the characterization of the interaction of aflatoxins B1 and G1 with calf thymus DNA in vitro. *Toxins (Basel)*. **9** (2017).
234. McKeague, M. *et al.* Screening and initial binding assessment of fumonisin B 1 aptamers. *Int. J. Mol. Sci.* **11**, 4864–4881 (2010).
235. Pinals, R. L. *et al.* Rapid SARS-CoV-2 Spike Protein Detection by Carbon Nanotube-Based Near-Infrared Nanosensors. *Nano Lett.* **21**, 2272–2280 (2021).
236. Jiang, S. *et al.* Surface-functionalized nanoparticles for biosensing and imaging-guided therapeutics. *Nanoscale* **5**, 3127–3148 (2013).

Bibliography

237. Thiruppathi, R., Mishra, S., Ganapathy, M., Padmanabhan, P. & Gulyás, B. Nanoparticle functionalization and its potentials for molecular imaging. *Adv. Sci.* **4** (2017).
238. Godin, A. G. *et al.* Single-nanotube tracking reveals the nanoscale organization of the extracellular space in the live brain. *Nat. Nanotechnol.* **12**, 238–243 (2017).
239. Chica, R. A., Doucet, N. & Pelletier, J. N. Semi-rational approaches to engineering enzyme activity: Combining the benefits of directed evolution and rational design. *Curr. Opin. Biotechnol.* **16**, 378–384 (2005).
240. Carvalho, J., Queiroz, J. A. & Cruz, C. Circular dichroism of G-Quadruplex: A laboratory experiment for the study of topology and ligand binding. *J. Chem. Educ.* **94**, 1547–1551 (2017).
241. Kikin, O., D’Antonio, L. & Bagga, P. S. QGRS Mapper: A web-based server for predicting G-quadruplexes in nucleotide sequences. *Nucleic Acids Res.* **34**, 676–682 (2006).
242. Wanrooij, P. H., Uhler, J. P., Simonsson, T., Falkenberg, M. & Gustafsson, C. M. G-quadruplex structures in RNA stimulate mitochondrial transcription termination and primer formation. *Proc. Natl. Acad. Sci. U. S. A.* **107**, 16072–16077 (2010).
243. Li, Q. J., Tong, X. J., Duan, Y. M. & Zhou, J. Q. Characterization of the intramolecular G-quadruplex promoting activity of Est1. *FEBS Lett.* **587**, 659–665 (2013).
244. Shiraki, T., Tsuzuki, A., Toshimitsu, F. & Nakashima, N. Thermodynamics for the Formation of Double-Stranded DNA-Single-Walled Carbon Nanotube Hybrids. *Chemistry* **22**, 4774–4779 (2016).
245. Alegret, N., Santos, E., Rodríguez-Forteza, A., Rius, F. X. & Poblet, J. M. Disruption of small double stranded DNA molecules on carbon nanotubes: A molecular dynamics study. *Chem. Phys. Lett.* **525–526**, 120–124 (2012).
246. Neaves, K. J., Huppert, J. L., Henderson, R. M. & Edwardson, J. M. Direct visualization of G-quadruplexes in DNA using atomic force microscopy. *Nucleic Acids Res.* **37**, 6269–6275 (2009).
247. Bloom, J. D. & Arnold, F. H. In the light of directed evolution: Pathways of adaptive protein evolution. *Proc. Natl. Acad. Sci.* **106**, 9995–10000 (2009).
248. Backman, T. W., Cao, Y. & Girke, T. ChemMine tools: An online service for analyzing and clustering small molecules. *Nucleic Acids Res.* **39**, 486–491 (2011).
249. Early, T. A., Olmsted, J., Kearns, D. R. & Lezius, A. G. Base pairing structure in the poly d(G-T) double helix: Wobble base pairs. *Nucleic Acids Res.* **5**, 1955–1970 (1978).
250. Gillen, A. J., Antonucci, A., Reggente, M., Morales, D. & Boghossian, A. A. Distinguishing dopamine and calcium responses using XNA-nanotube sensors for improved neurochemical sensing. *bioRxiv* (2021).
251. Pfohl, M. *et al.* Fitting Single-Walled Carbon Nanotube Optical Spectra. *ACS Omega* **2**, 1163–1171. arXiv: arXiv:1408.1149 (2017).

252. Simpson, J. R., Fagan, J. A., Becker, M. L., Hobbie, E. K. & Hight Walker, A. R. The effect of dispersant on defects in length-separated single-wall carbon nanotubes measured by Raman spectroscopy. *Carbon N. Y.* **47**, 3238–3241 (2009).
253. Yang, Q.-H. *et al.* Loosening the DNA wrapping around single-walled carbon nanotubes by increasing the strand length. *Nanotechnology* **20**, 195603 (2009).
254. Safaee, M. M., Gravely, M., Rocchio, C., Simmeth, M. & Roxbury, D. DNA Sequence Mediates Apparent Length Distribution in Single-Walled Carbon Nanotubes. *ACS Appl. Mater. Interfaces* **11**, 2225–2233 (2019).
255. Rahman, M. W., Alam, K. M. & Pramanik, S. Long Carbon Nanotubes Functionalized with DNA and Implications for Spintronics. *ACS Omega* **3**, 17108–17115 (2018).
256. Gravely, M., Safaee, M. M. & Roxbury, D. Oligonucleotide Length Determines Intracellular Stability of DNA-Wrapped Carbon Nanotubes. *bioRxiv* (2019).
257. Nißler, R. *et al.* Quantification of the Number of Adsorbed DNA Molecules on Single-Walled Carbon Nanotubes. *J. Phys. Chem. C* **123**, 4837–4847 (2019).
258. Ellington, A. & Pollard, J. D. Synthesis and Purification of Oligonucleotides. *Curr. Protoc. Mol. Biol.* **42**, 1–25 (1998).
259. Gillam, E., Copp, J. N. & Ackerley, D. F. *Directed Evolution Library Creation: Methods and Protocols* (2003).
260. Goldsmith, M., Kiss, C., Bradbury, A. R. & Tawfik, D. S. Avoiding and controlling double transformation artifacts. *Protein Eng. Des. Sel.* **20**, 315–318 (2007).
261. Citartan, M. *et al.* Asymmetric PCR for good quality ssDNA generation towards DNA aptamer production. *Songklanakarin J. Sci. Technol.* **34**, 125–131 (2012).
262. Liang, Z. *et al.* Solubilization of single-walled carbon nanotubes with single-stranded DNA generated from asymmetric PCR. *Int. J. Mol. Sci.* **8**, 705–713 (2007).
263. Wang, X., Lim, H. J. & Son, A. Characterization of denaturation and renaturation of DNA for DNA hybridization. *Environ. Health Toxicol.* **29**, e2014007 (2014).
264. Geiduschek, E. P. & Herskovits, T. T. Nonaqueous solutions of DNA. Reversible and irreversible denaturation in methanol. *Arch. Biochem. Biophys.* **95**, 114–129 (1961).
265. Markarian, S. A., Harutyunyan, L. R. & Harutyunyan, R. S. The properties of mixtures of sodium dodecylsulfate and diethylsulfoxide in water. *J. Solution Chem.* **34**, 361–368 (2005).
266. O'Neil, M. J. *The Merck Index: An Encyclopedia of Chemicals, Drugs, and Biologicals*. 14th ed. (ed Merck Research Laboratories) (2006).
267. Bazin, I. *et al.* Impact of pH on the stability and the cross-reactivity of ochratoxin A and citrinin. *Toxins (Basel)*. **5**, 2324–2340 (2013).
268. Bol, E. K., Araujo, L., Veras, F. F. & Welke, J. E. Estimated exposure to zearalenone, ochratoxin A and aflatoxin B1 through the consume of bakery products and pasta considering effects of food processing. *Food Chem. Toxicol.* **89**, 85–91 (2016).

Bibliography

269. Krska, R. *et al.* Determination of molar absorptivity coefficients for major type-B trichothecenes and certification of calibrators for deoxynivalenol and nivalenol. *Anal. Bioanal. Chem.* **388**, 1215–1226 (2007).
270. Wu, X., Murphy, P., Cunnick, J. & Hendrich, S. Synthesis and characterization of deoxynivalenol glucuronide: Its comparative immunotoxicity with deoxynivalenol. *Food Chem. Toxicol.* **45**, 1846–1855 (2007).
271. Kovalskaya, N. E., Kuznetsova, N. A. & Sokolova, I. V. Spectral determination of quantum yields of psoralen photodestruction in water and alcohol environments. *Atmos. Ocean. Opt.* **17**, 194–196 (2004).
272. Taniguchi, M. & Lindsey, J. S. Database of Absorption and Fluorescence Spectra of >300 Common Compounds for use in PhotochemCAD. *Photochem. Photobiol.* **94**, 290–327 (2018).

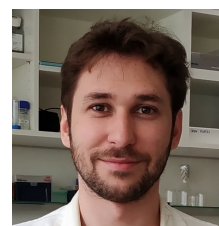
Benjamin Lambert

French

Born June 27th, 1994

boisriou@hotmail.fr

ORCID: 0000-0001-9847-8835



Education

- **Ecole Polytechnique Fédérale de Lausanne** Lausanne, Switzerland
Ph.D Chemical Engineering 2016 - 2021
- **Université Joseph Fourier** Grenoble, France
M.Sc. in Fundamental Physics and Nanosciences 2014 - 2016
- **Université de Rennes 1** Rennes, France
B.Sc. in Physics 2012 - 2014
- **Lycée Chateaubriand** Rennes, France
Preparatory school in Mathematics 2011 - 2012
- **Lycée Jean XXIII** Quintin, France
Baccalauréat with honours 2011

Research Experience

- **Master Thesis** EPFL, Switzerland
Laboratory of Nanobiotechnology, Prof. A. A. Boghossian Feb. 2016 - Aug. 2016
High-throughput screening using near-infrared fluorescence microscopy of bio-activated single-walled carbon nanotubes
Contact: ardemis.boghossian@epfl.ch
- **Research Assistant** Institut Néel, Grenoble
CNRS, Prof. H. Guillou Mar. 2015 - June 2015
Mounting of an optical setup for fluorescence microscopy and optical trapping
Contact: Herve.Guillou@neel.cnrs.fr
- **Research Assistant** Institut de Physique de Rennes, Rennes
CNRS, Prof. J. L. Le Garrec May 2014 - July 2014
Reactivity of charged species with neutral systems in gaseous phase
- **Research Assistant** Institut de Physique de Rennes, Rennes
CNRS, Dr D. Morineau May 2013 - June 2013
Study of ionic liquids confined in silica nanotubes by impedance spectroscopy
Contact: denis.morineau@univ-rennes1.fr

Publications List and Conferences Attended

- Gillen, A.*, **Lambert, B.***, Antonucci, A., Molina-Romero D., & Boghossian, A. A. (2021). Modulating the properties of DNA-SWCNT sensors using chemically modified DNA, bioRxiv. doi : 10.1101/2021.02.20.432105
- **Lambert, B.**, Gillen, A. & Boghossian, A. A. (2020). Synthetic Biology: A Solution for Tackling Nanomaterial Challenges, The Journal of Physical Chemistry Letters, Vol. 11 (p. 4791-4802). doi : 10.1021/acs.jpcclett.0c00929
- Kamaei, S., Saeidi, A., Jazaeri, F., Rassekh, A., Oliva, N., Cavalieri, M., **Lambert, B.** & Ionescu, A. M. (2020). An Experimental Study on Mixed-Dimensional 1D-2D van der Waals Single-Walled Carbon Nanotube-WSe2 Hetero-Junction, IEEE Electron Device Letters, Vol. 41 (p. 645-648). doi : 10.1109/LED.2020.2974400
- Gillen, A., Siefman, D., Wu, S-J., Bourmaud, C., **Lambert, B.** & Boghossian, A. A. (2019). Templating colloidal sieves for tuning nanotube surface interactions and optical sensor responses, Journal of Colloid and Interface Science, Vol. 565 (p. 55-62). doi : 10.1016/j.jcis.2019.12.058
- **Lambert, B.**, Gillen, A., Schuergers, N., Wu, S-J. & Boghossian, A. A. (2019). Directed evolution of the optoelectronic properties of synthetic nanomaterials, Chemical Communications, Vol. 55 (p. 3239-3242). doi : 10.1039/C8CC08670B
- Zubkovs, V., Antonucci, A., Schuergers, N., **Lambert, B.**, Latini, A., Ceccarelli, R., Santinelli, A., Rogov, A., Ciepielewski, D. & Boghossian, A. A. (2018). Spinning-disc confocal microscopy in the second near-infrared window (NIR-II), Scientific Reports, Vol. 8. doi : 10.1038/s41598-018-31928-y
- Zubkovs, V., Schuergers, N., **Lambert, B.**, Ahunbay, E. & Boghossian, A. A. (2017). Mediatorless, Reversible Optical Nanosensor Enabled through Enzymatic Pocket Doping, Small, Vol. 1701654 (p.1-10). doi : 10.1002/smll.201701654
- 235th ECS Meeting (2019), Dallas (US)
- 2019 AIChE Annual Meeting (2019), Orlando (US)
- SCS Fall Meeting (2021), virtual

Skills

- Programming and Software:
 - Mac OS, Windows
 - \LaTeX , Microsoft Office, Adobe Illustrator
 - ImageJ, Matlab, Python, ChemDraw, LabVIEW
- Instrumental
 - Absorbance and fluorescence spectroscopy, fluorescence microscopy
 - Microscope assembly, functionalisation of nanomaterials
 - PCR, gel electrophoresis
- Languages
 - *Native*: French
 - *Fluent*: English
 - *Beginner*: Spanish, Italian